

Excitation Energy Transfer in Pheophorbide *a* Complexes

A Mixed Quantum-Classical Description

D I S S E R T A T I O N

zur Erlangung des akademischen Grades

doctor rerum naturalium

(Dr. rer. nat.)

im Fach Physik

eingereicht an der
Mathematisch-Naturwissenschaftlichen Fakultät I
Humboldt-Universität zu Berlin

von

Dipl.-Phys. Jörg Megow

Präsident der Humboldt-Universität zu Berlin:
Prof. Dr. Jan-Hendrik Olbertz

Dekan der Mathematisch-Naturwissenschaftlichen Fakultät I:
Prof. Stefan Hecht PhD

Gutachter:

1. PD Dr. habil. Volkhard May
2. Prof. Dr. Ulrich Kleinekathöfer
3. Prof. Dr. Nikolaus Ernsting

eingereicht am: 25.09.2012

Tag der mündlichen Prüfung: 15.02.2013

Für Inna und Anna

Certainly no subject or field is making more progress on so many fronts at the present moment, than biology, and if we were to name the most powerful assumption of all, which leads one on and on in an attempt to understand life, it is that all things are made of atoms, and that everything that living things do can be understood in terms of the jiggings and wiggings of atoms. – Richard Phillips Feynman

[1]

Abstract

This thesis investigates the excitation energy transfer in pheophorbide *a* complexes. The P_4 and the P_{16} molecule consist of four and sixteen pheophorbide *a* molecules, respectively, which are covalently bound to a DAB dendrimer of the first (P_4) and third (P_{16}) generation. The P_N complexes in explicit ethanol solution are investigated utilizing a mixed quantum-classical methodology. Classical molecular dynamics simulations are carried out in order to generate nuclei trajectories of the system. The time-dependent Schrödinger equation is solved for the first excited electronic chromophore complex state, the particular Hamiltonian depends parametrically on the classical nuclear coordinates. This coordinate dependence consists of two parts. The first part is the electrostatic contribution, containing the electrostatic couplings of each pheophorbide *a* with the other pheophorbide *a* molecules, the DAB dendrimer and the solvent. The second part is the vibrational contribution, containing the potential energy fluctuation of each pheophorbide *a* due to vibration. In this thesis a method is introduced which allows the computation of this vibrational contribution in harmonic approximation, utilizing the second derivatives of the respective potential energy surfaces. The method is compared with other common approaches to compute this vibrational contribution, and the high quality of the method is proven.

Three different ansatzes were utilized to compute the time development of the excitation energy transfer within the chromophore complexes. First of all, the expansion coefficients that result from the solution of the time-dependent Schrödinger equation are utilized to compute averaged time-dependent populations. Secondly, the expansion coefficients are used to compute excitation energy transfer rates in second order of the excitonic coupling. Thirdly, the time scale of the excitation energy transfer is derived from the delay-time dependent transient anisotropy. The transient anisotropy is calculated by solving the time-dependent Schrödinger equation, including the transitions between the electronic ground and first excited chromophore complex state as well as the transitions between the electronic first and second excited chromophore complex state. Therefore, the electromagnetic field is included directly in the Hamiltonian of the system. The temporal behaviour of the excitation energy transfer is exactly the same for the three approaches.

In addition, the molecular dynamics data are utilized to compute linear and transient spectra of the chromophore complexes' Q_y band. For a single pheophorbide *a* in ethanol, additionally the Q_x band and the vibrational progression are computed. Furthermore, the linear absorption of pheophorbide *a* and P_{16} next to a gold nanoparticle is studied, and the amplification of the molecular absorption signal due to the presence of the nanoparticle can be shown. Finally, a new method is introduced to treat distance and conformation dependent screening of the excitonic coupling parametrically within a mixed quantum-classical description.

Zusammenfassung

Die Arbeit untersucht den Anregungsenergietransfer in supramolekularen Phäophorbid-*a*-Komplexen. Das P_4 - und das P_{16} -Molekül bestehen aus vier beziehungsweise sechzehn Phäophorbid-*a*-Molekülen, die kovalent an DAB-Dendrimere der ersten (P_4) und dritten (P_{16}) Generation gebunden sind. Die P_N -Komplexe in explizitem Lösungsmittel werden im Rahmen einer gemischt quanten-klassischen Methode untersucht. Klassische Molekulardynamik-Simulationen werden durchgeführt, um Kerntrajektorien zu berechnen. Die zeitabhängige Schrödingergleichung wird für den ersten elektronisch angeregten Chromophorkomplex-Zustand gelöst, der entsprechende Hamiltonoperator hängt parametrisch von den Kernkoordinaten ab. Diese Abhängigkeit von den Kernkoordinaten besteht aus zwei Anteilen. Der erste Anteil ist der elektrostatische Beitrag. Dieser enthält die entsprechende elektrostatische Kopplung der Phäophorbid-*a*-Moleküle mit den anderen Phäophorbid-*a*-Molekülen des Komplexes, mit dem DAB-Dendrimer und mit den Lösungsmittelatomen. Der zweite Anteil ist der Schwingungsbeitrag. Dieser enthält die schwingungsbedingte Energiefluktuation für jedes Phäophorbid-*a*-Molekül des Chromophorkomplexes. In dieser Arbeit wird eine Methode vorgestellt, die die Berechnung dieses Schwingungsbeitrags in harmonischer Näherung ermöglicht. Dabei werden die zweiten Ableitungen der entsprechenden Potentialenergieflächen des Moleküls benötigt. Die Methode wird mit anderen gängigen Ansätzen, den Schwingungsbeitrag zu berechnen, verglichen. Die Qualität der Methode wird bewiesen.

Es werden drei verschiedene Ansätze benutzt, um das Zeitverhalten des Anregungsenergietransfers innerhalb der Chromophorkomplexe zu berechnen. Die Expansionskoeffizienten, die von der Lösung der zeitabhängigen Schrödingergleichung resultieren, werden zunächst benutzt, um Anregungsenergietransferraten in zweiter Ordnung der exzitonischen Kopplung zu erhalten. Des weiteren werden die Expansionskoeffizienten verwendet, um gemittelte zeitabhängige Populationen zu berechnen. Zudem wird die Zeitskala des Anregungsenergietransfers aus der zeitabhängigen transienten Anisotropie erhalten. Die Berechnung der transienten Anisotropie beruht auf der Lösung der zeitabhängigen Schrödingergleichung, welche Übergänge zwischen dem elektronischen Grund- und ersten angeregten Zustand beziehungsweise Übergänge zwischen dem elektronisch ersten und zweiten angeregten Zustand durch explizite Betrachtung des elektromagnetischen Feldes enthält. Für alle drei Ansätze ergibt sich der gleiche zeitliche Verlauf des Anregungsenergietransfers.

Die Molekulardynamik-Trajektorien werden zudem benutzt, um lineare und transiente Spektren der Q_y -Banden der Chromophorkomplexe zu berechnen. Für ein einzelnes Phäophorbid-*a*-Molekül in Ethanol werden zusätzlich die Q_x -Bande und die Schwingungsprogression berechnet. Außerdem wird die lineare Absorption von Phäophorbid *a* und P_{16} neben einem Gold-Nanopartikel untersucht, die erwartete Verstärkung des Absorptionssignals durch die Präsenz des Nanoteilchens wird gezeigt. Abschließend wird eine neue Methode vorgestellt, die es erlaubt, die abstands- und konformationsabhängige Abschirmung der exzitonischen Kopplung parametrisch in die gemischt quanten-klassische Methode zu integrieren.

Contents

1	Introduction	1
2	The P_N dendrimer - a supramolecular complex	5
2.1	Pheophorbide <i>a</i> and P _N	5
2.1.1	The Pheo molecule	5
2.1.2	The P ₄ and P ₁₆ supramolecular complex	5
2.2	Optical spectra of Pheo, P ₄ , and P ₁₆	7
2.2.1	Linear absorption of Pheo, P ₄ , and P ₁₆	7
2.2.2	Transient absorption spectroscopy	7
2.2.3	Linear absorption of the Pheo dimer	9
3	The mixed quantum-classical methodology	11
3.1	Introduction	11
3.1.1	Approximate quantum descriptions	11
3.1.2	The Born-Oppenheimer approximation	14
3.1.3	The dynamical classical limit	14
3.1.4	Ehrenfest dynamics	15
3.1.5	Classical force fields	15
3.1.6	The ground state classical path approximation	16
3.2	The chromophore complex wave function	17
3.2.1	Frenkel excitons	18
3.3	The CC Hamiltonian	19
3.3.1	Kinetic energy	21
3.3.2	Potential energy due to intramolecular vibration	21
3.3.3	Coulomb interaction	22
3.4	Computation of the Hamiltonian matrix elements	25
3.4.1	Electronic ground state matrix element	25
3.4.2	First excited electronic state matrix elements	26
3.4.3	Second excited electronic state matrix elements	27
3.5	Energy gap function	28
3.6	Calculation of linear absorption	30
3.6.1	Linear absorption of the Q _x band	31
3.6.2	Vibrational progression	32
3.7	EET rates	34
3.7.1	Rate equations in the dynamical classical limit	35
3.7.2	Further approximations to the transfer rates	37
3.8	Calculation of transient absorption	37
3.8.1	Time-dependent polarization	39
3.8.2	Signal polarization, method I	40
3.8.3	Signal polarization, method II	41
3.8.4	Differential transient absorption	41
3.8.5	Transient anisotropy	41
3.9	Analytical calculation of the transient anisotropy	42
3.9.1	The density operator after pump pulse excitation	42

3.9.2	Transient absorption line shape	44
4	Methods	51
4.1	Molecular dynamics simulations	51
4.1.1	Utilized programs	51
4.1.2	MD parameters	51
4.1.3	Numerical integration	53
4.1.4	NVT and NPT ensemble	53
4.1.5	Computation of MD trajectories	54
4.1.6	Ensemble average	55
4.2	Electronic structure calculations	57
4.2.1	Estimation of the Stokes shift	58
4.3	Energy gap fluctuation and transition coupling from MD trajectories	59
4.3.1	Computing energy fluctuation due to solvent coupling	59
4.3.2	Computing the transition couplings	59
4.4	Intramolecular vibration in harmonic approximation	61
4.4.1	Rotation of the Pheo molecule	62
4.4.2	Molecular bending	63
4.4.3	Electronic ground state Pheo reference trajectory	64
4.4.4	Electronic first excited state Pheo reference trajectory	66
4.4.5	Errors within the energy gap function calculation	67
4.5	Solving the TDSE utilizing molecular dynamics trajectories	75
4.5.1	Solving the TDSE for singly excited P_N systems	75
4.5.2	Solving the TDSE including the electromagnetic field for P_4	76
5	Pheo, P_4 and P_{16}: EET and optical properties	77
5.1	The single Pheo molecule in ethanol solution	77
5.1.1	The energy gap function	77
5.1.2	Linear absorption	79
5.2	The P_4 dendrimer	83
5.2.1	Linear absorption	84
5.2.2	EET rates	87
5.2.3	Differential transient absorption	94
5.3	The P_{16} dendrimer	99
5.3.1	Linear absorption	99
5.3.2	Excitation energy transfer	99
6	Pheo and P_{16} near metal nano particles	105
6.1	Introduction	105
6.2	The P_N -MNP Hamiltonian and singly excited wave function	105
6.3	Linear absorption of Pheo and P_{16} next to a MNP	107
6.3.1	Amplification of the Pheo and P_{16} linear absorption signal	107
6.3.2	Linear absorption for a large number of molecules coupled to the MNP	109
6.3.3	Linear absorption of the Q_x band	110
7	Screening in supramolecular complexes	113
7.1	Introduction	113
7.2	Calculation of the screening factor utilizing the Poisson-TrEsp method	113
7.2.1	Poisson-TrEsp calculations	114
7.2.2	Poisson-TrEsp results for Photosystem I	116
7.3	Fitting of the Poisson-TrEsp calculated screening factor	116
7.3.1	Fitting procedure	116

7.3.2	Quality of the fitted screening	118
7.4	Results	118
7.4.1	Off-size screening factors and distance dependent screening factors	118
7.4.2	Linear absorption for different screening methods	119
7.4.3	Solution of the TDSE for different screening methods	120
8	Summary	123
Appendix A		125
1	Computing the correlation function	125
Appendix B		129
2	Computing the transient absorption for very short delay times	129
Appendix C		135
3	Computing the electronic ground state reference trajectories	135

1 Introduction

The excitation energy transfer (EET) between two chromophores or within large complexes of chromophores plays a fundamental role in science. The pioneering work of Theodor Förster on fluorescence resonance energy transfer (FRET), that describes an EET due to the dipole-dipole coupling of the involved molecules, provided the basis for a high number of applications. It helped to understand the primary processes of photosynthesis in bacteria and higher plants [8]. Moreover, FRET can be utilized to measure the distance between chromophores in several systems that are interesting in biology and chemistry [9]. It can be used, for example, to detect protein-protein interactions and protein conformational changes [10]. Furthermore, the formation of artificial light-harvesting antennae as an application in photovoltaics has given promising results [11, 12].

A detailed understanding of the EET dynamics in supramolecular complexes is essential for decoding light-harvesting in natural systems as well as developing and improving light-harvesting for artificial photosynthesis. In [13, 14] wavelike energy transfer in photosynthetic systems through quantum coherence was proven. The investigations on helical arranged porphyrin polymers in [15] or on linked porphyrin arrays in [16] are examples for the utilization of pump-probe spectra to uncover EET in artificial chromophore complexes. In [17] light-harvesting assemblies were constructed by displaying chromophores on a rod assembly of the tobacco mosaic virus coat protein, the EET was investigated with time-resolved fluorescence spectroscopy. EET in highly ordered systems were examined in [18, 19]. The so-called J-aggregates, or H-aggregates differ according to the mutual orientation of the chromophore transition dipole moments.

EET in supramolecular systems which consist of chromophores bound to dendrimeric structures were presented in [20] (utilizing single molecule spectroscopy) and in [21] (utilizing ensemble measurements). In [22] supramolecular pheophorbide *a* (**Pheo**) complexes P_N , where N is the number of Pheos bound to the repetitively branched diaminobutane (DAB) dendrimer, were investigated.

Within this thesis the P_4 and P_{16} are studied theoretically. The two Pheo complexes are good model systems to study EET. The theoretical description of those supramolecular complexes, treating the complex and the solvent in atomic detail, is to unravel details about the EET within those systems that are not accessible to corresponding experiments.

To ensure a full understanding of EET experiments a theoretical approach is necessary that treats the system in atomic detail. If EET between chromophores is analyzed, not only the chromophores themselves, but also the solvent or protein environment has to be taken into account [23]. The computational time of pure quantum mechanical ab initio methods scale with the number of atoms N^{at} from $(N^{\text{at}})^2 \log(N^{\text{at}})$ up to $(N^{\text{at}})^4$ for Hartree-Fock and density functional theory (DFT) methods [24, 25] or even higher in more sophisticated electron structure calculations [25]. P_4 and P_{16} consist of 370 as well as 1558 atoms. Beyond that the solvent molecules are to be treated directly. It is obvious that EET for such systems can not be treated purely quantum mechanically.

A general overview on the theory of EET within molecular systems is given in [26]. The method of choice for the computation of EET and optical spectra of P_N systems is the mixed quantum-classical description. Within this framework the motion of the nuclei is treated classically by molecular dynamics (MD) simulations. The electronic wave function is calculated quantum mechanically by solving the time-dependent Schrödinger equation (TDSE).

A critical task within mixed quantum-classical methods is computing the energy gap fluc-

1 Introduction

tuation caused by intramolecular vibration and electrostatic coupling to the solvent molecules. Those fluctuations affect optical properties (as the linear absorption linewidth), which can be measured experimentally.

In order to compute the vibrational part of this energy gap fluctuation, different methods have been proposed. Commonly used is the semiempirical ZINDO (Zerner's intermediate neglect of differential overlap) method [27, 28, 29, 30] used to compute the energy gap for each MD snapshot. In [27] the photoexcitation spectrum of an isolated protonated amino acid was calculated and compared with respective experiments. In [28] the EET in the light-harvesting system II was studied. The same authors published 2-dimensional spectra of the FMO (Fenna-Matthews-Olsen) light-harvesting complex in [29]. A very similar method was used in [30] to compute electronic-vibrational coupling in the photosynthetic reaction center of purple bacteria. Computationally more demanding DFT calculations were utilized in [31] to obtain the vibrational part of the energy gap function from each MD snapshot to investigate long-lived coherences in the FMO complex. However, none of the methods cited above result in a perfect agreement with the respective experimentally measured absorption linewidth.

In this thesis, a new method is presented to compute the energy gap fluctuation from MD simulations. The energy gap fluctuation is calculated in harmonic approximation to the single atom vibrations utilizing the MD data and precalculated Hessian matrices. The approach requires only one electronic structure calculation to obtain the harmonic potential energy surface (PES) for each considered electronic Pheo state, which in this thesis are the electronic ground state, the first excited electronic state and the second excited electronic state. Within this thesis only FRET will be treated [2], the Dexter transfer [3] is assumed to contribute only a small correction [4, 5, 6, 7] to the FRET and is therefore neglected.

The appropriateness of the calculated energy gap function is proven by the comparison between calculated and measured linear absorption spectra. Furthermore, possible sources of error are demonstrated and analyzed.

Being able to adequately calculate energy gap fluctuations of the Pheo molecule, the EET dynamics in the complexes P_4 and P_{16} can be investigated. The excitonic coupling between the Pheos within the P_N complex is treated via the Coulomb interaction between atomic transition partial charges [32].

Within this thesis three different approaches are utilized to determine the time scale of the EET for P_4 and P_{16} .

The most straight forward approach is to solve the TDSE for each MD sample. The resulting expansion coefficients are squared and afterwards averaged. Secondly, Förster-like EET rates are computed from the MD simulations in second order of the excitonic coupling. The EET rates are used with standard rate equations to compare the resulting population dynamics with the solution of the TDSE. The third approach on computing EET dynamics within P_4 complexes is the computation of pump-probe spectra. In order to compute pump-probe spectra the overall time-dependent polarization is required. The calculation of nonlinear response functions is circumvented by directly solving the TDSE including the electromagnetic field of the pump and probe pulse. The solution of this TDSE includes all orders of the polarization. Additionally, two different methods to obtain the polarization in probe pulse direction from the overall polarization are applied. The time scale of EET can then be analyzed by calculating the transient anisotropy.

The outline of this thesis is as follows: after an introduction to the P_N complexes in Chap. 2 the mixed quantum-classical methodology is introduced in Chap. 3. The equations of motion for the expansion coefficients of the chromophore complex (CC) wave function are derived. Respective quantum formulas are translated to their mixed quantum-classical analogs. It will be shown how linear absorption, transient absorption and EET rates may be calculated from classical nuclei trajectories within the dynamic classical limit (DCL). The required methods utilized within this thesis will be discussed in Chap. 4. The method to calculate the energy

gap fluctuation from MD trajectories is explained and all sources of error are investigated and analyzed. The results of these calculations will be shown in Chap. 5.

The additional chapters 6 and 7 treat subjects which are related to the content of this thesis but organized separately for the reason of a better overview. Both chapters include introduction, theory, methods and results for the particular subject as a whole.

In Chap. 6 the available MD data for Pheo and P₁₆ are utilized to study the coupling between the respective molecule and a metal nano particle (MNP). The TDSE is solved for the combined Pheo-MNP system. While the MNP is treated via parameters taken from recent experiments [33], the molecule (Pheo and P₁₆) is treated in atomic resolution. The respective calculations result in absorption amplifications of the combined molecule-MNP system compared to the molecular absorption that is in the same order of magnitude as measured in related experiments for similar molecules [33].

Finally, Chap. 7 will complete this thesis, discussing the screening of excitonic coupling. It is known that this screening depends not only on the distance of two chromophores, but also on their mutual orientation. Orientation dependent screening has not been treated within a mixed quantum-classical description so far. Distance dependent screening was utilized in [28, 29]. One possibility to compute orientation and distance dependent screening between two chromophores for fixed mutual chromophore conformations is the Poisson-TrEsp (transition charges from electrostatic potentials) method [34, 35]. In this thesis, for the first time a method is introduced that makes it possible to treat distance and orientation dependent screening within a mixed quantum-classical description. This is achieved by fitting Poisson-TrEsp calculated distance and orientation dependent screening between chromophores to screening functions that describe the screening between single atoms. The method is applied for the computation of P₁₆ linear absorption.

2 The P_N dendrimer - a supramolecular complex

2.1 Pheophorbide *a* and P_N

The chromophore complexes that are investigated theoretically in this thesis are two different Pheo complexes and a single molecule of Pheophorbide *a* (Pheo) in ethanol solution. The respective molecules were studied experimentally in the group of Beate Röder [22, 36].

2.1.1 The Pheo molecule

Pheo is a free-base tetrapyrrole. The structure of Pheo is shown in Fig. 2.1. Pheo is a chlorophyll decomposition product. The molecule is known due to its applicability in photodynamic therapy. More details concerning photodynamic therapy will be given in the following section.

2.1.2 The P_4 and P_{16} supramolecular complex

The P_4 and the P_{16} supramolecular complex consists of Pheo molecules that are covalently bound to (poly(propylene imine)) diaminobutane (DAB) dendrimers. The first synthesis of DAB dendrimers was presented in [37], a nuclear magnetic resonance (NMR) study of the structure and conformation of DAB dendrimers in solution was presented in [38]. P_4 consists of four Pheos that are bound to a DAB-4 dendrimer (1st generation) and P_{16} consists of sixteen Pheos that are bound to a DAB-16 dendrimer (3rd generation). Both DAB dendrimer structures are shown in Fig. 2.2.

The Pheo molecules are covalently bound to the dendrimer by peptide bonds. These systems show a large independence with respect to their mutual orientation (cf. [39]). In Fig. 2.3 and 2.4, P_4 and P_{16} , respectively, are shown. A DAB dendrimer with N connected Pheos is called P_N within this thesis, the DAB dendrimer itself will be referred to as dendrimer.

The P_N chromophore complexes as carriers for photosensitizers

Originally the Pheo dendrimers were planned as carriers of Pheo in photodynamic therapy [40]. The enhanced permeability and retention (EPR) effect [41] was to be used to ensure that the Pheo dendrimers get into the cancer tissue. The principal idea of the EPR effect is that the endothelial cells of tumor cells show wide fenestrations compared to healthy tissue. Those wide fenestrations allow the dendrimers to enter the pathogenic but not the healthy cells.

Inside the cancer tissue, the molecules were to be irradiated with visible light. This irradiation excites the Pheo molecules (or in general the photosensitizer) to the S_1 -state. Chromophores that are suitable photosensitizers in photodynamic therapy may traverse an intersystem crossing (ISC) to the triplet state T_1 [40] with a relatively high probability. This photosensitizer in the triplet state can exchange an electron with an oxygen molecule in the triplet state (the energetic ground state of O_2). After this exchange, the photosensitizer returns to the S_0 -state and oxygen is in the singlet state. The singlet oxygen reacts fast with components of the cell, this process will finally destroy the cell.

However, since the P_N systems did not show a controlled behavior after irradiation and were separated into many different molecules, they were no longer interesting for medical appliance. Nevertheless, they are a nice model system to study excitation energy transfer. The

2 The P_N dendrimer - a supramolecular complex

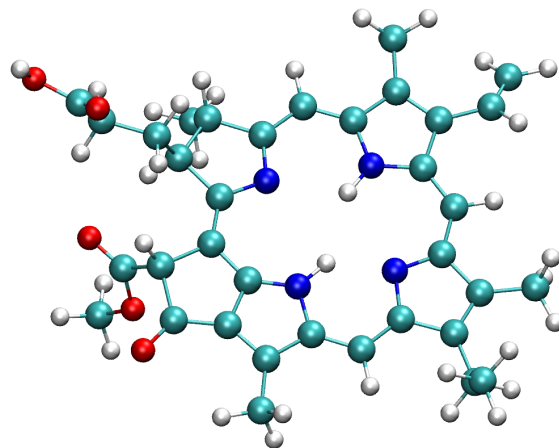


Figure 2.1: Single Pheo molecule. The color code for the atom types is H: white, C: green, N: blue, O: red.

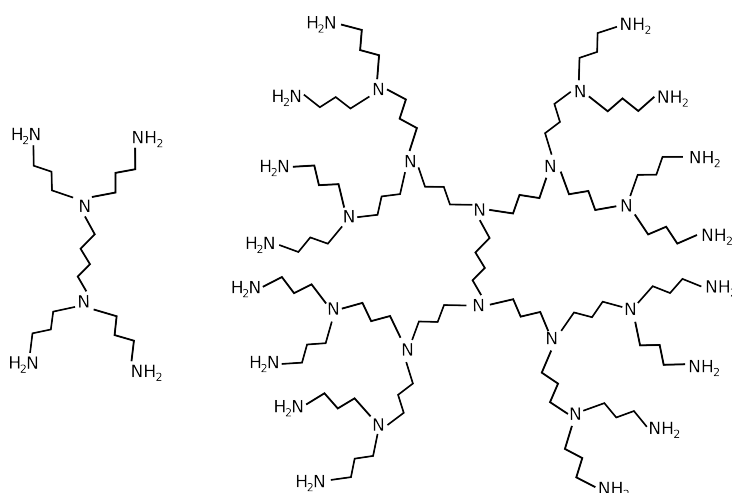


Figure 2.2: Left: the DAB-4 dendrimer (1st generation), right: the DAB-16 dendrimer (3rd generation).

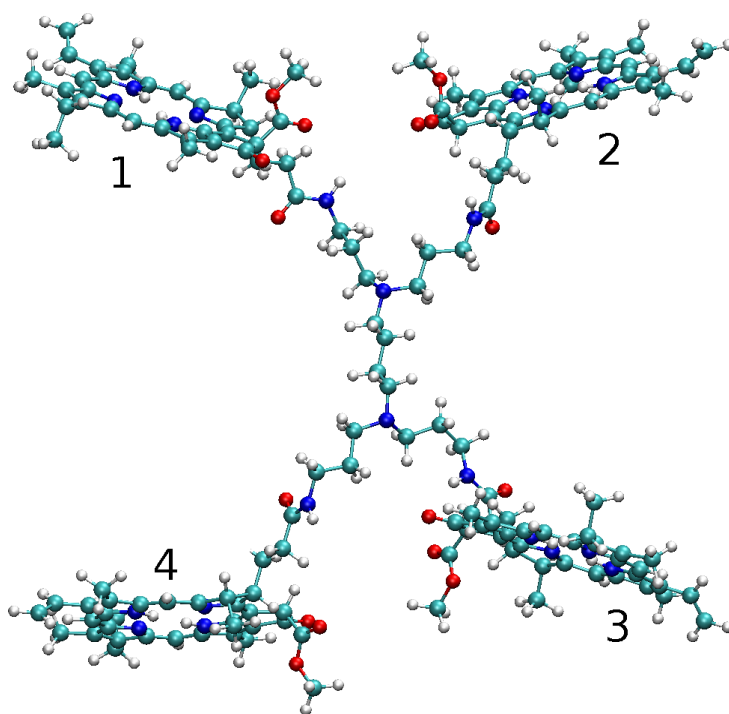


Figure 2.3: P_4 molecule. This conformation was utilized as initial conformation for the P_4 MD runs. The color code for the atom types is H: white, C: green, N: blue, O: red.

time scales of competing processes to the EET within the complexes are orders of magnitude slower. These processes are fluorescence ($4.3 \times 10^7 \text{s}^{-1}$), internal conversion ($1.3 \times 10^6 \text{s}^{-1}$) and intersystem crossing ($1.08 \times 10^8 \text{s}^{-1}$) [40]. The availability of Pheo and P_N to the group of Beate Röder allow a fast comparison of experimental and theoretical results.

2.2 Optical spectra of Pheo, P_4 , and P_{16}

2.2.1 Linear absorption of Pheo, P_4 , and P_{16}

As predicted by the four-orbital theory [42, 43], the Pheo Q_y and Q_x band split. This splitting is due to a symmetry breaking by the hydrogen atoms [40, 42]. The Q_y and Q_x bands represent the two first excited electronic states of Pheo. The other excitations accumulate in the Soret band of Pheo (Fig. 2.5).

The synthesis and the linear absorption measurements of Pheo, P_4 and P_{16} were performed by Steffen Hackbarth. The data from previous measurements were published in [22].

2.2.2 Transient absorption spectroscopy

In the group of Beate Röder a transient absorption spectrometer is set up, which can be utilized to measure transient absorption spectra of the P_N complexes in ethanol. The results of those measurements will enable a comparison of the transient absorption calculations done for this work (as for the transient anisotropy, results in Sec. 5.2.3) with experimental results. Unfortunately, at the moment this work is finished, transient absorption measurements for the P_N chromophore complexes could not yet be carried out.

2 The P_N dendrimer - a supramolecular complex

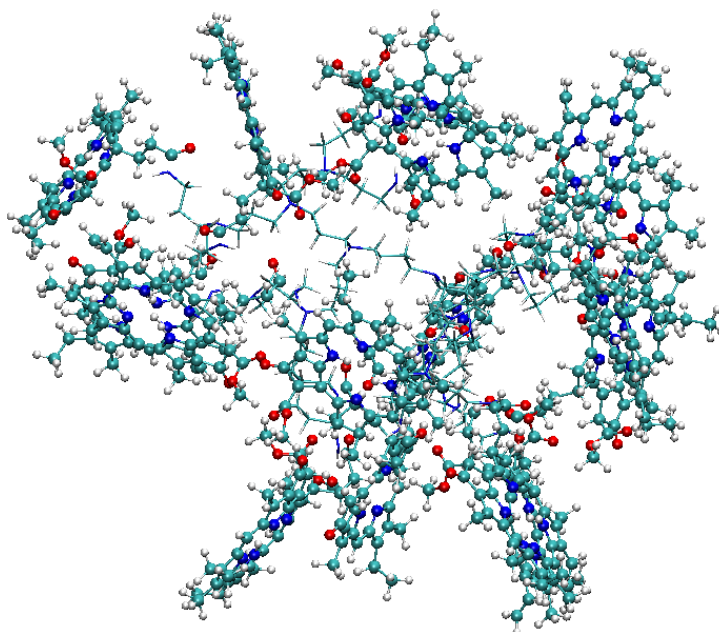


Figure 2.4: P_{16} molecule. The dendrimer is only represented by its bonds. The color code for the atom types is H: white, C: green, N: blue, O: red.

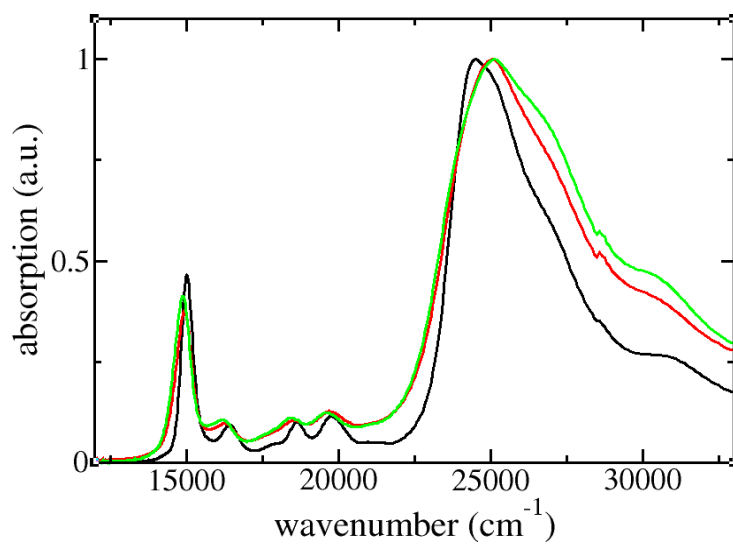


Figure 2.5: Measured absorption of Pheo (black), P_4 (red), and P_{16} (green) in ethanol (cf. [22]).

2.2.3 Linear absorption of the Pheo dimer

Some predictions concerning the optical properties of the P_N complexes can be made by interpreting the linear absorption spectra of Pheo dimers. Respective studies are presented in [36]. In this reference the scalar transition dipole moments of the single Pheo and the Pheo dimer were measured. The respective values of $d_M = 3.6 \pm 0.2$ for the monomer and $d_D = 4.6 \pm 0.6$ for the dimer indicate (within the margin of error) that the oscillator strength of the dimer can be interpreted in terms of the oscillator strengths of two single Pheos which build up the dimer. The oscillator strengths f_M for the monomer and f_D for the dimer are proportional to d_M^2 and d_D^2 , respectively. A dimer contains the double number of molecules compared to a monomer. Thus, the relation $d_D^2 = 2d_M^2$ holds, if the linear absorption of the Pheo dimer can be explained in terms of the linear absorption of two single Pheos. Within the margin of error the measurements presented in [36] confirm this relation. This indicates that Dexter couplings between the two Pheos have no large influence on the single Pheo wave functions, even when dimer formation occurs.

3 The mixed quantum-classical methodology

3.1 Introduction

3.1.1 Approximate quantum descriptions

The propagation in time of a quantum mechanical system can only be calculated numerically for systems with a few degrees of freedom. For larger systems, semiclassical theories have to give approximate descriptions for the quantum propagator. Those approximate descriptions depend on a partly classical treatment of the system. However, those semiclassical theories have to include quantum effects as much as possible, despite the fact that a part of the system is treated classically. In this section some of those approximations will be introduced.

Semiclassical and quasiclassical approaches

The starting point for the short introduction to semiclassical theories is a semiclassical equation that was formulated in the late twenties of the twentieth century. It gives the transition matrix element between an initial position state $|\mathbf{q}_i\rangle$ and a final position state $|\mathbf{q}_f\rangle$. The time-propagation is realized by the propagator $e^{-iHt/\hbar}$, with the Hamiltonian H . The standard semiclassical approximation for this transition is given by the Van Vleck-Gutzwiller propagator [44, 45]

$$\langle \mathbf{q}_i | e^{-iHt/\hbar} | \mathbf{q}_f \rangle_{\text{vVG}} = \sum_{\text{traj}} (2\pi i \hbar)^{-N/2} \left| \det \left(\frac{\partial \mathbf{q}_f}{\partial \mathbf{p}_i} \right) \right|^{-1/2} e^{iS(\mathbf{q}_f, \mathbf{q}_i)/\hbar - i\pi\nu/2}. \quad (3.1)$$

The sum includes all trajectories with the starting point $\mathbf{q}_0 = \mathbf{q}_i$ at $t = 0$, ν is the Maslov index that counts the zeros in the determinant. $S(\mathbf{q}_f, \mathbf{q}_i)$ is the classical action along the respective trajectory. The Van Vleck-Gutzwiller propagator is the result of a stationary phase approximation to the Feynman path integral representation of the quantum propagator. A further description can be found in [46].

In 1970 Miller expressed the final positions \mathbf{q}_f in Eq. 3.1 in terms of the initial momenta \mathbf{p}_i and yielded the so-called semiclassical initial value representation (SC-IVR) [47, 48]. The name IVR results from the fact that the computation of matrix elements can be achieved by an integration over the initial coordinates and momenta of the system. Since it is not the aim of this thesis to discuss semiclassical theories in general, the equations that are derived from Eq. 3.1 or are connected to Eq. 3.1 will not be given here. They can be found in the respective references. A lot of SC-IVR approaches include a balanced treatment of the positions and momenta. Those Herman-Kluk (HK) or coherent state SC-IVR methods [49, 50] have the property that the coherent states are localized in both coordinate and momentum space [45]. Furthermore, the HK-IVR does not cause singularities for real trajectories [51].

The problem in the application of SC-IVR is the strong oscillatory nature of the integrand [45] in Eq. 3.1, this oscillatory behavior also holds for the HK-IVR. It results in the mutual cancellation of positive and negative parts of the integrand and thus in a very bad convergence of the numerics. One way of partially circumventing this sign problem [45] is applying the IVR idea to time-correlation functions of the form

$$C_{AB}(t) = \text{tr} \left(A e^{iHt/\hbar} B e^{-iHt/\hbar} \right). \quad (3.2)$$

3 The mixed quantum-classical methodology

A and B are some arbitrary operators. Inserting a semiclassical propagator (like the Van Vleck-Gutzwiller propagator in Eq. 3.1) for the quantum propagators in Eq. 3.2 results in an integral over the two phase spaces $\{\mathbf{q}_0, \mathbf{p}_0\}$ and $\{\mathbf{q}'_0, \mathbf{p}'_0\}$.

From this point several kinds of approximations can be performed. Two of them will be discussed below.

The first approximation is linearizing the equation with respect to the difference variables $\mathbf{p}'_0 - \mathbf{p}_0$ as well as $\mathbf{q}'_0 - \mathbf{q}_0$ [52]. This approximation results in a quasiclassical single phase space integral that makes use of Wigner-transforms [53] of the operators A and B . The approximation is called linearized SC-IVR (LSC-IVR) or Wigner averaged classical limit. The word quasiclassical denotes that the only difference between the LSC-IVR and a classical formula is the correct quantum mechanical initial state in the LSC-IVR. This approach was later utilized by Shi and Geva [54, 55, 56], who compared several semi- and quasiclassical approaches and stated that the LSC-IVR approach gives qualitatively good results, even when compared to a much more computationally demanding method. It has to be mentioned here that the maximum entropy analytic continuation (MEAC) method [57] further enhances the quality of the LSC-IVR.

The second possible approximation to the double phase space integral in Eq. 3.2 was suggested by Makri and Thompson. They evaluated the forward and backward time propagation in Eq. 3.2 in a single step [58]. This method is called forward-backward IVR (FB-IVR) and eliminates the dominant terms of the classical action (between forward and backward path) and thus lacks the sign problem of the standard IVR. A review about the FB-IVR and other IVR methods is given in [59].

Another approach, which will be mentioned but not discussed in detail, is the Gaussian wavepacket method invented by Heller [60]. The heavy particles are decomposed into time-dependent wavepackets. Those wavepackets follow classical or nearly classical trajectories. A simplification of this method was the later proposed frozen Gaussian approximation (FGA) [61]. In the FGA the form of all Gaussian wave packets is kept fixed. The correlation is not reached for every single Gaussian wave packet, but it is achieved collectively by the superposition of several nearby packets [61].

All the methods discussed above have in common that, with present day computers, they are not capable of describing systems that have the size of the P_N systems in explicit solvent. The first reason is the large number of molecules in those systems that would require a massive computer power. The second reason is the fact that the direct treatment of a molecular system in a FB-IVR approach requires either the full quantum treatment of all present particles or approximations with respect to the interaction between bonded atoms. The former is not possible for large systems (P_N in solution) and the latter requires the knowledge of a variety of parameters.

Molecular dynamics approaches

The alternative to the semiclassical treatment of the nuclei is the classical treatment of all atoms via MD simulations. There exist mainly two types of MD simulations. The first type of simulation is called Ehrenfest dynamics. The nuclei move on one single PES that is a mean field with respect to the possible electronic states [62]. The second type of methods are so-called surface hopping approaches. The first of those surface hopping approaches was proposed by Tully [63, 64]. The system propagates on a PES that belongs to a specific electronic state. At certain points in time the system jumps to another PES.

The comparison of an Ehrenfest and a surface hopping approach, applied to a simple one-dimensional curve-crossing model, showed the superiority of the surface-hopping approach [63]. The calculated transmission and reflection probabilities matched the result of the accurate wave packet propagation [65] best. For complicated systems with multiple quantum degrees of freedom the surface hopping approach requires the computation of a large ensemble of trajec-

tories to achieve decoherence [66]. An alternative option is to damp the coherence [66, 67]. The method introduced by Tully in [63] is referred to as MDQT (molecular dynamics with quantum transitions) in literature. It was, for example, utilized to compute vibrational relaxation of the amide I mode of N-Methylacetamide in D₂O ([68] and references therein). Necessary for a MDQT calculation are the PESs of the important states. Those PESs have to be calculated first. Then the respective force fields have to be derived. For large supramolecular complexes this is hardly feasible. There exist calculations of excitation energy transfer in a so-called phenylene ethynylene dendrimer without solvent in [69]. The simulation time for this molecule was 40 fs. This time scale was long enough to show excitation energy transfer within the dendrimer. The application of this model to larger systems in direct solution seems not to be possible with present day computers.

The motion on a respective PES is most easily done utilizing classical force fields. The atoms are treated as classical particles. This is justified due to the Born-Oppenheimer approximation [70] (cf. Sec. 3.1.2). The interaction between the nearest neighbors within a molecule as well as the non-bonded (electrostatic and van der Waals) interaction to the solvent is approximated via a large set of parameters (cf. Sec. 3.1.5). Classical force fields represent Ehrenfest dynamics in the electronic ground state. Beside the classical force fields, there exist several approaches that treat the nuclear motion *ab initio*, without introducing force parameters. However, the basis for such approaches is also the separation of nuclear and electron degrees of freedom. There exist a variety of methods. While in Ehrenfest dynamics the electronic problem is solved after each time-step in order to compute the forces to the nuclei [62], within the Car Parinello (CP) method [71] nuclei and electronic wave function are propagated simultaneously. It combines MD with density functional theory (DFT), the electronic degrees of freedom are treated as dynamic variables utilizing a Lagrangian. Therefore, a fictitious electron mass has to be introduced, to make sure that the system stays in the electronic ground state. Details for different *ab initio* MD methods are given in [62]. The possibility of applying Car Parinello MD to systems of the same size as P_N in direct solution (several ten thousands of atoms) seems hardly possible. The system size that is manageable with CP methods is a several hundred atoms system at most [72].

Besides the Ehrenfest and surface hopping approaches discussed above there exist approaches that treat quantum effects for systems with many degrees of freedom. Such an approach using Bohmian trajectories was proposed in [73]. Even though the approach was just applied to a simple model system, the authors claim that the approach would even work for larger systems. It was later utilized for the calculation of pump-probe spectra of I₂ in rare gas in [74]. The comparison with experimental results showed quite promising results.

Mixed quantum-classical approaches

The method of choice when large molecular systems including the solvent are to be investigated is the mixed quantum-classical description. Within such an approach the nuclear dynamics are calculated utilizing classical force fields (cf. Sec. 3.1.5), making it possible to treat systems including several ten thousand atoms. The electronic problem is then computed quantum mechanically, parametrically dependent on the nuclear coordinates. Different mixed quantum-classical approaches can be found in [27, 29, 30, 31, 55, 75]. The several mixed quantum-classical methods differ in the approaches that are utilized to derive the electronic gap function from the classical coordinates. Details concerning this approaches can be found in Sec. 3.5. Often such approaches utilize the dynamical classical limit (DCL) to translate full quantum formulas into mixed quantum-classical formulas (cf. Sec. 3.1.3). Those mixed quantum-classical formulas that can be computed utilizing the energy gap functions allow the computation of a variety of optical properties of the system.

However, there exist as well approaches that compute the nuclei trajectories utilizing *ab initio* MD. Such an approach is introduced in [76]. In this reference, pump-probe spectra of I₂

in rare-gas environments are computed.

Comparison between different approaches

In 2005 and 2008 Shi and Geva published two papers comparing three different methodologies translating quantum formulas into mixed quantum-classical expressions that may utilize MD simulation trajectories [55, 56]: the DCL (cf. Sec. 3.1.3), the LSC-IVR, and the FB-IVR. The DCL includes an Ehrenfest MD simulation in the electronic ground state and is therefore applicable to a variety of molecular systems in solution. LSC-IVR and FB-IVR need the calculation of excited state PESs. Shi and Geva considered only mono-atomic particles. There exist IVR computations for small molecular systems. [77] treats I_2 in an argon-cluster, where potential between the iodine atoms is treated by a morse potential. [78] shows the computation of the vibrational spectra of CO_2 introducing IVR molecular dynamics (IVR-MD). The application to more complex molecules is difficult. The method is not capable of treating large systems (as P_N in solution) with present day computers.

The model system used by Shi and Geva consisted of a two state nonpolar monoatomic chromophore in a solvent of 25 nonpolar atoms in a 2D MD simulation, interacting via a Lennard-Jones potential. It is important to mention here that indeed the FB-IVR methods are not capable to treat such large systems as P_N in ethanol, while the application of the LSC-IVR approach would in principle be possible even for large molecular systems, given that the averaged PES (average between electronic ground and first excited state PES) is available for the particular system. The computation of such an averaged PES and the respective force field parameters is not trivial. Therefore, such a computation is no option for solvated P_N systems.

However, the results of Shi and Geva are pleasant concerning the quality of the DCL. For the calculation of the linear absorption it worked as well as the other approaches. Only the results for 2D spectra gave different results, since the wave function propagation in the first excited electronic state is not covered within the DCL.

3.1.2 The Born-Oppenheimer approximation

Ehrenfest MD is based on the Born-Oppenheimer ansatz [26, 62, 70]

$$\Phi_{BO}(r, R; t) = \sum_k \tilde{\zeta}_k(R; t) \phi_k(r, R). \quad (3.3)$$

The total wave function separates into the electronic wave functions $\phi_k(r, R)$ and the vibronic expansion coefficients $\tilde{\zeta}_k(R; t)$ [26]. In the Born-Oppenheimer ansatz in Eq. 3.3 the parametric time-dependence of the wave function $\Phi_{BO}(r, R; t)$ is due to the parametric time-dependence of the vibronic expansion coefficients $\tilde{\zeta}_k(R; t)$. If Eq. 3.3 is inserted into the TDSE

$$i\hbar \frac{\partial}{\partial t} \Phi(r, R, t) = H \Phi(r, R, t), \quad (3.4)$$

a coupled equation for the expansion coefficients $\tilde{\zeta}_k(R; t)$ in the different electronic states can be derived. The neglect of the non-adiabatic coupling finally decouples this equation. This approximation is called the Born-Oppenheimer approximation [26].

3.1.3 The dynamical classical limit

For the calculation of molecular optical properties the respective quantum formula have to be translated into a mixed quantum-classical form. It is well known that this translation is not unambiguous [55, 56]. The possible translation methods compete in both the conservation of the system's quantum properties and its numerical cost. The great advantage of the DCL is its

easy application to full quantum formulas. The trace expression of the quantum formulas is approximated as a multiple integral over initial vibrational coordinates weighted by the thermal distribution [26]. Those vibrational coordinate trajectories can be computed with classical force fields. In Sec. 3.6 it will be explained in detail how the DCL can be achieved for the linear absorption full quantum formula.

3.1.4 Ehrenfest dynamics

After inserting the Born-Oppenheimer ansatz (Eq. 3.3 in Sec. 3.1.2) into the TDSE (Eq. 3.4) and neglecting the non-adiabatic coupling, the TDSE for the electronic Hamiltonian H_{el} reads

$$i\hbar \frac{\partial}{\partial t} \Phi(r, R(t), t) = H_{\text{el}}(R(t)) \Phi(r, R(t), t). \quad (3.5)$$

Both the Hamiltonian and the wave function depend parametrically on the nuclei positions $R(t)$. The electronic positions r are assumed to adapt instantaneously to the $R(t)$. The wave function depends on $R(t)$ as well as on the electron coordinates r and is explicitly time-dependent. R and r both define a set of coordinates, that means $R(t) = \{\mathbf{R}_1(t), \mathbf{R}_2(t), \mathbf{R}_3(t), \dots\}$ and $r = \{\mathbf{r}_1, \mathbf{r}_2, \mathbf{r}_3, \dots\}$. The equation of motion for the nuclei reads

$$M_i \frac{\partial^2}{\partial t^2} \mathbf{R}_i(t) = -\nabla_i \langle \Phi(r, R(t)) | H_{\text{el}}(R(t)) | \Phi(r, R(t)) \rangle, \quad (3.6)$$

where i is the index for the nuclei. The force experienced by the nuclei is dependent on the actual electronic state. The trajectories $\mathbf{R}_i(t)$ may be computed utilizing MD simulations. The right hand side of Eq. 3.6 represents a mean field with respect to the possible electronic states. In honor of Paul Ehrenfest, who addressed the question how quantum mechanics affect the Newton's equations of motion [79], this approach is called Ehrenfest dynamics. One specific form of Ehrenfest dynamics are Ehrenfest dynamics in the electronic ground state. If the respective electronic ground state expectation value in 3.6 is approximated by non-bonded as well as next neighbor interactions, a classical MD force field is derived.

3.1.5 Classical force fields

The great advantage of classical MD simulations is the possibility to simulate very large systems (up to a hundred thousands of atoms for several nanoseconds or even more with special mainframe computers [80]). How to derive the equation of motion for the nuclei (Eq. 3.6) for a classical force field in the electronic ground state, is nicely shown in [62]. The derivation within this reference will shortly be summarized below.

One starts with the stationary Schrödinger equation for some set of coordinates R . The Born-Oppenheimer approximation (cf. Sec. 3.1.2) to decouple the equations of motion has already been made. The stationary electronic Schrödinger equation then reads

$$H_{\text{el}}(r; R) \Phi_k(r; R) = E_k \Phi_k(r; R). \quad (3.7)$$

Contrary to Eq. 3.5, the wave function in the stationary Schrödinger equation is not time-dependent. The E_k are the eigenenergies of the stationary Schrödinger equation, the $\Phi_k(r; R)$ are the respective eigenfunctions, which, like the electron Hamiltonian itself, depend parametrically on the set of nuclear coordinates R .

The next approximation is made via restricting the total electronic wave function Φ to the electronic ground state CC wave function ϕ_0 for the Hamiltonian $H_{\text{el}}(r; R)$. This ground state classical path approximation will be further discussed in Sec. 3.1.6.

While restricting the total electronic wave function Φ to the electronic ground state ϕ_0 , it has to be demanded that the nuclei move on a single potential energy surface $U_0(R(t))$ of the form

$$U_0(R(t)) = \int dr \phi_0^* H_{\text{el}} \phi_0 = E_0(R(t)). \quad (3.8)$$

The energy $E_0(R)$ that depends on the set of coordinates R can be calculated by solving the time-independent Schrödinger equation

$$H_{\text{el}}(r; R) \phi_0(r; R(t)) = E_0 \phi_0(r; R(t)). \quad (3.9)$$

Eq. 3.8 can be utilized to give the equations of motion

$$M_i \ddot{\mathbf{R}}_i = -\nabla_i U_0(R(t)), \quad (3.10)$$

i being the index counting the nuclei. Eq. 3.10 coincides with Eq. 3.6 in the electronic ground state.

In the next step the ground state potential $U_0(R)$ depending on the actual coordinates R is approximated. This approximation depends on the interaction between bonded atoms and additionally on the electrostatic and van der Waals interaction between non-bonded atoms. Thus, the potential may be written as

$$\begin{aligned} U_g(R(t)) \approx U_g^{\text{approx}}(R(t)) = & \sum_{2 \text{ neighbors}} v_{ij}(\mathbf{R}_i, \mathbf{R}_j) + \sum_{3 \text{ neighbors}} v_{ijk}(\mathbf{R}_i, \mathbf{R}_j, \mathbf{R}_k) \\ & + \sum_{\text{more neighbors}} \dots + \text{non-bonded interaction.} \end{aligned} \quad (3.11)$$

The first term sums over all interactions between two atoms that are covalently bound, the second term sums over all three atoms that are directly connected and so on. The v_{ij} and v_{ijk} are the respective energy coefficients. The non-bonded interaction is determined by Coulomb and van der Waals interactions. For the most classical force fields, two atoms with a direct connection within a molecule, which adds up to four bonds and more, are treated as non-bonded. How the potential $U_g^{\text{approx}}(R(t))$ is expressed in terms of bonds, angles and dihedrals will be discussed in Sec. 4.1.2. Eq. 3.10 then reads

$$M_i \ddot{\mathbf{R}}_i = -\nabla_i U_g^{\text{approx}}(R(t)). \quad (3.12)$$

The respective approximations that are made within the AMBER force field will be discussed in Sec. 4.1.2.

3.1.6 The ground state classical path approximation

The force field contains the forces on each nucleus, and it depends on the actual electronic state of the system. The main aim in this thesis is the calculation of EET and optical properties, like for example pump-probe spectra. If a chromophore absorbs a photon, the new electronic state affects the forces on the nuclei, Eq. 3.6. However, a classical MD simulation does not include electronic state dependent changes to the force field.

In many systems the ground state classical path approximation can be made. This approximation assumes that the change of the electronic state has only a weak effect on the motion of the nuclei [64]. For the large systems discussed in this thesis this approximation has to be made, since a force field for the excited electronic states is not available.

However, the ground state classical path approximation does not affect linear absorption calculations (cf. Sec. 3.6), since a vertical absorption to the electronic first excited state PES can be assumed. In this case, the nuclei motion on the PES of the first excited electronic state is of no importance. A comparison by Shi and Geva [55] between the absorption line shape in the DCL and the line shapes computed with other semiclassical approximations (cf. Sec. 3.1.1)

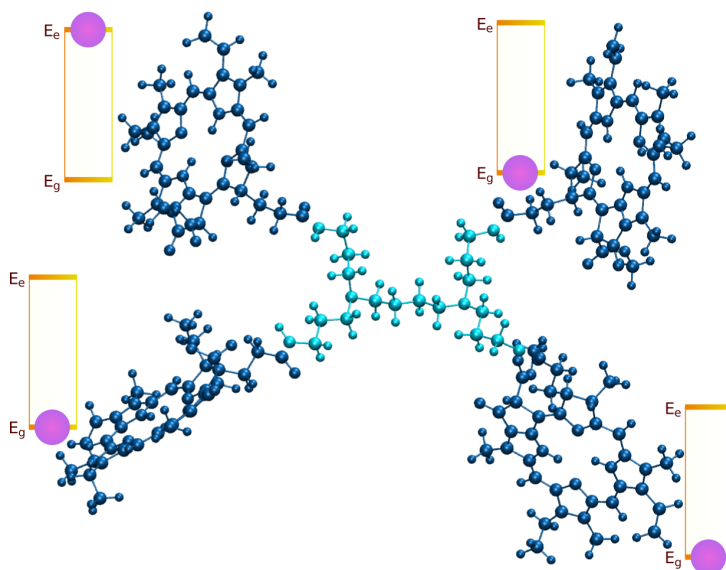


Figure 3.1: The singly excited P_4 . The bars at each chromophore represent the actual state of the chromophore (electronic ground or first excited state). One chromophore is excited while the others are in the electronic ground state. The figure is a graphical interpretation of Eq. 3.14.

confirmed the high quality of the DCL when linear absorption is computed.

3.2 The chromophore complex wave function

In the following section, the wave function for the P_N complexes will be introduced. The interchromophore electron exchange can be neglected. This is due to the fact that the averaged distance between the chromophores is about 10 Å or larger. It has to be mentioned here that there exist distances smaller than 10 Å. In those situations Dexter transfer [3] may become a small correction to the Foerster-type EET, but is neglected. Thus, one can write the CC electronic wave function as the product of the single chromophore electronic ground state wave functions

$$\phi_0(r; R) = \prod_m \psi_{mg}(r_m; R_m). \quad (3.13)$$

The semicolon suggests the parametrical dependence on the nuclear coordinates. Accordingly the singly excited CC states are written

$$\phi_m(r; R) = \psi_{me}(r_m; R_m) \prod_{n \neq m} \psi_{ng}(r_n; R_n). \quad (3.14)$$

The CC wave function, with chromophore m being in the first excited electronic state, is written as the product of the single chromophore wave functions. The wave function of chromophore m is the first excited electronic wave function, the wave functions of the other Pheos are wave functions in the electronic ground state. A graphical interpretation of Eq. 3.14 is given in Fig. 3.1. In the figure, one specific chromophore (the molecules are treated as two level systems) is in the electronic first excited state, while the others remain in the electronic ground state.

For the calculation of nonlinear optical effects, such as nonlinear absorption in a pump-probe scheme, the treatment of the second excited CC states is required. The excitation energy of the first excited electronic state of Pheo $\Delta E_{g \rightarrow e}$ is 1.86 eV. The energy $\Delta E_{e \rightarrow f}$ that is necessary to excite Pheo from the first excited to the second excited electronic state is 0.44 eV. Thus, it is not possible to excite a population from the first to the second excited electronic state with the

same laser that may excite a population from the electronic ground to the first excited state (with a frequency $\omega_{g \rightarrow e} = \Delta E_{g \rightarrow e} / \hbar$). There exists an excited state in the Soret band of Pheo at $2 \times 1.86 = 3.72 \text{ eV}$. There is a possibility that such a higher excited state relaxes to the second excited electronic state. However, in the model for the second excited CC states such excitations are neglected. With this approximation, the second excited electronic state of the Pheo CC in the molecular basis always contains two Pheos in the first excited electronic state and never a Pheo in the second excited electronic state, chromophores m and n excited:

$$\phi_{mn}(r; R) = \psi_{me}(r_m; R_m) \psi_{ne}(r_n; R_n) \prod_{p \neq m, n} \psi_{pg}(r_p; R_p), \quad (3.15)$$

with $n > m$. It is important to state that within a definition $n \neq m$, Eq. 3.14 would give $\phi_{mn}(r; R) \equiv \phi_{nm}(r; R)$. It is therefore important to introduce the condition $n > m$. In this way, no additional CC wave function is introduced that is identical to another one. As for the first excited electronic state, the product ansatz in Eq. 3.15 demands the Dexter-type energy transfer to be neglected.

Higher excitations are of no relevance for the investigations carried out in this work. The pump pulse energies in the performed calculations would result in populations of the third excited state that are too low to give a significant effect (cf. Sec. 3.8). Eqs. 3.13, 3.14 and 3.15 give the CC wave function, when it is in its electronic ground state, when only chromophore m is excited or when chromophores m and n are excited. In a system where optical transitions are allowed and excited states higher than the second excited state are neglected, the total CC wave function reads

$$\Phi(t) = A_0(t) |\phi_0\rangle + \sum_m A_m(t) |\phi_m\rangle + \sum_{m, n} A_{mn}(t) |\phi_{mn}\rangle = \sum_\alpha A_\alpha(t) |\phi_\alpha\rangle, \quad (3.16)$$

again with $n > m$. For reasons of simplification one may summarize the $A_0(t)$, $A_m(t)$ and $A_{mn}(t)$ as $A_\alpha(t)$. Note that the $A_\alpha(t)$ depend additionally on the nuclei coordinates R . This dependence will not be explicitly denoted in the following text. The complex superposition coefficients $A_\alpha(t)$ are normalized by

$$\sum_\alpha |A_\alpha(t)|^2 = 1. \quad (3.17)$$

The total CC wave function $\Phi(t)$ is defined by its components ϕ_0 , ϕ_m , and ϕ_{mn} . On the other hand, one may define the CC wave functions $\Phi_a(t)$ with $a \in \{g, e, f\}$ (compare with the Φ_k in the stationary SE in Eq. 3.7). Now, Eq. 3.16 can be rewritten as

$$\Phi(t) \approx \phi_0(t) + \phi_e(t) + \phi_f(t). \quad (3.18)$$

3.2.1 Frenkel excitons

An exciton is a bound state of an electron and a hole. In solid state physics a Frenkel exciton (as opposed to a Wannier-Mott exciton, [81]) is an exciton with a strong Coulomb coupling. In the case of the Frenkel exciton, electron and hole are located on the same atom, but this atom can be found everywhere in the crystal [81].

The expansion of the Frenkel exciton concept to chromophore complexes (CCs) is straightforward. The electron hole pair is located on the same molecule, but this molecule can be found everywhere in the CC. Thus, the electron hole pair in semiconductor physics corresponds to the S_1 state of a chromophore (in this picture, the electron in the lowest unoccupied molecular orbital is bound to the hole in the highest occupied molecular orbital). The S_1 state indicates the first excited electronic state (of Pheo). More precisely, the eigenstate of the singly excited CC including N chromophores at the conformation R , is a superposition of the N possible first

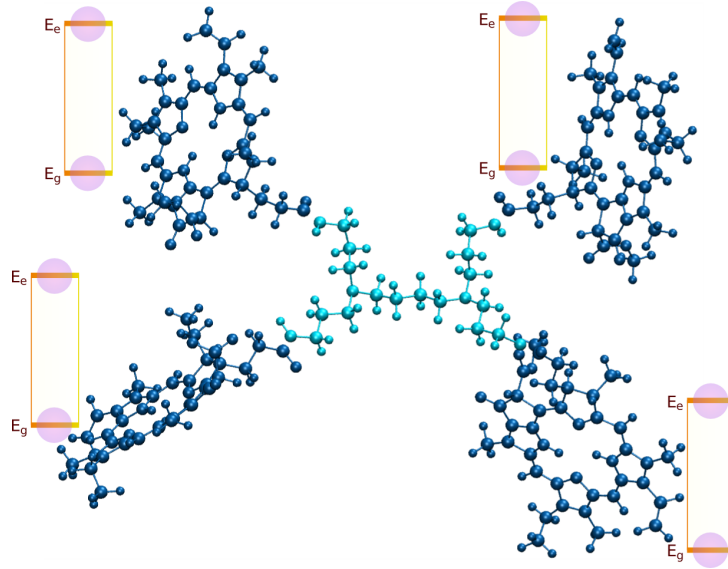


Figure 3.2: As in Fig. 3.1 the singly excited P_4 CC is shown. The excited state is drawn as a superposition over the four possible singly excited Pheo states. The bars at each chromophore represent the population of the electronic state of the chromophore, which is partly in the electronic ground and partly in the electronic excited state. The figure is a graphical interpretation of Eq. 3.19.

excited CC states (where one particular chromophore is excited)

$$\phi_e(R) = \sum_m A_m(R) | \phi_m \rangle, \quad (3.19)$$

with the expansion coefficients $A_m(R)$. Eq. 3.19 implies that the position of the excitation within the CC is not defined. This is shown graphically in Fig. 3.2. Like in Fig. 3.1 the CC is in the first excited electronic state, but the position of the excitation may be located everywhere in the CC, being delocalized.

3.3 The CC Hamiltonian

The Hamiltonian of the system has to include all electrostatic interactions of the CC and the surrounding solvent molecules, the vibrational potential energy, the kinetic energy, and the interaction with the external electromagnetic field. From here on, the notation of former work done by our group is utilized (cf. [39, 75, 82, 83, 84, 85]). For different Pheos the mutual chromophore wave function overlapping and exchange effects can be neglected due to the comparatively large distances between the Pheos. This can be written as

$$\langle \psi_{ma} | \psi_{nb} \rangle = \delta_{m,n} \delta_{a,b}, \quad (3.20)$$

with ψ_{ma} being the electronic wave function of chromophore m in state a , $a \in \{g, e\}$, with g denoting the electronic ground state, e the electronic excited state. Electronic coordinates of chromophore m will be abbreviated by r_m , nuclear coordinates of chromophore m by R_m . The total Hamiltonian of the CC is written

$$H_{CC}(t) = T_{\text{nuc}} + V_{CC} - \hat{\mu} \mathbf{E}(t), \quad (3.21)$$

3 The mixed quantum-classical methodology

with the kinetic energy operator of all involved nuclear coordinates $T_{\text{nuc}} = \sum_m T_m$, the dipole operator $\hat{\mu} = \sum_m \hat{\mu}_m$, the electric field strength E and the potential

$$V_{\text{CC}} = \sum_m H_m^{\text{el}} + \frac{1}{2} \sum_{m,n} V_{mn}. \quad (3.22)$$

H_m^{el} is the single chromophore electronic Hamiltonian of chromophore m , while the V_{mn} include all Coulomb interactions between chromophores m and n : the interaction between electrons $V_{mn}^{\text{el-el}}$, the interaction between electrons and nuclei $V_{mn}^{\text{el-nuc}}$ and $V_{mn}^{\text{nuc-el}}$ and the interaction between nuclei $V_{mn}^{\text{nuc-nuc}}$.

Till now, only the CC Hamiltonian and wave functions were discussed. In this thesis a CC in ethanol solution is investigated. Thus, the Hamiltonian in Eq. 3.21 has to include contributions due to the solvent molecules. Eq. 3.22 then reads

$$V_{\text{CC}} = \sum_m H_m^{\text{el}} + \sum_{\xi} H_{\xi}^{\text{el}} + \frac{1}{2} \sum_{m,n} V_{mn} + \frac{1}{2} \sum_{\xi,\zeta} V_{\xi\zeta} + \sum_{m,\xi} V_{m\xi}. \quad (3.23)$$

The ξ and ζ count the solvent molecules. Eq. 3.23 covers all interactions of the CC and the solvent. Since the Hamiltonian includes all solvent molecules, the CC wave functions in Eqs. 3.13,3.14,3.15 have to be multiplied by the solvent wave function $\prod_{\xi} \psi_{\xi g}(r_{\xi}; R_{\xi})$. The solvent molecules ξ remain in the electronic ground state.

Thus, the CC Hamiltonian $H_{\text{CC}}(t)$ is first separated into an explicitly time-dependent part $H_{\text{field}}(t)$ and one part that only implicitly depends on the time via the coordinates R . $H_{\text{CC}}(t)$ can then be approximated (higher excited electronic states than the second are neglected) [82]:

$$\begin{aligned} H_{\text{CC}}(t) &= H_{\text{CC}} + H_{\text{field}}(t) \\ &\approx \langle \phi_0 | H_{\text{CC}} | \phi_0 \rangle | \phi_0 \rangle \langle \phi_0 | + \sum_{m,n} \langle \phi_m | H_{\text{CC}} | \phi_n \rangle | \phi_m \rangle \langle \phi_n | \\ &\quad + \sum_{m,k} \sum_{n>m, l>k} \langle \phi_{mn} | H_{\text{CC}} | \phi_{kl} \rangle | \phi_{mn} \rangle \langle \phi_{kl} | \\ &\quad + \sum_m (\langle \phi_m | - \hat{\mu} E(t) | \phi_0 \rangle | \phi_m \rangle \langle \phi_0 | + H.c.) \\ &\quad + \sum_m \sum_{n>m} (\langle \phi_{mn} | - \hat{\mu} E(t) | \phi_m \rangle | \phi_{mn} \rangle \langle \phi_m | + H.c.). \end{aligned} \quad (3.24)$$

$\hat{\mu}$ is the dipole operator that can be written as

$$\hat{\mu} = \sum_m \mathbf{d}_m | \phi_0 \rangle \langle \phi_m | + \sum_m \sum_{n>m} \mathbf{d}_n | \phi_m \rangle \langle \phi_{mn} | + \sum_m \sum_{n<m} \mathbf{d}_n | \phi_m \rangle \langle \phi_{nm} | + H.c.. \quad (3.25)$$

The CC part of the Hamiltonian can be rewritten as

$$H_{\text{CC}} \approx H_0 + H_1 + H_2, \quad (3.26)$$

with the electronic ground state Hamiltonian

$$H_0 = \langle \phi_0 | H_{\text{CC}} | \phi_0 \rangle | \phi_0 \rangle \langle \phi_0 |. \quad (3.27)$$

The part treating the first excited electronic states is written as

$$H_1 = \sum_{m,n} \langle \phi_m | H_{\text{CC}} | \phi_n \rangle | \phi_m \rangle \langle \phi_n |, \quad (3.28)$$

while the part of the Hamiltonian that treats the second excited states is given by

$$H_2 = \sum_{m,k} \sum_{n>m, l>k} \langle \phi_{mn} | H_{CC} | \phi_{kl} \rangle | \phi_{mn} \rangle \langle \phi_{kl} |. \quad (3.29)$$

To solve the TDSE for the expansion coefficients A_α (cf. Sec. 3.2), the matrix elements given above have to be calculated. The matrix elements in H_0 , H_1 and H_2 contain all electrostatic interactions between the chromophores, the dendrimer and the surrounding solvent molecules, moreover the vibrational potential and kinetic energy, and will further be explained in Sec. 3.4.

3.3.1 Kinetic energy

Since the Hamiltonian H_{CC} contains the operator of kinetic energy T_{nuc} , the Hamiltonians H_0 , H_1 and H_2 (Eqs. 3.27, 3.28, 3.29) contain matrix elements of the kinetic energy T_{nuc} . This matrix elements are of the form $\langle \phi_0 | T_{\text{nuc}} | \phi_0 \rangle$, $\langle \phi_m | T_{\text{nuc}} | \phi_n \rangle$ and $\langle \phi_{mn} | T_{\text{nuc}} | \phi_{kl} \rangle$ [83]. In the next step, the operator of non-adiabatic coupling is defined as [26, 83]

$$\hat{\Theta}_{mab} = \langle \psi_{mg} | T_m | \psi_{mg} \rangle + \sum_i \frac{1}{M_i} \langle \psi_{ma} | \mathbf{P}_i | \psi_{mb} \rangle \mathbf{P}_i. \quad (3.30)$$

M_i and \mathbf{P}_i are the mass and momentum of the i th nucleus. The matrix element Θ_{maa} is defined as

$$\Theta_{maa} = \langle \psi_{ma} | \hat{\Theta}_{maa} | \psi_{ma} \rangle. \quad (3.31)$$

With the definition of the operator of non-adiabatic coupling, the matrix elements of the kinetic energy given above can be rewritten as [83]

$$\langle \phi_0 | T_{\text{nuc}} | \phi_0 \rangle = \sum_m (T_m + \Theta_{m gg}), \quad (3.32)$$

$$\langle \phi_m | T_{\text{nuc}} | \phi_n \rangle = \delta_{m,n} \left(T_{\text{nuc}} + \Theta_{mee} + \sum_{m' \neq m} \Theta_{m' gg} \right), \quad (3.33)$$

and

$$\langle \phi_{mn} | T_{\text{nuc}} | \phi_{kl} \rangle = \delta_{mk} \delta_{nl} \left(T_{\text{nuc}} + \Theta_{mee} + \Theta_{nee} + \sum_{m' \neq m,n} \Theta_{m' gg} \right). \quad (3.34)$$

In this thesis the operator of non-adiabatic coupling is neglected. It has to be stated that this is an approximation. The motivation for this approximation is the assumption that the differential operator (with respect to the nuclei coordinates) \mathbf{P}_i acts only weakly on the state $|\psi_{mb}\rangle$ (which only depends parametrically on the nuclei coordinates), in this case all matrix elements of the operator of non-adiabatic coupling disappear.

3.3.2 Potential energy due to intramolecular vibration

The potential energy due to the molecular conformation can be computed in harmonic approximation as [26]

$$U_{ma}^{\text{vib}}(R_m) = \hbar\omega_a + \sum_{\mu,\nu} \kappa_{\mu\nu}^a (R_{m\mu} - R_{m\mu,0}^a)(R_{m\nu} - R_{m\nu,0}^a). \quad (3.35)$$

$\hbar\omega_a$ denotes the energy minimum of the respective PES. κ^a denotes the Hessian matrix, the second derivative of the PES, in the electronic state a . Eq. 3.35 only holds for small deviations $R_{m\mu} - R_{m\mu,0}^a$. R_m is the actual conformation of the m th molecule, $R_{m\mu,0}^a$ is the equilibrium conformation of chromophore m in the electronic state a . $R_{m\mu}$ defines the μ th coordinate of chromophore m . It is important to understand that μ does not count the atom number i , but a

coordinate. This may be for example the x-coordinate of atom number i .

3.3.3 Coulomb interaction

The matrix elements within H_0 , H_1 and H_2 (Eqs. 3.27, 3.28, 3.29) contain all electrostatic interaction energies between the individual chromophores, the dendrimer and the surrounding solvent molecules.

In general, the Coulomb interaction between two chromophores may be written as

$$J_{mn}(ab, cd) = \int dr_m dr_n \psi_{ma}^*(r_m) \psi_{nb}^*(r_n) V_{mn} \psi_{nc}(r_n) \psi_{md}(r_m). \quad (3.36)$$

V_{mn} covers the complete Coulomb interaction between the chromophores m and n , and ψ_{ma} is the electronic wave function of chromophore m in the electronic state a .

The meaning brackets (ab, cd) in Eq. 3.36 can be explained as follows: if $a = b$ and $c = d$, this is the Coulomb interaction between two chromophores in the states a and c ; if $a \neq b$, the transition density of chromophore m while it changes its electronic state from a to b is denoted. The interaction between transition densities will be utilized later to describe electronic state transitions of the single chromophores via excitation energy transfer (cf. Sec. 3.3.3) within the CC.

To compute the couplings $J_{mn}(ab, cd)$, the electronic charge density

$$\zeta_{ab}^m(\mathbf{x}) = eN_m \int dr \delta(\mathbf{x} - \mathbf{r}_q) \psi_{ma}^*(r) \psi_{mb}(r). \quad (3.37)$$

is introduced. In the formula for ζ_{ab}^m , N_m is the number of electrons in chromophore m . In Eq. 3.37, the treatment of the charge density instead of the linear combination of products of wave functions decreases the actual phase space under consideration to the 3-dimensional Cartesian space.

Fitting the electronic charge density to partial charges

The electronic charge density of the chromophores can be fitted to partial charges located on the positions of the nuclei \mathbf{R}_i , as shown in [32]. However, the notation of [83] will be used since it is better aligned with the notation of the rest of this thesis. In order to simplify the formulas, new W -potentials are introduced. For the electron-electron interaction one may write

$$W^{\text{el-el}}(\mathbf{x} - \mathbf{x}') = \frac{e^2}{4\pi\epsilon_0} \frac{1}{|\mathbf{x} - \mathbf{x}'|}. \quad (3.38)$$

The W -potential for the electron-nucleus coupling is written as

$$W_m^{\text{el-nuc}}(\mathbf{x}) = \frac{e^2}{4\pi\epsilon_0} \sum_i \frac{Z_i}{|\mathbf{x} - \mathbf{R}_i|}. \quad (3.39)$$

The index m means that the nuclei of chromophore m are considered. Z_i is the atomic number and \mathbf{R}_i the position of atom i . According to the definitions given above the W -potential for the nucleus-nucleus interaction is

$$W_{mn}^{\text{nuc-nuc}}(\mathbf{x}) = \frac{e^2}{4\pi\epsilon_0} \sum_{i,j} \frac{Z_i Z_j}{|\mathbf{R}_i - \mathbf{R}_j|}. \quad (3.40)$$

With the definition of the single electron density of chromophore m , $\zeta_{ab}^m(\mathbf{x})$ (Eq. 3.37), the general interaction between two chromophores m and n can be written as

$$\begin{aligned} J_{mn}(ab, cd) = & \int d^3\mathbf{x} d^3\mathbf{x}' \zeta_{ad}^m(\mathbf{x}) W^{\text{el-el}}(\mathbf{x} - \mathbf{x}') \zeta_{bc}^m(\mathbf{x}') + \\ & + \delta_{cb} e \int d^3\mathbf{x} \zeta_{ad}^m(\mathbf{x}) W_n^{\text{el-nuc}}(\mathbf{x}) \\ & + \delta_{ad} e \int d^3\mathbf{x}' \zeta_{cb}^n(\mathbf{x}') W_m^{\text{el-nuc}}(\mathbf{x}) \\ & + \delta_{ad} \delta_{cb} e^2 W_{mn}^{\text{nuc-nuc}}. \end{aligned} \quad (3.41)$$

The charge density of the chromophore m is defined as

$$n_{ab}^m(\mathbf{x}) = \zeta_{ab}^m(\mathbf{x}) - \delta_{a,b} \sum_{i \in m} e Z_i \delta(\mathbf{x} - \mathbf{R}_i). \quad (3.42)$$

It consists of the nuclei charge contribution (nucleus i contributes the charge eZ_i at position \mathbf{R}_i) and the contribution of the electronic charge density $\zeta_{ab}^m(\mathbf{x})$ (Eq. 3.37). Inserting Eq. 3.42 into Eq. 3.41 results in

$$J_{mn}(ab, cd) = \frac{1}{4\pi\epsilon_0} \int d\mathbf{x} d\mathbf{x}' \frac{n_{ad}^m(\mathbf{x}) n_{bc}^n(\mathbf{x}')}{|\mathbf{x} - \mathbf{x}'|}. \quad (3.43)$$

The interactions between charge densities in Eq. 3.43 can be fitted to respective partial charges [32], as will be shown below.

Partial charges

Quantum-chemical computations may give the charge density $n_{ab}^m(\mathbf{x})$ of a system. However, the knowledge of the charge density does not help to compute the Coulomb interaction between two molecules for specific MD snapshots. The solution for this problem is the definition of a set of partial charges $\{q_{mi}(ab)\}$. The partial charge $q_{mi}(ab)$ is located at the position of atom i of molecule m , \mathbf{R}_{mi} . The $q_{mi}(ab)$ are chosen that way that the potential of the set of $q_{mi}(ab)$ equals the potential of the charge density $n_{ab}^m(\mathbf{x})$. There exist different methods to derive the partial charges from the charge density. The most common methods are explained and compared in [86].

Interaction between Pheos in the electronic ground state

While treating the Coulomb interaction of chromophores in the electronic ground state, Eq. 3.36 can be rewritten as

$$J_{mn}(gg, gg) = \int dr_m dr_n \psi_{mg}^*(r_m) \psi_{ng}^*(r_n) V_{mn} \psi_{ng}(r_n) \psi_{mg}(r_m). \quad (3.44)$$

The computation of the (electrostatic) coupling between chromophores and solvent molecules can be done in a uniform manner. The respective interaction between the electronic ground state charge densities is then given by

$$J_{mn}(gg, gg) = \frac{1}{4\pi\epsilon_0} \int d\mathbf{x} d\mathbf{x}' \frac{n_{gg}^m(\mathbf{x}) n_{gg}^n(\mathbf{x}')}{|\mathbf{x} - \mathbf{x}'|}. \quad (3.45)$$

The interaction between partial charges reads

$$J_{mn}(gg, gg) = \frac{1}{4\pi\epsilon_0} \sum_{i,j} \frac{q_{mi}(gg) q_{nj}(gg)}{|\mathbf{R}_{mi} - \mathbf{R}_{nj}|}. \quad (3.46)$$

Interaction between Pheos in the excited states

According to Eq. 3.46, the interaction between two Pheos in the states a and c can be written as

$$J_{mn}(ac, ca) = \frac{1}{4\pi\epsilon_0} \sum_{i,j} \frac{q_{mi}(aa)q_{nj}(cc)}{|\mathbf{R}_{mi} - \mathbf{R}_{nj}|}, \quad (3.47)$$

with $a, c \in \{g, e, f\}$, the electronic ground state g , the electronic first excited electronic state e , and the second excited electronic state f . If both chromophores are in the electronic ground state ($a = g, c = g$), Eq. 3.46 is reproduced.

Excitonic coupling

If Eq. 3.36 is translated to the interaction between two transition densities, it may be rewritten as

$$J_{mn}(ac, ac) = \frac{1}{4\pi\epsilon_0} \int d\mathbf{x} d\mathbf{x}' \frac{n_{ac}^m(\mathbf{x})n_{ca}^n(\mathbf{x}')}{|\mathbf{x} - \mathbf{x}'|}. \quad (3.48)$$

Both transition densities are represented by the charge density n_{ab}^m , since the interaction between those two transition densities leads to the de-excitation (excitation) of chromophore m from the state a to the state c , while chromophore n is excited (de-excited) from the electronic state c to the state a at the same time. In the current consideration, the charge density n_{ab}^m is identified with the charge density n_{eg}^m . Only the excitonic coupling between the Pheos in the electronic ground state and the Pheos in the first excited electronic state is taken into consideration.

From the transition densities, the respective transition partial charges may be calculated [32], and the excitonic coupling can be written as a sum of Coulomb interactions between those transition partial charges:

$$J_{mn}(ac, ac) = \frac{1}{4\pi\epsilon_0} \sum_{i,j} \frac{q_{mi}(ac)q_{nj}(ac)}{|\mathbf{R}_{mi} - \mathbf{R}_{nj}|}. \quad (3.49)$$

It has to be mentioned that (if the distance between both chromophores is large) this description is equivalent with the description of the excitonic coupling via the dipole-dipole interaction between transition dipole moments \mathbf{d}_m and \mathbf{d}_n . If the distance between the chromophores is much shorter than 10 Å, the description given above is the much better, since no approximation is included (cf. [75]). In terms of the transition partial charges, the transition dipole moment \mathbf{d}_m may be written as

$$\mathbf{d}_m = \sum_i q_{mi}(ac)\mathbf{R}_{mi}. \quad (3.50)$$

For this thesis, the Pheo transition dipole moment (as well as the respective partial charges) was normalized to the measured transition dipole moment of chlorophyll a (there exists no measurement for Pheo). The π -electron system is the same for both molecules, only one chain is longer for chlorophyll a . Thus, the assumption that the transition dipole moments of both molecules are the same is reasonable. The value of the transition dipole moment is 4.6 D.

Coupling between covalently bound molecules

The electrostatic interaction is interpreted as an intermolecular interaction, for example the interaction between chromophore m and chromophore n or the interaction between chromophore m and the dendrimer. This picture is not completely correct, since the dendrimer structure is covalently bound to each chromophore. Thus, the P_N complex is one molecule. The Coulomb interaction between each chromophore and the dendrimer contributes to the energy gap func-

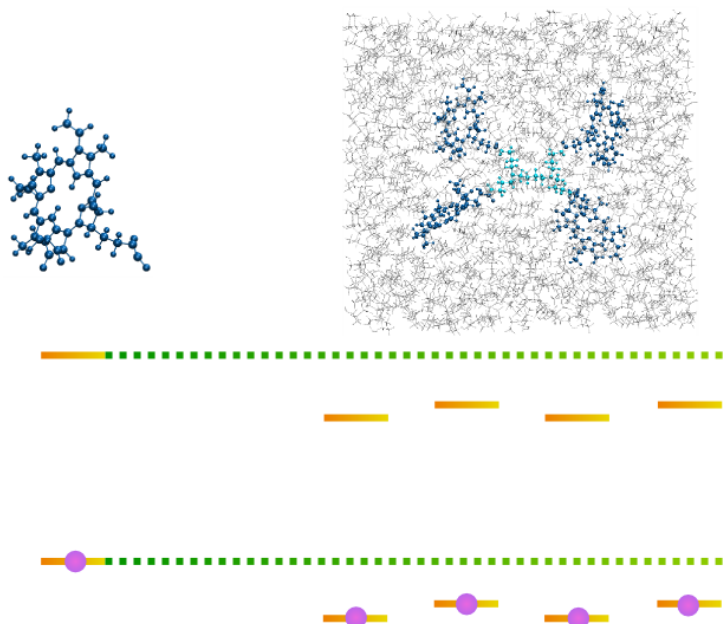


Figure 3.3: Left hand side: the energy gap for a single Pheo in vacuum. The respective electronic ground state level and the first excited state level are drawn. Right hand side: P₄ in explicit ethanol solution. It is illustrated that the respective electronic ground and excited state energies are shifted towards lower energies. The shift is not the same for each Pheo due to the different conformations of the respective solvent shells.

tion. But a sum over all Coulomb interactions between all atoms i of Pheo m and all atoms j of the dendrimer will assume a non-bonded Coulomb coupling between two atoms that are actually covalently bound. This electrostatic Coulomb coupling between the two covalently bound atoms will introduce an effective energy amount of about 5 meV. However, this energy is nearly constant and does not contribute to the energy gap fluctuation, but only to the energy shift. This energy shift can be corrected by the value given above. This, however, is not important, since the peak position in absorption calculations (linear or nonlinear) has to be corrected anyway (cf. Sec. 5.1.2).

3.4 Computation of the Hamiltonian matrix elements

The description of the CC Hamiltonian parts H_0 and H_1 will follow mainly [82]. The description of the Hamiltonian part H_2 is new, but adopts the notation of the two previous subsections for H_0 and H_1 [82].

The electronic ground and excited state energies of a chromophore within a CC in solution depend on the interactions of the chromophores with each other, with the dendrimer and with the solvent. This is illustrated in Fig. 3.4.2. It shows the electronic ground and first excited state for a single Pheo in vacuum and P₄ in ethanol. The respective energy shifts due to solvent and dendrimer coupling have to be treated by the respective Hamiltonians H_0 , H_1 and H_2 .

3.4.1 Electronic ground state matrix element

Next, the part H_0 of the CC Hamiltonian (cf. Eq. 3.27) will be defined. It can be rewritten as

$$H_0 = \mathcal{H}_0 |\phi_0\rangle \langle \phi_0| \quad (3.51)$$

with

$$\mathcal{H}_0 = \sum_m H_{mg} + \sum_{\xi} H_{\xi g} + \frac{1}{2} \sum_{m,n} J_{mn}(gg, gg) + \sum_{m,\xi} J_{m\xi}(gg, gg) + \frac{1}{2} \sum_{\xi,\zeta} J_{\xi\zeta}(gg, gg). \quad (3.52)$$

Here the H_{mg} are the single Pheo Hamiltonians in the electronic ground state (they include the Pheo PES and the kinetic energy operator T_m), the $H_{\xi g}$ are the solvent molecule (ethanol) Hamiltonians in the electronic ground state. The $J_{mn}(gg, gg)$ describe the Coulomb coupling between two Pheos m and n in the electronic ground state, the $J_{m\xi}(gg, gg)$ describe the Coulomb interaction between Pheo m and solvent molecule ξ , both in the electronic ground state, and the $J_{\xi\zeta}(gg, gg)$ treat the Coulomb interaction between the ground state solvent molecules ξ and ζ . The notation (gg, gg) , which simply means that both molecules are in the electronic ground state, was explained in detail in Sec. 3.3.3.

3.4.2 First excited electronic state matrix elements

The H_1 part of the Hamiltonian can be written as

$$H_1 = \sum_{m,n} (\delta_{m,n} \mathcal{H}_0 + \mathcal{H}_{mn}) |\phi_m\rangle \langle \phi_n|. \quad (3.53)$$

\mathcal{H}_0 was explained above and covers all molecules' electronic ground state PESs and interactions as well as the kinetic energy operators T_m . The diagonal part of H_1 can be written as the respective Hamiltonian of the system in the ground state plus an additional term \mathcal{H}_{mn} . This term may be written as

$$\mathcal{H}_{mn} = \delta_{m,n} \mathcal{H}_{meg} + (1 - \delta_{m,n}) J_{mn}(eg, eg). \quad (3.54)$$

The non-diagonal term $J_{mn}(eg, eg)$ describes the excitonic coupling between the Pheo molecules. The notation in the brackets (eg, eg) was explained in detail in Sec. 3.3.3. The diagonal part of \mathcal{H}_{mn} introduces the \mathcal{H}_{meg} (cf. Sec. 3.5). \mathcal{H}_{meg} introduces the change of vibrational energy and Coulomb coupling energies due to the single excited chromophore m in comparison to the ground state matrix element \mathcal{H}_0 . It reads

$$\begin{aligned} \mathcal{H}_{meg} = H_{me} - H_{mg} + \sum_{n \neq m} [J_{mn}(eg, ge) - J_{mn}(gg, gg)] \\ + \sum_{\xi} [J_{m\xi}(eg, ge) - J_{m\xi}(gg, gg)]. \end{aligned} \quad (3.55)$$

This can be understood as follows: the term $H_{me} - H_{mg} = U_{eg}^{\text{vib}} + \Delta E_{g \rightarrow e}$ describes the difference between the electronic first excited and the ground state for chromophore m . The kinetic energy operator T_m is included in H_{me} as well as H_{mg} and thus vanishes. The term depends on the conformation of chromophore m . This intramolecular contribution to the energy gap function $U_{eg}(t)$, $U_{eg}^{\text{vib}}(t)$, is intensively discussed in Sec. 3.3.2. The next term of Eq. 3.55, $\sum_{n \neq m} [J_{mn}(eg, ge) - J_{mn}(gg, gg)]$ gives the energy difference of the Pheo m Coulomb coupling to the other Pheos $n \neq m$ between the case when Pheo m is in the electronic excited state and the case when it is in the electronic ground state. The term $\sum_{\xi} [J_{m\xi}(eg, ge) - J_{m\xi}(gg, gg)] = U_{eg}^{\text{sol}}$ gives the energy difference of the Pheo m Coulomb coupling to the solvent molecules ξ between the case when Pheo m is in the electronic excited state and the case when it is in the electronic ground state. This term summarizes the energy gap fluctuation due to solvent coupling U_{eg}^{sol} and is discussed in Sec. 4.3.1.

When solving the TDSE (Eq. 3.4) for the first excited electronic CC state, the CC state is approximated as a superposition of product states (cf. Eqs. 3.19, 3.16). The Hamiltonian can be treated as an $N \times N$ -matrix, when the P_N complex is treated. The respective electronic ground

and second excited state expansion coefficients are set to zero:

$$\phi_e(t) = \sum_m A_m(t) |\phi_m\rangle. \quad (3.56)$$

This equation is in principle identical to Eq. 3.19. In Eq. 3.56 the explicit time-dependency of the wave function is denoted. The respective TDSE is

$$i\hbar \frac{\partial}{\partial t} \phi_e(t) = H_1 \phi_e(t). \quad (3.57)$$

Inserting Eq. 3.56 into Eq. 3.57 and multiplying with $\langle \phi_m |$ and $\langle \phi_0 |$ from the left, gives

$$i\hbar \frac{\partial}{\partial t} A_m(t) = \sum_n (\delta_{m,n} \mathcal{H}_0(t) + \mathcal{H}_{mn}(t)) A_n(t). \quad (3.58)$$

Matrix elements of the form $\langle \phi_0 | \partial/\partial t | \phi_0 \rangle$, $\langle \phi_0 | \partial/\partial t | \phi_m \rangle$ and $\langle \phi_m | \partial/\partial t | \phi_n \rangle$ are neglected [83]. This is reasonable if wave function overlap can be neglected and EET takes place on a picosecond time scale. With the ansatz

$$\tilde{A}_m(t) = A_m(t) \exp \left(\left(\int_0^t d\tau (\mathcal{H}_0(\tau) + \Delta E_{g \rightarrow e}) \right) / \hbar \right) \quad (3.59)$$

Eq. 3.58 becomes

$$i\hbar \frac{\partial}{\partial t} \tilde{A}_m(t) = \sum_n (\mathcal{H}_{mn}(t) - \delta_{m,n} \Delta E_{g \rightarrow e}) \tilde{A}_n(t). \quad (3.60)$$

The solution of Eq. 3.60 has the advantage that $\mathcal{H}_0(t)$ has not to be included in the computation. The populations calculated with Eq. 3.60 give the same result as the populations computed with Eq. 3.58, since the phase factor vanishes when the population $P_m(t) = |A_m(t)|^2 = |\tilde{A}_m(t)|^2$ is calculated.

3.4.3 Second excited electronic state matrix elements

As mentioned in Sec. 3.2 second excitations of a single chromophore are neglected in this thesis. The Hamiltonian which acts upon the second excited states is written as

$$H_2 = \sum_{m,n,k,l} (\delta_{m,k} \delta_{n,l} \mathcal{H}_0 + \mathcal{H}_{mn,kl}) |\phi_{mn}\rangle \langle \phi_{kl}|. \quad (3.61)$$

The second excited electronic states $|\phi_{mn}\rangle$ were defined in Eq. 3.15. For the second excited electronic CC wave function $\phi_{mn}(r; R)$ the condition $n > m$ holds, which avoided the definition of two CC wave functions $\phi_{mn}(r; R)$ and $\phi_{nm}(r; R)$ that would be identical (Sec. 3.2). In the definition of H_2 , \mathcal{H}_0 (Eq. 3.52) is included. It contains all the molecular PESs and interactions between molecules in the electronic ground state as well as the kinetic energy operators T_m . The respective changes of conformational energy and interaction energy to the solvent, when two chromophores of the CC are in the first excited state, are introduced by the matrix element

$$\mathcal{H}_{mn,kl} = \delta_{m,k} \delta_{n,l} \mathcal{H}_{mnfg} + \delta_{m,k} (1 - \delta_{n,l}) J_{nl}(eg, eg) + \delta_{n,l} (1 - \delta_{m,k}) J_{mk}(eg, eg). \quad (3.62)$$

The first term of the matrix element $\delta_{m,k} \delta_{n,l} \mathcal{H}_{mnfg}$ introduces the changes of the PESs and molecular interaction (including coupling to solvent, dendrimer and other Pheos) when two Pheos are in the first excited instead of the electronic ground state (the delta-functions make sure that this part only has an effect to the diagonal matrix elements). The last two terms of Eq. 3.62 treat the excitonic coupling between chromophores n and l as well as m and k . The \mathcal{H}_{mnfg} are

written as

$$\begin{aligned}
 \mathcal{H}_{mnfg} = & H_{me} - H_{mg} + H_{ne} - H_{ng} \\
 & + \sum_{k \neq m,n} [J_{mk}(eg, ge) + J_{nk}(eg, ge) - J_{mk}(gg, gg) - J_{nk}(gg, gg)] \\
 & + J_{mn}(ee, ee) - J_{mn}(gg, gg) \\
 & + \sum_{\xi} [J_{m\xi}(eg, ge) + J_{n\xi}(eg, ge) - J_{m\xi}(gg, gg) - J_{n\xi}(gg, gg)].
 \end{aligned} \tag{3.63}$$

The first part of Eq. 3.63, $H_{me} - H_{mg} + H_{ne} - H_{ng}$ describes the change of (coordinate dependent) energy for the two excited chromophores in comparison to the (coordinate dependent) energy of the same chromophores in the electronic ground state. In the electronic ground state matrix element \mathcal{H}_0 (Eq. 3.52) the term $\frac{1}{2} \sum_{m,n} J_{mn}(gg, gg)$ covers all the mutual Coulomb interactions, while all chromophores are in the electronic ground state. Another term in \mathcal{H}_0 , $\frac{1}{2} \sum_{\xi, \zeta} J_{\xi, \zeta}(gg, gg)$ treats the Coulomb interaction of the chromophores in the electronic ground state with the solvent molecules in the electronic ground state. Since two of the Pheos are in the electronic excited state for that case, the change to the Coulomb interaction energy has to be treated. The term $\sum_{k \neq m,n} [J_{mk}(eg, ge) + J_{nk}(eg, ge) - J_{mk}(gg, gg) - J_{nk}(gg, gg)]$ introduces the change of the Coulomb coupling of the two excited chromophores with other chromophores k , compared to the case when the two chromophores m and n are in the electronic ground state. The term $J_{mn}(ee, ee) - J_{mn}(gg, gg)$ treats the change of the Coulomb energy between the two electronic excited Pheos.

Finally, the term $\sum_{\xi} [J_{m\xi}(eg, ge) + J_{n\xi}(eg, ge) - J_{m\xi}(gg, gg) - J_{n\xi}(gg, gg)]$ treats the change of the Coulomb interaction energy due to the solvent coupling to the excited chromophores. The CC wave function for the second excited electronic state can be written as

$$\phi_f(t) = \sum_{m,n} A_{mn}(t) | \phi_{mn} \rangle, \tag{3.64}$$

with $n > m$. This is a superposition over $N(N-1)/2$ independent doubly excited CC wave functions. The respective Hamiltonian matrix $\mathcal{H}_{mn,kl}$ is a $N(N-1)/2 \times N(N-1)/2$ matrix.

3.5 Energy gap function

The calculation of the fluctuation of the energy gap function $U_{eg}(t)$ is a very sensitive part within a mixed quantum-classical calculation. $U_{eg}(t)$ introduces the parametrical dependence on the MD generated nuclei coordinates to the electronic Hamiltonian H_{el} . The energy gap consists of the intramolecular vibrational part $U_{eg}^{vib}(t)$ and the part due to solvent coupling $U_{eg}^{sol}(t)$:

$$U_{eg}(t) = U_{eg}^{vib}(t) + U_{eg}^{sol}(t). \tag{3.65}$$

The two parts of the energy gap function have been introduced previously in Eq. 3.55 and are presented separately now. The vibrational part of the energy gap function for chromophore m is

$$U_{eg}^{vib}(t) = (H_{me}(t) - H_{mg}(t)) - \Delta E_{g \rightarrow e} = \sum_m (U_{me}(t) - U_{mg}(t)) - \Delta E_{g \rightarrow e}, \tag{3.66}$$

with the transition energy between the electronic states $\Delta E_{g \rightarrow e}$. The difference between the vibrational Hamiltonians is expressed by the difference of the respective potential energy surfaces. Utilizing Eq. 3.35 that gives the potential energy of chromophore m in the electronic state a in harmonic approximation, the result for the energy gap function in harmonic approximation

is

$$U_{eg}^{\text{vib}}(t) = \sum_{\mu, \nu} (\kappa_{\mu\nu}^e (R_{m\mu}(t) - R_{m\mu}^e(t)) (R_{m\nu}(t) - R_{m\nu}^e(t)) - \kappa_{\mu\nu}^g (R_{m\mu}(t) - R_{m\mu}^g(t)) (R_{m\nu}(t) - R_{m\nu}^g(t))). \quad (3.67)$$

$R^g(t)$ and $R^e(t)$ are not fixed equilibrium conformations as the R_0^g and R_0^e in Eq. 3.35, but they are time-dependent reference trajectories. That means, they follow the translation, rotation and low frequency bending modes of the molecule (cf. Sec. 4.4).

The energy gap function due to solvent coupling for chromophore m is written as

$$U_{meg}^{\text{sol}}(t) = \sum_{n \neq m} [J_{mn}(eg, ge) - J_{mn}(gg, gg)] + \sum_{\xi} [J_{m\xi}(eg, ge) - J_{m\xi}(gg, gg)]. \quad (3.68)$$

A variety of methods for the calculation of the terms $U_{eg}^{\text{vib}}(t)$ and $U_{eg}^{\text{sol}}(t)$ can be found in the literature. All methods have the computation of solute and solvent conformations by MD simulation in common. These conformations are used to calculate the energy gap function due to the solute-solvent coupling. In the most methods also the energy fluctuation due to intramolecular vibration is calculated utilizing the trajectories. In some papers the intramolecular vibration is added via an additional broadening term including a respective broadening parameter [75, 82, 87]. In the group of Kleinekathöfer, the intramolecular and the intermolecular part is calculated using the ZINDO (Zerner's intermediate neglect of differential overlap) method, a semiempirical method which was originally parameterized for chromophores [27, 28, 29]. In the group of Shi the vibrational broadening was included parametrically via the calculation of the Huang-Rhys factors for the optimized structures with (TD)DFT [30]. In the group of Aspuru-Guzik the vertical excitation was calculated utilizing TDDFT, on BLYP level with a 321G basis set [31]. The utilization of ZINDO and (TD)DFT computations to compute $U_{eg}(t)$ has the disadvantage that the electronic structure calculations have to be done for a lot of snapshots of the MD simulation. Thus, the computational cost of the respective methods is very high. Another disadvantage is that there is a general problem to compute energy level values for large molecular systems utilizing quantum-chemical methods [88].

There exist mainly two approaches for the calculation of the solvent coupling part $U_{eg}^{\text{sol}}(t)$ on the gap function fluctuation $U_{eg}(t)$. In the approaches of Kleinekathöfer's and Aspuru-Guzik's group the chromophore wave function interacts with the solvent partial charges. The group of Shi calculated the solvent coupling by the same approach. They also computed $U_{eg}^{\text{sol}}(t)$ via the Coulomb coupling of partial charges. This is the same method that is utilized within this thesis (cf. Sec. 3.3.3).

The linear absorption linewidth that will be discussed in Sec. 3.6 is strongly dependent on the quality of the energy gap function $U_{eg}(t)$. The line shape that was computed in the Shi group had to be additionally broadened to get the experimental linewidth of bacteriochlorophyll *a* (BChl *a*) and bacteriopheophytin (BPhe) [30]. The linewidth of B800 and B850 computed in [28] was too narrow, as well. The linear absorption results of the Aspuru-Guzik for the FMO (Fenna-Matthews-Olsen) light-harvesting complex appear to be somewhat more accurate [31]. Even though, the linewidths of the single sites do not match the experimental result perfectly.

It was stated by Renger and co-workers that the coupling between partial charges is influenced by the dielectric medium ([35] and references therein), which may increase or decrease the respective coupling. However, in average the coupling will be decreased. None of the above-cited references, including our own publications about excitation energy transfer [39] and pump-probe spectroscopy [85], treat this screening effect in conformational detail. In [28, 29] the screening is included in terms of a constant screening factor F^{scr} . In Chap. 7 a method will be introduced that is able to treat the screening between two chromophores m and n in dependence on their distance and on their mutual atomic conformation. This method bases

on the Poisson-TrEsp-method [34, 35]. Within this thesis, distance and conformation dependent screening will be treated in Chap. 7.

The method that was utilized to compute the energy gap fluctuation $U_{eg}(t)$ in this thesis will be explained in Sec. 3.5.

3.6 Calculation of linear absorption

Utilizing the standard expression of the dipole-dipole correlation function the absorption cross-section for a system consistent of N chromophores can be written as [82]

$$I(\omega) = \text{Re} \int_0^\infty dt e^{i\omega t} \sum_{m,n}^N \text{tr}_{\text{vib}} \left\{ \hat{R}_0 \langle \phi_0 | e^{iH_0 t/\hbar} | \phi_0 \rangle d_{0m} \langle \phi_m | e^{-iH_1 t/\hbar} | \phi_n \rangle d_{n0} \right\}. \quad (3.69)$$

The formula was derived in [89] from the standard formulation of the absorption cross-section for a single chromophore. As in Eq. 3.69, this can be written as the Fourier transform of the chromophores dipole-dipole correlation function [82, 90, 91, 92, 93].

According to [82], Eq. 3.69 can be translated into its mixed quantum-classical form using the DCL. Therefore Eq. 3.69 is rewritten as

$$\begin{aligned} I(\omega) &= \text{Re} \int_0^\infty dt e^{i\omega t} \sum_{m,n}^N \text{tr}_{\text{vib}} \left\{ \hat{R}_0 e^{i\mathcal{H}_0 t/\hbar} d_{0m} \langle \phi_m | e^{-iH_1 t/\hbar} | \phi_n \rangle d_{n0} \right\} \\ &= \text{Re} \int_0^\infty dt e^{i\omega t} \sum_{m,n}^N \text{tr}_{\text{vib}} \left\{ \hat{R}_0 d_{0m}^{(0)}(t) e^{i\mathcal{H}_0 t/\hbar} \langle \phi_m | S_1(t, 0) | \phi_n \rangle d_{n0} \right\}. \end{aligned} \quad (3.70)$$

The S-operator (scattering matrix) is defined as [82]

$$S_1(t, 0) = \hat{T} \exp \left(-\frac{i}{\hbar} \int_0^t d\tau [H_1^{(0)}(\tau) - \mathcal{H}_0 \Pi_1] \right). \quad (3.71)$$

The time-dependent quantities $d_{0m}^{(0)}(t)$ and $H_1^{(0)}(t)$ represent d_{0m} and H_1 in the interaction representation [26]: $H_1^{(0)}(t) = \exp[i\mathcal{H}_0 t/\hbar] H_1 \exp[-i\mathcal{H}_0 t/\hbar]$. The same holds for the transition dipole moment $d_{0m}^{(0)}(t)$, for which the higher index (0) is dropped from here on. Π_1 is the projection operator to all first excited states of the CC ($\Pi_1 = \sum_m^N |\phi_m\rangle \langle \phi_m|$).

Carrying out the DCL to Eq. 3.70 results in a replacement of the trace-expression over the statistical operator \hat{R}_0 with an ensemble average over the initial conditions of the MD samples. This ensemble average over the MD simulation initial conformations will be introduced as $\langle \dots \rangle_{\text{ther}}$. Finally, one may replace the matrix element for the S-operator as [82]

$$\tilde{A}_m(t; n) = \langle \phi_m | S_1(t, 0) | \phi_n \rangle. \quad (3.72)$$

This finally gives for the absorption cross section [82]

$$I(\omega) = \text{Re} \int_0^\infty dt e^{i\omega t} \sum_{m,n} \langle d_{0m}(t) \tilde{A}_m(t; n) d_{n0} \rangle_{\text{ther}}. \quad (3.73)$$

The index 'ther' denotes the thermal averaging (due to the MD simulations). How to carry out the calculation of $\langle d_{0m}(t) \tilde{A}_m(t; n) d_{n0} \rangle_{\text{ther}}$ from the MD simulations will be explained in Sec. 4.5. Within this thesis, for the transition dipole moments holds: $d_{0m} = d_{m0} = d_m$.

The PESs of the ethanol molecules do not have to be included since in the frequency region of 14500-15500 cm^{-1} for the Q_y band and 17500-19000 cm^{-1} for the Q_x band, ethanol only absorbs weakly by high OH overtones [94].

In order to compute linear absorption curves that show the absorption intensity (as will be utilized in Chap. 5), the absorption cross section in Eq. 3.73 has to be multiplied by the energy of the respective photons. Thus, the intensity is proportional to $\omega \times I(\omega)$. This however, has only a weak influence on the line shape of the Q_y band.

3.6.1 Linear absorption of the Q_x band

The Q_x band of Pheo represents the second excited electronic state of Pheo. The computation of the Q_x band for a single Pheo in ethanol is the only calculation within this thesis, for which the second excited state denotes the S_2 state of a single Pheo. When chromophore complexes are described, a second excited state always denotes a CC which includes two singly excited Pheos (S_1 -state). The absorption cross section calculation for the Q_y band in Eq. 3.73 can as well be executed for the Q_x band, if the second derivatives of the PES may be computed. The Q_x absorption may not be calculated for Pheo complexes within this thesis, since the transition partial charges (or the transition dipole moments) are not available. In principle, those may be calculated utilizing electronic structure calculations. However, the expansion coefficients $\tilde{A}_1^f(t;1)$ (index 1 indicates that only a single Pheo is simulated, f indicates the second excited electronic state) have to be computed for a TDSE of the form

$$i\hbar \frac{\partial}{\partial t} \tilde{A}_1^f(t;1) = (\mathcal{H}_{1fg} - \Delta E_{g \rightarrow f}) \tilde{A}_1^f(t;1). \quad (3.74)$$

$\Delta E_{g \rightarrow f}$ is the transition energy between the electronic ground and second excited state. $\mathcal{H}_{1fg} - \Delta E_{g \rightarrow f} = U_{fg}(t)$, according to Eq. 3.55, is the energy gap function for a single Pheo in its second excited electronic state. This energy gap function can be written as

$$U_{fg}(t) = U_{fg}^{\text{vib}}(t) + U_{fg}^{\text{sol}}(t). \quad (3.75)$$

The two parts of the energy gap function in the second excited electronic state are written as

$$U_{fg}^{\text{vib}}(t) = H_{mf} - H_{mg} - \Delta E_{g \rightarrow f}, \quad (3.76)$$

and

$$U_{fg}^{\text{sol}}(t) = \sum_{n \neq m} [J_{mn}(fg, gf) - J_{mn}(gg, gg)] + \sum_{\xi} [J_{m\xi}(fg, gf) - J_{m\xi}(gg, gg)]. \quad (3.77)$$

To compute the respective energies, the Hessian matrices and the partial charges in the second excited electronic state are necessary. The Q_x band absorption cross section in Eq. 3.73 includes the transition dipole moments $d_m^f(t)d_n^f$. Those are not known for the second excited electronic state of Pheo. However, the electronic structure calculations provide the oscillator strengths f_a^{osc} of the first two excited electronic states $a = g$ and $a = f$. Utilizing the oscillator strengths, the product $d_1^f(t)d_1^f$ can thus be written in terms of the $d_m(t)d_n$:

$$d_1^f(t)d_1^f = \frac{f_f^{\text{osc}}}{f_e^{\text{osc}}} d_1(t)d_1. \quad (3.78)$$

Finally, Eq. 3.73 for the linear absorption cross section of the Q_y band of a CC can be reformulated to give the Q_x band for a single Pheo:

$$I(\omega) = \frac{f_f^{\text{osc}}}{f_e^{\text{osc}}} \text{Re} \int_0^\infty dt e^{i\omega t} \langle d_1(t) \tilde{A}_1^f(t;1) d_1 \rangle. \quad (3.79)$$

3.6.2 Vibrational progression

In a linear absorption curve of one respective electronic transition, several peaks may be observable. Those peaks are generally called vibrational satellites.

The explanation starts with the line shape function for a system that may be described by independent harmonic oscillators. The absorption cross section (Sec. 3.6) is proportional to the line shape function. The line shape function for the system that consists of independent harmonic oscillators is written [26] as

$$\mathcal{D} = \frac{1}{2\pi\hbar} \int_{-\infty}^{\infty} dt e^{i(\omega - \omega_{eg})t + G(t)} \quad (3.80)$$

with the transition frequency ω_{eg} between the electronic ground and first excited state of the chromophore and the time-dependent function

$$G(t) = \sum_{\xi} (g_e(\xi) - g_g(\xi))^2 \left[(e^{-i\omega_{\xi}t} - 1)(1 + n(\omega_{\xi})) + (e^{i\omega_{\xi}t} - 1)n(\omega_{\xi}) \right]. \quad (3.81)$$

$(g_e(\xi) - g_g(\xi))^2$ is the so-called Huang-Rhys factor [95], ξ counts the vibrational modes of the system (the number of independent harmonic oscillators that couple to the electronic transition) and $n(\omega_{\xi})$ is the Bose-Einstein distribution function.

According to [26], the line shape function for a single vibrational coordinate coupling to the electronic transition between two shifted harmonic PESs can be rewritten by expanding the exponential functions:

$$\begin{aligned} \mathcal{D} &= \frac{1}{\hbar} e^{-\Delta g^2(1+n(\omega_{\text{vib}}))} \sum_{M,N=0}^{\infty} \frac{1}{M!} [\Delta g^2(1+n(\omega_{\text{vib}}))]^M \\ &\times \frac{1}{N!} [\Delta g^2 n(\omega_{\text{vib}})]^N \delta(\omega - \omega_{eg} - (M - N)\omega_{\text{vib}}). \end{aligned} \quad (3.82)$$

This equation can be reformulated as

$$\mathcal{D} = \sum_{M,N=0}^{\infty} \mathcal{D}_{MN}, \quad (3.83)$$

with

$$\begin{aligned} \mathcal{D}_{MN} &= \frac{1}{\hbar} e^{-\Delta g^2(1+n(\omega_{\text{vib}}))} \frac{1}{M!} [\Delta g^2(1+n(\omega_{\text{vib}}))]^M \\ &\times \frac{1}{N!} [\Delta g^2 n(\omega_{\text{vib}})]^N \delta(\omega - \omega_{eg} - (M - N)\omega_{\text{vib}}). \end{aligned} \quad (3.84)$$

The single \mathcal{D}_{MN} determine the different vibrational satellites. When a mixed quantum-classical computation is carried out, the quantum character of the line shape function is not conserved as a whole. Since the trajectories of the nuclear coordinates are calculated utilizing standard MD simulations, the form of the line shape function \mathcal{D} changes. In what follows, the line shape function will be calculated for a system with harmonic PESs, while a thermal distribution of the normal modes is assumed. This assumption will result in the same vibrational progression as the absorption line shape calculated from an MD simulation of the respective system would show. The result of this 'classical' calculation of the line shape function will be compared with Eq. 3.82.

The starting point of the following computation is the mixed quantum-classical form of the line shape function (cf. Eq. 3.73). For simplification, only one mode couples to the electronic transition (the generalization to more modes is straightforward). The index ξ is dropped. The

line shape function has the form

$$\mathcal{D}^{\text{cl}} = \frac{1}{\mathcal{Z}} \text{Re} \int_0^\infty dt e^{i(\omega - \omega_{eg})t} \int \int dx_g dp_g \exp \left[-\frac{p_g^2}{2} + \frac{1}{2} \omega_{\text{vib}}^2 x_g^2 \right] e^{-i\eta(t)}. \quad (3.85)$$

The argument in the numerator is the total energy of the harmonic mode that couples to the transition. The normalization function \mathcal{Z} is written as

$$\mathcal{Z} = \int \int dx_g dp_g \exp \left[-\frac{p_g^2}{2} + \frac{1}{2} \omega_{\text{vib}}^2 x_g^2 \right] = \frac{2\pi k T \hbar}{\omega_{\text{vib}}}. \quad (3.86)$$

The function

$$\eta(t) = \frac{1}{\hbar} \int_0^t d\tau [U_e(x(\tau)) - U_g(x(\tau))] \quad (3.87)$$

is the time integral over the energy gap function $U_{eg}(x(t)) = U_e(x(t)) - U_g(x(t))$. The first exponential function in Eq. 3.85 contains the Boltzmann averaging of the initial coordinates and momenta with respect to the Hamilton function of a harmonic oscillator. The energy gap function $U_e(x(t)) - U_g(x(t))$ in harmonic approximation can be written as

$$U_e(x(t)) - U_g(x(t)) = \frac{1}{2} \omega_{\text{vib}}^2 (x_e^2 - x_g^2) + 2x(t)(x_g - x_e), \quad (3.88)$$

where x_e and x_g are the equilibrium positions of the coordinates for the respective electronic state. The general solution of the oscillator equation $x(\tau)$ that has to be inserted into Eq. 3.88, is

$$x(t) = x_g \cos(\omega t) + \frac{p_g}{\omega_{\text{vib}}} \sin(\omega t). \quad (3.89)$$

As the integration over the time τ in Eq. 3.87 is done, $\eta(t)$ gives

$$\eta(t) = \frac{\omega_{\text{vib}}^2}{2\hbar} \left[(x_e^2 - x_g^2)t + 2(x_g - x_e) \left(\frac{x_g \sin(\omega_{\text{vib}} t)}{\omega_{\text{vib}}} - \frac{p_g (\cos(\omega_{\text{vib}} t) - 1)}{\omega_{\text{vib}}^2} \right) \right]. \quad (3.90)$$

With this information about $\eta(t)$, the integral (over the coordinate and momentum space) in Eq. 3.85 may be calculated. The exponential function (cf. Eqs. 3.88, 3.89) contains one term linear in x_0 and one term linear in p_0 . The Boltzmann function in Eq. 3.85 contains one term quadratic in x_0 and one term quadratic in p_0 . After completing the square, the phase space integration in Eq. 3.85 reduces to the calculation of Gaussian integrals and gives the line shape function after thermal averaging. Like in [26], the variable g_a was introduced as $x_a^2 = g_a \frac{2\hbar}{\omega_{\text{vib}}}$, with $a \in g, e$. After expanding the cosine function, \mathcal{D}^{cl} reads

$$\begin{aligned} \mathcal{D}^{\text{cl}} = & \frac{1}{\hbar} e^{-\Delta g^2 \frac{kT}{\hbar \omega_{\text{vib}}}} \sum_{M, N=0}^{\infty} \frac{1}{M!} \left[\Delta g^2 \frac{kT}{\hbar \omega_{\text{vib}}} \right]^M \frac{1}{N!} \left[\Delta g^2 \frac{kT}{\hbar \omega_{\text{vib}}} \right]^N \\ & \times \delta(\omega - \omega_{eg} - \omega_{\text{vib}}(g_e^2 - g_g^2) - (M - N)\omega_{\text{vib}}). \end{aligned} \quad (3.91)$$

This equation can be rewritten (according to Eq. 3.83 for the full quantum line shape function) to get

$$\mathcal{D}^{\text{cl}} = \sum_{M, N=0}^{\infty} \mathcal{D}_{MN}^{\text{cl}}, \quad (3.92)$$

with

$$\mathcal{D}_{MN}^{\text{cl}} = \frac{1}{\hbar} e^{-\Delta g^2 \frac{kT}{\hbar \omega_{\text{vib}}}} \frac{1}{M!} \left[\Delta g^2 \frac{kT}{\hbar \omega_{\text{vib}}} \right]^M \frac{1}{N!} \left[\Delta g^2 \frac{kT}{\hbar \omega_{\text{vib}}} \right]^N \times \delta(\omega - \omega_{eg} - \omega_{\text{vib}}(g_e^2 - g_g^2) - (M - N)\omega_{\text{vib}}). \quad (3.93)$$

The $\mathcal{D}_{MN}^{\text{cl}}$ give the different vibrational satellites for the classical computed line shape function. The classically calculated line shape function is shifted by $\omega_{\text{vib}}(g_e^2 - g_g^2)$.

The linear absorption formula in the DCL (Eq. 3.73) depends on classical molecular dynamics. The resulting vibrational progression will be a classical one. To correct this error a correction factor f_{MN} can be computed and multiplied with the respective vibrational satellite. f_{MN} is defined as

$$f_{MN} = \frac{\mathcal{D}_{MN}}{\mathcal{D}_{MN}^{\text{cl}}}. \quad (3.94)$$

Note that $f_{MN} = f_{MN}(\omega_{\text{vib}}, T)$ depends on the vibrational frequency ω_{vib} and the temperature T . In Sec. 5.1.2 this correction will be utilized to compute the quantum amplitude for the first vibrational satellite \mathcal{D}_{10} . It has to be noted that \mathcal{D}_{01} (in comparison to \mathcal{D}_{10} , note the permutation of the index) is very small (compare to the \mathcal{D}_{MN} in Eq. 3.83). This is due to the fact that the Bose-Einstein distribution gives a very small value for T at room temperature. This correction factor f_{10} gives quite satisfactory results when the computed linear absorption is compared to the experimental curve (the results will be given in Sec. 5.1.2).

3.7 EET rates

In this section, the formulas for EET rates between Pheos within a P_N complex will be derived in the DCL. In the present discription, a dilute solution of P_N complexes in ethanol is assumed. Thus, EET between chromophores bound to different complexes may be neglected. If the dendrimers are close to each other, this approximation does not hold. A respective description of exciton states that belong to different complexes is given in [96]. However, for P_N complexes in ethanol, this approximation is reasonable.

The most important quantity for the calculation of the EET rate between two chromophores is the excitonic coupling. The computation of the excitonic coupling evolved during the last decade [32, 97, 98, 99, 100]. However, the utilization of quantum chemical methods overestimates the chromophore transition dipole moment [32] and thus the effect of the transition partial charges that are fitted to the potential of the transition density. The factor of overestimation can be found by comparing computed and measured values of the vacuum transition dipole moment. A large number of chromophore transition dipole moments was measured by Knox and Spring [101].

The use of the dipole-dipole coupling for the computation of the EET rate results in a $1/X_{mn}^6$ dependence of the transition rate, with X_{mn} being the distance of the centers of molecules m and n . This $1/X_{mn}^6$ dependence is known from classical Förster theory [2]. More involved ansatzes than the Förster theory are rather rare in present literature [102, 103, 104]. In this thesis, the EET rate is given in second order of the excitonic coupling (like in Förster theory), but the excitonic coupling itself is not assumed to be constant, but it varies with the conformational change of the system.

The full quantum rate for the EET from molecule m to molecule n [32, 39, 105] is

$$k_{m \rightarrow n} = 2\text{Re} \int_0^\infty dt C_{m \rightarrow n}(t). \quad (3.95)$$

According to [39, 106] the correlation function $C_{m \rightarrow n}(t)$ can be written as

$$C_{m \rightarrow n}(t) = \frac{1}{\hbar^2} \text{tr}_{\text{vib}} \left\{ \hat{R}_m e^{iH_m t/\hbar} J_{mn} e^{-iH_n t/\hbar} J_{nm} \right\}. \quad (3.96)$$

Comparing with the notation in Eq. 3.48, the excitonic coupling between chromophores m and n may be written as $J_{mn} = J_{mn}(ge, ge) = J_{mn}(eg, eg)$. For the strength of the excitonic coupling between two chromophores m and n it is not important which of the chromophores is initially excited. H_m and H_n are Hamiltonians for the singly excited CC, where the respective chromophores m or n are excited (diagonal parts of the Hamilton matrix in Eq. 3.53):

$$H_m = \mathcal{H}_0 + \mathcal{H}_{meg}. \quad (3.97)$$

If both chromophores m and n are sufficiently far away from each other, they do not share any common vibrational modes [39]. Therefore, it is assumed that the molecules m and n described by the Hamiltonians H_{me} and H_{ne} are characterized by separate vibrational modes. The Hamiltonians H_{mg} and H_{me} cover the intramolecular vibration and the coupling to the solvent (cf. Eq. 3.55) for chromophore m (the indices g, e describe the actual electronic state of chromophore m). The correlation function for a respective mutual orientation and distance between two molecules m and n (with respective excitonic coupling J_{mn}) can be written as [39]

$$C_{m \rightarrow n}(t) = \frac{|J_{mn}|^2}{\hbar^2} C_{me \rightarrow g}(t) C_{ng \rightarrow e}(t), \quad (3.98)$$

where

$$C_{me \rightarrow g}(t) = \text{tr}_{\text{vib}} \left\{ \hat{R}_{me} e^{iH_{me} t/\hbar} e^{-iH_{mg} t/\hbar} \right\} \quad (3.99)$$

describes the de-excitation of chromophore m and

$$C_{ng \rightarrow e}(t) = \text{tr}_{\text{vib}} \left\{ \hat{R}_{ng} e^{iH_{ng} t/\hbar} e^{-iH_{ne} t/\hbar} \right\} \quad (3.100)$$

describes the excitation of chromophore n . \hat{R}_{me} and \hat{R}_{ng} are the respective ground and excited state statistical operators.

If the single-molecule correlation functions are Fourier-transformed, the rate between chromophores m and n can be given in the standard form of Förster theory [39]:

$$k_{m \rightarrow n} = \frac{|J_{mn}|^2}{2\pi\hbar^2} \int d\omega C_{me \rightarrow g}(-\omega) C_{ng \rightarrow e}(\omega). \quad (3.101)$$

As argued in [39] the frequency integral corresponds to the spectral overlap of the emission spectrum of chromophore m and the absorption spectrum of chromophore n .

3.7.1 Rate equations in the dynamical classical limit

The starting point for the translation of the correlation function to the DCL is Eq. 3.96. It may be rewritten as [39]

$$C_{m \rightarrow n}(t) = \text{tr}_{\text{vib}} \left\{ \hat{R}_m J_{mn}^{(m)}(t) e^{iH_m t/\hbar} e^{-iH_n t/\hbar} J_{nm} \right\}. \quad (3.102)$$

This is possible with the definition of [39] (cf. Sec. 3.6)

$$J_{mn}^{(m)}(t) = e^{iH_m t/\hbar} J_{mn} e^{-iH_m t/\hbar}. \quad (3.103)$$

3 The mixed quantum-classical methodology

In order to carry out the dynamical classical limit, the product of time-evolution operators in Eq. 3.102 is replaced by the S-operator [26, 39]. The S-operator can be written as [39]

$$S(t, 0) = e^{iH_m t/\hbar} e^{-iH_n t/\hbar} = \hat{T} \exp \left(-\frac{i}{\hbar} \int_0^t d\tau e^{iH_m \tau/\hbar} [H_n - H_m] e^{-iH_m \tau/\hbar} \right). \quad (3.104)$$

The S-operator $S(t, 0)$ is related to the $S_1(t, 0)$ in Eq. 3.71, utilized for the computation of linear absorption in Sec. 3.6. While $S(t, 0)$ is the propagator for a transition between two CC states $|\phi_m\rangle$ and $|\phi_n\rangle$, $S_1(t, 0)$ is the propagator for a transition between electronic ground state $|\phi_0\rangle$ and electronic first excited state $|\phi_e\rangle$ (Eq. 3.56). Then the correlation function reads [39]

$$C_{m \rightarrow n}(t) = \text{tr}_{\text{vib}} \left\{ \hat{R}_m J_{mn}^{(m)} S(t, 0) J_{nm} \right\}. \quad (3.105)$$

The dynamical classical limit is done by approximating the S-operator (Eq. 3.104) as [39]

$$S(t, 0) = \exp [-i\eta_n(t, 0) + i\eta_m(t, 0)], \quad (3.106)$$

with

$$\eta_m(t, 0) = \frac{1}{\hbar} \int_0^\infty d\tau \mathcal{H}_{meg}(R^m(\tau)) \quad (3.107)$$

and

$$\eta_n(t, 0) = \frac{1}{\hbar} \int_0^\infty d\tau \mathcal{H}_{neg}(R^n(\tau)). \quad (3.108)$$

The \mathcal{H}_{meg} were defined in Eq. 3.55. The indices m or n at a set R of classical nuclear coordinates indicate that the respective chromophore m or n is excited. This has to be treated by the respective force field that is utilized to get the particular coordinate set. Finally, the utilization of the ground state classical path approximation (cf. Sec. 3.1.6) makes it possible to drop the requirement of using excited state force fields.

In order to obtain the semiclassical equation for the transition rate from Eq. 3.95 together with Eq. 3.106, one has to approximate the trace together with the equilibrium statistical operator. This trace is replaced by the thermal average with respect to different initial conformations of the CC during the MD simulation (cf. Sec. 4.1.6). This thermal average will be denoted by the angle bracket $\langle \dots \rangle_{\text{ther}}$. The $J_{mn}(t)$ are the time-dependent couplings between chromophores m and n during the simulation. The result for the transition rate in the DCL is [39]

$$k_{m \rightarrow n}^{\text{DCL}} = 2\text{Re} \int_0^\infty dt C_{m \rightarrow n}^{\text{DCL}}(t), \quad (3.109)$$

with

$$C_{m \rightarrow n}^{\text{DCL}}(t) = \frac{1}{\hbar^2} \left\langle S_{\text{DCL}}(t, 0) J_{mn}^{(m)}(t) J_{mn}(0) \right\rangle_{\text{ther}}. \quad (3.110)$$

This equation automatically gives $k_{m \rightarrow n}^{\text{DCL}} = k_{n \rightarrow m}^{\text{DCL}}$. Detailed balance is not fulfilled. This is only an acceptable approximation if the energy levels of all involved chromophores do not differ too much. The CCs observed here contain identical molecules which can be assumed to have the same energy. Of course, there is some slight energy difference, since all chromophores couple somewhat differently to their solvation shell. However, this energy difference is negligible compared to $k_b T$ at room temperature (T being the temperature, k_b the Boltzmann constant).

3.7.2 Further approximations to the transfer rates

If the $J_{mn}(t)$ is assumed to be time-independent, the rate $k_{m \rightarrow n}$ can be calculated in approximation by utilizing the correlation function [39]

$$C_{m \rightarrow n}^{\text{app.1}}(t) = \frac{|J_{mn}|^2}{\hbar^2} \langle S_{\text{DCL}}(t, 0) \rangle_{\text{ther}}. \quad (3.111)$$

The respective rate calculated with this approximation will be denoted as $k_{m \rightarrow n}^{\text{app.1}}$. The approximation is possible if the mutual orientation and distance between two chromophores m and n does not change dramatically during the simulation time. Since the CC structure does not change too much for a simulation time of 10 ps, the restriction to such short time scales permits this approximation.

A further approximation is possible if the energy gap fluctuations of both chromophores m and n are uncorrelated. $\langle S_{\text{DCL}}(t, 0) \rangle$ may be factorized into two independent contributions. The respective rate using this second approximation (which will be denoted as $k_{m \rightarrow n}^{\text{app.2}}$) is calculated via integrating the correlation function $C_{m \rightarrow n}^{\text{app.2}}$ [39]:

$$C_{m \rightarrow n}^{\text{app.2}}(t) = \frac{|J_{mn}|^2}{\hbar^2} \langle e^{i\eta_m(t,0)} \rangle \langle e^{-i\eta_n(t,0)} \rangle_{\text{ther}}. \quad (3.112)$$

Obviously, the rate $k_{m \rightarrow n}^{\text{app.2}}$ corresponds to the EET rate given in Eq. 3.101.

3.8 Calculation of transient absorption

In the following section, the formula for the computation of the transient absorption will be derived. A widespread approach is calculating the third order optical response via the respective nonlinear response function (cf. [107, 108, 109]). Two dimensional spectra calculated via nonlinear response functions are shown in [110, 111].

To circumvent the computation of a function with a triple time-dependence [85] in this thesis, the transient absorption is calculated by solving the TDSE directly, including the electromagnetic field. With this approach the time-dependent polarization can be calculated directly. This polarization can then be utilized to calculate an absorption spectrum of a probe pulse, after an initial pump pulse has excited the system. The approach of directly calculating the total polarization has already been presented by the Geva group in [112] (for a two-level chromophore in a mono-atomic liquid). However, the P_4 system in solution that will be the model system for transient absorption in this thesis is a much more complex system.

It is important to remind that the previously defined second excited state wave function of the CC always reckons two chromophores of the CC in the first excited electronic state. The double excitation of one chromophore in the complex is not allowed (additional comments have been made in Sec. 3.2).

In the current model the excitation of the CC from the electronic ground state to the first excited electronic state and the excitation from the first excited electronic state of the CC to the second excited electronic state of the CC is treated. An excitation of more than two Pheos within the complex is neglected. This approximation is reasonable, since for the utilized field strengths the total population of the second excited state of the CC is much smaller than the population of the first excited state. The population of a third excited electronic state of the CC, even if it was allowed, would be very small.

The respective TDSE is written

$$-i\hbar \frac{\partial}{\partial t} \Phi(t) = (H_0 + H_1 + H_2 + H_{\text{field}}(t)) \Phi(t). \quad (3.113)$$

3 The mixed quantum-classical methodology

The CC wave function $\Phi(t)$ was defined in Eq. 3.2 and includes the electronic ground, first excited and second excited state. The respective matrix elements H_0 , H_1 and H_2 were explained in Sec. 3.3. The electromagnetic field Hamiltonian H_{field} was already included in Eq. 3.24, but is given here again to improve the understandability of the following text:

$$H_{\text{field}}(t) = - \sum_m (\langle \phi_m | \hat{\mu} \mathbf{E}(t) | \phi_0 \rangle | \phi_m \rangle \langle \phi_0 | + H.c.) \\ - \sum_m \sum_{n>m} (\langle \phi_{mn} | \hat{\mu} \mathbf{E}(t) | \phi_m \rangle | \phi_{mn} \rangle \langle \phi_m | + H.c.). \quad (3.114)$$

The dipole operator $\hat{\mu}$ was defined in Eq. 3.25. For P_4 , the CC wave function $\Phi(t)$ is a superposition over eleven states, one ground state, four different first excited and six different second excited electronic states. Together with the definitions of H_0 , H_1 and H_2 (Eqs. 3.27, 3.28, 3.29) and the CC wave function $\Phi(t)$ (Eq. 3.2), the TDSE in Eq. 3.113 can be rewritten in terms of the expansion coefficients A_α . This gives the three equations

$$-i\hbar \frac{\partial}{\partial t} A_0(t) = \mathcal{H}_0(t) A_0(t) - \sum_m \mathbf{d}_m^*(t) \mathbf{E}(t) A_m(t), \quad (3.115)$$

$$-i\hbar \frac{\partial}{\partial t} A_m(t) = \sum_k \mathcal{H}_{mk}(t) A_k(t) - \mathbf{d}_m(t) \mathbf{E}(t) A_0(t) \\ - \sum_{n>m} \mathbf{d}_n^*(t) \mathbf{E}(t) A_{mn}(t) - \sum_{m>n} \mathbf{d}_n^*(t) \mathbf{E}(t) A_{nm}(t), \quad (3.116)$$

and

$$-i\hbar \frac{\partial}{\partial t} A_{mn}(t) = \sum_{k,l} \mathcal{H}_{mn,kl}(t) A_{kl}(t) \\ - \sum_{n>m} \mathbf{d}_n(t) \mathbf{E}(t) A_m(t) - \sum_{m>n} \mathbf{d}_m(t) \mathbf{E}(t) A_n(t). \quad (3.117)$$

The definition of the $A_{mn}(t)$ in Sec. 3.2 demands that $n > m$, to avoid two definitions $A_{mn}(t)$ and $A_{nm}(t)$ of the same expansion coefficient.

Similar to Eq. 3.59, an ansatz to the expansion coefficients was made that eliminates the phase factor caused by the transition energy $\Delta E_{g \rightarrow e}$, the electronic ground state interactions as well as the kinetic energy operators T_m , all included in \mathcal{H}_0 . The ansatz is different for the electronic ground, first and second excited state expansion coefficient:

$$\tilde{A}_0 = A_0 \exp \left(i \int_0^t d\tau \mathcal{H}_0(\tau) / \hbar \right), \quad (3.118)$$

$$\tilde{A}_m = A_m \exp \left(i \left[\int_0^t d\tau (\mathcal{H}_0(\tau) + \Delta E_{g \rightarrow e} t) \right] / \hbar \right), \quad (3.119)$$

and

$$\tilde{A}_{mn} = A_{mn} \exp \left(i \left[\int_0^t d\tau (\mathcal{H}_0(\tau) + 2\Delta E_{g \rightarrow e} t) \right] / \hbar \right). \quad (3.120)$$

Inserting Eqs. 3.118 and 3.119 into Eq. 3.115 gives

$$i\hbar \frac{\partial}{\partial t} \tilde{A}_0(t) = \sum_n (\mathcal{H}_0(t)) \tilde{A}_0(t) - \sum_m \mathbf{d}_m^*(t) \mathbf{E}(t) \tilde{A}_m(t) e^{-i\Delta E_{g \rightarrow e} t / \hbar}. \quad (3.121)$$

Inserting Eqs. 3.118, 3.119 and 3.120 into Eq. 3.116 yields

$$i\hbar \frac{\partial}{\partial t} \tilde{A}_m(t) = \sum_n (\mathcal{H}_{mn}(t) - \delta_{m,n} \Delta E_{g \rightarrow e}) \tilde{A}_n(t) - \mathbf{d}_m(t) \mathbf{E}(t) e^{i\Delta E_{g \rightarrow e} t / \hbar} \tilde{A}_0(t) - \sum_{n>m} \mathbf{d}_n^*(t) \mathbf{E}(t) e^{-i\Delta E_{g \rightarrow e} t / \hbar} \tilde{A}_{mn}(t) - \sum_{m>n} \mathbf{d}_n^*(t) \mathbf{E}(t) e^{-i\Delta E_{g \rightarrow e} t / \hbar} \tilde{A}_{nm}(t). \quad (3.122)$$

Inserting Eqs. 3.119 and 3.120 into Eq. 3.117 gives

$$-i\hbar \frac{\partial}{\partial t} \tilde{A}_{mn}(t) = \sum_{k,l} (\mathcal{H}_{mn,kl}(t) - 2\delta_{m,k} \delta_{n,l} \Delta E_{g \rightarrow e}) \tilde{A}_{kl}(t) - \sum_{m<n} \mathbf{d}_n^*(t) \mathbf{E}(t) e^{i\Delta E_{g \rightarrow e} t / \hbar} \tilde{A}_m(t) - \sum_{n>m} \mathbf{d}_m^*(t) \mathbf{E}(t) e^{i\Delta E_{g \rightarrow e} t / \hbar} \tilde{A}_n(t). \quad (3.123)$$

The electromagnetic field $\mathbf{E}(t)$, which is already included in the formulas given above, is written as

$$\mathbf{E}(t) = \mathcal{E}_{\text{pu}}(t) e^{i\Psi_{\text{pu}}} + \mathcal{E}_{\text{pr}}(t) e^{i\Psi_{\text{pr}}} + c.c., \quad (3.124)$$

with

$$\mathcal{E}_p(t) = \mathbf{e}_p E_p(t) e^{-i\omega_p t}, p \in \{\text{pu}, \text{pr}\}, \quad (3.125)$$

with the pump and probe beam frequencies ω_{pu} , ω_{pr} , the respective phases Ψ_{pu} , Ψ_{pr} , with the polarization vectors of the pump and the probe beam \mathbf{e}_{pu} and \mathbf{e}_{pr} and the respective field envelopes E_{pu} and E_{pr} . The formulas for the electromagnetic field (Eqs. 3.124 and 3.125) are inserted into the Eqs. 3.121, 3.122, 3.123 for the expansion coefficients $\tilde{A}_\alpha(t)$. At this point the so-called rotating wave approximation [113] is applied. All terms that include an exponential function of the form $\exp(2i\omega_p t)$ or $\exp(-2i\omega_p t)$ (those terms oscillating with high frequency) are neglected [114].

3.8.1 Time-dependent polarization

After solving Eq. 3.113, the calculated time-dependent wave function $\Phi(t)$ can be utilized to calculate the time-dependent dipole moment expectation value defined as [85]

$$\mathbf{d}(t, \mathbf{E}) = \langle \langle \Phi(R(t), t, \mathbf{E}) | \hat{\boldsymbol{\mu}} | \Phi(R(t), t, \mathbf{E}) \rangle \rangle_{\text{ther}} = \langle \langle \Phi(t) | \hat{\boldsymbol{\mu}} | \Phi(t) \rangle \rangle_{\text{ther}}. \quad (3.126)$$

The t - and \mathbf{E} -dependence in $\Phi(t) = \Phi(R(t), t, \mathbf{E})$ denotes that the calculated expansion coefficients $\tilde{A}_\alpha(\tau)$ (cf. Eq. 3.2 for the CC wave function) at time $t = \tau$ depend directly on the actual MD trajectory and the field envelope between $t = 0$ and $t = \tau$. The thermal average $\langle \dots \rangle_{\text{ther}}$ is carried out with respect to the equilibrium distribution of nuclear coordinates. In terms of the expansion coefficients $\tilde{A}_\alpha(t)$, the dipole moment expectation value reads [85]

$$\mathbf{d}(t, \mathbf{E}) = \langle \sum_{\alpha, \beta} \mathbf{d}_{\alpha\beta} \tilde{A}_\alpha^*(t, \mathbf{E}) \tilde{A}_\beta(t, \mathbf{E}) \rangle_{\text{ther}}. \quad (3.127)$$

The polarization (dipole density) is then calculated as

$$\mathbf{P}(t, \mathbf{E}) = n_{\text{CC}} \mathbf{d}(t, \mathbf{E}), \quad (3.128)$$

with the CC density n_{CC} . However, to calculate transient absorption spectra, the probe pulse polarization in signal direction has to be derived from the overall polarization $\mathbf{d}(t, \mathbf{E})$. In the next step, two different methods will be presented, which allow to carry out this calculation.

3.8.2 Signal polarization, method I

Dohmke and co-workers proposed a method [113] that will be mainly utilized within this thesis. According to the two beams in Eq. 3.124, a power expansion with respect to the polarization at some point \mathbf{r} is carried out. This power expansion can be written as [113, 115]

$$\mathbf{P}(\mathbf{r}, t) = \sum_{m,n} e^{i(m\mathbf{k}_{pu}\mathbf{r} + n\mathbf{k}_{pr}\mathbf{r})} \mathbf{P}^{(mn)}(t). \quad (3.129)$$

Here, for once, m and n do not count chromophores, they run over all integers and the $\mathbf{P}^{(mn)}(t)$ are the polarization amplitudes of the different spectroscopic signals in the direction $m\mathbf{k}_{pu} + n\mathbf{k}_{pr}$. If the phases Ψ_p are defined as $\Psi_p = \mathbf{k}_p \mathbf{r}$, with $p \in \{\text{pu}, \text{pr}\}$, Eq. 3.129 can be interpreted as a Fourier transform [115, 116]:

$$\mathbf{P}(t; \Psi_{pu}, \Psi_{pr}) = \sum_{m,n} e^{i(m\Psi_{pu} + n\Psi_{pr})} \mathbf{P}^{(mn)}(t). \quad (3.130)$$

Such an interpretation would yield the following conclusion: if $\mathbf{P}(t; \Psi_{pu}, \Psi_{pr})$ is known for the whole Ψ_{pu}, Ψ_{pr} configuration space, the respective inverse Fourier transform would generate all amplitudes $\mathbf{P}^{(mn)}$ [115]. In practice, it is only possible to compute $\mathbf{P}(t; \Psi_{pu}, \Psi_{pr})$ for a finite set of phases $(\Psi_{pu}^l, \Psi_{pr}^{l'})$. If \mathcal{N} different values $\mathbf{P}(t; \Psi_{pu}^l, \Psi_{pr}^{l'})$ are calculated for \mathcal{N} different combinations of $(\Psi_{pu}^l, \Psi_{pr}^{l'})$, \mathcal{N} different values of the polarization amplitudes $\mathbf{P}^{(mn)}$ may be calculated via the following equation [115]:

$$\mathbf{P}(t; \Psi_{pu}^l, \Psi_{pr}^{l'}) = \sum_{[m,n]} e^{i(m\Psi_{pu}^l + n\Psi_{pr}^{l'})} \mathbf{P}^{(mn)}(t). \quad (3.131)$$

$[m, n]$ indicates a finite sum over m and n , according to the \mathcal{N} different pairs of $(\Psi_{pu}^l, \Psi_{pr}^{l'})$.

It was shown in [113] that (if the rotating wave approximation is used) only a signal into the direction $m\mathbf{k}_{pu} + (1 - m)\mathbf{k}_{pr}$ appears. If higher order terms ($m, n > 2$) are neglected, Eq. 3.131 can be rewritten as [115]

$$\begin{aligned} \mathbf{P}(t; \Psi_{pu}^l, \Psi_{pr}^{l'}) &= e^{i\Psi_{pu}^l} \mathbf{P}^{(10)}(t) + e^{i\Psi_{pr}^{l'}} \mathbf{P}^{(01)}(t) \\ &+ e^{i(2\Psi_{pu}^l - 1\Psi_{pr}^{l'})} \mathbf{P}^{(2-1)}(t) + e^{i(-\Psi_{pu}^l + 2\Psi_{pr}^{l'})} \mathbf{P}^{(-1+2)}(t). \end{aligned} \quad (3.132)$$

$\mathbf{P}^{(10)}$ is the polarization due to the pump pulse, $\mathbf{P}^{(01)}$ is the polarization due to the probe pulse and the $\mathbf{P}^{(2-1)}$ and $\mathbf{P}^{(-1+2)}$ represent combined contributions in the directions $2\mathbf{k}_{pu} - \mathbf{k}_{pr}$ as well as $-\mathbf{k}_{pu} + 2\mathbf{k}_{pr}$. If for the pairs $(\Psi_{pu}^l, \Psi_{pr}^{l'})$ the values $(0, 0)$, $(\pi/2, 0)$, $(\pi, 0)$, $(3\pi/2, 0)$ are chosen, the following result can be derived for the polarization in probe pulse direction [113, 115]:

$$\mathbf{P}^{(01)} = \frac{1}{4} (\mathbf{P}(t; 0, 0) + \mathbf{P}(t; \pi/2, 0) + \mathbf{P}(t; \pi, 0) + \mathbf{P}(t; 3\pi/2, 0)). \quad (3.133)$$

If the additional approximation that both pulses are not overlapping in time can be made, Eq. 3.133 can further be simplified. In this case only two contributions have to be calculated [113]. However, in this work always Eq. 3.133 will be utilized. This rendered it possible to calculate the polarization in probe pulse direction for overlapping as well as for non-overlapping pulses.

3.8.3 Signal polarization, method II

Another very intuitive approach for the calculation of the signal polarization was suggested by Pullerits and co-workers in [117, 118]. It is assumed that a lot of CCs are distributed in space, each numbered by the index j . The polarization in probe pulse direction \mathbf{k}_{pr} is then calculated via

$$\mathbf{P}(\mathbf{k}_{\text{pr}}, t) = \sum_j e^{i\mathbf{k}_{\text{pr}}\mathbf{r}_j} \mathbf{P}(\mathbf{r}_j, t; \mathbf{E}(\mathbf{r}_j, t)). \quad (3.134)$$

At first, the local polarization at a lot of points \mathbf{r}_j is calculated. Of course, at each point \mathbf{r}_j the local electromagnetic field $\mathbf{E}(\mathbf{r}_j, t)$ has a different phase. The summation over all the different local polarizations with the local phase prefactors $e^{i\mathbf{k}_{\text{pr}}\mathbf{r}_j}$ gives the polarization in probe pulse direction. However, since the $e^{i\mathbf{k}_{\text{pr}}\mathbf{r}_j}$ depend very sensitively on \mathbf{r}_j and fluctuate between negative and positive values, the convergence of this method is extremely bad. Millions of local polarizations have to be taken into account to achieve a convergence of the formula (cf. Sec. 5.2.3).

3.8.4 Differential transient absorption

The frequency dependent transient absorption after the delay time t_{delay} can be written as [85, 113]

$$\Delta S(\omega, t_{\text{delay}}) = 2\omega \text{Im} \left[\mathcal{E}_{\text{pr}}^*(\omega) \Delta \mathbf{P}(\mathbf{k}_{\text{pr}}, \omega) \right], \quad (3.135)$$

with the frequency ω , the Fourier transformed electromagnetic field

$$\mathcal{E}_{\text{pr}}(\omega) = \int_{-\infty}^{\infty} dt e^{i\omega t} \mathcal{E}_{\text{pr}}(t), \quad (3.136)$$

and the Fourier transformed differential polarization in probe pulse direction

$$\Delta \mathbf{P}(\mathbf{k}_{\text{pr}}, \omega) = \int_{-\infty}^{\infty} dt e^{i\omega t} \Delta \mathbf{P}(\mathbf{k}_{\text{pr}}, t). \quad (3.137)$$

The differential polarization in probe pulse direction can be written as

$$\Delta \mathbf{P}(\mathbf{k}_{\text{pr}}, t) = \mathbf{P}(\mathbf{k}_{\text{pr}}, t; \mathbf{E}_{\text{pu}} \neq 0) - \mathbf{P}(\mathbf{k}_{\text{pr}}, t; \mathbf{E}_{\text{pu}} = 0). \quad (3.138)$$

The differential polarization is simply the polarization of the system when a pump pulse was present, minus the polarization of the system, when the pump pulse was absent.

It should be mentioned here that Eq. 3.135 follows directly (via Fourier transform) from the formula for the total energy that is dissipated or gained by the probe pulse in a medium [85, 113]:

$$S = \int_{-\infty}^{\infty} dt \mathcal{E}_{\text{pr}}^*(t) \mathbf{P}(\mathbf{k}_{\text{pr}}, t). \quad (3.139)$$

3.8.5 Transient anisotropy

In the last section, the differential transient absorption $\Delta S(\omega, t_{\text{delay}})$ (Eq. 3.135) was introduced. Next, it will be distinguished between the case when pump and probe pulse polarization are parallel ($\mathbf{e}_{\text{pu}} \parallel \mathbf{e}_{\text{pr}}$) and the case when they are orthogonal ($\mathbf{e}_{\text{pu}} \perp \mathbf{e}_{\text{pr}}$). The respective differential transient absorptions are noted ΔS^{\parallel} and ΔS^{\perp} . From ΔS^{\parallel} and ΔS^{\perp} the transient anisotropy r can be calculated. The computation of r gives a quantity that may be compared directly to experimental measurements. It is written as (cf. [9])

$$r = \frac{\Delta S^{\parallel} - \Delta S^{\perp}}{\Delta S^{\parallel} + 2\Delta S^{\perp}}. \quad (3.140)$$

3.9 Analytical calculation of the transient anisotropy

In this section, the transient anisotropy will be calculated analytically. In order to shorten the formulas, the projection operators for the different electronic states are introduced. The projection operator for the electronic ground state reads

$$\Pi_0 = |\phi_0\rangle\langle\phi_0|. \quad (3.141)$$

The projection operator for the first excited electronic states of the CC is

$$\Pi_1 = \sum_m |\phi_m\rangle\langle\phi_m|, \quad (3.142)$$

while the projection operator for the second excited electronic states can be written as

$$\Pi_2 = \sum_{n>m} |\phi_{mn}\rangle\langle\phi_{mn}|. \quad (3.143)$$

It is also useful to have the following definitions of H_0 , H_1 and H_2 (Eqs. 3.27, 3.28, 3.29):

$$H_0 = \mathcal{H}_0\Pi_0, \quad (3.144)$$

$$H_1 = \mathcal{H}_1\Pi_1, \quad (3.145)$$

and

$$H_2 = \mathcal{H}_2\Pi_2. \quad (3.146)$$

The first equation, Eq. 3.144, corresponds to Eq. 3.51.

3.9.1 The density operator after pump pulse excitation

For the subsequent computation of the transient absorption line shape, the density operator after pump pulse excitation has to be computed. Due to the relatively short pump pulse time of 12 fs full width half maximum (FWHM) and the pump pulse field strength of 2.5×10^8 V/m, only the first excited electronic state of the CC will be populated significantly (about 10 percent of the P_4 molecules are singly excited after the pump pulse, the population of the second excited electronic CC state is almost two orders of magnitude lower). In approximation, the excitation of the second excited CC state by the pump pulse can be neglected. The respective Hamiltonian is written as

$$H_{CC}^{eg}(t) = \mathcal{H}_0\Pi_0 + \mathcal{H}_1\Pi_1 - \mathbf{E}(t)\hat{\boldsymbol{\mu}}. \quad (3.147)$$

The higher index *ge* indicates that only the electronic ground and first excited state are treated. The electromagnetic field was defined in Eq. 3.124, the dipole operator $\hat{\boldsymbol{\mu}}$ in 3.25. With the projection operators Π_0 and Π_1 and the restriction to the electronic ground and first excited state, $\hat{\boldsymbol{\mu}}$ may be approximated as

$$\hat{\boldsymbol{\mu}}^{eg} = \Pi_0\hat{\boldsymbol{\mu}}\Pi_1 + \Pi_1\hat{\boldsymbol{\mu}}\Pi_0 = \hat{\boldsymbol{\mu}}_{01}^{eg} + \hat{\boldsymbol{\mu}}_{10}^{eg}. \quad (3.148)$$

The equation of motion for the density operator $\hat{W}(t)$ may be written as [26]

$$i\hbar \frac{\partial}{\partial t} \hat{W}(t) = H_{CC}^{eg}(t)\hat{W}(t) - \hat{W}(t)H_{CC}^{eg}(t). \quad (3.149)$$

Since only the electronic ground state and the first excited state are considered, the statistical operator may be written as sum over matrix elements \hat{W}_{uv} , with

$$\hat{W}_{uv}(t) = \Pi_u \hat{W}(t) \Pi_v, \quad (3.150)$$

and $u, v \in 0, 1$. Inserting this definition of the statistical operator into the equation of motion (Eq. 3.149) gives the four coupled equations

$$i\hbar \frac{\partial}{\partial t} \hat{W}_{00}(t) = \mathcal{H}_0 \hat{W}_{00}(t) - \mathbf{E}(t) \hat{\mu}_{01}^{eg} \hat{W}_{10}(t) - \hat{W}_{00}(t) \mathcal{H}_0 + \mathbf{E}(t) \hat{W}_{01}(t) \hat{\mu}_{10}^{eg}, \quad (3.151)$$

$$i\hbar \frac{\partial}{\partial t} \hat{W}_{10}(t) = \mathcal{H}_1 \hat{W}_{10}(t) - \mathbf{E}(t) \hat{\mu}_{10}^{eg} \hat{W}_{00}(t) - \hat{W}_{10}(t) \mathcal{H}_0 + \mathbf{E}(t) \hat{W}_{11}(t) \hat{\mu}_{10}^{eg}, \quad (3.152)$$

$$i\hbar \frac{\partial}{\partial t} \hat{W}_{01}(t) = \mathcal{H}_0 \hat{W}_{01}(t) - \mathbf{E}(t) \hat{\mu}_{01}^{eg} \hat{W}_{11}(t) - \hat{W}_{01}(t) \mathcal{H}_1 + \mathbf{E}(t) \hat{W}_{00}(t) \hat{\mu}_{01}^{eg}, \quad (3.153)$$

and

$$i\hbar \frac{\partial}{\partial t} \hat{W}_{11}(t) = \mathcal{H}_1 \hat{W}_{11}(t) - \mathbf{E}(t) \hat{\mu}_{10}^{eg} \hat{W}_{01}(t) - \hat{W}_{11}(t) \mathcal{H}_1 + \mathbf{E}(t) \hat{W}_{10}(t) \hat{\mu}_{01}^{eg}. \quad (3.154)$$

The integration of these four equations, with the definition

$U_u(t - t_0) = \exp(-it\mathcal{H}_u/\hbar)$ and the initial condition $\hat{W}_{uv}(t_0) = \delta_{u,0}\delta_{v,0}$, gives

$$\begin{aligned} \hat{W}_{00}(t) &= U_0(t - t_0) \hat{W}_{00}(t_0) U_0^+(t - t_0) \\ &\quad + \frac{i}{\hbar} \int_{t_0}^t d\tau \mathbf{E}(\tau) U_0(t - \tau) (\hat{\mu}_{01}^{eg} \hat{W}_{10}(\tau) - \hat{W}_{01}(\tau) \hat{\mu}_{10}^{eg}) U_0^+(t - \tau), \end{aligned} \quad (3.155)$$

$$\hat{W}_{10}(t) = \frac{i}{\hbar} \int_{t_0}^t d\tau \mathbf{E}(\tau) U_1(t - \tau) (\hat{\mu}_{10}^{eg} \hat{W}_{00}(\tau) - \hat{W}_{11}(\tau) \hat{\mu}_{10}^{eg}) U_0^+(t - \tau), \quad (3.156)$$

$$\hat{W}_{01}(t) = \frac{i}{\hbar} \int_{t_0}^t d\tau \mathbf{E}(\tau) U_0(t - \tau) (\hat{\mu}_{01}^{eg} \hat{W}_{11}(\tau) - \hat{W}_{00}(\tau) \hat{\mu}_{01}^{eg}) U_1^+(t - \tau), \quad (3.157)$$

and

$$\hat{W}_{11}(t) = \frac{i}{\hbar} \int_{t_0}^t d\tau \mathbf{E}(\tau) U_1(t - \tau) (\hat{\mu}_{10}^{eg} \hat{W}_{01}(\tau) - \hat{W}_{10}(\tau) \hat{\mu}_{01}^{eg}) U_1^+(t - \tau). \quad (3.158)$$

For short times t the matrix elements of the statistical operator $\hat{W}(t)$ can be computed up to the second order in the field strength $\mathbf{E}(t)$. This is due to the initial condition $\hat{W}_{uv}(t_0) = \delta_{u,0}\delta_{v,0}$. The non-diagonal matrix elements are thus proportional to $\mathbf{E}(t)$. Eqs. 3.156, 3.157 can be approximated as

$$\hat{W}_{10}(t) \approx \frac{i}{\hbar} \int_{t_0}^t d\tau U_1(t - \tau) [\mathbf{E}(\tau) \hat{\mu}_{10}^{eg}] \hat{W}_{00}(\tau) U_0^+(t - \tau) \quad (3.159)$$

and

$$\hat{W}_{01}(t) \approx \frac{i}{\hbar} \int_{t_0}^t d\tau U_0(t - \tau) \hat{W}_{00}(\tau) [\mathbf{E}(\tau) \hat{\mu}_{01}^{eg}] U_1^+(t - \tau). \quad (3.160)$$

The diagonal matrix elements $\hat{W}_{00}(t)$ and $\hat{W}_{11}(t)$ are thus quadratic in the field strength (cf. Eqs. 3.155, 3.158). Inserting Eqs. 3.159, 3.160 for the non-diagonal elements into Eqs. 3.155, 3.158 results in

$$\begin{aligned} \hat{W}_{00}(t) &\approx 1 - \frac{1}{\hbar^2} \sum_{k,l} [\mathbf{e}_{\text{pu}} \mathbf{d}_k^*] [\mathbf{e}_{\text{pu}} \mathbf{d}_l] \int_{t_0}^t d\tau_1 \int_{t_0}^{\tau_1} d\tau_2 E(\tau_1) E(\tau_2) \\ &\quad \times [\langle \phi_k | U_1(\tau_1 - \tau_2) | \phi_l \rangle U_0^+(\tau_1 - \tau_2) + U_0(\tau_1 - \tau_2) \langle \phi_k | U_1^+(\tau_1 - \tau_2) | \phi_l \rangle] \end{aligned} \quad (3.161)$$

and

$$\begin{aligned}
 \hat{W}_{11}(t) &\approx \frac{1}{\hbar^2} \sum_{k,l} [\mathbf{e}_{\text{pu}} \mathbf{d}_k] [\mathbf{e}_{\text{pu}} \mathbf{d}_l^*] \int_{t_0}^t d\tau_1 \int_{t_0}^{\tau_1} d\tau_2 E(\tau_1) E(\tau_2) U_1(t - \tau_1) \\
 &\quad \times (|\phi_k\rangle U_0(\tau_1 - \tau_2) \langle \phi_l | U_1^+(\tau_1 - \tau_2) + U_1(\tau_1 - \tau_2) |\phi_k\rangle U_0^+(\tau_1 - \tau_2) \langle \phi_l |) \\
 &\quad \times U_1^+(t - \tau_1) \\
 &= \sum_{m,n} W_{mn}(t) |\phi_m\rangle \langle \phi_n|.
 \end{aligned} \tag{3.162}$$

The submatrix $W_{mn}(t)$ that replaces the statistical operator matrix element for the first excited electronic state $\hat{W}_{11}(t)$ is written as

$$\begin{aligned}
 W_{mn}(t) &= \frac{1}{\hbar^2} \sum_{k,l} [\mathbf{e}_{\text{pu}} \mathbf{d}_k] [\mathbf{e}_{\text{pu}} \mathbf{d}_l^*] \int_{t_0}^t d\tau_1 \int_{t_0}^{\tau_1} d\tau_2 E(\tau_1) E(\tau_2) \\
 &\quad \times [\langle \phi_m | U_1(t - \tau_1) | \phi_k \rangle U_0(\tau_1 - \tau_2) \langle \phi_l | U_1^+(t - \tau_2) | \phi_n \rangle \\
 &\quad + \langle \phi_m | U_1(t - \tau_2) | \phi_k \rangle U_0^+(\tau_1 - \tau_2) \langle \phi_l | U_1^+(t - \tau_1) | \phi_n \rangle].
 \end{aligned} \tag{3.163}$$

$W_{00}(t)$ as well as $W_{mn}(t)$ are quadratic in the electromagnetic field. This is the important message from the formulas given above. The scalar dipole moments are defined as

$$d_m = \mathbf{e}_{\text{pu}} \mathbf{d}_m. \tag{3.164}$$

The delay time is very short (premise) and the coupling is small (in average about 1-2 meV for P_4). The matrix elements $\langle \phi_m | U_1(t - \tau_1) | \phi_n \rangle$ may be approximated as $\langle \phi_m | U_1(t - \tau_1) | \phi_n \rangle = \delta_{m,n} \langle \phi_m | U_1(t - \tau_1) | \phi_n \rangle$. With the scalar dipole moments d_m , the $W_{mn}(t)$ in Eq. 3.163 may be written as

$$W_{mn}(t) = d_m d_n^* X_{mn}. \tag{3.165}$$

Eq. 3.165 will later be utilized. The explicit form of the X_{mn} will then be of no importance. However, the X_{mn} are written as

$$\begin{aligned}
 X_{mn} &= \frac{1}{\hbar^2} \int_{t_0}^t d\tau_1 \int_{t_0}^{\tau_1} d\tau_2 E(\tau_1) E(\tau_2) \\
 &\quad \times [\langle \phi_m | U_1(t - \tau_1) | \phi_m \rangle U_0(\tau_1 - \tau_2) \langle \phi_n | U_1^+(t - \tau_2) | \phi_n \rangle \\
 &\quad + \langle \phi_m | U_1(t - \tau_2) | \phi_m \rangle U_0^+(\tau_1 - \tau_2) \langle \phi_n | U_1^+(t - \tau_1) | \phi_n \rangle].
 \end{aligned} \tag{3.166}$$

The considerations about the statistical operator after pump pulse excitation will be utilized to compute the transient absorption line shape due to the probe pulse excitation in the next subsection.

3.9.2 Transient absorption line shape

In order to obtain the transient absorption line shape $I(\omega)$, the time-dependent term [26]

$$I(t) = \text{tr} \{ \hat{\mu} U [\hat{\mu}, \hat{W}] U^+ \} \tag{3.167}$$

has to be calculated. This is the dipole-dipole correlation function for the statistical operator after pump pulse excitation. The Fourier transform of this term gives the absorption line shape $I(\omega)$. In Eq. 3.167 $\text{tr}\{\dots\}$ denotes the calculation of the trace over the electronic and vibrational coordinates, $[\dots, \dots]$ is the commutator, and $U = \exp[-iHt/\hbar]$ is the time evolution operator. $\hat{\mu}$ is the dipole operator that was given in detail in Eq. 3.25. If only the statistical operator matrix element of the electronic ground state \hat{W}_{00} is populated, the Fourier transform of Eq. 3.167 gives the linear absorption line shape. If other matrix elements than \hat{W}_{00} are populated due to

a pump pulse excitation, Eq. 3.167 gives the transient absorption line shape for the probe pulse.

Since the sum $\Pi_0 + \Pi_1 + \Pi_2$ projects on the complete Hilbert space of the system that is considered here, it can be inserted everywhere into Eq. 3.167. Higher excited states than the second excited electronic state are neglected (cf. Sec. 3.2). Thus, the commutator reads

$$\begin{aligned}
 [\hat{\mu}, \hat{W}] &= \hat{\mu}\hat{W} - \hat{W}\hat{\mu} = \\
 &= (\Pi_0 + \Pi_1 + \Pi_2)\hat{\mu}(\Pi_0 + \Pi_1 + \Pi_2)(\hat{W}_{00}\Pi_0 + \hat{W}_{11}\Pi_1) \\
 &- (\hat{W}_{00}\Pi_0 + \hat{W}_{11}\Pi_1)(\Pi_0 + \Pi_1 + \Pi_2)\hat{\mu}(\Pi_0 + \Pi_1 + \Pi_2) \\
 &= -\Pi_1\hat{W}_{11}\Pi_1\hat{\mu}\Pi_2 + \Pi_2\hat{\mu}\Pi_1\hat{W}_{11}\Pi_1 - \Pi_1\hat{W}_{11}\Pi_1\hat{\mu}\Pi_0 \\
 &+ \Pi_0\hat{\mu}\Pi_1\hat{W}_{11}\Pi_1 - \Pi_0\hat{W}_{00}\Pi_0\hat{\mu}\Pi_1 + \Pi_1\hat{\mu}\Pi_0\hat{W}_{00}\Pi_0 \\
 &+ \text{non-diagonal terms.}
 \end{aligned} \tag{3.168}$$

The statistical operator is separated into its parts acting upon the ground and first excited electronic state of the system. In the last subsection, it was assumed that the pump pulse may not excite the CC to a state higher than the first excited CC state. The respective statistical operator matrix elements after pump pulse excitation were calculated earlier in this section (Eqs. 3.155, 3.158, 3.159, 3.160). Their concrete form is of no importance for the following calculations, as will become clear later in this section. Important is the linearity in $\mathbf{E}(t)$ for the non-diagonal matrix elements and the quadratic dependence on $\mathbf{E}(t)$ for the diagonal matrix elements.

Only the diagonal matrix elements with respect to the electronic state are taken into account here. This is due to the fact that the non-diagonal matrix elements of $\hat{W}(t)$ depend linearly on $\mathbf{E}(t)$. As will become clear later in this section, terms linear in $\mathbf{E}(t)$ (as well as linear in $[\mathbf{E}(\tau)\hat{\mu}_{01}^{eg}]$) will disappear because of the ensemble averaging. Ensemble averaging means computing the trace with respect to the electronic and vibrational states.

According to Eq. 3.167 the dipole operator and the time evolution operators act upon the commutator (Eq. 3.168); taking the trace, the expression results in

$$\begin{aligned}
 \text{tr}\{\hat{\mu}U[\hat{\mu}, \hat{W}]U^+\} &= \text{tr}\{-\Pi_2\mu_{21}U_1\hat{W}_{11}\mu_{12}U_2^+\Pi_2 + \Pi_1\mu_{12}U_2\mu_{21}\hat{W}_{11}U_1^+\Pi_1 \\
 &- \Pi_0\mu_{01}U_1\hat{W}_{11}\mu_{10}U_0^+\Pi_0 + \Pi_1\mu_{10}U_0\mu_{01}\hat{W}_{11}U^+\Pi_1 \\
 &- \Pi_1\mu_{10}U_0\hat{W}_{00}\mu_{01}U_1^+\Pi_1 + \Pi_0\mu_{01}U_1\mu_{10}\hat{W}_{00}U_0^+\Pi_0 + \text{non-diagonal terms}\}.
 \end{aligned} \tag{3.169}$$

The Fourier transform of the trace expression in Eq. 3.167 gives the transient absorption line shape. In order to calculate the differential transient absorption, the absorption line shape of the probe pulse has to be computed for two cases. In the first case no pump pulse was active before the probe pulse, the whole population is at the electronic ground state, before the probe pulse interacts with the system. In the second case the pump pulse was active and excited some population of the system to the first excited electronic state. The same procedure is done in respective measurements of the differential transient absorption. Thus, the differential transient absorption line shape may be written as (cf. [82, 89])

$$\Delta S_{\text{pr}}(\omega) = \text{Re} \int_0^\infty dt e^{-i\omega t} (\text{tr}\{\hat{\mu}U[\hat{\mu}, \hat{W}(\mathbf{E}_{\text{pu}} \neq 0)]_- U^+\} - \text{tr}\{\hat{\mu}U[\hat{\mu}, \hat{W}(\mathbf{E}_{\text{pu}} = 0)]_- U^+\}). \tag{3.170}$$

Next, the transient anisotropy (calculated after Eq. 3.140) for very short and for very long delay times t_{delay} is calculated analytically utilizing Eq. 3.170 and Eq. 3.169, under the premise of a small excitonic coupling. After inserting Eq. 3.169 into Eq. 3.170 the resulting equation is inserted into the formula for the transient anisotropy, Eq. 3.140. The idea is to bring Eq. 3.169 into a form that is a multiplication of a function $f(d)$ of the scalar transition dipole moments d and a Fourier integral over the respective matrix elements. This is possible via some approximations

which will be justified in the next step.

The first approximation is that EET between chromophores that are bound to different P_4 complexes, is neglected. This is an appropriate assumption when a dilute solution is investigated. The second approximation that has to be made is that the dipole moments of the Pheos in P_4 are not correlated. This means that the P_4 structure is so flexible that the orientation of chromophore 1 in average does not affect the orientations of the chromophores 2, 3 and 4. This approximation is valid, as can be seen, when the average product of the dipole moments of each Pheo pair within P_4 is computed. It is 54.7 degrees for each pair. This means that the approximation given above is reasonable (cf. [9]).

The probe pulse absorption in Eq. 3.172 includes a sum over terms proportional to $d_i d_j^*$. Thus, the trace expression is proportional to sums of the terms $d_m d_n^* d_i d_j^*$; in the following considerations the dipole moments are real.

With the above-mentioned approximation, the ensemble average over a term of the form $d_m d_n d_i d_j$ becomes zero if a single index occurs only one time in the product. That means for example, if $m \neq n, m \neq i, m \neq j$. An ensemble average over d_m will then give zero (integral over the cosine from 0 to 2π):

$$\langle d_m \rangle_{\text{ther}} = 0. \quad (3.171)$$

The conformational independence of the single dipole moments reduces an ensemble average over $d_m d_n d_i d_j$ to the form $\langle d_m d_n d_i d_j \rangle = \langle d_m \rangle \langle d_n \rangle \langle d_i \rangle \langle d_j \rangle$, if the indices are all different. Thus, in Eq. 3.172 only those parts have to be considered, which are proportional to terms of the form $d_m d_m d_i d_i$. Utilizing this approximation, in App. A it will be shown that Eq. 3.169 may be written as

$$\begin{aligned} \text{tr}\{\hat{\mu}U[\hat{\mu}, \hat{W}]U^+\} &= \text{tr}\{2\text{Im} \sum_{i,k,q} \sum_{j>i} \sum_{l>k} [(\hat{W}_{lq} d_j d_k^* + \hat{W}_{kq} d_j^* d_l) \langle \phi_q | U_1^+ | \phi_i \rangle \\ &\quad + (\hat{W}_{kq} d_i d_l^* + \hat{W}_{lq} d_i^* d_k) \langle \phi_q | U_1^+ | \phi_j \rangle] \langle \phi_{ij} | U_2 | \phi_{kl} \rangle + \\ &\quad + 2\text{Im} \sum_i \sum_k \sum_q d_i d_k^* \hat{W}_{kq} \langle \phi_q | U_1^+ | \phi_i \rangle \langle \phi_0 | U_0 | \phi_0 \rangle + \\ &\quad + 2\text{Im} \sum_i \sum_k \hat{W}_{00} d_i d_k^* \langle \phi_i | U_1 | \phi_k \rangle \langle \phi_0 | U_0^+ | \phi_0 \rangle\}. \end{aligned} \quad (3.172)$$

The first two lines on the right hand side of Eq. 3.172 describe the second excited state absorption, the third line describes the stimulated emission and the last line covers the excitation of the first excited state.

The transient anisotropy for very short delay times

With the approximation that the excitonic coupling between the chromophores is (relative) small (below 10 meV, which is reasonable for the very most P_4 conformations), Eq. 3.172 may be further simplified. Details can be found in App. B. One may write

$$\text{tr}\{\hat{\mu}U[\hat{\mu}, \hat{W}]U^+\} \approx 4\text{tr}\{\text{Im} \sum_i [(1 - W_{ii}(t_{\text{delay}} \rightarrow 0)) d_i d_i e^{\frac{i\hbar}{\hbar}(\Delta E_{g \rightarrow e})}]\}, \quad (3.173)$$

with the transition energy $\Delta E_{g \rightarrow e}$ between the electronic ground and first excited state. It has to be noted that not only the small excitonic coupling but also the independence of the single Pheos' dipole moments results in Eq. 25 (cf. App. A). It is mentioned here again (cf. App. B) that a small excitonic coupling denotes a coupling that is responsible for an EET that is slow compared to the dephasing time of the averaged TDSE expansion coefficients. Eq. 25 reveals that the dip in the transient absorption is due to the $-W_{ii}$ in Eq. 25, that means it is due to the previous excitation of chromophores by the pump pulse.

This result can be directly inserted into the formula for the differential transient absorption

(Eq. 3.170), which is then written as

$$\begin{aligned}\Delta S_{\text{pr}}(\omega; t_{\text{delay}} \rightarrow 0) &= \text{Re} \int_0^\infty dt e^{-i\omega t} (\text{tr}\{\hat{\mu}U[\hat{\mu}, \hat{W}(\mathbf{E}_{\text{pu}} \neq 0, t_{\text{delay}} \rightarrow 0)] - U^+\} \\ &\quad - \text{tr}\{\hat{\mu}U[\hat{\mu}, \hat{W}(\mathbf{E}_{\text{pu}} = 0, t_{\text{delay}} \rightarrow 0)] - U^+\}) \\ &\approx -4\text{Re} \int_0^\infty dt e^{-i\omega t} \langle \text{Im} \left[\sum_i W_{ii}(t_{\text{delay}} \rightarrow 0) d_i d_i e^{\frac{i}{\hbar}(\Delta E_{g \rightarrow e})} \right] \rangle_{\text{ther}}.\end{aligned}\quad (3.174)$$

The trace expression was substituted by the thermal average $\langle \dots \rangle$. It is possible to rewrite the diagonal statistical operator matrix elements as $W_{ii}(t_{\text{delay}} \rightarrow 0) = X_{ii}(t_{\text{delay}} \rightarrow 0) d_i^{\text{pu}} d_i^{\text{pu}}$ (Eq. 3.166). d_i is the scalar dipole moment of chromophore i with respect to the pump pulse polarization \hat{e}^{pu} :

$$\Delta S_{\text{pr}}(\omega; t_{\text{delay}} \rightarrow 0) = -4 \sum_i \langle d_i^2 d_i^{\text{pu}2} \rangle_{\text{ther}} \text{Re} \int_0^\infty dt e^{-i\omega t} \text{Im} \left[X_{ii}(t_{\text{delay}} \rightarrow 0) e^{\frac{i}{\hbar}(\Delta E_{g \rightarrow e})} \right]. \quad (3.175)$$

As mentioned earlier, the mutual conformation of the chromophores is not restricted. This means that the averaging of the scalar dipole moments will give the same result for the different chromophores 1, 2, and so on:

$$\Delta S_{\text{pr}}(\omega; t_{\text{delay}} \rightarrow 0) = -4N \langle d_1^2 d_1^{\text{pu}2} \rangle_{\text{ther}} \text{Re} \int_0^\infty dt e^{-i\omega t} \text{Im} \left[\sum_i X_{ii}(t_{\text{delay}} \rightarrow 0) e^{\frac{i}{\hbar}(\Delta E_{g \rightarrow e})} \right] \quad (3.176)$$

d_1 is the scalar dipole moment (with respect to the probe pulse polarization) of chromophore 1. If Eq. 3.140 is used together with Eq. 3.176, the transient anisotropy for very short delay times is calculated in approximation as

$$r(t_{\text{delay}} \rightarrow 0) \approx \frac{\langle d_1^4 \rangle_{\text{ther}} - \langle d_1^2 (d_1^\perp)^2 \rangle_{\text{ther}}}{\langle d_1^4 \rangle_{\text{ther}} + 2 \langle d_1^2 d_1^{\perp 2} \rangle_{\text{ther}}}, \quad (3.177)$$

where d_1^\perp is the scalar dipole moment with respect to the pump beam polarization, if the pump beam polarization is perpendicular to the probe pulse polarization. In what follows, the thermal average with respect to the scalar dipole moments will be carried out. The dipole moment of chromophore i can be written as

$$\mathbf{d}_i = d \begin{pmatrix} \sin(\theta_i) \cos(\varphi_i) \\ \sin(\theta_i) \sin(\varphi_i) \\ \cos(\theta_i) \end{pmatrix}. \quad (3.178)$$

θ_i and φ_i are the spherical coordinate angles of the dipole moment of chromophore i . The polarization vector of the probe pulse may be written without loss of generality (w.l.o.g.) as

$$\mathbf{e}_{\text{pr}} = \begin{pmatrix} 0 \\ 0 \\ 1 \end{pmatrix}. \quad (3.179)$$

The polarization vector of the pump pulse in the case of orthogonal polarization of pump and probe beam may be written (w.l.o.g.) as

$$\mathbf{e}_{\text{pr}}^\perp = \begin{pmatrix} 0 \\ 1 \\ 0 \end{pmatrix}. \quad (3.180)$$

3 The mixed quantum-classical methodology

Together with the definitions in Eqs. 3.179 and 3.180, the dipole moment of chromophore i is

$$(\mathbf{d}_i \mathbf{e}_{\text{pr}})^2 = d^2 \cos(\theta_i)^2 \quad (3.181)$$

for the probe pulse polarization and

$$(\mathbf{d}_i \mathbf{e}_{\text{pu}}^\perp)^2 = d^2 \sin(\theta_i)^2 \sin(\varphi_i)^2 \quad (3.182)$$

for an orthogonal pump pulse polarization. For the calculation of the anisotropy r for very short delay times the following averages will be used. The spherical volume element $\sin(\theta)$ is used, the integral is carried out over the unit sphere:

$$\langle d_1^4 \rangle_{\text{ther}} = \frac{1}{4\pi} d^4 \int_0^\pi \int_0^{2\pi} \sin(\theta_1) \cos(\theta_1)^4 d\varphi_1 d\theta_1 = d^4 \frac{1}{5}, \quad (3.183)$$

$$\langle d_1^2 d_1^{\perp 2} \rangle_{\text{ther}} = \frac{1}{4\pi} d^4 \int_0^\pi \int_0^{2\pi} \sin(\theta_1)^3 \cos(\theta_1)^2 \sin(\varphi_1)^2 d\varphi_1 d\theta_1 = d^4 \frac{1}{15}. \quad (3.184)$$

With Eqs. 3.183 and 3.184, Eq. 3.177 gives

$$r(t_{\text{delay}} \rightarrow 0) \approx \frac{\langle d_1^4 \rangle_{\text{ther}} - \langle d_1^2 (d_1^\perp)^2 \rangle_{\text{ther}}}{\langle d_1^4 \rangle_{\text{ther}} + 2 \langle d_1^2 d_1^{\perp 2} \rangle_{\text{ther}}} = 0.4. \quad (3.185)$$

The range of anisotropy values is between $r_{\text{min}} = -0.2$ and $r_{\text{max}} = 0.4$ [9]. A value of $r = 0.4$ can be expected, if no EET took place [119]. Thus, $r = 0.4$ is the expected result for very short delay times.

The transient anisotropy for very long delay times

In the next step, the transient anisotropy for very long delay times $t_{\text{delay}} \rightarrow \infty$ is calculated. This means that t_{delay} , on the one hand, is long enough for the formation of an equilibrium distribution of the excitation energy. On the other hand, it is small enough to prevent the single chromophore from losing the energy via other mechanisms than excitation energy transport: fluorescence ($4.3 \times 10^7 \text{s}^{-1}$), internal conversion ($1.3 \times 10^6 \text{s}^{-1}$) or intersystem crossing ($1.08 \times 10^8 \text{s}^{-1}$) [40]. An appropriate choice for a very long delay time would be between 30 and 40 ps (cf. [85]). However, in what follows, the formulation $t_{\text{delay}} \rightarrow \infty$ will be utilized. As mentioned above, the EET between chromophores bound to different P_N complexes is neglected. To calculate the transient anisotropy for $t_{\text{delay}} \rightarrow \infty$, Eq. 3.174 is the starting point. All the approximations of this section made till Eq. 3.174 hold for the long delay times limit. That means in particular the independence of mutual orientations between the single chromophores. The differential transient absorption reads

$$\Delta S_{\text{pr}}(\omega; t_{\text{delay}} \rightarrow \infty) = -4\text{Re} \int_0^\infty dt e^{-i\omega t} \langle \text{Im} \left[\sum_i W_{ii}(t_{\text{delay}} \rightarrow \infty) d_i d_i e^{\frac{i\hbar}{\hbar} (\Delta E_{g \rightarrow e})} \right] \rangle_{\text{ther}}. \quad (3.186)$$

Of course, the matrix elements shortly after pump pulse excitation

$W_{ii} = W_{ii}(t_{\text{delay}} \rightarrow 0)$ can not be used. But the $W_{ii}(t_{\text{delay}} \rightarrow \infty)$ can be calculated from the $W_{ii}(t_{\text{delay}} \rightarrow 0)$ since one may assume that the excitation energy is equally distributed over the CC after a very long delay time $t_{\text{delay}} \rightarrow \infty$. Thus, one may write (with the number of chromophores in the P_N complex N)

$$W_{ii}(t_{\text{delay}} \rightarrow \infty) = \frac{1}{N} \sum_j W_{jj}(t_{\text{delay}} \rightarrow 0). \quad (3.187)$$

According to Eq. 3.176, Eq. 3.186 may be written as

$$\Delta S_{\text{pr}}(\omega; t_{\text{delay}} \rightarrow \infty) = -4 \langle \sum_j d_j^2 d_1^{\text{pu}2} \rangle_{\text{ther}} \text{Re} \int_0^\infty dt e^{-i\omega t} \text{Im} \left[\sum_i X_{ii}(t_{\text{delay}} \rightarrow 0) e^{\frac{it}{\hbar} (\Delta E_{g \rightarrow e})} \right]. \quad (3.188)$$

Eq. 3.140 together with Eq. 3.188 is used to calculate the transient anisotropy for very long delay times:

$$r(t_{\text{delay}} \rightarrow \infty) \approx \frac{\langle \sum_j d_j^2 d_1^2 \rangle_{\text{ther}} - \langle \sum_j d_j^2 (d_1^\perp)^2 \rangle_{\text{ther}}}{\langle \sum_j d_j^2 d_1^2 \rangle_{\text{ther}} + 2 \langle \sum_j d_j^2 d_1^{\perp 2} \rangle_{\text{ther}}}. \quad (3.189)$$

Due to the independence of different chromophores' dipole moments one may rewrite Eq. 3.189 as

$$r(t_{\text{delay}} \rightarrow \infty) \approx \frac{\langle d_1^4 \rangle_{\text{ther}} + (N-1) \langle d_1^2 \rangle_{\text{ther}} \langle d_2^2 \rangle_{\text{ther}} - \langle d_1^2 d_1^{\perp 2} \rangle_{\text{ther}} - (N-1) \langle d_1^2 \rangle_{\text{ther}} \langle d_2^{\perp 2} \rangle_{\text{ther}}}{\langle d_1^4 \rangle_{\text{ther}} + (N-1) \langle d_1^2 \rangle_{\text{ther}} \langle d_2^2 \rangle_{\text{ther}} + 2 \left(\langle d_1^2 d_1^{\perp 2} \rangle_{\text{ther}} + (N-1) \langle d_1^2 \rangle_{\text{ther}} \langle d_2^{\perp 2} \rangle_{\text{ther}} \right)} \quad (3.190)$$

with the scalar dipole moment d_2 of chromophore 2, w.l.o.g.. Choosing this second index to be 2 is arbitrary. It is only important that the index is different from 1. For the calculation of the anisotropy r for very long delay times the following integrals will be used to compute the ensemble average. Note again the use of the spherical volume element $\sin(\theta)$, the integrals are carried out over the unit sphere:

$$\langle d_1^2 \rangle_{\text{ther}} = \frac{1}{4\pi} d^2 \int_0^\pi \int_0^{2\pi} \sin(\theta_1) \cos(\theta_1)^2 d\phi_1 d\theta_1 = d^2 \frac{1}{3}, \quad (3.191)$$

$$\langle d_1^{\perp 2} \rangle_{\text{ther}} = \frac{1}{4\pi} d^2 \int_0^\pi \int_0^{2\pi} \sin(\theta_1)^3 \sin(\phi_1)^2 d\phi_1 d\theta_1 = d^2 \frac{1}{3}. \quad (3.192)$$

Together with the Eqs. 3.183, 3.184, 3.191, and 3.192 give the transient anisotropy (Eq. 3.190)

$$r(t_{\text{delay}} \rightarrow \infty) \approx \frac{0.4}{N}, \quad (3.193)$$

which gives a transient anisotropy value for long delay times of 0.1 for P_4 , as was calculated in Sec. 5.2.3 utilizing the mixed quantum-classical methodology.

4 Methods

4.1 Molecular dynamics simulations

4.1.1 Utilized programs

There exist several MD force fields, which include the necessary parameters to carry out the simulation of P_N complexes in ethanol solution. The most commonly used are CHARMM (chemistry at Harvard macromolecular mechanics) [120], AMBER (assisted model building with energy refinement) [121] and GROMACS (Groningen machine for chemical simulations) [122]. In the tradition of our group it was straightforward to utilize the existing input files for Pheo and P_4 in ethanol [75, 82, 83, 87]. Thus, the MD simulations of Pheo, P_4 and P_{16} solved in ethanol have been carried out with the NAMD (not (just) another molecular dynamics program) program package [123]. The AMBER force field [121] was used with the PARM99 and GAFF parameter sets [124]. Parameters for the ethanol solvent model were taken from [125].

The simulations were done for a single P_N within a finite solvent box. The electrostatic interactions between all partial charges of the system were computed by the particle mesh Ewald method (PME) [126]. This is necessary since the Coulomb interaction is a long range interaction. Each molecule couples to molecules that are located a few boxes away. In order to apply the PME method, periodic boundary conditions are used. The PME method interpolates the reciprocal space Ewald sums [127] and analyzes the resulting convolutions via fast Fourier transformations.

4.1.2 MD parameters

As mentioned above, the GAFF (general AMBER force field) is used. GAFF was a further development of the Parm99 force field [128]. In Sec. 3.1.5 it was shown that the conformational energy of an atomic system at a specific conformation can be approximated as the sum over respective few neighbor interaction energies. One contribution to this sum covers the interaction between next neighbors. In the meaning of this thesis, bonded atoms denote two atoms that are directly connected by covalent bonds. Essential for the molecular conformational energy due to bonded interaction are two atoms that are covalently bound, two atoms that are both covalently bound to a third atom (1 – 3) and two atoms with two additional covalently bound atoms between them (1 – 4). An additional contribution to the total energy sum is the interaction between non-bonded atoms. It covers the Coulomb and van der Waals interaction. This non-bonded interaction is calculated for all pairs of atoms, even though there exists a direct connection of covalent bonds between the atoms. If two atoms are bonded (by less than four bonds) the non-bonded interaction is scaled by a factor of 1/1.2 [128]. This is often referred to as 1-4 scaling.

The total force field energy calculated as the sum over bonded and non-bonded interaction energies is

$$E^{\text{FF}} = E^{\text{bonds}} + E^{\text{angles}} + E^{\text{dihedrals}} + E^{\text{Coul}} + E^{\text{vdW}}. \quad (4.1)$$

Here, the bond energy E_{bonds} covers the 1 – 2 interaction. The 1 – 3-interaction is treated by the angle energy E_{angles} and the 1 – 4-interaction by the dihedral energy $E_{\text{dihedrals}}$. The two parts of the non-bonded interaction are the Coulomb interaction between all pairs of atoms E_{Coul} and the respective van der Waals interaction between all atom pairs E_{vdW} . More detailed

4 Methods

information about the generalized AMBER force field is given in [116]. The notation of this reference is utilized within this whole section.

Bond parameters

The bond energy is written as

$$E^{bonds} = \sum_{bonds} k_{ij} (R_{ij} - R_{ij}^{eq})^2. \quad (4.2)$$

R_{ij} is the actual distance between two atoms i and j and R_{ij}^{eq} is the respective equilibrium distance between those two atoms. The equilibrium distance denotes the distance for which the energy contribution of this atom pair becomes minimal. k_{ij} is the respective force constant, which determines how much a variation of the distance between the two atoms affects the increase of the total energy. The potential is harmonic in the difference between actual atom distance and equilibrium distance $R_{ij} - R_{ij}^{eq}$.

Angle parameters

The angular energy is

$$E^{angles} = \sum_{angles} k_{ijk} (\theta_{ijk} - \theta_{ijk}^{eq})^2. \quad (4.3)$$

If three atoms are numbered by i , j and k , θ_{ijk} is the angle between the bonds $i - j$ and $j - k$. θ_{ijk}^{eq} is the respective equilibrium angle and k_{ijk} is the force constant. The angle potential arising from three single atoms is harmonic in the difference between the actual angle and the respective equilibrium angle $\theta_{ijk} - \theta_{ijk}^{eq}$.

Dihedral parameters

The effect of torsion to the interaction energy is summarized in the term

$$E^{dihedrals} = \sum_{dihedrals} \frac{v_n}{2} [1 + \cos(n\psi - \lambda_{ijkl})]. \quad (4.4)$$

The multiplicity n gives information on the periodicity of the respective torsional movement of the atoms i , j , k and l . The force constant for the respective torsion depends on the multiplicity n . The phase angle for the torsion is λ_{ijkl} .

Improper torsion parameters

Even though improper torsions are generally part of the AMBER force field [121], they are not part of GAFF [124]. Improper torsions summarize single atom out of plane motions in reference to a plane defined by three other atoms. It belongs to the 1 – 4 interaction. In the GAFF the respective energy contribution due to improper torsions is included within the other parts of the energy sum, mainly in the angle- and dihedral term.

Non-bonded interaction

The non-bonded interactions consist of the Coulomb interaction, on the one hand, and the van der Waals interaction, on the other hand.

The Coulomb energy between two partial charges q_i and q_j (of atoms i and j), with the distance R_{ij} is computed as

$$E_{ij}^{\text{Coul}} = \frac{1}{4\pi\epsilon_0} \frac{q_i q_j}{R_{ij}}, \quad (4.5)$$

ϵ_0 being the vacuum permittivity.

The van der Waals energy between two atoms i and j can be written by a Lennard-Jones potential [121]

$$E_{ij}^{\text{vdW}} = \epsilon_{ij} \left[\left(\frac{R_{ij}^{\text{eq}}}{R_{ij}} \right)^{12} - 2 \left(\frac{R_{ij}^{\text{eq}}}{R_{ij}} \right)^6 \right]. \quad (4.6)$$

The equilibrium distance (in the Lennard-Jones potential) R_{ij}^{eq} between two atoms i and j is given by

$$R_{ij}^{\text{eq}} = (R_i^{\text{eq}} + R_j^{\text{eq}}) / 2. \quad (4.7)$$

R_i^{eq} is the equilibrium distance in the Lennard-Jones potential between two atoms of the same atom type as atom i . Accordingly the well depth ϵ_{ij} is computed as [121]

$$\epsilon_{ij}^{\text{eq}} = \sqrt{\epsilon_i^{\text{eq}} \epsilon_j^{\text{eq}}}, \quad (4.8)$$

with the well depths ϵ_i^{eq} and ϵ_j^{eq} of the individual atom types of the atoms i and j .

4.1.3 Numerical integration

For constant energy simulations NAMD uses the Velocity Verlet algorithm. The positions of all atoms at time $n\Delta t$, $n \in \mathbb{N}$ are the $R(n\Delta t)$, and the velocities are denoted as $v(n\Delta t)$. The positions and velocities at time $(n+1)\Delta t$, $R((n+1)\Delta t)$ and $v((n+1)\Delta t)$ can be computed, if the forces on the atoms $F(n\Delta t)$ are known, M is the set of masses [123]:

$$\begin{aligned} v((n+1/2)\Delta t) &= v(n\Delta t) + M^{-1}F(n\Delta t)\Delta t/2, \\ r((n+1)\Delta t) &= r(n\Delta t) + v((n+1/2)\Delta t)\Delta t, \\ F((n+1)\Delta t) &= F(r((n+1)\Delta t)), \\ v((n+1)\Delta t) &= v((n+1/2)\Delta t) + M^{-1}F((n+1)\Delta t)\Delta t/2. \end{aligned} \quad (4.9)$$

The Verlet algorithm is symplectic and time reversible. It conserves the linear and angular momentum and requires only one computation of F per time-step [123].

Such a simulation represents a microcanonical (NVE) ensemble with a constant number of atoms (N), constant volume (V) and constant energy (E).

4.1.4 NVT and NPT ensemble

The integrator of an MD simulation has to generate a correct ensemble distribution for the respective temperature and pressure. To generate the Boltzmann distribution for an NVT ensemble (with a constant number of atoms (N), volume (V) and temperature (T)), NAMD utilizes a stochastic Langevin equation of the form [123, 129]

$$M\dot{v} = F(R) - \gamma v + \sqrt{\frac{2\gamma k_b T}{M}} G(t), \quad (4.10)$$

with the friction coefficient γ and the gaussian random force $G(t)$. The treatment of a Langevin equation within a Velocity Verlet algorithm was introduced in [129].

Like the temperature, also the pressure in a box of molecules does fluctuate. The respective ensemble is an NPT ensemble with constant number of atoms (N), pressure (P) and temperature (T). During the years different approaches were invented to treat this fluctuation. NAMD utilizes a combination of the Nose-Hoover constant pressure method that was proposed in [130] and the piston fluctuation control suggested in [131]. The equations of motion that are solved in NAMD are given in [132].

4.1.5 Computation of MD trajectories

NAMD is able to compute trajectories in parallel. The program may use several cores of a computer, or a computer network, to compute a single MD trajectory. However, for this thesis each MD trajectory was computed on a single core, since those calculations were more effective. The calculation of a single trajectory, using eight cores in parallel, would increase the velocity of the simulation by a factor of about 5 to 6 (cf. [133], the explicit solvent test case). The calculation of eight different single trajectories on separate cores thus generates more MD data at the same time. Of course, the calculated trajectories finally do not represent one single trajectory. This, however, is not necessary in order to achieve ensemble average, if the single trajectories are much longer than the time scale of conformational change within the system.

The time scale of conformational change for a P_4 complex is between 50 and 100 ps (the conformations are more or less stable on a 10 ps time scale and start to change after about 50ps). After a few 100 ps the conformations of the single runs are completely different. The time scale of the conformational change of the P_4 complex leads to the conclusion that the single trajectories have to last at least a few nanoseconds to produce the required ensemble average.

Each production run was started simultaneously on eight cores. The respective initial conformations were the same for the eight Pheo and P_4 runs. For P_{16} , long (8 ns) simulations with the same initial conformations and short (1.3 ns) simulations with (16) different initial conformations, were carried out (Sec. 4.1.6). Even though the time scale of conformational change is the same for P_{16} as for P_4 , a complete ensemble average is not possible for this system within 8 ns, since the conformational space of P_{16} is much larger than the conformational space of P_4 . Thus, for P_{16} the usage of the same initial conformations does not lead to an adequate ensemble average of the complex conformations. Nevertheless, the symmetry of the P_{16} molecule makes sure that no complete ensemble average for P_{16} is necessary (explained in detail in Sec. 4.1.6) to calculate reasonable results for the linear absorption (Sec. 5.3.1) and the excitation energy transfer (Sec. 5.3.2).

NAMD configuration file

The NAMD configuration file contains all the informations for NAMD program package needed run an MD simulation. It contains the name of the input and output sizes, the dimension and position of the periodic box (in solvent simulations), the size of the PME grid, the parameters for the temperature and pressure control, possible approximations for the simulation of the hydrogen atoms, the step length, restrictions for the non-bonded interaction and finally the simulation length and respective output files.

The most of those parameters are standard for NAMD simulations with the AMBER force field (information on which parameters should be used can be found in [134]). Since the position of the hydrogen atoms affects directly the calculation of the vibrational energy, an MD time-step of 1 fs was used, and the hydrogen motion was not restricted.

Minimization, heating and equilibration

After setting up the box, including solute and solvent, a minimization was carried out. This minimization ensures that the nuclei positions of the different molecules are not too close to prevent large forces in the beginning of the simulation. The minimization, of course, acts upon the structure of the molecules themselves. The Pheo molecules were all optimized with DFT (cf. Sec. 4.2), while the dendrimer was optimized with the Hartree-Fock method, and the ethanol structure was taken from the NAMD developers [125].

The default minimization method in NAMD uses a conjugate gradient and line search algorithm. Details on the algorithm can be found in [132].

After minimizing the box, it is subsequently heated from 0 K to the simulation temperature (in the production runs this temperature was $T = 300$ K). The heating was carried out by increasing the MD simulation temperature by 1 K each 30 fs till the set temperature is reached. While doing this, a constant pressure control was utilized to resize the box, when the temperature increases. If the system is heated too much and the box size is not adjusted via the constant pressure control during the heating, the MD simulation will result in extreme forces on the box walls, which will lead to an extremely fast enlargement of the box, and the respective forces will no longer represent a pressure of 1 bar. For 300 K heating without constant pressure control no such behavior, but only a readjustment of the box size during the first picoseconds was observed. For 1000 K heating, the mentioned problems occurred.

Since the heating of the box is a non-equilibrium process, the heated box should be simulated at 300 K for some time. This additional equilibration run prevents possible non-equilibrium behavior of the nuclei trajectories to effect the calculations of excitation energy transfer or optical properties. A simulation time of 50 ps was used to finalize the equilibration of the system.

Production runs

After the equilibration, the production runs were started. Each production run lasted 10 ps, and after this time the final coordinates and velocities were saved to start another MD simulations with this final coordinate and velocity files as input files. Since the calculation on each core produced 10 ns long trajectories, 1000 MD parts (each 10 ps long) were computed per core. The reason for this partitioning of the MD data is twofold. On the one hand, a simulation can easily be restarted if a computer crashes, without losing too much time and data. On the other hand, the trajectories require a lot of memory. When a system with more than 30000 atoms is simulated, terabytes of data are produced within a week. It is therefore necessary to calculate the energy gap function (cf. Sec. 3.5) after 10 ps of simulated time, and delete the respective MD trajectory afterwards.

4.1.6 Ensemble average

Ensemble average for Pheo and P₄

For reaching an adequate ensemble average for a single Pheo in ethanol and the P₄ complex in ethanol, respectively, 80 ns MD simulations were produced. For both cases the MD data consists of eight times 10 ns, starting with the same initial condition. The quality of the ensemble average could be tested by calculating the respective average transition rates to the other chromophores (cf. Sec. 5.2.2). Since the error range is below 10 % (cf. Fig. 5.18), the ensemble average is satisfying. If the ensemble average is good for the P₄ systems, it is also good for the single Pheo in ethanol. It should be mentioned that the actual simulation data of 80 ns for P₄ do not show a formation of a dimer consistent of two Pheo molecules. Simulations of artificial Pheo dimer conformations within a P₄ complex indicated that such dimers may be stable. This could mean that for the P₄ systems dimer formations have to be simulated independently,

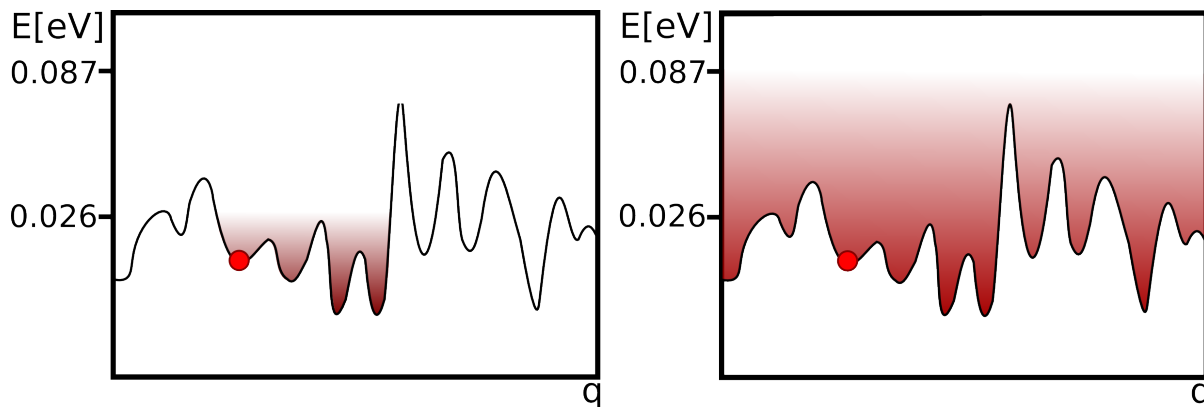


Figure 4.1: Sketch of a one-dimensional PES. The red circle indicates the initial conformation. Left panel: at 300 K ($k_B T = 0.026$ eV), only a part of the conformational space can be explored. Right panel: at 1000 K ($k_B T = 0.087$ eV), all of the conformations can occur.

since the energy barrier between both conformations is too high to be overstepped during a 10 ns MD simulation at 300 K.

Ensemble average for P_{16}

As argued in Sec. 4.1.5, the simulations of P_{16} in ethanol will not give a good ensemble average, if the simulations are started with the same initial conformation. Even though the time scale of conformational change is the same as for P_4 , the P_{16} is much more complex than the P_4 system and thus has a much larger conformational space. This may not be explored within several nanoseconds of MD simulation.

In what follows, it will be stated why the determination of the complete P_{16} conformational space is not necessary to calculate ensemble-averaged optical properties. Afterwards it will be explained, how the ensemble average may be improved by calculating different initial conformations of P_{16} at 1000 K.

The distribution of mutual conformations for two Pheo pairs m, n , and k, l of the P_{16} CC is not the same after 10 ns of simulation. This, however, does not necessarily mean that the optical properties calculated from this MD data are erroneous.

The symmetry of P_{16} ensures that ensemble average of the computed spectra converges faster than the ensemble average for the conformation of the whole molecule. The excitonic coupling between the Pheos is largest for molecules that are spatially near to each other. The average of the mutual conformations of the spatially near Pheos is more important for the calculation of the systems' optical properties than the ensemble average of the complete CC. If the distribution of mutual orientations is similar for those Pheo pairs within P_{16} that are spatially near to each other, the computation of the optical properties as well as of the EET within P_{16} will give reasonable results.

High temperature simulation

It is possible to improve the conformational ensemble average by choosing initial conformations of the whole system. Those initial conformations were calculated utilizing high temperature MD simulations. This is twofold, on the one hand, the conformational change at 1000 K is much faster, on the other hand, 300 K simulations may be restricted to local minima of the PES. This is illustrated in Fig. 4.1. The temperature of 1000 K was chosen, since a formation and de-formation of Pheo dimers within P_{16} was observed at this temperature within 100 ps. At 300 K a formation and de-formation of Pheo dimers could only be observed after several nanoseconds.

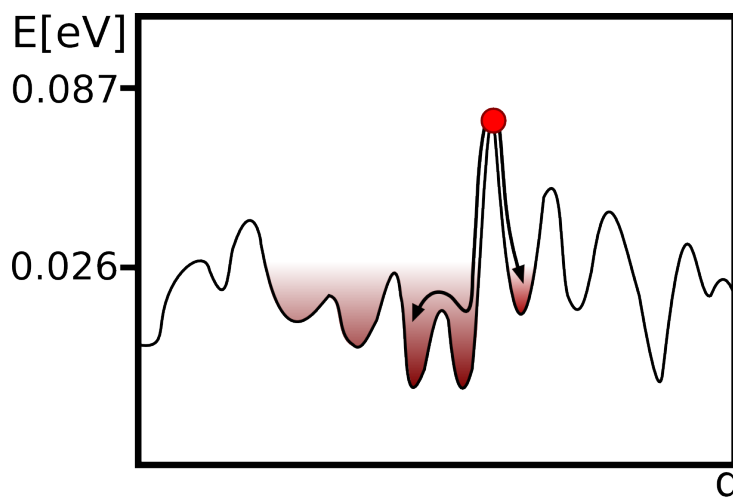


Figure 4.2: Sketch of a one-dimensional PES after a 1000 K MD simulation. The red circle indicates a conformation that does not occur within a 300 K simulation. During the equilibration run, the conformation adapts to the actual temperature.

Hence, eight 2.5 ns long MD simulations of P₁₆ in ethanol at 1000 K were executed to obtain different initial conformations for the room temperature simulations. If enough MD simulations at 1000 K have been done, the respective conformational average converts against the 1000 K conformational ensemble average. It was found within this thesis that the variety of conformations within the 1000 K MD data is quite satisfactory. This will be shown in Sec. 5.3.2. After the 1000 K simulations, various conformations from the 1000 K simulation are taken as initial conformations for respective 300 K simulations. The idea is borrowed from the simulated annealing method [135]. Low-temperature protein motion was studied in this reference by cooling down high temperature systems. Slow cooling yielded low energy structures with an atomic fluctuation much closer to experimental levels than earlier simulations.

However, for this thesis no cooling was done, and the high temperature conformations were directly used as input for a 100 ps long equilibration run. This relatively long equilibration was done to prevent the system from staying in a conformation that does in general not occur at 300 K. This is illustrated in Fig. 4.2. The result of this equilibration run gave the initial conformations for the 300 K MD simulations.

4.2 Electronic structure calculations

The execution of electronic structure calculations was not part of this thesis. Since such calculations are not an area of expertise in our group, the accurate computation of the quantum chemical properties of Pheo required to be done by an expert.

The Hessian matrices for the Pheo ground, first and second excited electronic state and the respective nuclear equilibrium configurations were computed with the Gaussian09 program package [136] by our co-worker Alexander Kulesza. Those Hessian matrices, partial charges and equilibrium conformations were used as input for the calculation of the energy gap function $U_{eg}(t)$ (Sec. 3.5).

The Hessian matrix, the ground state structure, and the atomic partial charges of Pheo were determined using density functional theory (DFT). The excited state properties were obtained utilizing linear response time-dependent DFT (TDDFT). Those methods are implemented in the Gaussian09 program package [136]. For all computations, the hybrid B3LYP functional for exchange and correlation [137, 138, 139] was used together with the 6-311(d,p) AO basis sets [140]. It was proven in [141] that this method gives accurate results for the heat of formation

and isomerization energies of organic molecules. The stationary points were fully optimized and characterized by vibrational frequency calculations. This (standard) procedure ensured that the computed structures represent minima of the Pheo PES. The coupling to the solvent was taken into account (for the ground, first and second excited electronic states) via the polarizable continuum model (PCM, [142, 143, 144]), making use of the dielectric constant for ethanol. The atomic partial charges (that were fitted to the potential of the Pheo charge density) were obtained by the CHelpG [145] method. They reproduce the experimentally measured molecular dipole moment and were earlier utilized in MD simulations [146, 147]. The partial charges of the dendrimer were computed by a former group member [75]. Electron structure calculation for the dendrimer were carried out using the Hartree-Fock method implemented in Gaussian09 [136] together with the 6-31 AO basis set. The AMBER internal RESP method [121] was used to fit the partial charges to the potential of the charge density. Besides the RESP and the CHelpG method, there exist other methods for the fitting of the electrostatic potential to atomic partial charges. It was shown in [86] that changing the choice of the fitting method does not result in crucial deviations of the molecular dipole moment. The transition partial charges were computed by Madjet (computations were done for [75]) with the TrEsp method [32]. DFT (TDDFT) with the hybrid B3LYP functional and the 6-31(d,p) AO basis set were utilized to compute the electronic structure for the ground and first excited electronic state. The TrEsp method [32] was used to fit the transition density to respective transition partial charges. The transition dipole moment (and thus the transition partial charges) was fitted against the experimental value for the Chl *a* transition dipole moment of 4.6 D [101].

4.2.1 Estimation of the Stokes shift

The Stokes shift for Pheo in ethanol is about 10 nm (0.03 eV) [22]. Utilizing the energies from the (TD)DFT calculations of the electronic ground and first excited state for the optimized conformations of both electronic states, the Stokes shift S may be calculated as

$$S = 2E_{\text{reorg}} = E_e(R_g) - E_g(R_g) - (E_e(R_e) - E_g(R_e)), \quad (4.11)$$

with R_g being the optimized Pheo nuclei positions in the electronic ground state and R_e being the positions of the nuclei in the first excited electronic state. The energies calculated by (TD)DFT with Gaussian09, the B3LYP exchange-correlation function and the 6-311G(d,p) basis set are $E_e(R_g) = 53089.550$ eV, $E_g(R_g) = 53091.584$ eV, $E_e(R_e) = 53089.598$ eV and $E_g(R_e) = 53091.542$ eV. E_{reorg} is the reorganization energy. The Stokes shift is then calculated as $S = 0.09$ eV, which is larger than the experimental value of about 0.03 eV [22]. The reader has to consider a standard error of quantum-chemical energy calculations of 0.1 eV for molecular systems (even with a large basis set) [88]. Taking this error into account, the difference between the calculated Stokes shift and the experimental value is not very surprising. It is important to note that this deviation does not allow to make a statement on the quality of optimized structures and for the Hessian matrices (for all involved electronic states). On the one hand, the Stokes shift is calculated as a difference between two energy differences, both with an error of about 0.1 eV. On the other hand, electronic structure calculations are known to reproduce molecular normal mode vibrations with a much smaller error [88].

Another possibility to estimate the reorganization energy (and therefrom the Stokes shift) is the averaged energy gap function $\langle U_{eg} \rangle$ [84]. The vibrational part of $U_{eg}(t)$ is written as $U_{eg}^{\text{vib}}(t) = U_e^{\text{vib}}(t) - U_g^{\text{vib}}(t)$ (cf. Eq. 3.67). The respective average $\langle U_{eg}^{\text{vib}} \rangle$ can be related to the reorganization energy. The gap function due to solvent coupling $U_{eg}^{\text{sol}}(t)$ gives a small correction to this reorganization energy (about -0.01 eV). Thus, the equation for the Stokes shift S can be approximated by $S \approx 2\langle U_{eg} \rangle$ (cf. Eq. 4.11). The Stokes shift that can be estimated from the 80 ns of MD data is 0.08 eV (0.09 eV without the correction due to the solvent coupling) and thus corresponds to the value that was computed from (TD)DFT calculations. The difference to the

value that was presented in [84] is due to the much larger amount of MD data that were used for this thesis.

4.3 Energy gap fluctuation and transition coupling from MD trajectories

In a mixed quantum-classical methodology the TDSE has to be solved. The Hamiltonian in such a method depends parametrically on the classical computed nuclei trajectories. The Hamiltonian matrix elements in terms of the systems' nuclei positions is described in Sec. 3.4. Within this thesis the DCL (Sec. 3.1.3) is utilized to translate full quantum formulas to mixed quantum-classical expressions. In order to compute those expressions and to compute absorption spectra (linear or nonlinear), the TDSE has to be solved. The respective diagonal Hamiltonian matrix elements include the energy gap function $U_{eg}(R(t))$ (for the Pheo Q_x band $U_{fg}(R(t))$), cf. Eqs. 3.60 and 3.121 to 3.123.

The energy gap function $U_{ag}(R(t))$ was defined in Sec. 3.4.2 and consists of the energy gap fluctuation due to solvent coupling $U_{ag}^{\text{sol}}(R(t))$ and the energy gap fluctuation due to intramolecular vibration $U_{ag}^{\text{vib}}(R(t))$ with $a \in \{g, e\}$:

$$U_{ag}(R(t)) = U_{ag}^{\text{sol}}(R(t)) + U_{ag}^{\text{vib}}(R(t)). \quad (4.12)$$

4.3.1 Computing energy fluctuation due to solvent coupling

The energy gap fluctuation of Pheo m due to solvent coupling $U_{m,ag}^{\text{sol}}(R(t))$ is defined as (cf. Eq. 3.55)

$$U_{m,ag}^{\text{sol}}(R(t)) = \sum_{\xi} [J_{m,\xi}(bg, gb) - J_{m,\xi}(ag, ga)]. \quad (4.13)$$

$\sum_{\xi} [J_{m,\xi}(bg, gb) - J_{m,\xi}(ag, ga)]$ gives the energy difference of the Coulomb coupling to the solvent molecules ξ (in the state g) between the cases when the chromophore m is in the electronic state b and the case when it is in the electronic state a . When the energy gap for Pheo m is computed utilizing Eq. 4.13, the other Pheos $n \neq m$ and the dendrimer are treated like solvent molecules. $U_{m,ag}^{\text{sol}}(R(t))$ can easily be calculated from the MD trajectories if the electronic partial charges of the solvent in the electronic ground state and the electronic partial charges of the chromophore in the electronic states a and b are known.

When computing $U_{m,ag}^{\text{sol}}(R(t))$, one has to be careful when interpreting the resulting energy fluctuations. The Coulomb coupling $J_{m,\xi}(ag, ga)$ between chromophore m in the state a and solvent molecule ξ in the state g is a long range interaction. The MD simulation, however, only includes a finite number of solvent molecules. In Fig. 4.3 the energy fluctuation due to solvent coupling $U_{m,ag}^{\text{sol}}(R(t))$ was computed for different cutoff lengths for the Coulomb interaction. Even though the cutoff lengths do not vary a lot, the gap functions look completely different.

However, that does not mean that advanced methods (like PME, cf. Sec. 4.1.1) have to be utilized to compute the electrostatic coupling for an infinite solvent box. Fig. 4.4 shows the histograms over the energy gaps from Fig. 4.3. It can be seen that the fluctuation of the energy gap function does not vary for the different cutoff lengths. Since the fluctuation of the energy gap is the aim of the computation, it is adequate to compute the electrostatic coupling for a finite box. It has to be taken care that chromophore m couples to the solvent molecules as if it was located in the center of the periodic box.

4.3.2 Computing the transition couplings

The transition coupling between two Pheos m and n is calculated via summing up the Coulomb interactions between the sets of transition partial charges $q_m(ge)$ and $q_n(ge)$ (Eq. 3.49). For

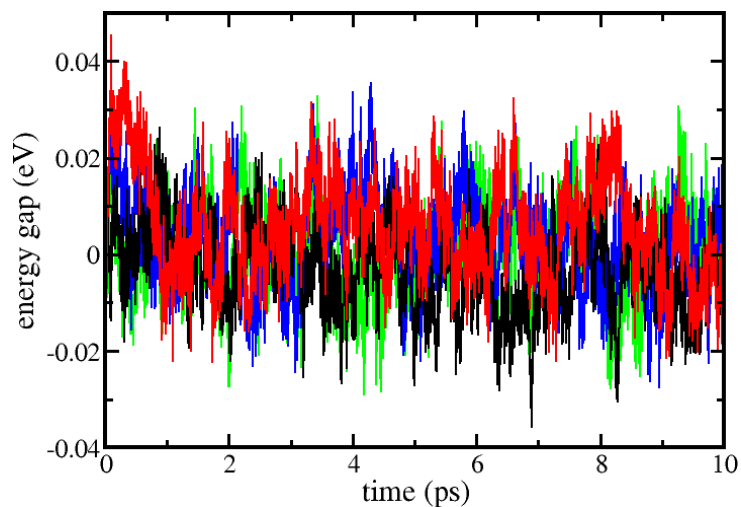


Figure 4.3: Energy gap function (for a 10 ps MD sample) of a single Pheo due to ethanol solvent coupling for four different cutoff lengths. Black: 15 Å, green: 16 Å, blue: 17 Å, red: 18 Å.

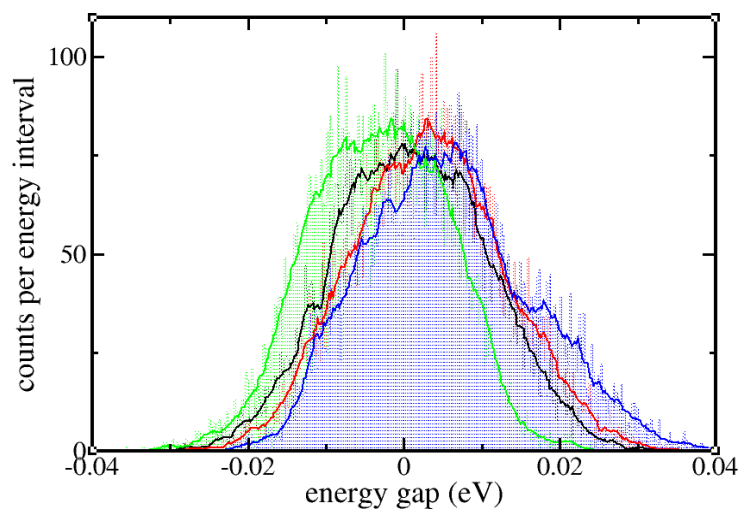


Figure 4.4: Energy gap histogram over the energy gap functions shown in Fig. 4.3. Black: 15 Å, green: 16 Å, blue: 17 Å, red: 18 Å. The full lines represent averages over 5 neighboring values, making it easier to compare the results.

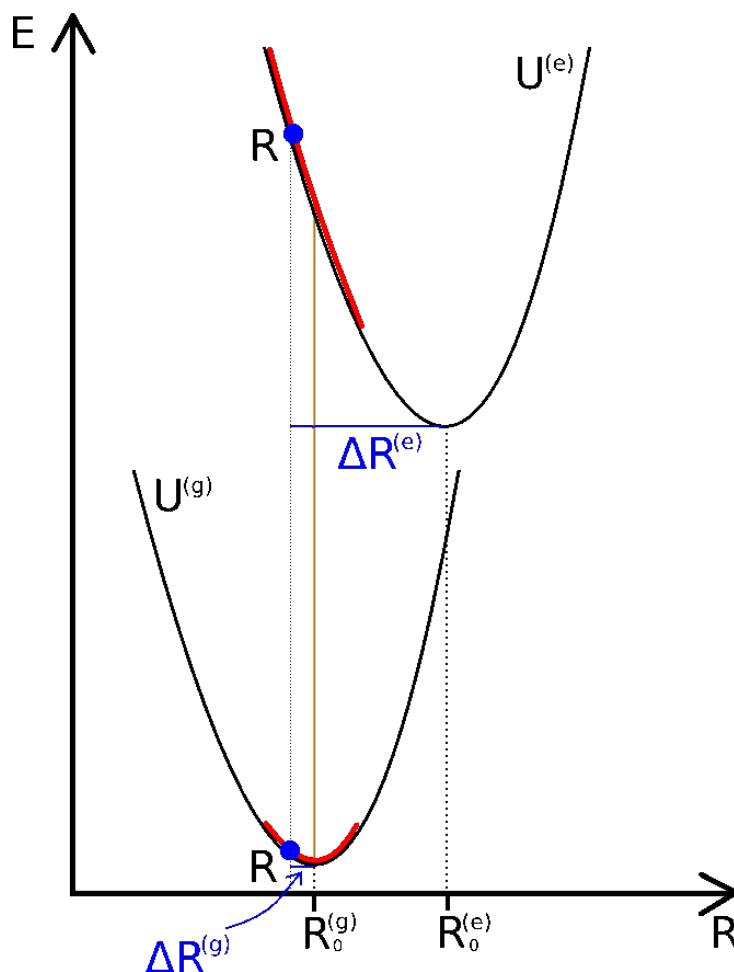


Figure 4.5: One-dimensional PESs of the electronic ground state (U_g) and the electronic excited state (U_e). The positions R_0^g and R_0^e indicate the respective equilibrium conformations of the electronic ground and excited state. The yellow line represents the vertical excitation. The red region indicates the energy margin due to intramolecular vibration

every MD time step, Eq. 3.49 is calculated for each Pheo pair m, n in order to compute the time-dependent transition couplings (excitonic coupling) $J_{mn}(t)$.

4.4 Intramolecular vibration in harmonic approximation

Eq. 3.67 calculates the vibrational energy gap function of a molecule in harmonic approximation. The main idea is illustrated in Fig. 4.5. The fluctuation of the energy gap between electronic ground and first excited state PES has to be computed for ensemble-averaged conformations R of the respective molecule. In order to carry out this calculation, the actual coordinates R , the Hessian matrix elements κ_{uv}^a ($a = g, e(f)$) and the Pheo reference trajectories R^a (cf. Sec. 3.5) are necessary. While the coordinates are taken from the MD trajectory, the Hessian matrices were calculated by our co-workers (Sec. 4.2). The Pheo reference trajectories are not just spatially rotated equilibrium conformations (of the corresponding electronic states g, e) but the Pheo molecules undergo bending modes at low frequency which may not be described within the harmonic approximation.

One additional comment has to be made in the beginning. The aim of this section is the calculation of the energy gap function due to intramolecular vibration. The word 'intramolecular' refers to a single Pheo, even though Pheo is covalently bound to the dendrimer in the case of P_4 and P_{16} . This is reasonable, since the approach has to work the same for covalently and

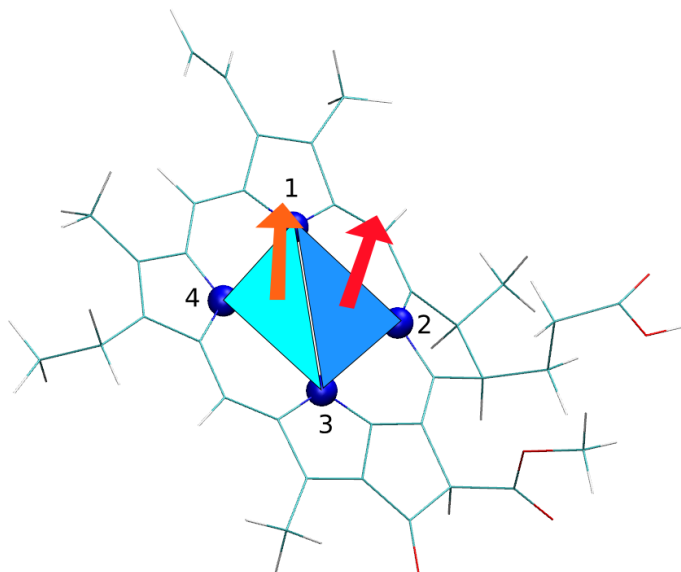


Figure 4.6: The normal vector of Pheo is defined by the average of the normal vectors defined by the two planes spanned by nitrogen atoms 1, 2, and 3, as well as 1, 3, and 4. The arrows (normal vectors) indicate the possible deforming of the Pheo plane, the maximum working angle is about 5 percent. To guarantee stability, the normal vector is additionally time-averaged over 1 ps.

non-covalently bound supramolecular complexes.

The formula for the energy due to intramolecular vibration was given in Eq. 3.35. If the Hessian matrix elements (for the electronic ground and first excited state) and the equilibrium conformation of the electronic ground state are known (computed with (TD)DFT), the energy for a small deviation from the equilibrium conformation can be computed directly from Eq. 3.35. However, after a few dozen femtoseconds of MD simulation the deviations are not small anymore. On the one hand, the Pheo molecule is translated and rotated in space, and on the other hand, it underlies several bending modes. The bending modes are the crucial problem in the computation of the energy fluctuation in the electronic ground state. If there were no bending modes, only the rotation of the Pheo molecule had to be corrected to calculate the deviations between the MD trajectory and the equilibrium conformation. Since there are bending modes, this is not possible.

Eq. 3.35 calculates the vibrational energy gap function in harmonic approximations. Contrary to Eq. 3.35, it does not depend on the equilibrium conformations R_0^g and R_0^e , but on the reference trajectories $R^g(t)$ and $R^e(t)$ that undergo the translations, rotations and bending modes of the molecules. Thus, Eq. 3.35 may compute the energy gap function for the whole MD data, if the reference trajectories $R^g(t)$ and $R^e(t)$ can be specified.

4.4.1 Rotation of the Pheo molecule

Since the Hessian matrix elements that are utilized in Eq. 3.35 were calculated for a defined spatial orientation, the coordinate system of the MD Pheo has to be rotated back. This back rotation is necessary, because the Hessian matrix elements $\kappa_{\mu\nu}$ give the raise of energy (the unit is energy per length square) for a displacement of coordinate μ and coordinate ν . Remember that μ and ν do not count the N^{atoms} atoms of the molecule, but the $3N^{\text{atoms}}$ coordinates that include all the Cartesian coordinates of all N^{atoms} atoms. If the Pheo of the MD trajectory is not rotated back to the orientation in which the (TD)DFT calculations of the Hessian matrices were done (see Sec. 4.2), the resulting energy gap fluctuation will not represent the correct energy fluctuation.

Nevertheless, Pheo is not rigid during the simulation, and normal as well as in-plane axes

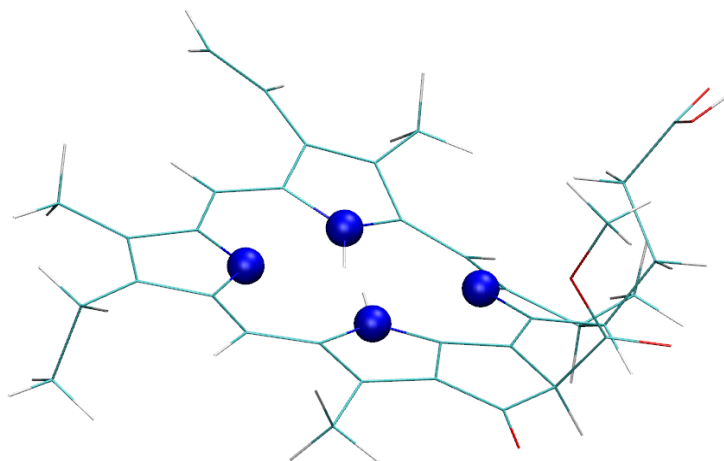


Figure 4.7: Molecular bending deforms the plane structure of Pheo.

have to be determined. Those are necessary to calculate the respective angles in between the Pheo normal and in-plane vectors during the MD simulation and the normal and in-plane vectors of the Pheo orientation that was used for the electronic structure calculations. This is necessary for the adequate back rotation of Pheo to this orientation. The first in-plane axis is defined as the average connecting line (averaged over 1 ps - the time scale of Pheo rotation in ethanol is about 100 ps) between the two hydrogen bound nitrogen atoms. This axis is the most stable in the Pheo molecule (see Fig. 4.7). The normal axis is defined as the respective normalized averaged vector (also averaged over 1 ps), orthogonal to both normalized vectors connecting the opposed pairs of nitrogen and such (in average) defining the Pheo plane. An illustration of this description can be found in Fig. 4.6.

There have to be made some additional remarks considering the Pheo side chains. The atoms in the ring (that means within the extended π -electron system) are relatively rigid. There is some bending of the ring, which makes it impossible to treat the system as rigid, but the plane working angle α (cf. Fig. 4.7) does not exceed 5%. For the side chains such a constraint is not existent. On the other hand, the high flexibility of the side chains affects the respective Hessian matrix elements in such a way that they are nearly coordinate independent. This makes the above-explained procedure applicable for the whole Pheo molecule - the quasi rigid molecular plane and the high mobile side chains.

4.4.2 Molecular bending

Without molecular bending modes, the reference trajectory of Pheo could simply be described by the equilibrium structure that was time-dependently translated and rotated in space. The harmonic approximation will only give a correct result, if two conditions are fulfilled: on the one hand, the molecules' intramolecular vibrations must have a harmonic character (that seems to be valid for Pheo [84]); on the other hand, the deviation between MD conformation and equilibrium conformation must not include deviations due to molecular bending, but only deviations due to the vibration of all atoms around their actual equilibrium position. The presence of molecular bending changes those equilibrium positions in time. Thus, the assumption of a rigid Pheo reference trajectory leads to large errors if the molecular vibration involves bending modes. At each time step the molecular conformation has its own atomic equilibrium positions and Hessian matrix elements. The molecular conformations of two points in time, that are very close to each other, have rather similar atomic equilibrium positions and Hessian matrix elements. To calculate the energy fluctuation due to intramolecular vibrations, further approximations have to be made.

First: the equilibrium structure Hessian matrix elements $\kappa_{\mu\nu}^a$ are used for all possible geome-

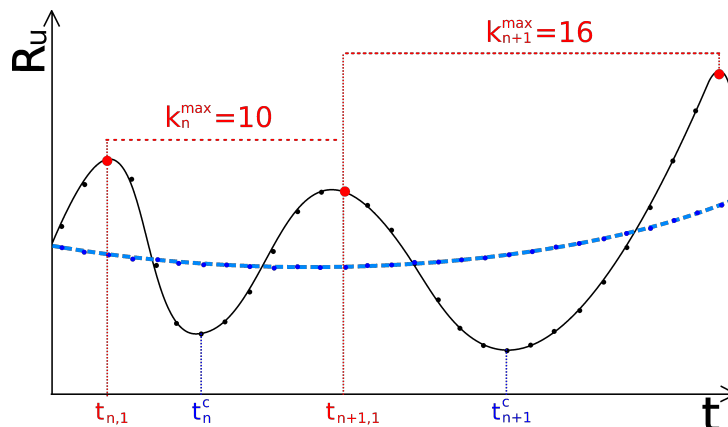


Figure 4.8: Scheme of the time-dependent averaging procedure. After appointing the consecutive maxima of each coordinate trajectory, the respective distances in femtoseconds between adjacent maxima at $t_{n,1}$ and $t_{n+1,1}$, k_n^{max} are calculated. At the center point between two maxima t_n^c , the trajectory is averaged over the neighboring k_n^{max} x-coordinate values.

tries. The molecular bending indeed changes the positions of single atoms dramatically. But the geometry change itself (and with it the change of the PES and its derivatives) is rather small (compare with the molecular bending in Fig. 4.7). One can imagine a 2-dimensional figure of a molecule on a sheet of paper. If the sheet of paper is curled slightly, the angles between neighboring atoms are only changed slightly, but the positions of the outer atoms of the molecule are changed dramatically.

Second: the energy fluctuation due to molecular bending is not treated. The approximation is necessary, since there is no direct way to calculate this energy fluctuation due to molecular bending. The approximation is possible because it can be assumed that the slow molecular bending proceeds on a much more flat potential energy surface than the much faster single atomic vibrations, since the system has much more time to adopt to the respective minimum energy geometry.

4.4.3 Electronic ground state Pheo reference trajectory

The electronic ground state Pheo reference trajectory can be interpreted as a trajectory of actual (local) equilibrium structures that have their origin in the molecular bending. The calculation of the respective reference trajectory of Pheo m (in the electronic ground state) $R_m^g(t)$ exploits the fact that the equilibrium conformations at two close points in time do not deviate too much.

The intramolecular vibration is separated into the bending modes and the single atom vibrations. A single atom at some time t_0 will per definition vibrate around its actual equilibrium conformation. The electronic ground state Pheo reference trajectory can be calculated by a respective averaging of the MD trajectories. It has to be mentioned here that this non-direct calculation of $R_m^g(t)$ leads to no additional errors in general, even though there will occur numeric errors during the average procedure.

Moving window averaging

A moving window average is an average where the actual value of a function $g(t_0)$ at $t = t_0$ is given as the average of some function $f(t_n)$ at time $t_n = t_0 + n\Delta t$ with some finite time step Δt . The moving window averaged function F can be calculated as $F = \sum_{n=-N}^N f(t_n) / (2N + 1)$.

The averaging procedure is applied to every coordinate of every atom. In what follows, one coordinate (for example the x-coordinate) of an arbitrary atom is discussed. The time-dependency may be as in in Fig. 4.8. To obtain the current average x-coordinate, the x-coordinates of the neighboring points in time are averaged.

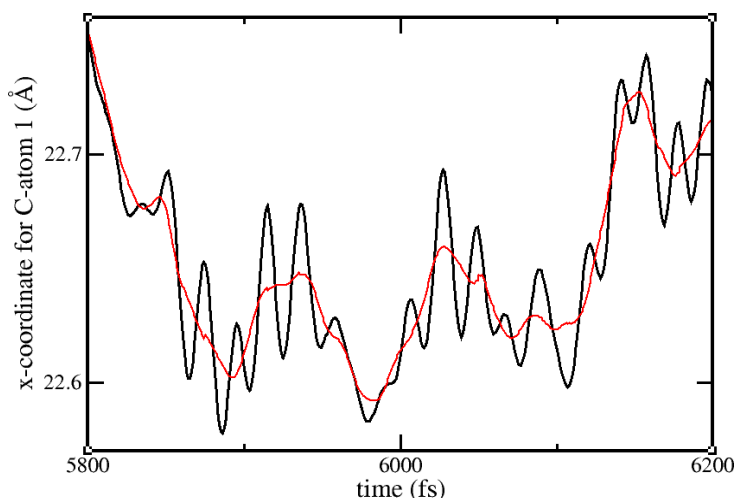


Figure 4.9: The x -coordinate of carbon atom number 1 within the porphyrin ring. Black line: trajectory during the MD simulation, red line: reference trajectory.

If the average x -coordinate (like in Fig. 4.8) has to be computed from an MD trajectory, an additional problem occurs: the periods of oscillation for the single coordinates in a molecule like Pheo adopt very fast in time. Extreme changes, like an increase or decrease of the actual period of oscillation $T_\mu(t)$ (of some coordinate μ) to 50 % within a single oscillation period, are possible. Hence, the varying of the length of the respective moving window over time is essential.

Moving window average with time-dependent window length

To apply a moving window average with time-dependent window length, the time and coordinate dependent period of oscillation $T_\mu(t)$ for coordinate μ at time t has to be calculated for every coordinate for the whole time of the simulation. In the following discussion, the index μ is dropped for the matter of simplicity.

For every coordinate the program searches all occurring maxima within the trajectory (searching the minima would be equivalent). According to Fig. 4.8, the points in time between two neighboring maxima are defined as the temporal center points t_n^c , and the maxima are numerated by an index n . The period of oscillation for such a temporal center point t_n^c , $T(t_n^c)$ is defined by the distance between the two neighboring maxima at $t_{n,1}$ and $t_{n+1,1}$ (cf. Appendix C). The period of oscillation for the points in time between the t_n^c is linearly interpolated. A more detailed description on how to compute the ground state reference trajectory is given in App. C.

Before this computation can be done, the distance between the single maxima that were detected during the first run has to be checked. From the number of maxima in the trajectory of coordinate μ an approximate average period of oscillation for this coordinate $\langle T \rangle^{\text{approx}}$ is calculated. This number is only an approximation for the following reason: it was mentioned earlier that the intramolecular vibration can be separated into the bending modes and single atom vibrations. It was also written that the bending mode periods of oscillation are much longer than the single atom periods of oscillation (cf. Fig. 4.10), which in general makes it possible to separate both. However, due to the fact that the bending modes have a much larger effect on the atomic positions, a bending mode may superpose the period of oscillation of some coordinate in that way that the maxima (and the following minima) disappear and only an inflection point remains. The program recognizes if the actual period of oscillation at some time t_n^c is twice or more the approximate average period of oscillation, which occurs when $T(t_n^c) > 2\langle T \rangle^{\text{approx}}$. If the maximum period of oscillation is exceeded, respective additional

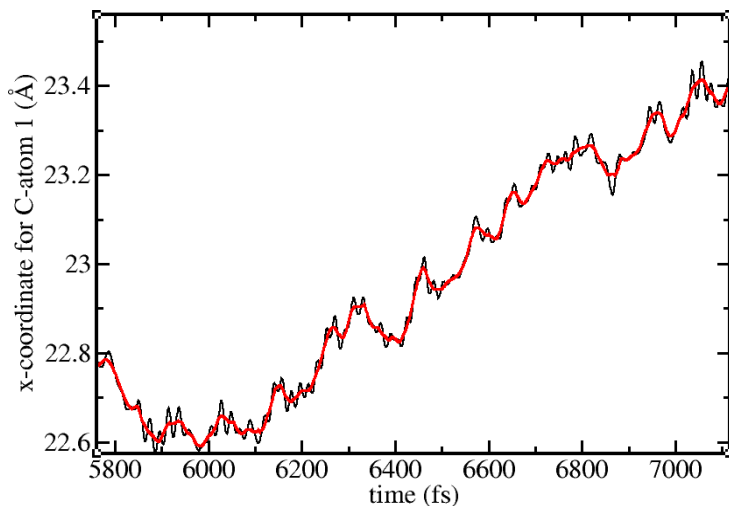


Figure 4.10: The same result as in Fig. 4.10 is shown, only for a longer simulation time. The different time scales of molecular bending can clearly be seen.

maxima are assumed between the corresponding maxima. The general idea is to assume rather too many than too few maxima, since the error is quadratic in the deviation between Pheo MD and Pheo reference trajectory. In any case, the program was tested with different maximum periods of oscillation and the results depend only weakly on them.

On the one hand, the search for inflection points itself would circumvent this procedure. On the other hand, this is much more complicated than the search for extrema. And it has to be mentioned that the period of oscillation of an H atom is about 10 fs, while the time-step of the MD simulation is 1 fs. This makes the numerical search for inflection points much more error-prone.

The result of the averaging can be seen in Fig. 4.10 for a larger time scale and in Fig. 4.9 for a few hundred femtoseconds. In the ground state reference trajectory the molecular bending modes affect the position of a single atom much more than the single atom vibration.

4.4.4 Electronic first excited state Pheo reference trajectory

To compute the energy gap function, the potential energy for Pheo not only for the electronic ground state but also for the electronic first excited state is necessary. This requires the knowledge of the Pheo reference trajectory in the electronic first excited state $\mathbf{R}^e(t)$. As mentioned in Sec. 3.1, a ground state classical path approximation is utilized in this thesis. This means, all MD simulations have been executed in the electronic ground state. Thus, the calculation of $\mathbf{R}^e(t)$ is not possible in the same way as for $\mathbf{R}^g(t)$. In what follows, an method is proposed that makes it possible to compute $\mathbf{R}^e(t)$ directly from $\mathbf{R}^g(t)$. It was stated earlier in this section that the all Pheo conformations from the MD trajectories have to be rotated - adapted to the Pheo orientation in the (TD)DFT calculation (Sec. 4.2) - to calculate the excited electronic state Pheo reference trajectory. The deviation vectors ΔR^{eq} between the electronic first excited (R_0^e) and electronic ground state (R_0^g) Pheo equilibrium conformations were computed as

$$\Delta R^{\text{eq}} = \{\Delta \mathbf{R}_1^{\text{eq}}, \Delta \mathbf{R}_2^{\text{eq}}, \dots\} = R_0^e - R_0^g. \quad (4.14)$$

Adding these deviation vectors ΔR^{eq} to the (back-rotated) Pheo reference trajectory in the electronic ground state $\mathbf{R}^g(t)$ gives a good approximation for the Pheo reference trajectory in the electronic first excited state $\mathbf{R}^e(t)$. The utilization of this approximation can be justified in a similar manner as the utilization of the equilibrium conformation Hessian matrix elements for all conformations (cf. Sec. 4.4.2): a 2-dimensional figure of a molecule on a sheet of paper was

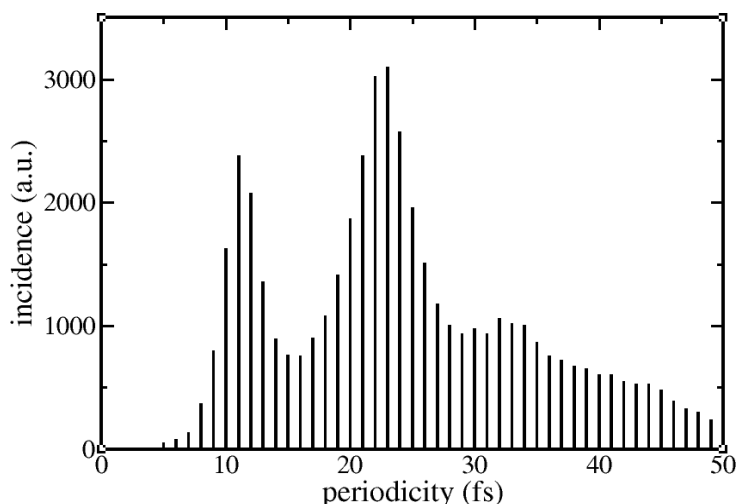


Figure 4.11: The incidence of vibrational periodicities for all atoms of a single Pheo (for the whole MD data of 80 ns).

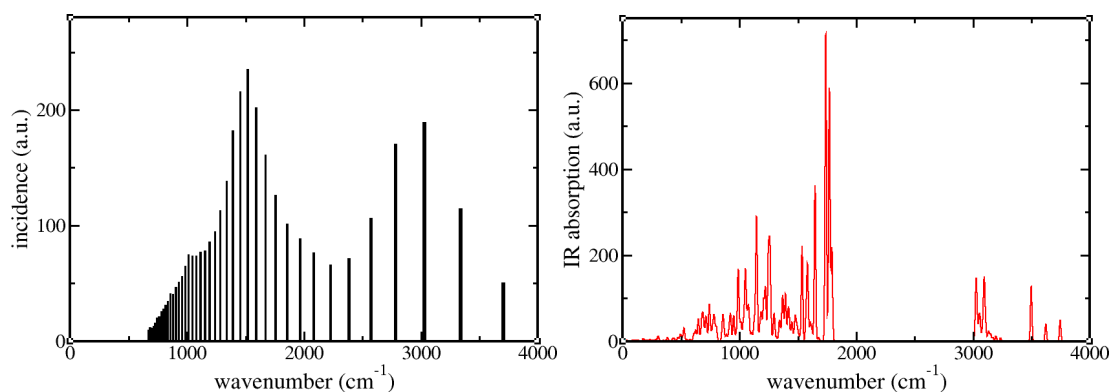


Figure 4.12: Left panel: the incidence of vibrational wave numbers (calculated from the periodicities in Fig. 4.11) for all atoms of a single Pheo (cf. Fig. 4.11). Right panel: IR spectrum of a single Pheo in the electronic ground state calculated from the DFT normal mode analysis.

imagined. Slightly curling the sheet of paper changes the angles between neighboring atoms only a bit. This illustration, of course, is no prove. A variety of electronic structure calculations for different MD conformations would be necessary to actually prove the approximation.

4.4.5 Errors within the energy gap function calculation

In the following subsection, all approximations within the method to compute the vibrational part of the energy gap function $U_{eg}^{\text{vib}}(t)$ will be discussed in detail. Aside from the possible errors, some results are shown that indicate the quality of the new approach to compute $U_{eg}^{\text{vib}}(t)$ in harmonic approximation.

In the beginning, it has to be mentioned that the energy gap function can be utilized to compute the linear absorption lineshape as derived in Sec. 3.6. Those spectra can be compared with respective linear absorption experiments, as will be done in Sec. 5.1.2. The linewidths of the calculated Q_y and Q_x bands agree perfectly with the experiment. The same holds for the vibrational satellites. Much more details and results will be given in Sec. 5.1.2, it has only to be mentioned here that those results indicate the good quality of the method.

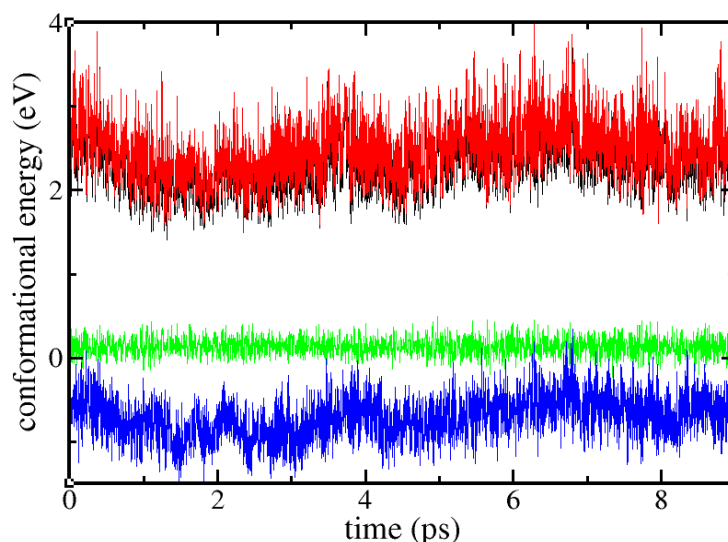


Figure 4.13: Energy fluctuation of a 10 ps MD sample for a single Pheo in ethanol. Black line: electronic ground state energy fluctuation due to intramolecular vibration calculated in harmonic approximation (cf. Sec. 4.4). Red line: electronic excited state energy fluctuation calculated in harmonic approximation. Green line: energy gap function. Blue line: conformation dependent energy during the simulation due to the MD force field.

Influence of the quality of the trajectories

Fig. 4.11 shows the histogram over the vibrational periodicities that occur in the MD data. The vibrational periodicity at each time t for every coordinate μ can be calculated with the same program that is utilized to compute the reference trajectories (cf. Sec. 4.4.3). This periodicities can be recalculated as wave numbers. In Fig. 4.12 the incidence of this wave numbers within the MD data for a single Pheo is compared with the IR spectrum of the Pheo electronic ground state. The IR intensities were calculated by the Gaussian09 program package within the normal mode analysis that was necessary to compute the Hessian matrices (Sec. 4.2). The first order IR intensities are calculated by Gaussian09 as $|d\mu^{\text{el}}/dQ_v|^2$ [148]. μ^{el} is the static dipole moment of the molecule, and the Q_v determine the normal mode coordinates. In order to compute the vibrational absorption spectra, the IR intensities are convoluted with Gaussian functions with a FWHM of 15 cm^{-1} . This convolution is a usual procedure when computing IR spectra [149].

Note that only the wave numbers ought to be compared in Fig. 4.12. The IR spectrum can not be correlated directly with the incidence of the respective frequencies within Pheo MD simulations. Nevertheless, the occurrences of the wave numbers in both panels of Fig. 4.12 seem worth to be shown in this thesis and indicate a good quality of the force field. The IR spectrum shows a gap that does not occur in the left frame of Fig. 4.12. However, it can not be expected from a classical force field to reproduce the eigenfrequencies of a quantum-mechanical system without diviances.

Influence of the quality of the Hessian matrices

The conformational energy in harmonic approximation (cf. Eq. 3.35) is linear dependent on the respective Hessian matrix elements. The error of the vibrational modes (and thus the average error of the Hessian matrix elements) can in general be assumed to be well below 10 % due to error cancellation [88].

The quality of the Hessian matrices can also be shown by comparing the vibrational energy fluctuation in harmonic approximation with the conformational energy fluctuation due to the MD force field. In terms of the MD force field, the conformation dependent MD (force field) energy E^{FF} of Pheo is given as the sum over next neighboring atom interaction energies as well

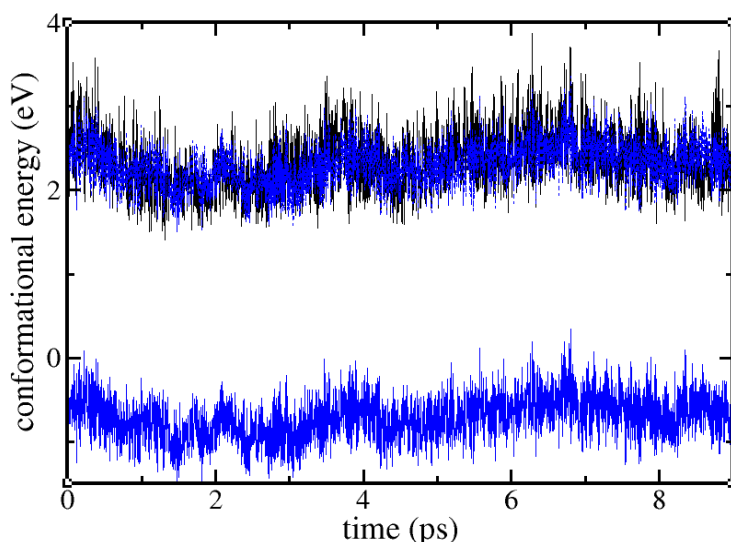


Figure 4.14: Energy fluctuation of a 10 ps MD sample for a single Pheo in ethanol. Black line: electronic ground state energy due to intramolecular vibration in harmonic approximation. Full blue line: conformational energy due to the MD force field. Dashed blue line: conformational energy due to the MD force field, shifted up in energy by 3 eV.

as the non-bonded interactions within Pheo (cf. Eq. 4.1). Note that the intramolecular forces due to an MD force field consist of non-bonded (cf. Sec. 4.1.2) and bonded contributions, while the Hessian matrix includes all the interactions within the molecule. This conformation dependent MD energy can be compared with the Pheo energy due to intramolecular vibration, calculated in harmonic approximation (Eq. 3.35 with Pheo being in the electronic ground state). Fig. 4.13 shows the electronic ground and excited state energy fluctuation, the energy gap function and the MD conformational energy for a 10 ps MD sample.

The MD conformational energy is shifted against the electronic ground state energy in harmonic approximation. However, the absolute value of the potential energy can not be assumed to be the same for the MD force field and the electronic structure calculation. Important for the MD force field is the effective force on the nuclei. The comparable quantity between both approaches is the resulting potential energy fluctuation.

In Fig. 4.14 the MD conformational energy is shifted up by 3 eV to make the respective energy fluctuation more comparable with the fluctuation of the vibrational energy $U_g^{\text{vib}}(t)$ calculated in harmonic approximation (cf. Eqs. 3.66, 3.67). Fig. 4.15 shows the difference between the shifted MD conformational energy and the calculated vibrational energy in detail. The similarity of both curves is remarkable. This result not only indicates the high quality of the Hessian matrices, but it shows that the calculation of the whole electronic ground state energy fluctuation is very good. This includes the calculation of the MD trajectories, the quality of the reference trajectories and the neglecting of the bending modes that will be discussed in what follows.

Influence of the quality of the reference trajectories

In Sec. 4.4.3, the Figs. 4.10 and 4.9 showed the MD trajectory of a C atom from the porphyrin ring and its respective component of the electronic ground state Pheo reference trajectory. Especially Fig. 4.9 shows that the time-dependent moving window method works. Of course, the calculation of the reference trajectory is not error-free. This is clear when looking at the fast changing vibrational frequencies of the single coordinate trajectories. However, the errors for the difference ΔR can be estimated to be below 10 - 20 % in average (cf. Fig. 4.9). The most crucial argument is that the errors occur in both directions, that is why a large part of the total error disappears due to error cancellation.

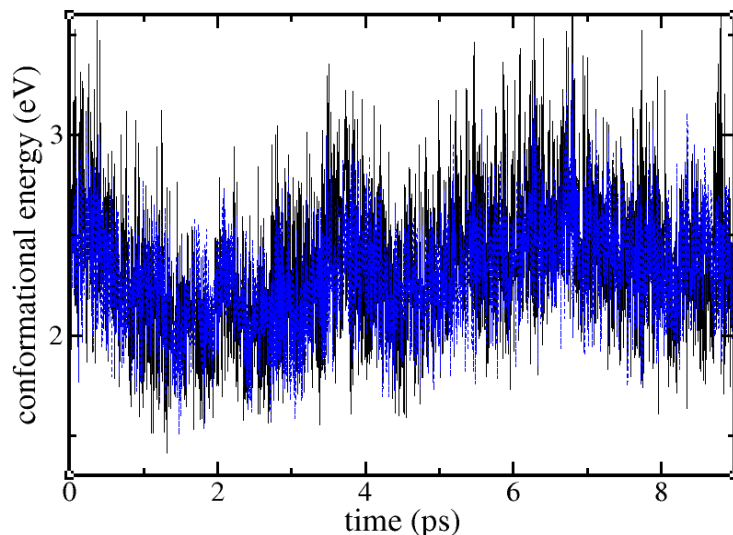


Figure 4.15: Same result as in Figs. 4.13 and 4.14. Black line: electronic ground state energy due to intramolecular vibration. Dashed blue line: conformational energy due to the MD force field, shifted up in energy by 3 eV. The similarity is remarkable.

Influence of the neglect of molecular bending modes

It has been indicated indirectly in Fig. 4.15 that the influence of neglecting the molecular bending modes on the quality of the energy fluctuation is rather small. Nevertheless, further investigations support this thesis. The method introduced in Sec. 4.4 to calculate the energy gap fluctuation generates the Pheo reference trajectories. In order to compute the force field energies of the reference trajectory as well as force field energies of the MD trajectory, the NAMD internal method ‘NAMD energy’ was utilized [132]. Fig. 4.16 shows the conformational energy fluctuation of a 10 ps MD run as well as the conformational energy fluctuation of the respective electronic ground and excited state Pheo reference trajectories due to the MD force field. In Fig. 4.17, the conformational energy fluctuation of the electronic ground reference trajectory is shifted. This makes a direct comparison between the conformational energy fluctuations of the MD trajectory and the reference trajectory possible. The energy fluctuation of the reference trajectory is considerably smaller.

Fig. 4.18 shows the respective histogram over the energy fluctuations from Fig. 4.16 (conformational energy of the MD run and of the reference structure trajectory). It can be seen that the width of the energy distribution calculated from the reference structure trajectory is half as broad as the width calculated from the MD trajectory. The histograms over this energies are approximately normal distributed. It is further assumed that the energy distribution of the reference structure represents the energy fluctuation due to molecular bending and the energy distribution of the MD trajectory represents the energy fluctuation due to the complete intramolecular vibrations. For the distribution of a sum of two normal distributed random numbers the following two statements hold: firstly, the resulting distribution is also normally distributed; secondly, for the width of a general Gaussian distribution one may write $\Gamma_{\text{total}} = \sqrt{\Gamma_b^2 + \Gamma_{\text{iv}}^2}$, where Γ_b and Γ_{iv} are the widths of the distributions of two random numbers. Γ_{total} is identified with the conformational energy distribution due to the complete intramolecular vibration, and Γ_b is identified with the energy distribution due to molecular bending (energy distribution of the reference structure). For $\Gamma_{\text{total}} = 2\Gamma_b$ (linewidths can be estimated from Fig. 4.18), $\Gamma_{\text{iv}} = 0.87\Gamma_{\text{total}}$ is obtained.

Since Γ_{iv} represents the intramolecular vibrational energy distribution width without molecular bending, it is obvious that there is some dependency of the MD conformational energy on the reference structure energy fluctuation. Altogether, this discussion provides an indication

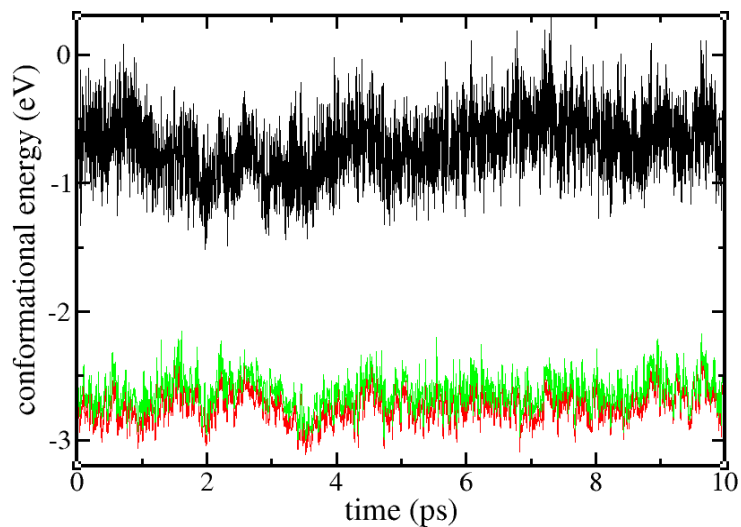


Figure 4.16: Energy fluctuation of a 10 ps MD sample for a single Pheo in ethanol. Black line: conformational energy of the MD trajectory. The red and green line show the conformational energies of the respective electronic ground and first excited state reference structures.

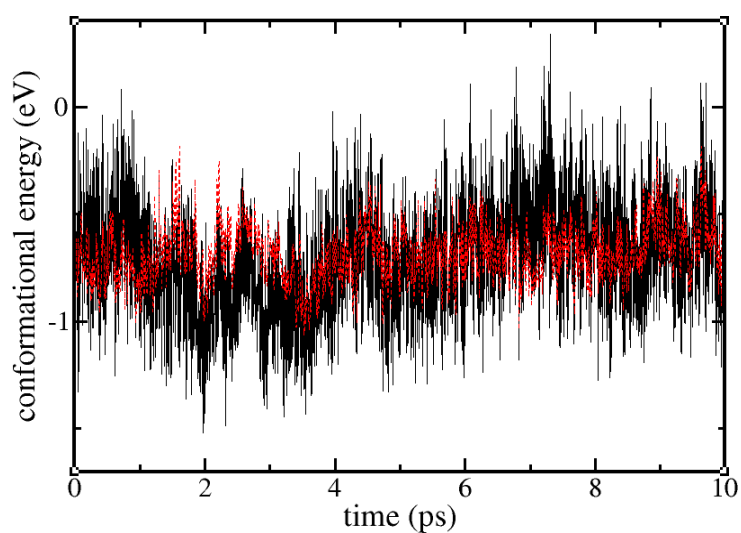


Figure 4.17: Energy fluctuation of a 10 ps MD sample for a single Pheo in ethanol. Black line: conformational energy of the MD trajectory. Dashed red line: shifted conformational energy of the electronic ground state reference structure.

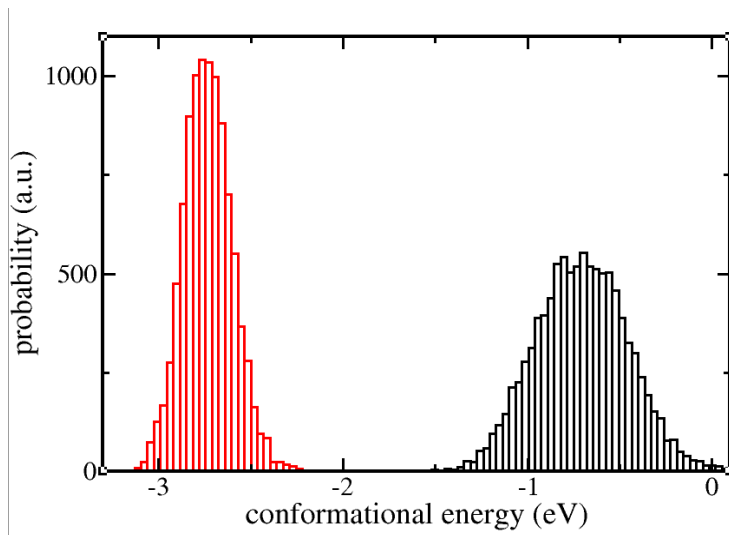


Figure 4.18: Energy fluctuation histogram from a 10 ps MD sample for a single Pheo in ethanol. Black: conformational energy of the MD trajectory. Red: conformational energy of the respective electronic ground state reference structure.

that neglecting the molecular bending energy fluctuation leads to an error of the total energy fluctuation. This error is proportional to the value of slightly above 10 % ($\Gamma_{iv} = 0.87\Gamma_{total}$).

The above discussion relates the intramolecular vibrational energy fluctuation in the electronic ground state without molecular bending with the total intramolecular energy fluctuation in the electronic ground state (including molecular bending). Actually, the effect of molecular bending on the gap function has to be considered. Fig. 4.13 showed the electronic ground and first excited state energy fluctuations and the respective energy gap function. In this figure it is obvious that the low frequency energy fluctuation for the electronic ground and excited state energy have no effect on the energy gap. This indicates that the error received when the low frequency bending modes are neglected is not about 10 %, but probably much smaller.

Influence of the quality of the optimized structures

Fig. 4.19 shows the effect of a change of the deviation vectors ΔR^{eq} between the optimized electronic ground state and the optimized excited state structure (R_0^g and R_0^e) on the fluctuation of the energy gap functions for a 10 ps trajectory of Pheo in ethanol. The deviation vectors ΔR^{eq} are multiplied with the number f , with $f = \{0.5, 0.8, 0.9, 1.0, 1.1, 1.2, 1.5\}$.

The resulting energy fluctuation linewidths are shown in Fig. 4.19. The dependence of the energy gap fluctuation computation on the quality of the deviance vectors is acceptable. A respective error of 10 % for the deviation vectors ΔR^{eq} (cf. Eq. 4.14) changes the width of the distribution by about 5 %. A larger error than 10 % for the complete set of deviation vectors is not expected. However, this is not proven here. At this point, it is not clear which part a possible error cancellation would have, if the deviation vectors ΔR_μ^{eq} have different errors for different coordinates μ . Nevertheless, concerning the other contributions to the error of the gap function, the quality of the optimized structures seems to be one of the most error-prone parts of the gap function calculation. This is interesting, since the quality of this part of the calculation can be controlled somehow by choosing the best possible quantum chemistry method or basis set. The calculation done by our co-workers with (TD)DFT, a B3LYP-exchange-correlation potential and the 6-311(d,p) basis set is at a very high level. But concerning the rapidly enhancing quality of computing machines, even the utilization of larger basis sets may be possible in the future.

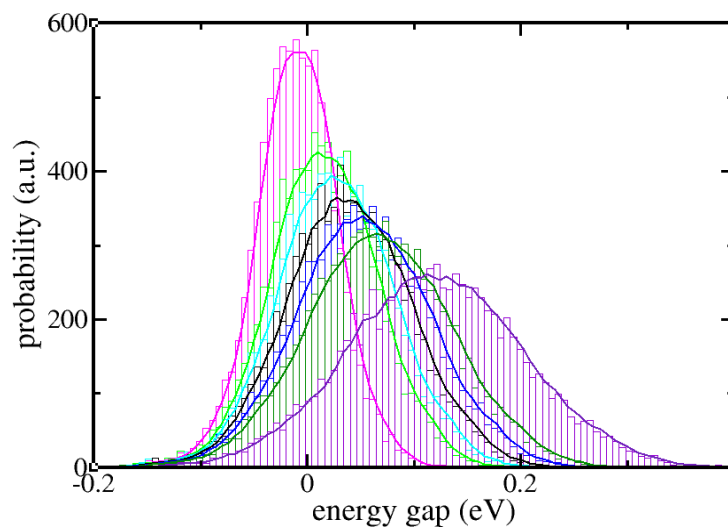


Figure 4.19: Histograms over the energy gap fluctuations of Pheo in ethanol for different deviation vectors $f\Delta R^{\text{eq}}$. The real number f acts as a factor on ΔR^{eq} (cf. Eq. 4.14). Black: $f=1.0$, light blue: $f=0.9$, dark blue: $f=1.1$, light green: $f=0.8$, dark green: $f=1.2$, magenta: $f=0.5$, violet: $f=1.5$. The full lines show respective averages over five neighboring values.

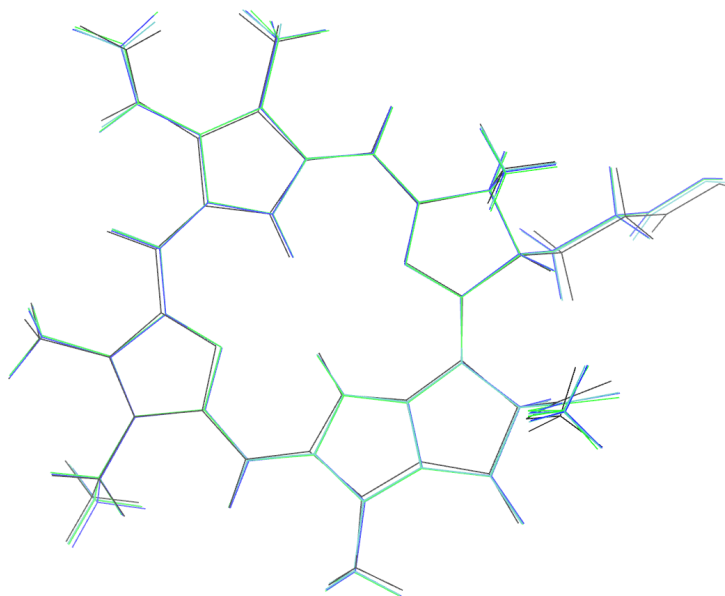


Figure 4.20: Pheo equilibrium conformations. The black structure shows the MD force field equilibrium conformation of Pheo. The respective equilibrium conformations of the electronic ground state, first excited and second excited state are drawn in cyan, blue and green.

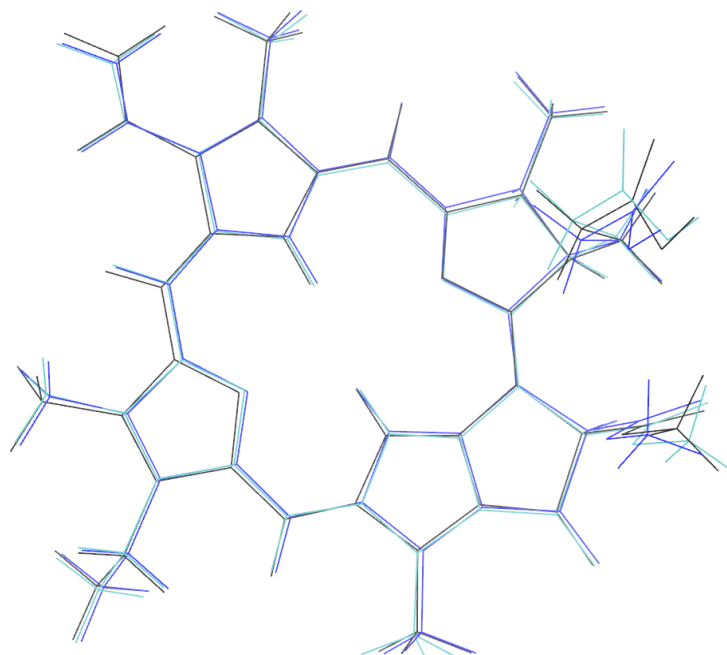


Figure 4.21: Pheo equilibrium conformations. The black structure shows the MD force field equilibrium conformation of Pheo. The respective equilibrium conformations of the electronic Hartree-Fock ground state and the CIS first excited state are drawn in cyan and blue.

To underline the importance of the equilibrium structures for the different excited states, Fig. 4.20 and Fig. 4.21 have to be compared. While Fig. 4.20 shows the equilibrium structures calculated by our co-workers (electronic ground, first, and second excited state), Fig. 4.21 shows the equilibrium structures for Hartree-Fock and configuration interaction singles (CIS) calculations (Hartree-Fock for the electronic ground state and CIS for the electronic first excited state, both with the 6-31* basis set), previously calculated by a former group member. Both figures additionally include the MD minimum conformation. The difference of the structures calculated with Hartree-Fock and CIS are extremely large. The respective energy for the excited state calculated with the deviation vectors ΔR^{eq} between the ground and the excited electronic state has an equivalently large error. This illustrates how important the appropriate computation of the molecular equilibrium geometries in the electronic ground, first excited, and second excited state is.

Other influences on the quality

The calculation of the excited state reference structure via the deviation vectors ΔR^{eq} (cf. Eq. 4.14) between electronic ground and excited state equilibrium structures (R_0^g and R_0^e , respectively) depend on the appropriate back-rotation of the MD Pheo orientation to the Pheo orientation of the electronic structure calculations. In order to carry out this back-rotation, the calculation of the plane normal vector of Pheo is necessary. The procedure is explained in detail in Sec. 4.4.1. In the calculation a respective Savitzky-Golay average of the time-dependent normal vector is done. A Savitzky-Golay average performs a local polynomial regression [150] on the time-dependent normal vector. The average is taken over 1 ps. Fig. 4.22 shows the energy fluctuation due to intramolecular vibration, calculated via Eq. 3.35. One curve is calculated with Pheo normal vectors that are averaged over 1 ps, while the other curve uses an average window of 100 fs. Both curves give nearly the same result. The effect on the energy gap fluctuation is marginal.

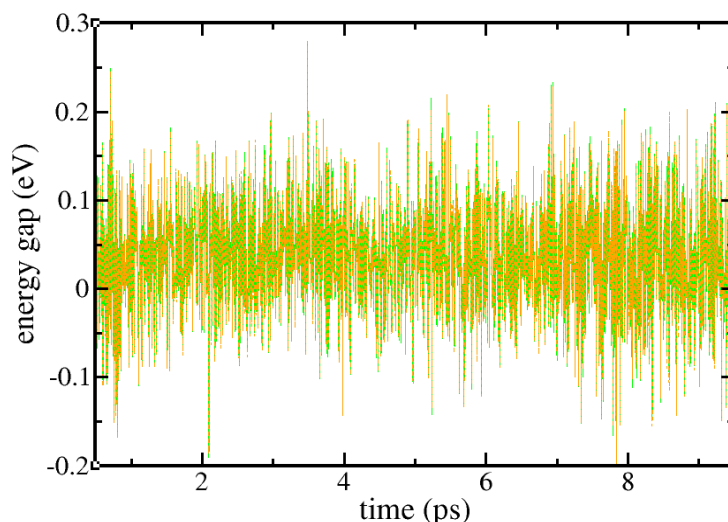


Figure 4.22: Energy gap fluctuation for a single Pheo in ethanol. Green line: energy gap function for a 10 ps MD sample. The normal vector of the molecule was Savitzky-Golay smoothed over 1 ps. Orange dashed line: same result for the molecular normal vector averaged over 100 fs. The difference between both curves is very small.

4.5 Solving the TDSE utilizing molecular dynamics trajectories

The computation of optical properties, linear absorption, or transient absorption (cf. Secs. 3.6 and 3.8) requires the computation of the CC wave function expansion coefficients \tilde{A}_α (cf. Eq. 3.16). For the computation of linear absorption only those \tilde{A}_α become finite which represent a singly excited wave function. However, in the following section it will be clarified how the solution of the TDSE is derived from the nuclear trajectories.

As described in Secs. 4.4 and 4.3.1, for each chromophore m the energy gap function $U_{meg}(t)$ is computed. For each chromophore pair m and n , the transition coupling $J_{mn}(t)$ is computed.

For all P_N systems, MD data of 8 trajectories, each with a length of 10 ns (8 ns for P_{16}), are available. For P_{16} additional MD data were produced (16 runs with different initial conformations). In what follows, it will be described how the TDSE can be solved for the available MD data.

4.5.1 Solving the TDSE for singly excited P_N systems

Starting with the first MD sample length (200 fs of MD data) of P_N in ethanol, the values for the energy gap function $U_{eg}(t; t^{\text{MD}} = 0)$ and the transition couplings $J_{mn}(t; t^{\text{MD}} = 0)$ are inserted into the TDSE for the expansion coefficients (Eq. 3.60), with t^{MD} being the time in the MD trajectory that is the initial time ($t = 0$) for the solution of the TDSE (Eq. 3.60). Eq. 3.60 is then solved for the N different initial conditions $\tilde{A}_\alpha(t = 0) = 1$. If the chromophores within a CC are excitonically coupled, this initial condition does not represent the initial electronic excited state of a CC shortly after the excitation. The electronic excited state will then be a superposition over different \tilde{A}_α , since the CC is excited to an excitonic state. However, for P_4 and P_{16} it is assumed that single Pheos are excited (concerning the time scale of the EET transfer above 1 ps, this approximation seems to be reasonable). The sample length of 200 fs is chosen because of the good convergency of the respective dipole-dipole correlation function after the ensemble averaging. The dipole-dipole correlation function vanishes after about 50 fs due to dephasing. The length of the MD sample (sample length) will be referred to as Δt_{sample} in what follows. Δt_{sample} has to be larger than 50 fs, since this is the convergence time of the averaged expansion coefficients \tilde{A}_α .

After solving the TDSE for N times (for N different initially excited Pheos) for the first MD

4 Methods

sample, the MD time t^{MD} is set to $t^{\text{MD}} = t^{\text{offset}}$. The expansion coefficients thus depend parametrically on t^{MD} , which is indicated in the definition $\tilde{A}_m(t; n, t^{\text{MD}})$ (cf. Eq. 3.59). The offset-time t^{offset} must not be larger than 200 fs, otherwise some MD data are not utilized for the computation. However, it is possible to choose $t^{\text{offset}} < \Delta t_{\text{sample}}$. The respective procedure will be called ‘nesting’ in this thesis, each part of the trajectory is then utilized several times to increase the convergence of the method. Whether nesting is required or not depends on the available MD data. If linear absorption for 80 ns of MD data is computed, nesting will not be necessary. If 10 ps of the MD simulation are utilized to compute the averaged expansion coefficients (for example, to compute a conformation dependent transition rate), nesting has to be used to achieve convergence. If not optical properties but populations are to be calculated from the solution of the TDSE, the sample length was set to $\Delta t_{\text{sample}} = 10$ ps. In this case, nesting is also necessary.

After solving the TDSE for all available MD data, the averaged expansion coefficients are written as

$$\tilde{A}_m^{av}(t; n) = \frac{1}{K} \sum_k^K \tilde{A}_m(t; n, kt^{\text{offset}}). \quad (4.15)$$

K counts, how often the TDSE was solved. The formula for the linear absorption in Eq. 3.73 includes the term $\langle d_{0m}(t) \tilde{A}_m(t; n) d_{n0} \rangle$. Since the scalar dipole moment $d_{0m}(t)$ changes only marginally in time, this term converges as fast as the averaged expansion coefficients (Eq. 4.15). After 50 fs, the dipole-dipole correlation function approaches zero. Thus, the choice of $\Delta t_{\text{sample}} = 200$ fs is justified for the computation of linear absorption (and also for the computation of EET rates).

4.5.2 Solving the TDSE including the electromagnetic field for P_4

The solution of the TDSE including the electromagnetic field directly requires the solution of the coupled Eqs. 3.121, 3.122 and 3.123. The procedure is exactly the same as for a singly excited P_4 complex. However, the MD sample time Δt_{sample} has to be long enough to include the pump and probe beam and some time (50 fs) before the maximum of the pump pulse (finite width of the pulses) and after the maximum of the probe pulse (200 fs, cf. Sec. 4.5.1). Thus, the sample length is computed as $\Delta t_{\text{sample}} = t_{\text{delay}} + 250$ fs with the delay time t_{delay} . The pump pulse arrives at $t = 50$ fs, and the full width half maximum value for both the pump and the probe beam is 12 fs. To achieve convergence for MD data of 80 ns, the offset-time is chosen as $t^{\text{offset}} = 100$ fs.

5 Pheo, P₄ and P₁₆: EET and optical properties

In this chapter, the results of the mixed quantum-classical calculations, utilizing the formulas explained in Chap. 3 and the methods of Chap. 4, are presented. In the first section, the results for the single Pheo in ethanol are shown. In the following sections, P₄ and P₁₆ are discussed.

5.1 The single Pheo molecule in ethanol solution

5.1.1 The energy gap function

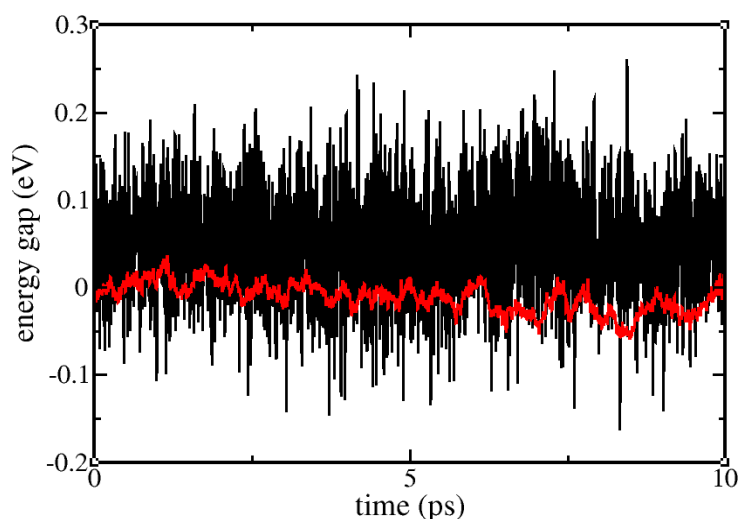


Figure 5.1: Energy gap fluctuation of a single Pheo in ethanol for a 10 ps MD sample. Black line: energy gap fluctuation due to intramolecular vibration $U_{eg}^{vib}(t)$ (Eq. 3.66). Red line: energy gap fluctuation due to solvent coupling $U_{eg}^{sol}(t)$ (Eq. 3.68). Published in [84].

The energy gap function is the key to the optical properties of the system, if the DCL is used to translate the full quantum formulas to their mixed quantum-classical representations (cf. Sec. 3.5). Fig. 5.1 shows the energy gap function for a 10 ps MD run and compares the intramolecular and intermolecular contributions. The intramolecular vibrational contribution dominates the contribution due to solvent coupling. Two statements concerning the energy gap fluctuation in Fig. 5.1 have to be made.

Firstly, compared to the energy gap function shown in Fig. 5.1, in the calculations in the group of Kleinekathöfer not the intramolecular but the intermolecular contribution to the energy gap function dominates [28]. Note that an intramolecular contribution denotes the vibrational contribution of a single Pheo, whereas the intermolecular contribution denotes the electrostatic coupling to the other Pheos, the dendrimer, and the solvent. In the group of Shi, who used the same method for the solvent coupling contribution (ZINDO) as the Kleinekathöfer group, the intramolecular vibration dominates (vibrational broadening is included parametrically utilizing Huang-Rhys factors [30]). On the other hand, the line shape for the Q_y absorption, which depends on the energy gap function fluctuation, has to be broadened in the calculations of Shi (as well as the B800/B850 absorption in [28]), while ZINDO calculations on Pheo in ethanol (Fig. 5.2) show a far too broad linewidth. The ZINDO energy gap function on Pheo was kindly

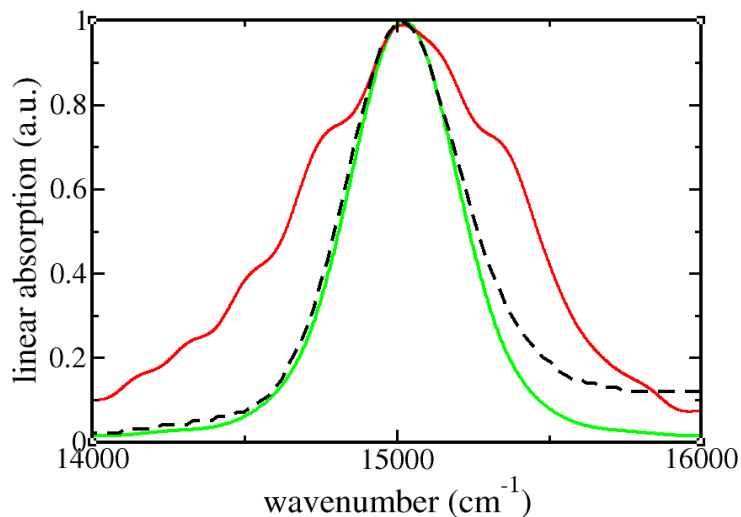


Figure 5.2: Linear absorption of the Q_y band of Pheo dissolved in ethanol. Black line: experimental result. Green line: linear absorption calculated as explained in Secs. 3.6 and 3.5 (the vibrational part of the energy gap function is calculated in harmonic approximation). Red curve: linear absorption result obtained from the energy gap function that was computed utilizing ZINDO (in the group of Kleinekathöfer).

provided by the group of Kleinekathöfer. It has to be mentioned here that only a short MD trajectory (100 ps) was calculated in order to test ZINDO with Pheo in ethanol, which is the only reason for the bad convergence of the lineshape in Fig. 5.2.

Secondly, there are several indications that the calculation of the energy gap fluctuation due to solvent coupling U_{eg}^{sol} is much more error-prone than the calculation of the intramolecular contribution. The classical force field does not include polarization effects directly. Even if screening is treated (cf. Sec. 7.3), polarization may have an influence on the partial charges themselves and therefore on the nuclei trajectories. The most error-prone part in the computation of U_{eg}^{sol} is the calculation of the difference between partial charges $\{q_{mi}^a - q_{mi}^s\}$, with a being either the first or second excited electronic state (the difference between partial charges is included in the formula for U_{eg}^{sol} , Eq. 3.68). The comparison of the partial charge data used by Zhu in [75, 82, 83, 87] (calculated with the B3LYP exchange-correlation potential and a 6-31G(d,p) basis set, without PCM) and the partial charge data calculated by Kulesza (B3LYP, 6-311**, PCM) shows a difference in the energy fluctuation amplitude of nearly 50 %. Such a large difference, dependent on slight changes of the basis set, reveals a large problem, rating the quality of the Δq_i values. The Δq_i may be normalized by respective measured values from Stark experiments [32]. Stark-hole burning experiments may yield the difference of the electrostatic dipole moments in the electronic ground and first excited state $\Delta d_{eg}^{\text{stat}}$. However, there exist Stark hole-burning experiments for chlorophyll a (optical properties are about the same as for Pheo), but the data for $f \times \Delta d_{eg}^{\text{stat}}$ differ by about 50% (from 0.5 D to 0.8 D) [151, 152], f being the local field correction factor that can not be measured directly. Assuming a Lorentzian local field correction ($f_{\text{Lorentz}} = (\epsilon(\omega_{eg}) + 2)/3$) [153], the measured $\Delta d_{eg}^{\text{stat}}$ values for chlorophyll a differ from 0.4 D to 0.6 D (the dielectric constant $\epsilon(\omega_{eg})$ for ethanol is 1.86, and ω_{eg} is the transition frequency). $\Delta d_{eg}^{\text{stat}}$ for Pheo in ethanol, calculated from the partial charges utilized in this thesis (DFT, B3LYP, 6-311**, PCM), is 0.5 D, indicating a good quality of the DFT calculations.

If the solvent coupling contribution to the energy gap function becomes important, a high level computation of the partial charges has to be carried out, to prevent large errors when the partial charge difference is computed.

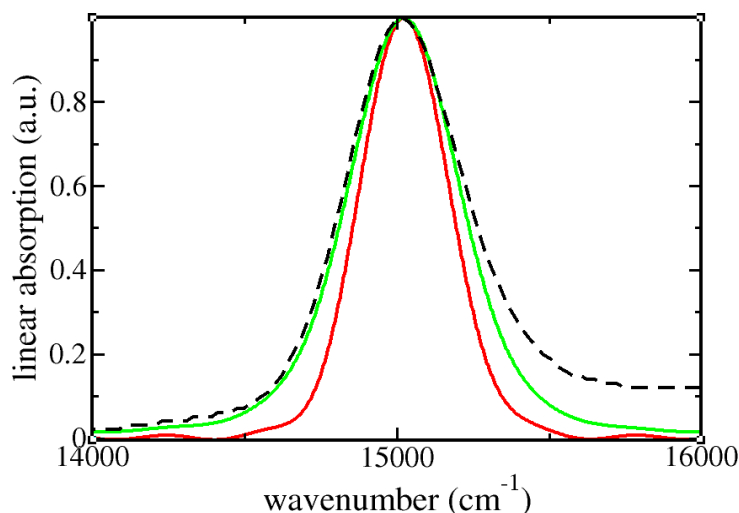


Figure 5.3: Linear Q_y band absorption of Pheo in ethanol. Black line: experimental absorption for Pheo in ethanol. Red line: linear absorption calculated without the intramolecular vibration. Green line: linear absorption result for the complete energy gap function. The peak maxima were fitted to the experimental result. 80 ns of MD simulation were utilized to achieve the ensemble average.

5.1.2 Linear absorption

Fig. 5.3 shows the result for the calculation of the linear absorption line shape function for the Q_y band absorption of a single Pheo in ethanol solution. The position of the maximum was taken as a parameter, while the linewidth itself was calculated without any free parameters. The perfect agreement with the experimental curve indicates the very good quality of the energy gap function calculation. The difference between calculated and measured curve at the high energy wing is due to a vibrational progression. The vibrational progression is included within the mixed quantum-classical calculation, but with a classical amplitude. This classical amplitude is a factor $1/f_{MN}(\omega_{\text{vib}}, T)$ smaller than the quantum mechanically calculated amplitude of the vibrational progression (cf. Sec. 3.6.2). It is important to mention that the factor $f_{MN}(\omega_{\text{vib}}, T)$ depends explicitly on the vibrational frequency ω_{vib} and on the temperature T (cf. Eq. 3.94 in Sec. 3.6.2). In Fig. 5.4, the absorption linewidths for the Q_y and the Q_x band are shown. This results were calculated utilizing 80 ns of MD simulation (8 times 10 ns started with the same initial conformation).

The solution of the TDSE from the MD data and the respective averaging of the expansion coefficients have been explained in Sec. 4.5. The averaged expansion coefficient can be interpreted as the respective S -operator matrix elements (cf. Sec. 3.6) and be inserted into the equation for the linear absorption cross section (Eq. 3.73).

When the mixed quantum-classical vibrational progression is to be adjusted by the correction factors $f_{MN}(\omega_{\text{vib}}, T)$, the single peaks have to be fitted to Gaussian functions. Inhomogeneous broadening dominates against homogeneous broadening, thus the line shapes can be approximated as Gaussian shaped. After the fitting, the contributions of the main peak and the satellites can be separated.

The upper panels in Fig. 5.4 show the results of the respective calculation with Eqs. 3.73 and 3.79 for a single Pheo in ethanol. The red lines show different Gaussian fits for the calculated absorption curves.

The Q_y and Q_x peaks are mainly Gaussian line shaped. Only the wings of the absorption curves have to be fitted with at least one additional Gaussian function to receive the mixed quantum-classically calculated result. When looking at the wings of the Q_x peak in the right upper panel of Fig. 5.4, on both sides of the main peak a vibrational progression is observable. This vibrational progression is also there for the Q_y peak in the left upper panel of Fig. 5.4, but

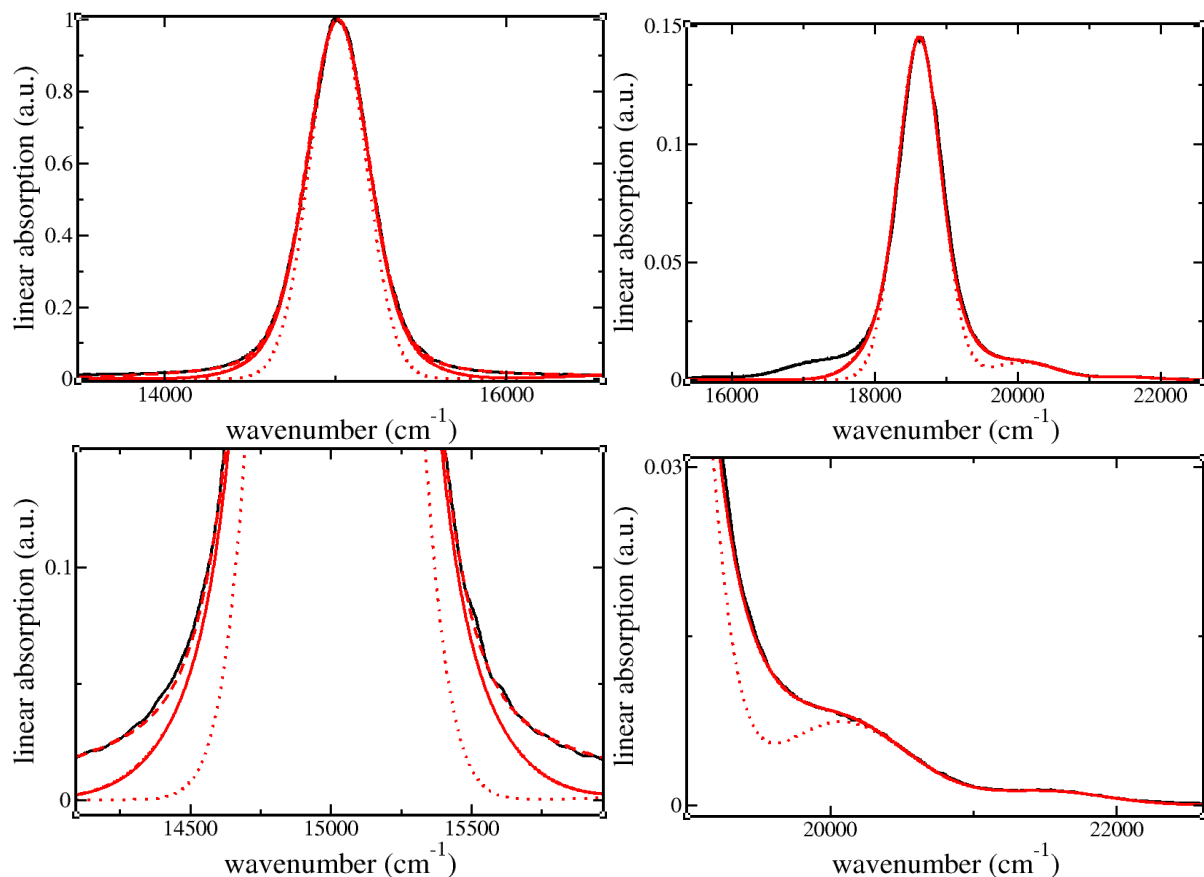


Figure 5.4: Linear absorption of Pheo in ethanol, computed from 80 ns of MD simulation. Left panels: Q_y band, right panels: Q_x band. The lower panels show the lower parts of the respective absorption band in detail. Red dotted line: single Gaussian fit for the lineshape. Red full line: fit containing two Gaussian functions for the main peak and one Gaussian function for each vibrational satellite. Red dashed line: fit containing four Gaussian functions for the main peak and one Gaussian function for each vibrational satellite (only for the Q_y band). The maximum of the main peaks was taken as parameter from [22].

it is much weaker.

In what follows, a very simplified picture is considered: if the vibrational progression is caused by a single vibronic coordinate that couples to the transition, this will result in a main peak with equidistant vibrational satellites on both sides of the main peak (cf. Sec. 3.6.2), with a distance in energy of $\hbar\omega_{\text{vib}}$. In this approximation a Gaussian shaped main peak will be accompanied by Gaussian shaped vibrational progression peaks that have the same linewidth. However, in the experimental and in the calculated spectra the distance between the peaks is not equidistant. Furthermore, the linewidths are not the same.

Vibrational progression

The fitting of the main and of the two vibrational peaks on the high energy wing (quantum mechanically calculated vibrational progression occurs on the high energy wing, cf. Eq. 3.84) with Gaussian functions enables to separate the single peaks and to quantify their respective amplitudes. The classically derived amplitude of the vibrational progression can then be corrected utilizing the factor f_{MN} derived in Sec. 3.6.2 (cf. [154]).

The vibrational progressions of the Q_x and the Q_y band in Fig. 5.4 and the respective fits can be observed in much more details in the two lower panels. It can be seen that the calculation result can be fitted properly with one Gaussian function for each satellite and two Gaussian functions for the Q_x main peak as well as with four Gaussian functions for the Q_y main peak. For the fitting of the Q_y main peak, more Gaussian functions are necessary, since the vibrational satellites have a much lower amplitude. If the amplitude of the vibrational peak is small, the contribution of the main peak at the frequency of the vibrational peak becomes of importance. Moreover, if the frequency is far away from the resonance energy (15015 cm^{-1} for the Q_y band), the single Gaussian fit approximates the respective part of the lineshape rather inadequately.

It has to be stated here that on the one hand, the fitting of the main peak with more Gaussian functions yields a better agreement with the calculated result. But on the other hand, for weak vibrational progression (as for the Q_y band), it is not clear which part of the total absorption cross section belongs to which peak (main peak or vibrational satellite).

In Fig. 5.5, the Gaussian fits shown in the Fig. 5.4 are utilized to calculate the Pheo (in ethanol) absorption spectrum in the optical range (except the Soret band). The positions of the main peaks were used as fit-parameters from the experiment [22]. The maximum of Q_y main band intensity was normalized to 1. The ratio between the Q_y band and the Q_x band intensity was computed from the oscillator strengths that were calculated with DFT (cf. Sec. 4.2). In order to correct the mixed quantum-classical vibrational progression, the vibrational satellites were increased by the frequency-dependent factor $f_{01}(\omega_{\text{vib}}, T)$ (cf. Sec. 3.6.2). This was done for all the four fitted vibrational peaks. The underlying assumption is that the two vibrational progression peaks of each band (Q_x and Q_y band) consist of a variety of vibrational modes coupling to the electronic transition, not only the two vibrational modes that correspond to the two visible vibrational satellites. Thus, the whole vibrational progression is given as a first order vibrational progression of all the vibrational modes that couple to the electronic transition. The respective result matches the experimentally measured absorption curve [22] quite well.

In Fig. 5.5, the dashed green line shows a spectrum which was computed by overestimating the vibrational satellites by a factor of 2. This was done to demonstrate that the linewidths of the first vibrational satellites have the same linewidths as the measured vibrational satellites. Those are broader than the Q_x and Q_y main peaks. This indicates that not only two, but a variety of vibrational modes couple to the electronic transitions. The two second vibrational satellites (the second satellite of the Q_y main peak and the one of the Q_x main peak) are both multiplied by the factor f_{01} , not by the factor f_{02} . Nevertheless, the second visible vibrational satellite for both of the electronic transitions is modelled quite well. This indicates that this second visible satellite in the experiment consists of two contributions. The first contribution is

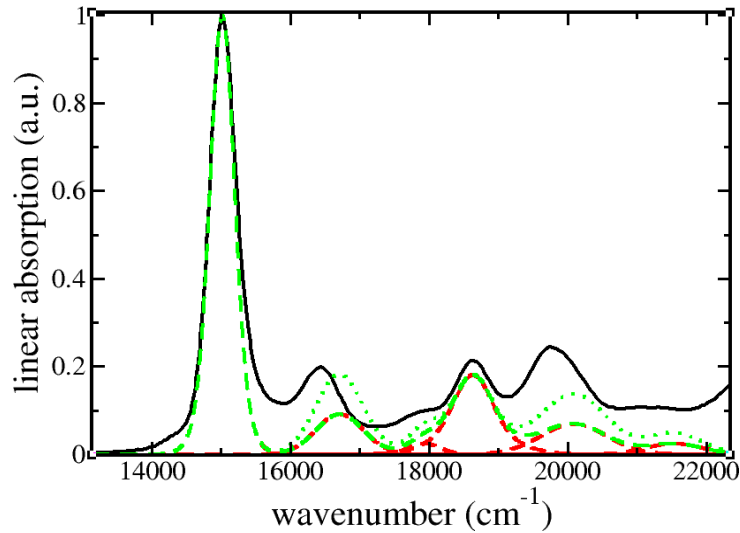


Figure 5.5: Linear absorption of Pheo in ethanol. The only parameters utilized for the calculated curves are the maxima of the two peak positions taken from [22]. Black line: experimental result. Red lines: single Gaussian fit functions from the calculated results including the Q_y band, the Q_x band, and all vibrational satellites (cf. Fig. 5.4). Dashed green line: sum over the red lines. Dotted green line: same result as dashed green line, but the vibrational satellites are multiplied with a factor of 2. This makes it possible to compare the linewidths of the first vibrational satellites which match the experimental result quite well.

due to a vibrational progression of hydrogen vibrational modes (the wave number is about 3000 cm^{-1}) and the second contribution is due to a second order vibrational progression of carbon and nitrogen vibrational modes. This, however, can not be determined conclusively within this work, since the contributions of the first and the second order vibrational progressions can not be separated.

Finally, the high energy wing of the Q_y band is to be discussed. Fig. 5.3 shows that the computed lineshape matches the measured lineshape, aside from the high energy wing of the peak. Considering the results of this section, it seems to be clear that low frequency vibrational modes as well couple to the electronic transition. The vibrational progression due to this low frequency modes thus affects the main peak itself. This low frequency vibrational progression can not be separated from the main peak. Thus, it can not be amplified by a factor $f_{01}(\omega_{\text{vib}}, T)$ in order to correct the mixed quantum-classical vibrational progression.

5.2 The P_4 dendrimer

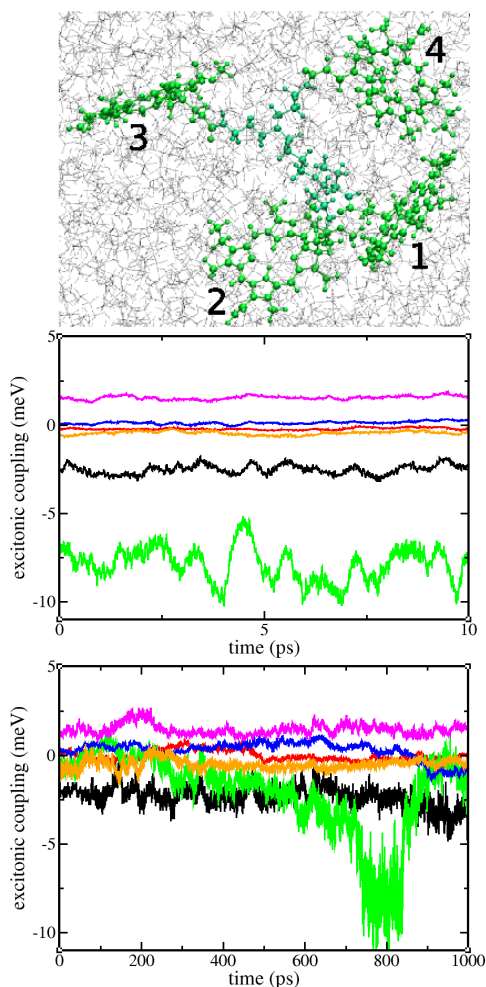


Figure 5.6: P_4 in ethanol conformation and excitonic couplings. Upper panel: P_4 conformation of run 6, after 790 ps. Middle panel: 10 ps MD trajectory starting with the conformation of the upper panel. Black: excitonic coupling between Pheos 1 - 2, red: 1 - 3, green: 1 - 4, blue: 2 - 3, magenta: 2 - 4, orange: 3 - 4. Lower panel: excitonic coupling for the first nanosecond of the MD trajectory (run 1), same color code as for the middle panel.

The conformations shown in Figs. 5.6 and 5.7 represent only a very small part of a large amount of possible P_4 conformations. It will be shown in this section that the optical properties of P_4 are highly affected by the very different conformations that emerge during the trajectories.

Fig. 5.8 shows not only the excitonic coupling between the four Pheos, but also the energy gap function due to intramolecular vibration and solvent coupling for the conformation shown in the left upper panel of Fig. 5.7. The solvent coupling also includes the coupling to the dendrimer structure. Fig. 5.8 demonstrates that the fluctuation of the energy gap function due to intramolecular vibration dominates the total energy fluctuation. The energy values of the excitonic couplings are rather small. For some special conformations, values about 30 meV are possible, but for the most parts of the simulation data it is between -10 and 10 meV (compare

The EET within P_4 and the optical properties of P_4 depend on the very different possible P_4 conformations, which account for a large number of different sets of excitonic couplings between the single Pheos that are bound to the dendrimer.

Figs. 5.6 and 5.7 show P_4 conformations from different MD runs. 8 runs (all of them 10 ns long) were carried out, starting from the same initial conformation (shown in Fig. 2.3). The time scale of the conformational change in the P_4 system at 300 K is about 50 ps. Thus, starting the 8 different MD runs from the same initial conformation is not expected to affect the quality of the ensemble average dramatically. The chosen initial conformation was an unfolded one to increase the accessible conformational space within a preferably short simulation time.

At this point, a comment concerning the phrase ‘ensemble average’ has to be made. By the means of this thesis, the ‘quality of the ensemble average’ implies, how well the accessible MD data reproduce the ensemble average that occurs in a respective experiment.

The conformations shown in Figs. 5.6 and 5.7 indicate the flexibility of the P_4 dendrimer. Beside the P_4 conformations, the respective excitonic coupling between the single Pheos is shown. While each of the middle panels shows the excitonic coupling between the four chromophores within a simulation time of 10 ps (on this time scale, the P_4 conformation can be assumed to remain stable), the lower panels show the excitonic coupling for the simulation time of one complete nanosecond. While the excitonic couplings in the middle panels of Figs. 5.6 and 5.7 are relatively stable, the excitonic coupling between Pheos 1 and 4 on the lower panels of Fig. 5.7 is fluctuating on a picosecond time scale, with an amplitude of several meV.

with the middle panels of Figs. 5.6 and 5.7), and the averaged absolute value of the excitonic coupling is below 2 meV.

5.2.1 Linear absorption

The linear absorption of the Q_y band of P₄ in ethanol was calculated from Eq. 3.73. The result is shown in Fig. 5.9 and compared to the single Pheo absorption. The maxima of the absorption curves are parameters taken from the Pheo in ethanol linear absorption experiment. Taking the P₄ in ethanol peak position as parameter for the respective curve would not help comparing the line shapes for Pheo and P₄ absorption. However, the linear absorptions of Pheo and P₄ differ basically due to the excitonic coupling in P₄, which is of no importance in a dilute solution of Pheo in ethanol. The coupling of the Pheo molecules to the dendrimer in P₄ gives no significant broadening effect compared to the coupling of a single Pheo to its ethanol solvation shell. This was proven by calculating the linear absorption without excitonic coupling between the Pheos. The resulting absorption linewidths for P₄ and for Pheo in ethanol are exactly the same.

The broadening of the P₄ absorption linewidth is due to the excitonic coupling between the Pheos. However, this broadening is rather weak. It can be explained as follows: in a simple model of two two-level systems with the same energy levels and thus the same excitation energy $\Delta E = E_1 - E_0$ and coupled by the excitonic coupling J , two excitonic energy levels are formed [26]. They have the energies $E_{\text{exc}}^{(1)} = \Delta E + J$ and $E_{\text{exc}}^{(2)} = \Delta E - J$. In P₄ four instead of two Pheos are coupled. The maximum energy splitting, if more than two chromophores are involved, may be larger than $2J$ (for a linear chain of molecules with next neighbor interaction it is $4J$ [26]). There exist innumerable P₄ conformations and thus countless combinations of the mutual excitonic couplings between the Pheos in P₄. In the experiment, not the linear absorption line shape of a single P₄ conformation but a line shape averaged with respect to all possible P₄ conformations is measured. Thus, during the P₄ MD simulations an acceptable ensemble average with respect to all possible P₄ conformations has to be achieved.

The measured spectrum of Pheo and P₄ was shown in Fig. 2.5. A direct comparison with the calculated data is not shown. The experimentally measured linewidths are broader than the calculated ones. The first idea was that there could exist dimer formations within the P_N complexes with a much enhanced excitonic coupling that does not occur in the previous simulations. Artificial dimer and Pheo stack formations were created that were more or less stable within a nanosecond of MD simulation. However, the calculated linear absorption for P₄ molecules that included dimer conformations was in general not much broader than the linear absorption calculated for P₄.

The broadening in the P₄ and P₁₆ linear absorption measurements compared to the linear absorption of Pheo was more than 200 cm⁻¹. In principle, such a broadening may occur due to an excitonic coupling. The maximum exciton splitting in a system with multiple two-level-systems, excitonically coupling with J , is here approximated as $4J$ (this is the maximum energy splitting for the linear chain [26]). For an average excitonic coupling of 10 meV (such a value is possible for Pheo dimers with parallel transition dipole moments), the broadening can be approximated as 322 cm⁻¹. However, the averaged coupling that was calculated from the MD simulations was about 1-2 meV, resulting in a maximum broadening of 32-64 cm⁻¹. This corresponds to the result shown in Fig. 5.9.

It is possible that the measured samples of P₄ and P₁₆ in ethanol included unknown contributions (Pheo may have reacted during the synthesis). Another hint is the linear absorption measurement for pyropheophorbide *a* (Pyropheo) molecular systems in [155]. The linear absorption lineshapes for the different system sizes (one, two and six Pyropheos bound) do not vary as dramatically as in [22]. Besides, in [36], a linear absorption of Pheo dimers was measured that featured a smaller linewidth than the P₂ linear absorption in [22].

This may also be the reason for the absorption shift of P₄ to smaller energies in comparison

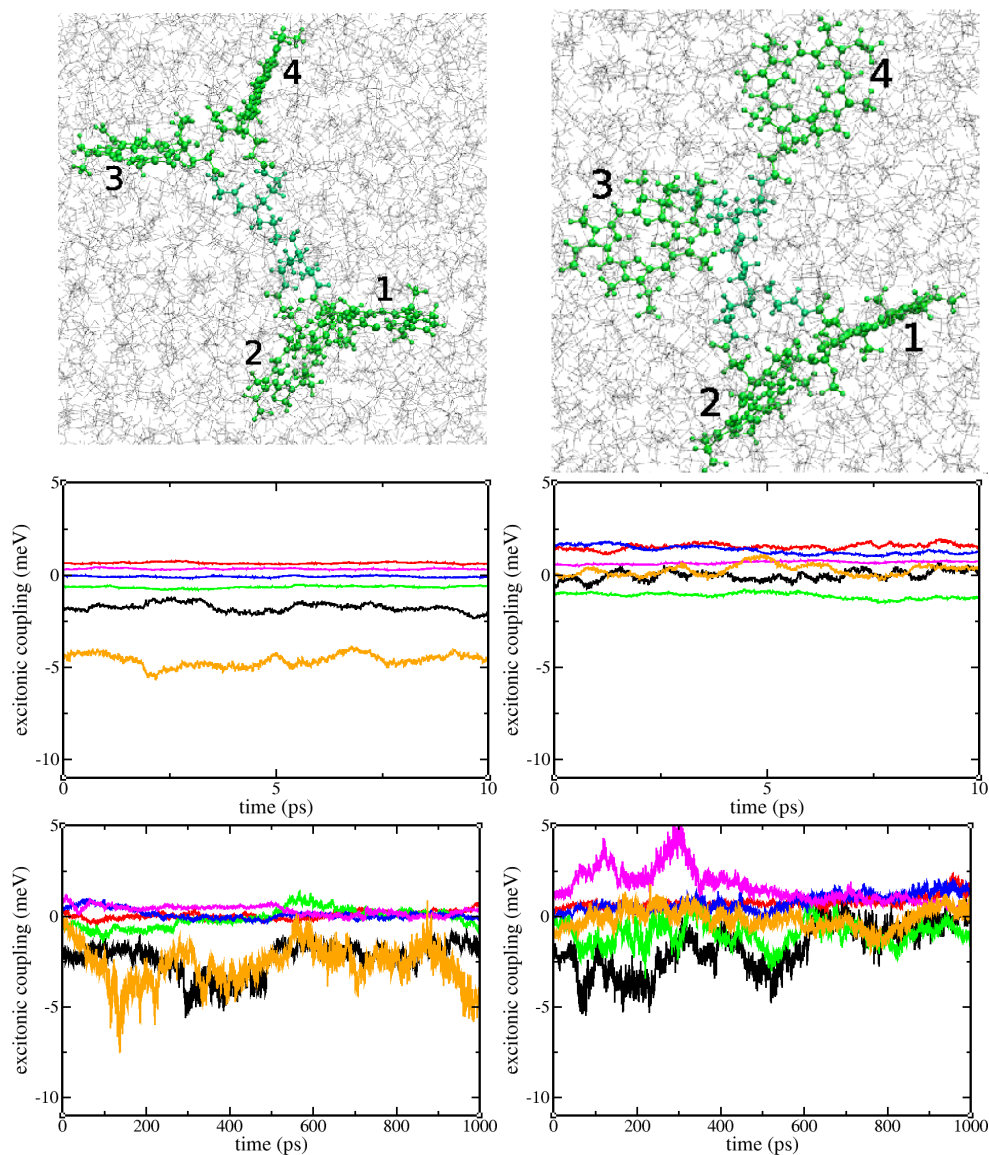


Figure 5.7: P_4 in ethanol conformations and excitonic couplings. Left panels: MD run 1, after 990 ps, right panels: MD run 4, after 990 ps. Upper panels: P_4 conformations. Middle panels: 10 ps MD trajectory starting with the conformation of the upper panels. Black: excitonic coupling between Pheos 1 - 2, red: 1 - 3, green: 1 - 4, blue: 2 - 3, magenta: 2 - 4, orange: 3 - 4. Lower panels: excitonic coupling for the first nanosecond of the MD trajectory (run 1), same color code as for the middle panel.

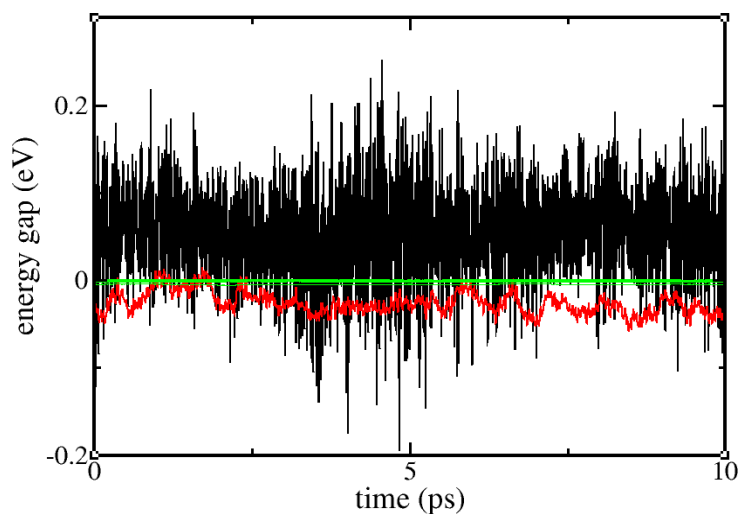


Figure 5.8: Intramolecular vibrational energy gap (black), the solvent coupling energy gap (red) and the excitonic couplings (all in green) for a 10 ps MD trajectory of P_4 in ethanol. The black and the red line show the result for Pheo 1 (cf. Fig. 2.3). Run 1, beginning after 990 ps.

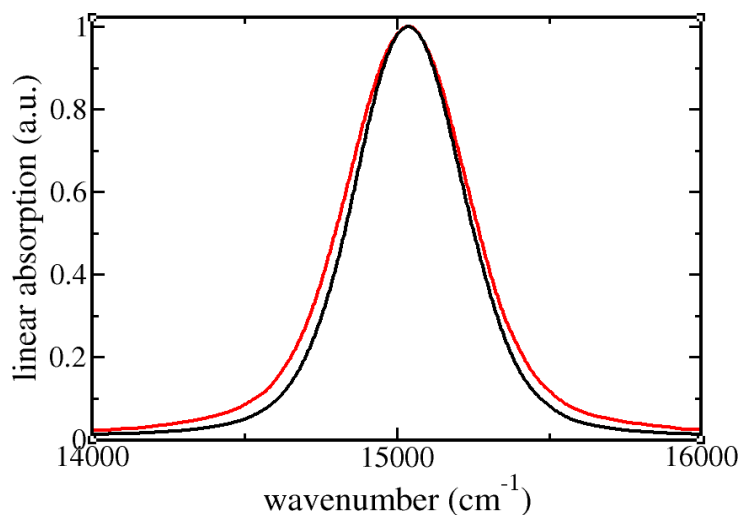


Figure 5.9: Linear absorption for P_4 (red) and Pheo (black) in ethanol, both calculated from 8 times 10 ns of MD simulation. Peak maxima were shifted to 15015 cm^{-1} (Pheo in ethanol experimental value).

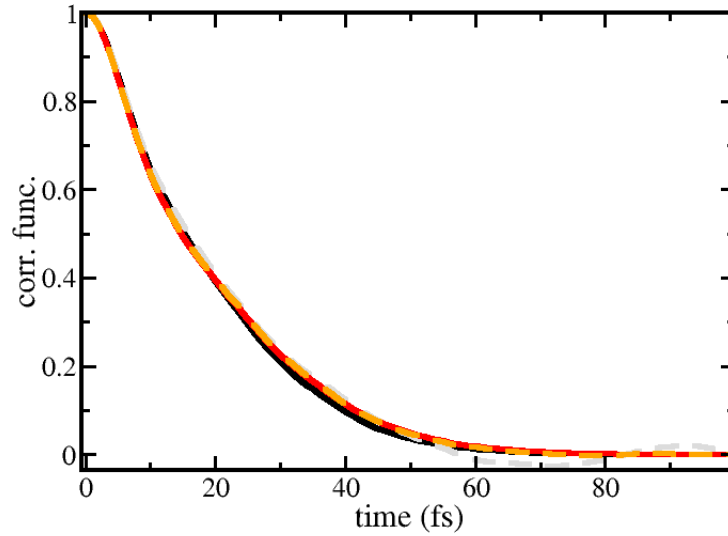


Figure 5.10: Correlation function for the EET between chromophores 1 – 2. Full lines: Eq. 3.112 was utilized, dashed lines: Eq. 3.111 was utilized. Black line and grey dashed line: the result was calculated from 8 times 100 ps of MD data. Red line and orange dashed line: the result was calculated from 8 times 1 ns. Both approximations finally yield the same result, though it is shown that Eq. 3.112 converges faster.

to the Pheo absorption. The excitonic coupling shifts the P_4 peak slightly to higher energies in the calculations (this is not shown in Fig. 5.9, as the peak position was taken as a parameter from the Pheo absorption). The respective peak shift from the solvent coupling, that is not the same for Pheo and P_4 , converges very bad. Thus, the result from the available MD data is ambiguous. In any case, a shift as shown in the measured curve can be ruled out.

5.2.2 EET rates

In the following subsection, the results for the EET rate calculations are presented. Utilizing Eq. 3.109 (derived and explained in Sec. 3.7), the EET rate between two Pheos m and n within the P_4 CC may be computed. The formula for the EET rate $k_{m \rightarrow n}$ in Eq. 3.109 includes the square of the excitonic coupling J_{mn} between the two chromophores and the correlation function $C_{m \rightarrow n}(t)$. This correlation function can be approximated either by Eq. 3.111 or by Eq. 3.112.

Before discussing the results for the EET rates, the two approximations for $C_{m \rightarrow n}(t)$, $C_{m \rightarrow n}^{\text{app}1}(t)$ and $C_{m \rightarrow n}^{\text{app}2}(t)$, are discussed. The first important result is that both approximations give the same result, if the correlation function is converged. The convergence is much faster for Eq. 3.112. In Fig. 5.10, the result for the averaged correlation function (between the Pheo pair 1,2) is shown for two different simulation times for each of the two approximations ($\langle C_{m \rightarrow n}^{\text{app}1}(t) \rangle_{\text{ther}}$ and $\langle C_{m \rightarrow n}^{\text{app}2}(t) \rangle_{\text{ther}}$). After altogether 8 ns of simulations both methods give the same result. After 800 ps of MD simulation Eq. 3.111 did not finally converge. Nevertheless, the difference to the result of Eq. 3.112 is not dramatical. The results have been computed utilizing a sample length $\Delta t_{\text{sample}} = 200$ fs and an offset time $t^{\text{offset}} = 200$ fs. That means that every MD snapshot is used once in the transfer rate calculation. More details are given in Sec. 4.5. Decreasing the offset-time t^{offset} would make sure that both the Eqs. 3.111 and 3.112 converge faster.

Fig. 5.11 shows the averaged correlation function, calculated via Eq. 3.112 for the Pheo pairs m, n . It can be seen in Fig. 2.3 (which shows the P_4 structure) that the Pheo pair 1,2 has a shorter connection (shorter dendrimer chain between the Pheos) than the pairs 1,3 or 1,4, respectively. The same holds for the Pheo pair 3,4 in comparison with the pairs 3,1 and 3,2. Still, that does not mean that at any P_4 conformation the Pheo pair 1,2 is spatially closer than the Pheo pairs 1,3 or 1,4. But in average, this statement is true.

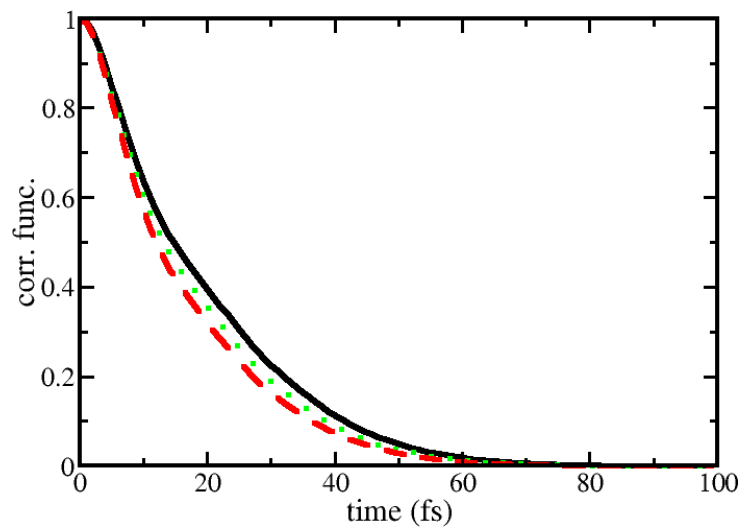


Figure 5.11: Correlation functions calculated utilizing Eq. 3.112 and 8 times 1 ns of MD data. Black line: chromophores 1 – 2, red dashed line: 3 - 4, green dotted line: other pairs (not distinguishable). The figure is from [39].

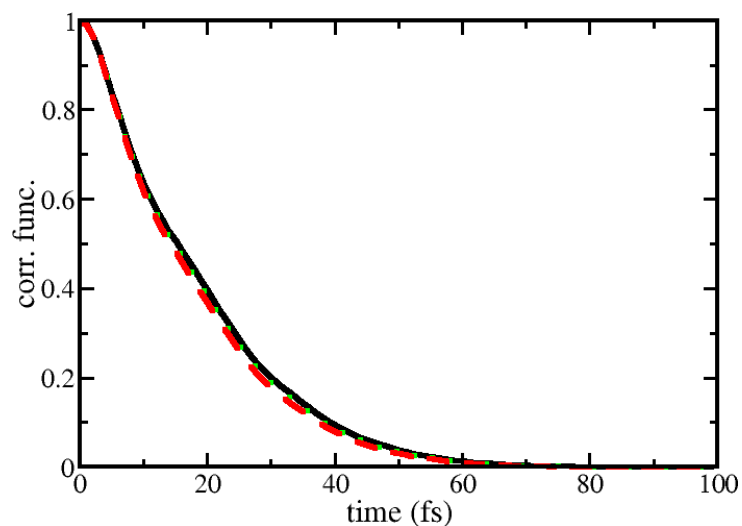


Figure 5.12: Correlation functions calculated utilizing Eq. 3.112 and 8 times 10 ns of MD data. Black line: chromophores 1 – 2, red dashed line: 3 - 4, green dotted line: all others (not distinguishable).

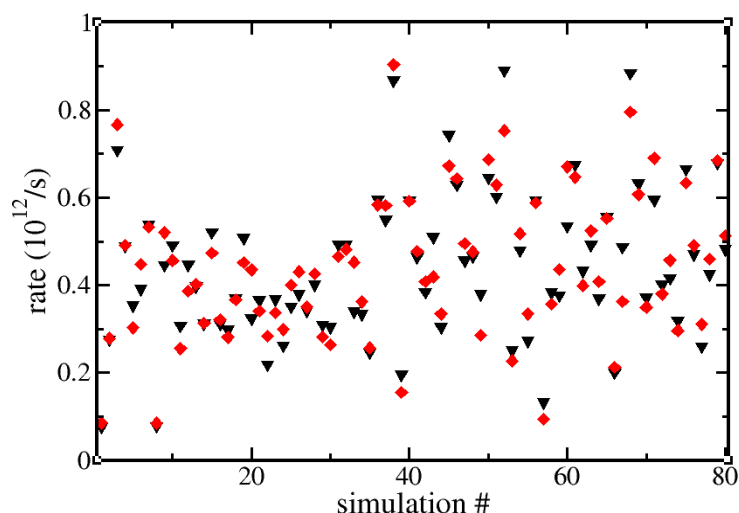


Figure 5.13: EET rates calculated from 80 times 50 ps of MD simulations with the same initial P_4 conformation. Shown is the rate between chromophore 1 and chromophore 2. Black: calculated via Eq. 3.112, red: calculated via Eq. 3.111. Both differ only weakly. It is shown that even if the initial P_4 conformation is the same, the results for the transfer rate between two chromophores calculated from different runs vary greatly.

In Fig. 5.11 the correlation for the Pheo pairs 1,2 as well as 3,4 are shown in different colors. The correlation functions between the four other pairs of Pheo are drawn in the same color since they are nearly indistinguishable. Fig. 5.11 indicates that there is some dependency of the correlation function on the Pheo pair. However, the result in Fig. 5.12 shows that this is not the case. The figure shows in principle the same result as Fig. 5.11, but the achieved ensemble average for Fig. 5.12 is much better. For this calculation of Fig. 5.12 the whole data of eight times 10 ns were utilized. The correlation functions of all the different Pheo pairs have the same shape. The reason for the slight but significant difference in Fig. 5.11 is the fact that the ensemble average of the P_4 system was not reached after 8 times 1 ns of MD simulation.

Utilizing the whole data of MD simulations (eight times 10 ns) and applying formula 3.109 together with Eq. 3.111, the ensemble-averaged transfer rates $\langle k_{mn} \rangle_{\text{ther}}$ were calculated. Ensemble-averaged means that the whole available MD data including all the different P_4 conformations are utilized to compute $\langle k_{mn} \rangle_{\text{ther}}$. The ensemble-averaged EET rates have values between $10^{11}/s$ and $4 \times 10^{11}/s$.

Dependence of the transfer rate on the correlation function approximation compared to its dependence on the conformational change

Before further discussing the transfer rate, some additional results will be presented that may help to give some further insight on how the calculated rates depend on the conformation and on the approximation for the correlation function (Eq. 3.111 or 3.112). Beside the 80 ns of MD simulation data, for P_4 80 additional MD runs, each run starting with the same initial conformation were executed. The atom trajectories between $t = 10$ ps and $t = 50$ ps were utilized to compute the respective rates utilizing Eq. 3.109 for the transfer rate, with both Eqs. 3.111 and 3.112 for the correlation functions. The result is shown in Fig. 5.13. The results for Eqs. 3.111 and 3.112 are nearly similar. Since the convergence of Eq. 3.111 is much better, this approximation can be utilized to compute rates for even shorter MD time slices (such as 10 ps, which will be utilized later). Furthermore, it is obvious that the EET rates differ greatly for the particular simulations. This indicates that within the 50 ps of simulation the P_4 conformation must have changed. The EET rate depends on the distance X_{mn} between the centers of Pheos m and n with $k_{mn} \propto 1/X_{mn}^6$ (compare with Sec. 3.7). This dependence results in the fact that even small

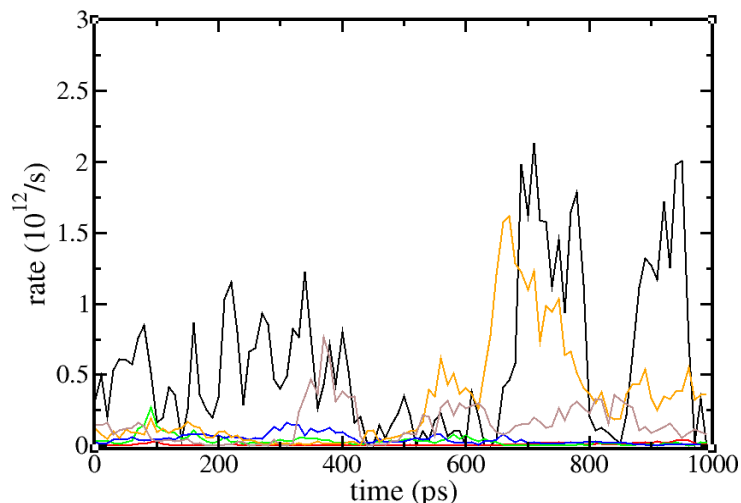


Figure 5.14: EET within P_4 . The EET rates calculated for 1 ns of simulation are drawn, each point represents 10 ps of simulation utilized to calculate the rate. Shown are the rates between black: chromophore 1 - chromophore 2, red: 1 - 3, green: 1 - 4, blue: 2 - 3, magenta: 2 - 4, orange: 3 - 4.

conformational changes can result in dramatical changes of the rates.

Conformation dependent transfer rates

Henceforward, the transfer rates computed from the 8 times 10 ns of simulation will be discussed. The rates, calculated with Eq. 3.109 from the whole MD data, represent ensemble-averaged rates. Those ensemble-averaged rates are averaged rates computed for a lot of different P_4 conformations. The foregoing discussion indicates that EET rates can be calculated utilizing Eq. 3.109 for the rate and Eq. 3.112 for the correlation function even for short MD slices of 10 ps. Within such a short time slice the P_4 molecule has a more or less stable conformation. Thus, the transfer rates calculated for short parts of the MD trajectory during which the conformation is stable will be referred to as conformation dependent rates. Fig. 5.14 shows the conformation dependent rates for the first ns of MD run 1.

The rates for the several 10 ps MD pieces were calculated for the first nanosecond of (each of) the eight MD runs. The conformation dependent rates of the whole MD data of 80 ns were printed to a histogram shown in Fig. 5.15. The figure does not only show the rate histogram for the six different chromophore pairs but also the average over this six histograms. The logarithmic scale denotes that the occurring transfer rates between the Pheo of P_4 molecules vary by six to seven orders of magnitude.

Solving the rate equation utilizing the ensemble-averaged transfer rate

The DCL formula for the rate, Eq. 3.109 together with the correlation function from Eq. 3.112, gives the transfer rates $k_{m \rightarrow n}^{\text{DCL}}$ in second order to the excitonic coupling J_{mn} between two chromophores m and n . It is necessary to compare the respective results with the solution of the TDSE, in order to confirm the quality of the calculated EET rates. The populations calculated from the solution of the TDSE for a single 10 ps MD sample oscillate due to the excitonic coupling between all Pheos. This was shown in [83]. In the ensemble average (average over the complete MD data), dephasing occurs and the populations reveal the time-dependence of the EET as can be seen in Fig. 5.16 (cf. [39]).

However, in order to compare the populations computed from the solution of the TDSE with the populations resulting from the calculated EET rates, one may use the rates $\langle k_{mn} \rangle_{\text{ther}}$ to solve

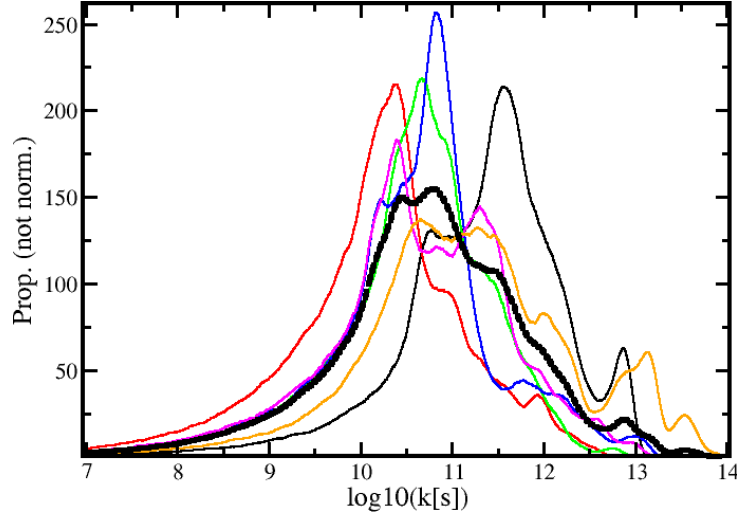


Figure 5.15: EET within P_4 . A histogram over the EET rates between all chromophores for MD data of 8 times 10 ns. Black: chromophore 1 - chromophore 2, red: 1 - 3, green: 1 - 4, blue: 2 - 3, magenta: 2 - 4, orange: 3 - 4. The thick line shows an average over all rates.

the respective rate equation for the populations $P_m(t)$

$$\frac{\partial}{\partial t} P_m^{(k)}(t; l) = - \sum_{n \neq m} (\langle k_{mn} \rangle_{\text{ther}} P_m(t; l) - \langle k_{nm} \rangle_{\text{ther}} P_n(t; l)), \quad (5.1)$$

with the four different initial conditions $P_m(0; l) = \delta_{m,l}$. The index l indicates that chromophore l was excited at $t = 0$. The results for the 8 times 1 ns are given in Fig. 5.16. Comparing the populations of the primary excited chromophores in Fig. 5.16 makes clear that the ensemble average achieved during the MD simulations is acceptable, but not perfect. One has to expect from the symmetry of the P_4 molecule that the distribution of the conformation dependent transfer rates k_{12} and k_{34} , k_{13} and k_{24} , as well as k_{14} and k_{23} , are the same, when the ensemble average is achieved. Thus, the resulting time-dependent populations $P_m(t; m)$ calculated from Eq. 5.1 are to be the same for every initial excited Pheo m .

The populations derived from the rate equation Eq. 5.1 have to be compared with the result of the TDSE for the A_m

$$\frac{\partial}{\partial t} A_m(t; l) = - \sum_n \mathcal{H}_{mn}(R) A_n(t; l). \quad (5.2)$$

Therefore, the complete MD data were sliced into $N^{\text{slices}} = 8000$ parts of 10 ps length. The TDSE was then solved for each part i , with the initial conditions equivalent to those for the rate equations $A_m^i(0; l) = \delta_{m,l}$, where again l indicates the chromophore that was excited at $t = 0$. Finally, the populations were averaged:

$$P_m(t; l)_{\text{TDSE}} = \frac{1}{N^{\text{slices}}} \sum_i^{N^{\text{slices}}} |A_m^i(t; l)|^2. \quad (5.3)$$

Fig. 5.16 compares the result of the TDSE $P_m(t; 1)_{\text{TDSE}}$ with the solution of the rate equations $P_m(t; 1)_{\langle k \rangle}$ for the averaged rates $\langle k_{mn} \rangle_{\text{ther}}$. The result of the solution of the TDSE gives a slower decay than the solution of the rate equations (Eq. 5.1) for the averaged rates $\langle k_{mn} \rangle_{\text{ther}}$. This, however, is not surprising, since the rate equation was solved for the MD averaged rates $\langle k_{mn} \rangle_{\text{ther}}$. The first panels in Figs. 5.6 and 5.7 indicated the variety of P_4 conformations within the ensemble average. The highly flexible structure of P_4 that changes on a 50-100 ps time scale (compare with Fig. 5.14) results in a variety of transition rates depending on the P_4 confor-

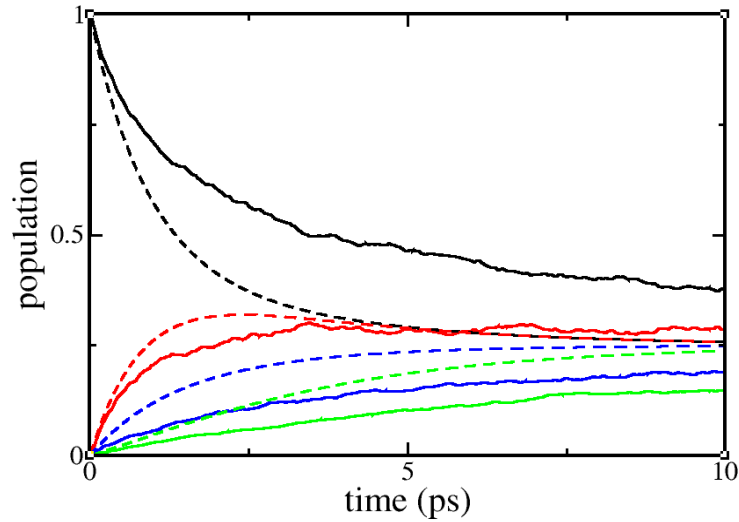


Figure 5.16: EET within P_4 . Dashed lines: solution of the rate equations, utilizing the mean rates calculated from 8 times 1 ns of MD data. The rate equations were solved four times, each with the initial condition that chromophore 1 is excited at $t=0$. Solid lines: averaged populations, calculated from the TDSE, solved with the equivalent initial condition ($\tilde{A}_m(t=0,1) = \delta_{m,1}$). With respect to Fig. 2.3 the color code is black: Pheo 1 (initially excited), red: Pheo 2, green: Pheo 3, blue: Pheo 4.

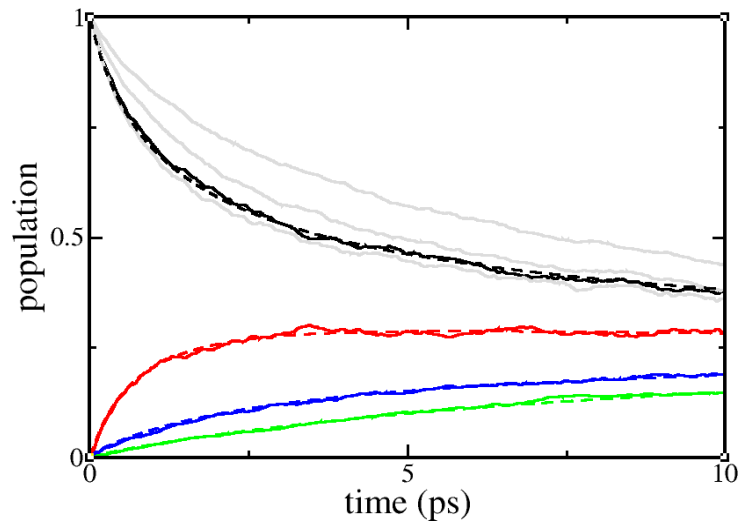


Figure 5.17: EET within P_4 . Dashed lines: solution of the rate equations, utilizing the rates calculated from each 10 ps MD piece of overall 8 ns MD of data (eight times 1 ns). For each 10 ps MD piece the rate equations were solved with the initial condition that chromophore 1 is excited at $t=0$. Finally, the populations were averaged. Solid lines: averaged populations, calculated from the TDSE, solved with the equivalent initial condition ($\tilde{A}_m(t=0,1) = \delta_{m,1}$). Color code as in Fig. 5.16. For comparison, the population curves for the initially excited chromophores 2, 3 and 4 are drawn in grey ($\tilde{A}_m(t=0,n) = \delta_{m,n}, n > 1$).

mation. Thus, the energy transfer dynamics of the system can not be described by averaged rates.

Solving the rate equation for the conformation dependent rates

The dynamics have to be described by the conformation dependent rates k_{mn}^i . The k_{mn}^i were calculated for different conformations i . Like for the solution of the TDSE, the MD data for the eight times 1 ns were sliced into 8000 parts of 10 ps length, since the conformations of P_4 are nearly stable on this time scale and the approximated correlation function in Eq. 3.112 is converged after 10 ps. For each time slice i the respective rates k_{mn}^i were calculated. For each set of k_{mn}^i the respective rate equation

$$\frac{\partial}{\partial t} P_m^i(t;l) = - \sum_{n \neq m} \left(k_{mn}^i P_m^i(t;l) - k_{nm}^i P_n^i(t;l) \right) \quad (5.4)$$

was solved, again with the initial conditions $P_m^i(0;l) = \delta_{m,l}$. Finally, the averaged populations $P_m^{\{k_i\}}(t;l)$ (compare with the populations $P_m^{\langle k \rangle}(t;l)$ that were calculated for the averaged rates $\langle k_{m \rightarrow n} \rangle$) were obtained:

$$P_m^{\{k_i\}}(t;l) = \frac{1}{N} \sum_i P_m^i(t;l). \quad (5.5)$$

Fig. 5.17 shows the result for the $P_m^{\{k_i\}}(t;1)$ and compares it with $P_m^{\text{TDSE}}(t;1)$. The figure shows a perfect agreement of both the rate equation and the TDSE solutions, which allows the following two conclusions. First, the calculation of the rates in second order to the coupling is a very good approximation. The dynamics resulting from the rate description are the same as for the dynamics resulting from solving the TDSE. The solution of the TDSE in turn treats all orders of the excitonic coupling between the single Pheos. Second, the EET dynamics depend on the contribution of every P_4 conformation. The attempt to describe the EET dynamics with averaged rates $P_m(t;1)_{\langle k \rangle}$ fails, which can be seen clearly in Fig. 5.16. When comparing the populations of the different initially excited Pheos in 5.17, four different curves can be seen. Due to the symmetry of the P_4 system one would expect four similar curves, when ensemble average is reached. This is due to the fact that the EET dynamics within P_4 should be the same, regardless of which Pheo was initially excited. This is obviously not the case after 1 ns of simulation for each of the 8 MD runs.

In Fig. 5.18, the populations calculated from the solution of the TDSE for the whole data of MD simulation (80 ns) are shown. The respective result for the rate equations is not printed in Fig. 5.18, the respective curves match the populations calculated from the solution of the TDSE perfectly. In comparison with Fig. 5.17 one may see that the achieved ensemble average is much better in Fig. 5.18. While the blue and red curves show the populations of the Pheos that are neighbors of the Pheo excited at $t = 0$, the green curve shows the population of the Pheo molecule that is the diagonal counterpart to the primarily excited Pheo. What is meant with a 'diagonal counterpart' can be seen in Fig. 2.3. The Pheo pairs 1,2 and 2,3 and 3,4 as well as 4,1 are directly neighboring, while the pairs 1,3 and 2,4 are the respective diagonal counterparts. It can be seen from Fig. 5.18 that the ensemble average describes the population transfer to next neighbors (Pheo pairs 1,2 and 2,3 and 3,4 as well as 4,1) very well. On the other hand, the population transfer between the two Pheo pairs 1,3 and 2,4, respectively (indicated by the green lines), does not fully agree for the available MD data. The population transfer between the Pheo molecules 1,3 (2,4) will additionally depend on the respective conformations of the Pheos 2,4 (1,3) that may serve as bridge molecules in the EET between the Pheo molecules 1,3 (2,4). The population transfer between the Pheos 1,3 will be the same as the population transfer between the Pheos 2,4, if the ensemble average is achieved for the whole conformation of P_4 . However, the ensemble average is good enough to make a clear statement concerning

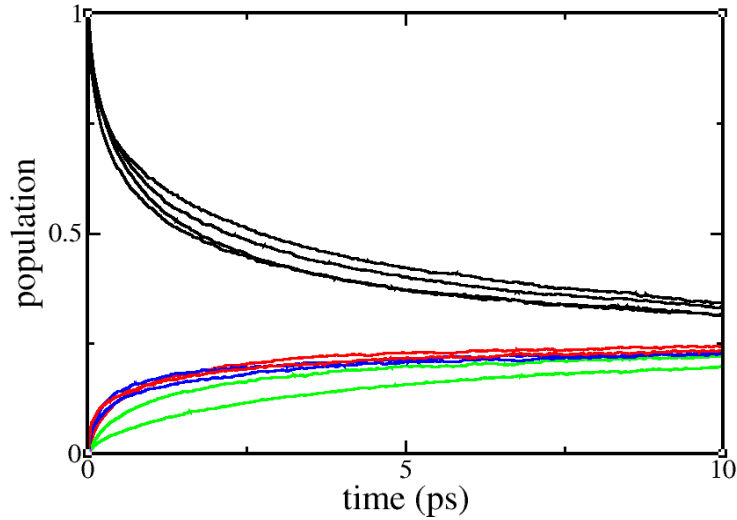


Figure 5.18: EET within P_4 . Averaged populations calculated from the TDSE, solved with the initial condition $\tilde{A}_m(t = 0, n) = \delta_{m,n}$. The populations of the initially excited Pheos are drawn in black. The populations of the other Pheos are drawn in red, green and blue. The green curves represent the populations of the diagonal counterparts to the initially excited Pheos. The achieved ensemble average is much better than after 8 times 1 ns of MD simulation.

the time scale of EET. The time when the population of the initially excited Pheo reaches a value of $1/N + (1 - 1/N)/e$ (represents a decrease to $1/e$ if N goes to infinity) is about 2 to 3 ps.

5.2.3 Differential transient absorption

To calculate the transient absorption from polarization in probe pulse direction, Eq. 3.135 was utilized. The polarization in probe pulse direction was calculated from the time-dependent total polarization via Eq. 3.133 (Eq. 3.134 was only utilized for the curve in Fig. 5.22). The time-dependent total polarization was calculated utilizing Eqs. 3.128 and 3.127. The TDSE was solved and the respective expansion coefficients were utilized to compute the time-dependent polarization. It was explained in Sec. 4.5 how the TDSE was solved directly including the electromagnetic field.

Fig. 5.19 shows the envelopes of the Gaussian-like pump and probe beam, as it was utilized in the calculations of the transient absorption. In the calculations done for this thesis, the field strength of the pump pulse was 2×10^8 V/m, the field strength of the pump pulse 5×10^6 V/m. 2×10^8 V/m is a very strong laser pulse, however, the intensity of the pump pulse was chosen to excite about 10 % of the P_4 molecules. The high percentage of pump pulse excited P_4 molecules ensures a good convergence of transient absorption curves. It does not change the kinetics of the EET. The intensity of the probe pulse is much smaller than that of the pump pulse. A small probe pulse intensity is necessary to ensure that the probe pulse absorption obeys the Beer-Lambert law [40].

After the time-dependent dipole moment $\mathbf{d}(t, \mathbf{E})$ (and therefrom the total polarization $\mathbf{P}(t, \mathbf{E})$) was calculated with the Eqs. 3.128 and 3.127, the polarization in probe pulse direction $\mathbf{P}(\mathbf{k}_{pr}, t)$ was calculated using the two methods suggested in Sec. 3.8.1 (Eqs. 3.133 and 3.134).

Calculation of the differential transient absorption utilizing method I

The transient absorption was computed for two different set-ups of pump and probe pulse polarization vectors. In the first set-up pump and probe beam polarization vectors are parallel, in the second one they are orthogonal.

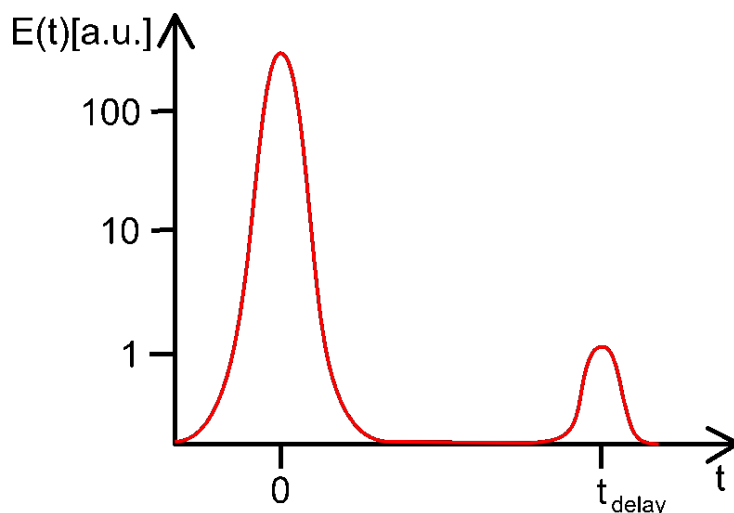


Figure 5.19: Illustration of the laser beam envelope at the probe. The pump pulse has a much higher field strength than the probe pulse.

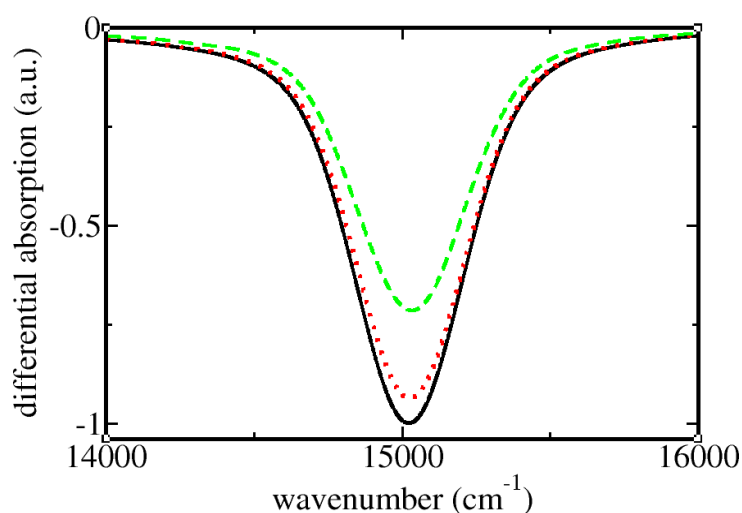


Figure 5.20: P_4 in ethanol differential transient absorption for parallel pump and probe beams is shown for three different delay times. Black: $t_{\text{delay}} = 150$ fs, red: $t_{\text{delay}} = 250$ fs, green: $t_{\text{delay}} = 750$ fs. Published in [85].

Fig. 5.20 shows the differential transient absorption for the P_4 complex for three different delay times, with a set-up of parallel pump and probe pulse polarization vectors. All curves show a dip, which decreases when the delay time becomes larger. A differential transient absorption shows the probe pulse absorption after a pump pulse excited the system minus the probe pulse absorption without a pump pulse acting on the system. A dip in the differential transient absorption thus means that the Q_y band absorption of the probe pulse without previous pumping is stronger than the respective probe pulse absorption with previous pumping. The explanation of this result is easy: when the pump pulse arrives at the probe, it does not excite arbitrary Pheos, but it excites those chromophore more likely, whose transition dipole moments have a small angle with the electromagnetic field polarization vector. A parallel probe pulse that arrives shortly after the pump pulse excites the same Pheos with higher probability, but only those that were not yet excited by the pump pulse. This is the reason why the probe pulse excites less Pheos and shows less linear absorption if there was a pump pulse present.

For longer delay times between pump and probe pulse, EET occurs between the Pheos of the CC. This is due to the excitonic coupling between the Pheos. The Pheos that are excited by the

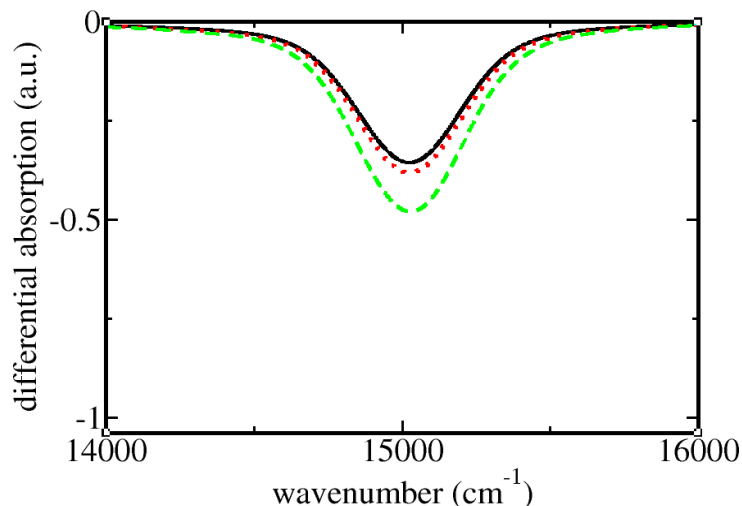


Figure 5.21: P_4 in ethanol differential transient absorption for orthogonal pump and probe beams is shown for three different delay times. Black: $t_{\text{delay}} = 150\text{fs}$, red: $t_{\text{delay}} = 250\text{fs}$, green: $t_{\text{delay}} = 750\text{fs}$. Published in [85].

pump pulse are in average characterized by their transition dipole moment. The EET gives rise to an excitation energy redistribution. Thus, for large supramolecular complexes, after long delay times the transition dipole moments of the excited Pheos are not related to the transition dipole moments of the initially excited Pheos. A parallel probe pulse could now excite more chromophores than before the energy redistribution. This is the reason why the dip in Fig. 5.20 decreases when the delay time increases.

The explanation of Fig. 5.21 is similar. The dip is small for short delay times and grows with increasing delay time. At very short delay times, no energy transfer took place. The pump pulse again excites those chromophores with the highest probability which were oriented along the pump pulse polarization vector. The orthogonal probe pulse now excites chromophores with highest probability whose transition dipole moments are oriented orthogonal to those excited by the pump pulse. This leads to the following statement: if the delay time is very short, mainly those chromophores are excited which only have a very low probability to be excited by the probe pulse. This is the reason why the dip is very low. However, it is important to note that in any case there will be a dip, if a pump pulse was present.

After very long delay times, the probability for a Pheo being in the first excited electronic state does not depend on its transition dipole moments angle with the electromagnetic field polarization. Hence, for very long delay times (assuming that there is no energy loss) both parallel and orthogonal pump and probe pulse setup will give the same dip. It should be possible to observe this in femtosecond transient absorption experiments, since the competing mechanisms as de-excitation or internal conversion in Pheo happen on larger time scales (cf. [40]). Respective experiments for P_4 are planned but have not yet been carried out (Sec. 2.2). The complete reorganization of the excitation energy in the P_4 complex happens on a time scale of about 20 ps.

Calculation of the differential transient absorption utilizing method II

The result for the probe pulse absorption after initial pump pulse excitation (the delay time was 100 fs) is given in Fig. 5.22. The calculation was done as follows: for a time slice length of $\Delta t_{\text{sample}} = 350\text{fs}$ the total polarization was computed via Eqs. 3.128 and 3.127. A prefactor $e^{i\theta_r}$ with the random phase $0 < \theta_r < 2\pi$ was multiplied to each computed value of the total polarization. In order to ensure a large number of total polarization values, the offset time t^{offset} was set to 1 fs (cf. Sec. 4.5.1). That means that each timestep t of each MD run was utilized 350

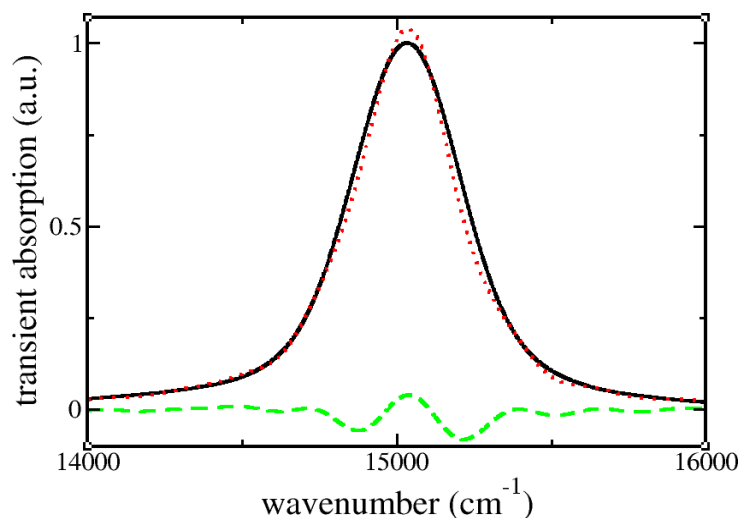


Figure 5.22: P_4 in ethanol transient absorption. Black line: transient absorption after pump and probe pulse utilizing Eq. 3.133 for the polarization amplitude in probe pulse direction $\mathbf{P}(\mathbf{k}_{pr}, t)$. Red line: transient absorption obtained utilizing Eq. 3.134 for the calculation of $\mathbf{P}(\mathbf{k}_{pr}, t)$. The difference between both curves (green line) is due to the bad convergence of Eq. 3.134. The delay time was 100 fs.

times in order to solve the TDSE (cf. Sec. 4.5.1), since 1 fs was the MD simulation time step. Altogether nearly 24 million time slices (using 8 times 3 ns of the MD data) were utilized to calculate the polarization amplitude in probe pulse direction $\mathbf{P}(\mathbf{k}_{pr}, t)$.

Fig. 5.22 compared the differential transient absorption lineshapes, calculated utilizing the methods I and II (Eqs. 3.133 and 3.134). It is obvious that the convergence of Eq. 3.134 (method II) is very bad. It has to be stated that the computation of Eq. 3.133 was about a factor 100 faster than the computation of Eq. 3.134. However, the correlation function did not completely converge. Nevertheless, it can be seen from Fig. 5.22 that both methods yield the same result (same linewidth of the probe pulse absorption). The differential curve between the absorption curves calculated by the two different methods indicates the bad convergence of Eq. 3.134. Hence all transient absorption results presented in this thesis were calculated utilizing method I (Dohmke, Eq. 3.133).

Transient anisotropy

The transient anisotropy is a quantity that may be computed from the differential transient absorption. In order to compute the transient anisotropy from Eq. 3.140 the computation of the differential transient absorption has to be carried out for parallel as well as for orthogonal polarized pump and probe beams. Fig. 5.23 shows the calculated result for the transient absorption. For chromophores in an isotropic medium, the anisotropy has a value between -0.2 and 0.4 [9]. In the calculations that have been carried out for this thesis, the anisotropy is 0.4 for very short delay times and approaches a value of 0.1 for long delay times (>10 ps). An anisotropy value of 0.4 means that no conformational change of the molecule occurred between the pump and the probe pulse [9]. In a lot of experiments such a change of the average transition dipole moment would be due to rotational motion [9]. In the P_4 system the rotational motion occurs on a much longer time scale (above 100 ps) than the excitation energy transfer. Thus, nearly all the changes of the anisotropy values in the P_4 system on the observed time scale of below 10 ps are due to excitation energy transfer.

Thus, the calculated value of approximately 0.4 for short time scales can be explained. For longer time scales a redistribution of the excitation energy occurs. An anisotropy value of 0.0 would exhibit that there is no dependency of the chromophores conformation after the delay time on its conformation during the pump pulse [9]. This, however, is never the case in P_4 .

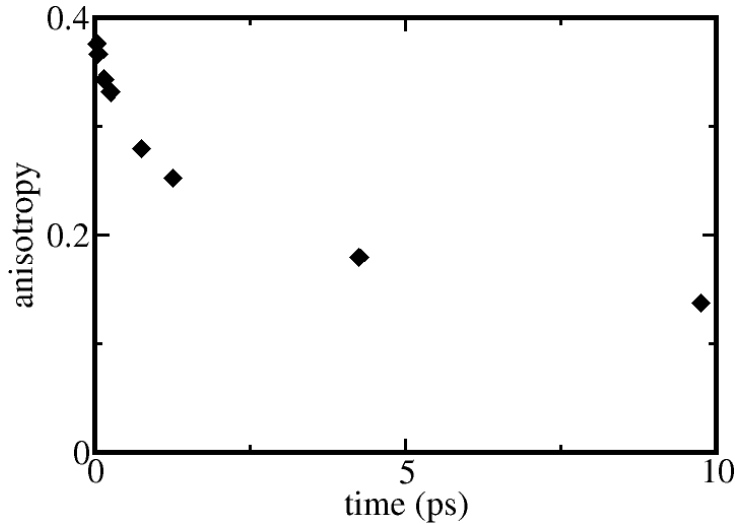


Figure 5.23: The P_4 in ethanol transient anisotropy is drawn for eight different delay times. Published in [85].

After a long delay time t^{delay} the first excited state population of the initially excited Pheo is 0.25, since P_4 consists of four Pheos. The remaining population of the first excited state is equally distributed over the other three Pheos. The mutual orientations of the Pheos are completely uncorrelated (the average angle between the transition dipole moments of different Pheos is $\approx 54.7^\circ$ (cf. [9])). The transition dipole moment is not correlated with the initial excited Pheo transition dipole moment, if the excitation is located on one of the other three Pheos in P_4 . Thus, the transient anisotropy computation in Sec. 3.9 that results in Eq. 3.193 ($r = 0.1$ for P_4 after long delay times) can be verified by the computed anisotropy values. This can be explained as follows: after long delay times, the population of the first excited electronic state of the initially excited Pheo is 0.25, and the corresponding anisotropy is 0.4. For the remaining population of the first excited electronic state, the respective anisotropy value is zero, since the conformations and thus the transition dipole moments of the single Pheos are in average not correlated. The transient anisotropy value for very long delay times is thus $r_\infty = 0.1$. The above considerations are also valid if the EET dynamics are observed in a coherent scheme, however, the respective considerations in terms of populations are more complicated. In the end, they give the same result.

In what follows, the EET time scale, that is revealed by the delay time dependent transient anisotropy, is compared with the solution of the TDSE and with the solution of the rate equations (Sec. 5.2.2). The anisotropy value $r(t)$ has to be identified with a respective population $P_r(t)$. Taking into account the above discussions and thus knowing the anisotropy values $r(0) = 0.4$ and $r(\infty) = 0.1$ it occurs to be straightforward to multiply $r(t)$ by a factor 2.5 in order to identify the value of the anisotropy with the population of a chromophore in P_4 that was excited at $t = 0$. Hence, the population shortly after the excitation is $P_r(0) \approx 1$ and the population after a very long delay time is $P_r(\infty) = 0.25$, which is exactly the expected result that is additionally confirmed by the solution of the TDSE in Sec. 5.2.2.

Fig. 5.24 shows the populations resulting from the three available methods to calculate EET (TDSE, EET rates, and transient anisotropy). The results of all three approaches agree perfectly. The delay time dependent transient anisotropy uncovers the EET dynamics as well as the populations calculated from the TDSE. At the same time it gives a value that can be measured by respective experiments. Experimental measurements of the transient absorption and thus the transient anisotropy of P_4 are planned.

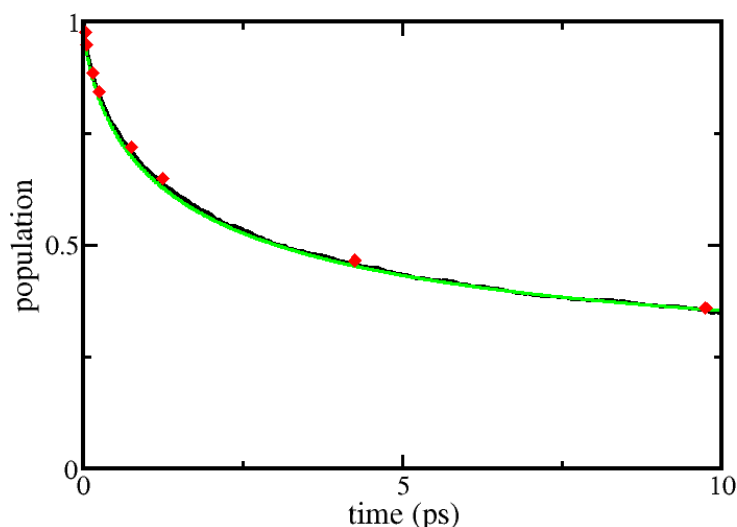


Figure 5.24: The time-dependent populations of an initially excited Pheo in P_4 computed from the transient anisotropy (red diamonds), from the TDSE (black) and from the conformation dependent rates (green) are compared. The results match perfectly.

5.3 The P_{16} dendrimer

5.3.1 Linear absorption

The Q_y band linear absorption of P_{16} in ethanol is calculated from Eq. 3.73. The first part of the MD data for P_{16} in ethanol includes eight MD runs per 8 ns, all starting from the same initial conformation. The linear absorption result computed from these MD data is shown in Fig. 5.25. The maxima of the three calculated absorption curves are parameters, taken from the maximum of the Pheo in ethanol linear absorption experiment. As can be seen from Fig. 2.5, the Q_y band maxima of P_4 and P_{16} are shifted to lower energies in the experiment. However, the figure reveals the broadening due to the excitonic coupling, and the energy shifts of the maxima are not the object of investigation. The broadening due to the excitonic coupling increases significantly with the number of Pheos attached to the dendrimer. However, this broadening is not very strong (cf. Sec. 5.2). For P_{16} in ethanol the linewidth increases about 20 % against the result for Pheo in ethanol. This rather small broadening compared to the experimentally observed broadening in Fig. 2.5 has been discussed in Sec. 5.2.1 for P_4 . The same argumentation holds for P_{16} . Probably the broad linewidths in the experiment result from impurities in the measured samples, since the filtration for the P_N complexes is very complicated [22].

5.3.2 Excitation energy transfer

It has been shown in Sec. 5.2.2 for the P_4 dendrimer that all the information about the EET is gained by solving the TDSE. For the P_4 system it was discussed that the ensemble average should be adequate for the eight runs a 8 ns of simulation (each started with the same initial conformation). That this does not hold for P_{16} is indicated in Fig. 5.26. 8 times 8 ns of MD simulation were utilized to solve the TDSE. The figure shows the time-dependent populations of each chromophore m that was excited at $t = 0$. It is not necessary to distinguish between the different initially excited chromophores m . But it is possible to compare the different decays of the initially excited chromophores (16 curves for the sixteen different initial conditions $P_m(0) = 1$). Further it is possible to observe the curves of the chromophores which are the next neighbors to the initially excited chromophores. If one follows the branches of P_{16} from the CC center to the single chromophores (cf. dendrimer structure in Fig. 2.2), the two Pheos which are connected by the last two branches are defined as the next neighbors. They do not necessarily have the

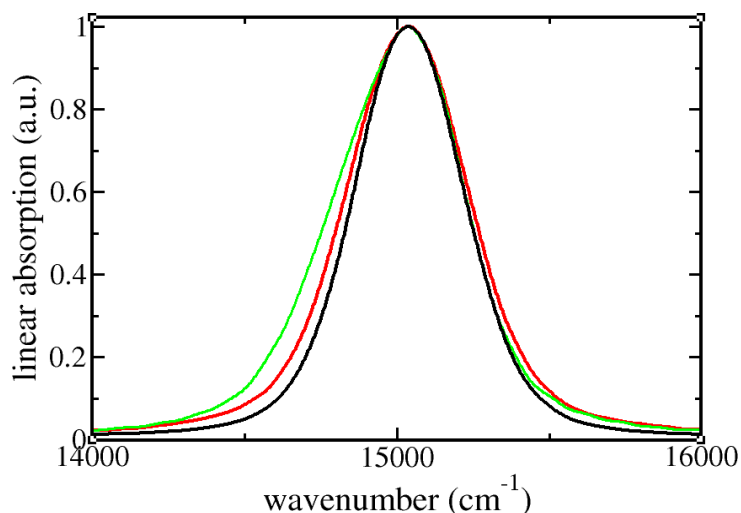


Figure 5.25: Linear absorption of P_{16} (green), P_4 (red), and Pheo (black) in ethanol. P_{16} was computed from the total MD data of 64 ns, while for P_4 and Pheo 8 times 10 ns of MD data have been used. Peak maxima were shifted to 15015 cm^{-1} (Pheo in ethanol experimental value).

closest spacial distance to each other at any time of the CC trajectory.

The achieved ensemble average for the 8 times 8 ns of MD simulation (in the following discussion referred to as MD data I) is not very good, as can be seen from Fig. 5.26. The curves that are computed with different initial conditions, concerning the fact which Pheo was excited at $t = 0$, show completely different decays of the populations.

To reach ensemble average, high temperature simulations (1000 K for 2.5 ns) were carried out (as explained in Sec. 4.1.6) to obtain 16 different conformations of P_{16} in ethanol that were utilized as initial conformations for 300 K runs. The result is shown in Fig. 5.27. The ensemble average for 16 runs a 1.3 ns (in the following discussion referred to as MD data II) is much better than for the simulation runs started from the same initial conformation (MD data I).

Fig. 5.27 shows a satisfactory ensemble average. Additionally, it allows some comparison with the EET observed within P_4 . The EET is obviously faster in the case of P_{16} , the complete excitation energy is distributed over all Pheos after 5 ps. This indicates a much stronger excitonic coupling in average. This much stronger excitonic coupling is consistent with the broader absorption linewidth of P_{16} compared to P_4 . This excitonic coupling in average is stronger due to the fact that the number of Pheos per volume is higher for Pheos attached to the P_{16} dendrimer compared to Pheos connected to a P_4 dendrimer. This holds even though the dendrimer structure in P_{16} is larger than the one in P_4 (310 instead of 58 atoms). The average population of a previously excited Pheo reaches the value $1/N + (1 - 1/n)/e$ after 0.25 ps for MD data I and 0.3 ps for MD data II (cf. Fig. 5.28). Nevertheless, for both simulation data the population is not equally distributed after 3 ps. This is due to the fact that the excitation energy is at first distributed around the nearest Pheos. After the time of about 0.3 ps the excitation energy is located around the originally excited Pheos and their neighbors. It needs additional 5 ps to distribute the excitation energy equally over the CC.

Fig. 5.28 compares the EET dynamics that were calculated from the MD data I to the EET dynamics calculated from MD data II. It can be seen that the EET from both simulation data is approximately the same. As was shown in Fig. 5.27, the ensemble average for the different initial conformations (MD data II) was much better than the ensemble average that was achieved by the MD runs that were started with the same initial conformation (MD data I). Nevertheless, the EET time scale derived from both MD data seems to be reliable.

Finally, the MD data II are utilized to compute conformation dependent rates, as done in Sec. 5.2.2. The correlation function was calculated as done in Eq. 3.112. The resulting rates were used to solve the rate equations, Eq. 5.4. The resulting populations for each conformation

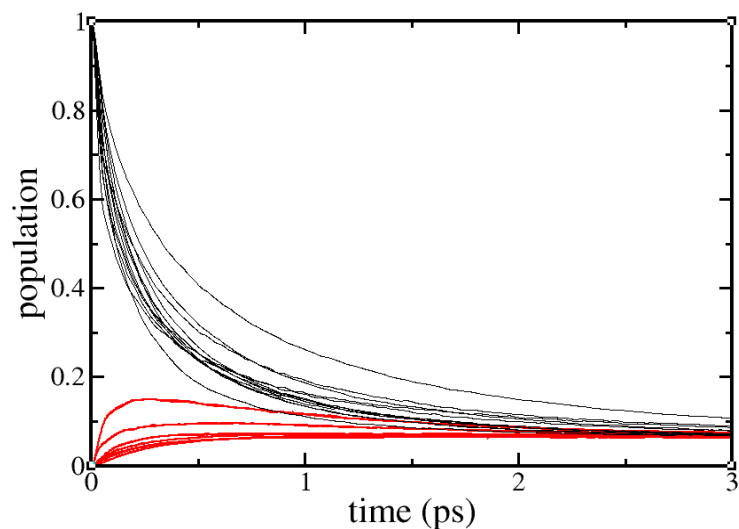


Figure 5.26: EET within P_{16} . The populations were computed from the solution of the TDSE, calculated from MD data I. The black curves show the populations of the initially excited Pheos. The red curves show the population for the Pheos that are located next to the respective initially excited Pheos.

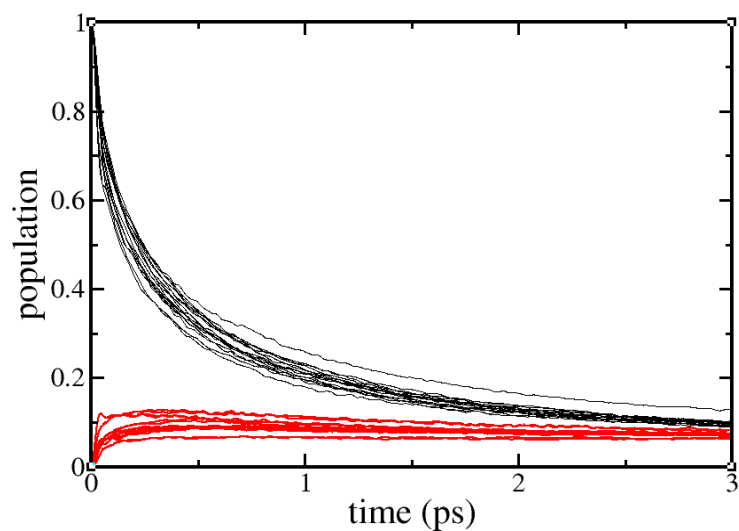


Figure 5.27: EET within P_{16} . The populations were computed from the solution of the TDSE, calculated from MD data II. Same color code as in Fig. 5.26.

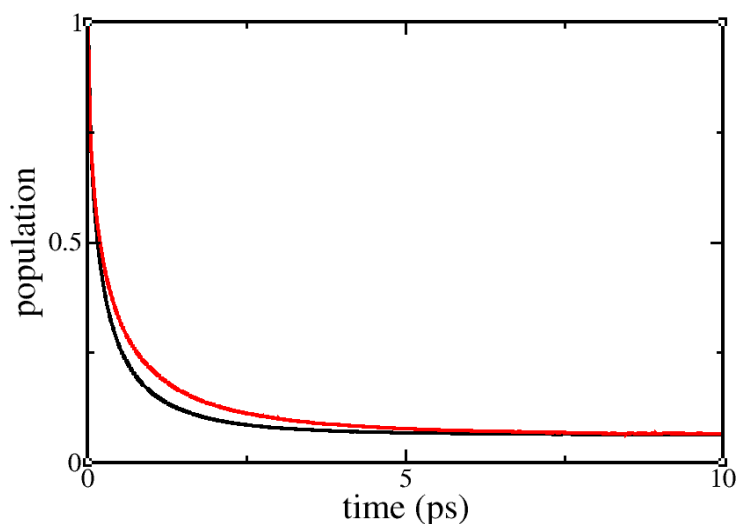


Figure 5.28: EET within P_{16} . Black line: averaged populations of the respective initially excited Pheos within P_{16} , calculated from MD data II. Red line: averaged populations of the initially excited Pheos within P_{16} , calculated from MD data I (cf. Figs. 5.26, 5.27).

are averaged and compared with the populations from the solution of the TDSE. The comparison is shown in Fig. 5.29. Even though the averaged rates in P_{16} are larger than $10^{12}/s$, the EET dynamics calculated from EET rates (that are computed in second order of the excitonic coupling) match the result of the TDSE very well.

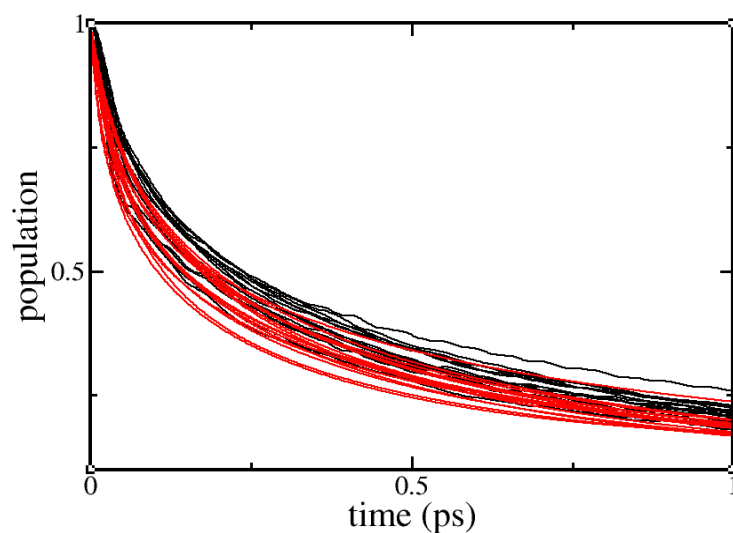


Figure 5.29: EET within P_{16} . Comparison between the solution of the TDSE and conformation dependent rates. Black lines: populations of an initially excited Pheo within P_{16} , calculated from the solution of the TDSE (from MD data II). Red lines: populations calculated from conformation dependent rates. Even for P_{16} with an average EET rate between two Pheos of more than $10^{12}/s$, the conformation dependent rates, computed in second order of the excitonic coupling, describe the EET dynamics quite well.

6 Pheo and P₁₆ near metal nano particles

6.1 Introduction

During the last decade it has become of increasing interest to study the optical properties of chromophores near MNPs. The strong coupling between the chromophores and the surface plasmons of the MNP has led to previously unexpected optical properties of the combined chromophore - MNP system. A recent overview about this topic and plasmonics in general can be found in [156]. [157] gives hints that the coupling between an MNP and dye molecules at the MNP surface changes the exciton spectrum of the dye aggregate. In [158], the chlorophyll absorption was enhanced, when the photosystem I was attached to spherical silver and gold MNPs.

Also, experimental results concerning molecular monolayers deposited on thin metal films should be mentioned. In 2004, a strong excitonic coupling between a cyanide dye J-aggregate and a thin silver film [159] (a J-aggregate is a dye that shows a shift to longer wavelengths when aggregating, which was firstly described by Jelley [160]). In 2006, the strong coupling between a J-aggregate and nano-voids within a gold film was measured [161]. In [162], the strong coupling between a dye mono-layer and a nanostructured silver film was detected.

Furthermore, it was shown experimentally in [163] that MNPs can be utilized for spatiotemporal control of optical excitations. The MNP induced spatiotemporal localization of the excitation energy was discussed theoretically in [164].

In the last few years, several theoretical approaches have been developed concerning chromophores, or chromophore complexes near MNPs. In [157, 165, 166] a single-resonance dielectric function was utilized to describe the chromophore-MNP system. In [167, 168] the Maxwell equations were solved for an ensemble of transition dipole moments (representing the chromophores) around an MNP. In our group the interaction between a supramolecular complex (SC) and an MNP was studied [169, 170]. In the model applied, all components of the combined SC-MNP system were treated in a complete quantum description.

This chapter aims to utilize the available simulations of Pheo and P₁₆ in ethanol to simulate the case when those molecules are located on the surface of a spherical metal nano particle (MNP) (cf. [171]). Whenever an MNP is mentioned in the following discussion, a spherical MNP is meant. The TDSE which has to be solved for such a combined CC-MNP system is quite similar to the one that has been solved already. The changes that have to be made will be discussed in the next section.

6.2 The P_N-MNP Hamiltonian and singly excited wave function

In the following section, linear absorption and excitation energy transfer will be discussed for the combined P_N-MNP system (cf. [172]). As explained in Secs. 3.6 and 3.7 those calculations require the solution of the TDSE. The first excited state Hamiltonian $H_1^{\text{mol-MNP}}$ (cf. Eq. 3.53) for the molecule-MNP system as well as the respective singly excited CC-MNP states $|\psi_B\rangle$ have to be defined. The Hamiltonian $H_1^{\text{mol-MNP}}$ can be derived from H_1 (Eq. 3.53) as follows [170]:

$$H_1^{\text{mol-MNP}} = H_1 + \sum_I (\mathcal{H}_0 + \hbar(\Omega_1 - \Omega_0)) |\psi_I^{\text{mol-MNP}}\rangle \langle \psi_I^{\text{mol-MNP}}| + \sum_{m,I} (V_{mI} |\psi_m^{\text{mol-MNP}}\rangle \langle \psi_I^{\text{mol-MNP}}| + H.c.). \quad (6.1)$$

\mathcal{H}_0 was defined in Eq. 3.52 and describes the static interactions between each Pheo with all the other molecules of the system (the other Pheos, the dendrimer and the solvent molecules) in the electronic ground state. Additionally, it includes the kinetic energy operators T_m . V_{mI} is the coupling energy between chromophore m and the MNP. The MNP ground state energy is Ω_0 . The respective excited state energy is Ω_1 . $|\psi_I^{\text{mol-MNP}}\rangle$ is the first excited state of the CC-MNP system, when the excitation is located at the MNP. The first excited electronic state of the combined CC-MNP system is denoted as $|\psi_B^{\text{mol-MNP}}\rangle$. If one of the chromophores in the CC is excited, $|\psi_B^{\text{mol-MNP}}\rangle$ can be written as

$$|\psi_m^{\text{mol-MNP}}\rangle = |\Psi_{me}\rangle \prod_{n \neq m} |\Psi_{ng}\rangle |0\rangle. \quad (6.2)$$

The reader should compare this definition with the first excited CC wave function $|\psi_m\rangle$ that was defined for the CC system in Eq. 3.14. $|0\rangle$ indicates that the MNP is in the electronic ground state.

The CC-MNP wave function for the first electronic excited state $|\psi_B^{\text{mol-MNP}}\rangle$ localized at the MNP is written as

$$|\psi_I^{\text{mol-MNP}}\rangle = \prod_n |\Psi_{ng}\rangle |I\rangle. \quad (6.3)$$

The first excited state of the MNP is threefoldly degenerated with transition dipole moments in the direction of the three Cartesian coordinate axes \mathbf{e}_i , $i \in \{x, y, z\}$ [169]. This threefold degeneracy allows the electron cloud in the MNP to couple to each chromophore dipole moment, no matter in what direction it points to. The general wave function of the CC-MNP system is a superposition over the $N + 3$ different singly excited wave functions of the CC-MNP system (N single excited CC-MNP wave functions for each chromophore of P_N and three singly excited CC-MNP wave functions for the 3 different wave functions $|\psi_I^{\text{mol-MNP}}\rangle$):

$$|\Psi^{\text{mol-MNP}}\rangle = \sum_B A_B^{\text{mol-MNP}} |\psi_B^{\text{mol-MNP}}\rangle. \quad (6.4)$$

In order to solve the TDSE with the Hamiltonian $H_1^{\text{mol-MNP}}$ and to compute the expansion coefficients within $|\Psi^{\text{mol-MNP}}\rangle$, the couplings between the chromophores and the MNP, V_{mI} (cf. Eq. 6.1), have to be determined.

As described in detail in Sec. 3.3.3, the excitonic coupling J_{mn} between two chromophores m and n is calculated via the interactions between the respective transition partial charges. For small distances between the chromophores this picture is more precise than the description via the dipole-dipole coupling between the chromophores transition dipole moments.

However, the description of the excitonic coupling via dipole-dipole coupling is a good approximation for the excitonic coupling between the chromophores and the MNP, if the distance between the center of the MNP and the chromophore is larger than one nanometer. It is written

$$V_{mI} = ([d^{\text{MNP}} \mathbf{e}_I \mathbf{d}_m^*] - 3[\mathbf{n}_{m,\text{MNP}} d^{\text{MNP}} \mathbf{e}_I][\mathbf{n}_{m,\text{MNP}} \mathbf{d}_m^*]) / |\mathbf{R}_{m,\text{MNP}}|^3. \quad (6.5)$$

$\mathbf{n}_{m,\text{MNP}}$ is defined as $\mathbf{n}_{m,\text{MNP}} = \mathbf{R}_{m,\text{MNP}} / |\mathbf{R}_{m,\text{MNP}}|$, while $\mathbf{R}_{m,\text{MNP}}$ is the distance vector between the center of chromophore m and the center of the MNP. The scalar dipole moment of the MNP d^{MNP} may be calculated for spherical MNPs with some approximations. This, however, is beyond the scope of this thesis. Here, a value for d^{MNP} will be used that was measured in recent experiments [33] for gold MNP with a radius of $r^{\text{MNP}} = 30$ nm. The value for the MNP dipole moment was $d^{\text{MNP}} = 3800$ D.

With all parts of the Hamiltonian $H_1^{\text{mol-MNP}}$ being defined, the TDSE can be solved for the available MD data. The related equations of motions for the expansion coefficients (cf. Sec. 3.4.2)

are written (the higher index 'mol-MNP' is dropped)

$$i\hbar \frac{\partial}{\partial t} \tilde{A}_m(t) = \sum_n (\mathcal{H}_{mn}(t) - \delta_{m,n} \Delta E_{g \rightarrow e}) \tilde{A}_n(t) + \sum_I V_{mI}(t) \tilde{A}_I(t), \quad (6.6)$$

and

$$i\hbar \frac{\partial}{\partial t} \tilde{A}_I(t) = \hbar (\omega_I - \omega_{eg} - i\gamma_I) \tilde{A}_I(t) + \sum_m V_{Im}(t) \tilde{A}_m(t). \quad (6.7)$$

The dephasing rate γ_I is chosen to produce the linewidth of the experimentally utilized gold MNPs [33]. The value of $\gamma_I = 0.18$ eV reproduces the measured MNP linewidth. It has to be mentioned that a measured linewidth may be affected by the size distribution of the MNPs. This, however, is neglected. ω_I is the transition frequency between the electronic ground and first excited electronic state of the MNP. ω_I is also taken from the MNP linear absorption measurements [33].

Solving this TDSE requires the same procedure as solving the TDSE for a CC without MNP (cf. Sec. 4.5). For 100 fs of the MD simulation the TDSE is solved for all possible initial conditions $\tilde{A}_B(t=0) = 1$. After this is done the next 100 fs long MD sample is used to solve the TDSE and so on. The resulting $\tilde{A}_B(t)$ can then be utilized to compute the linear absorption spectrum.

6.3 Linear absorption of Pheo and P₁₆ next to a MNP

For the computation of linear absorption, Eq. 3.73 is adapted to include the linear absorption of the combined molecule-MNP system. The linear absorption cross section can then be calculated as

$$I(\omega) = \text{Re} \int_0^\infty dt e^{i\omega t} \sum_{A,B} \langle d_A(t) \tilde{A}_A(t; B) d_B \rangle, \quad (6.8)$$

with $A, B \in \{\{m\}, \{I\}\}$. The time-dependence of the dipole moment $d_I(t)$ is neglected. This approximation is necessary, since in this description, no information on the fluctuation of the MNP transition dipole moment is available. This results in $d_I(t) = d^{\text{MNP}}$.

6.3.1 Amplification of the Pheo and P₁₆ linear absorption signal

In order to compute the amplification of the linear absorption signal, the Q_y band absorption for Pheo and P₁₆ is calculated with and without the coupling to a neighboring MNP. If only one P₁₆ and one MNP are considered, the molecular absorption is lower by orders of magnitude, compared to the MNP absorption (due to the enormous dipole moment of the MNP that is by three orders of magnitude larger than the Pheo dipole moment). In Figs. 6.1 and 6.2, not the linear absorption of the molecule-MNP system, but the difference between the molecule-MNP linear absorption and the linear absorption of the MNP is shown. This makes it possible to compare the linear absorption due to the coupling between the molecule and the MNP with the linear absorption of a single molecule.

The absorption spectra show several features. The absorption peak of the molecule is followed by a dip that is supposed to be a Fano resonance [173]. Fano resonances result from the interaction between continuous states and discrete energy levels. A similar, but smaller, feature is observable at the MNP resonance frequency. At the time of the finishing of this thesis, not all features of the molecule-MNP linear absorption in Figs. 6.1 and 6.2 could be defined.

The amplification factor of the Q_y band linear absorption was 62 for Pheo and 47 for P₁₆. This is reasonable, as will be discussed next.

The dipole moment of a single Pheo is perpendicular to the connection line between Pheo and the MNP center. According to Eq. 6.5 the average absolute value of the coupling is $d^{\text{MNP}} d_m$.

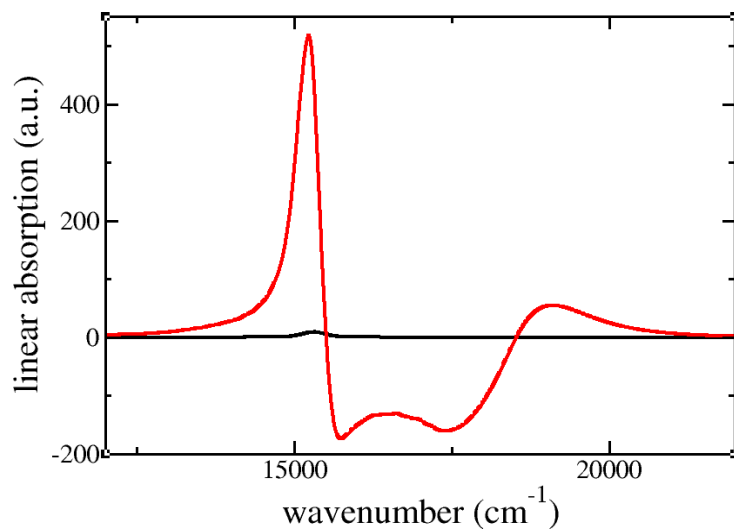


Figure 6.1: Q_y band linear absorption for the Pheo-MNP system in ethanol. Black line: linear absorption band calculated for a Pheo molecule. Red line: difference between the linear absorption of Pheo next to a MNP and the linear absorption of the MNP.

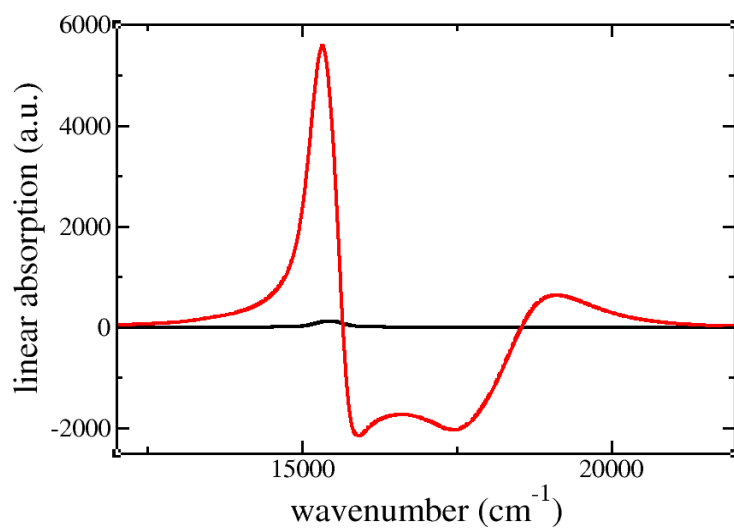


Figure 6.2: Q_y band linear absorption for the P_{16} -MNP system in ethanol. Black line: linear absorption calculated for a P_{16} -molecule. Red line: difference between the linear absorption of P_{16} next to a MNP and the linear absorption of the MNP.

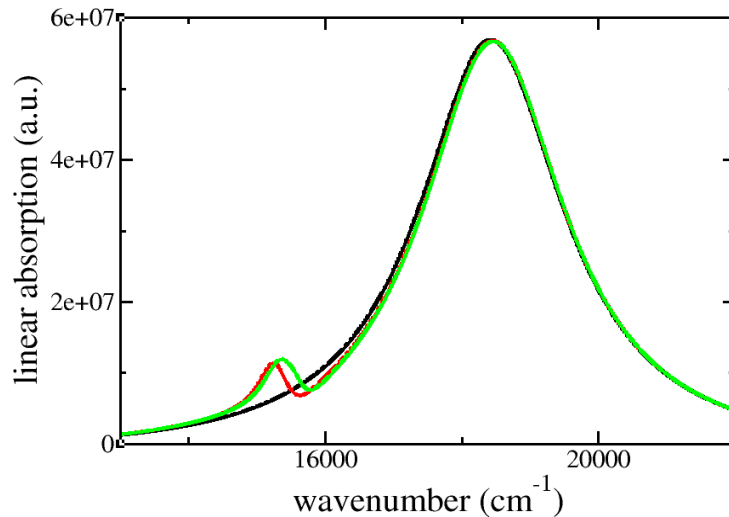


Figure 6.3: Q_y band linear absorption for a MNP covered with molecules in ethanol. Black line: linear absorption band of the MNP. Red line: linear absorption of 10000 Pheos on the surface of a MNP. Green line: linear absorption of 930 P_{16} molecules on the surface of an MNP. The respective numbers of molecules on the MNP surfaces are chosen to cover the complete surface of the MNP with a radius of 30 nm.

This is not the case for the Pheos within P_{16} - their mutual orientation is assumed to be arbitrary. This assumption is reasonable concerning the discussion for P_4 in Sec. 5.2. According to Eq. 6.5, the average absolute value of the coupling is also $d^{\text{MNP}} d_m$ (the average of cosine square was calculated in Eq. 3.191 as $2/3$). On the other hand, the Pheos in P_{16} are further away from the MNP. If the average distance between a Pheo within P_{16} and the MNP center is 32 nm (the diameter of P_{16} is about 4 nm), the presented results for the amplification of linear absorption are reasonable.

6.3.2 Linear absorption for a large number of molecules coupled to the MNP

In experimental measurements the proportion between the number of MNPs and the number of molecules in general is not 1 : 1. In most cases the number of molecules exceeds the number of MNPs by a factor of $N^{\text{mol}} / N^{\text{MNP}}$ [33], with the respective numbers of molecules N^{mol} and the number of MNPs N^{MNP} .

In terms of the above introduced methodology that treats the molecules in atomic detail and the MNP parametrically, linear absorption experiments with systems including a single MNP coupling to hundreds of molecules may be simulated in two ways. On the one hand, the TDSE can be solved for the whole system, including the excitonic coupling between each Pheo and the MNP and including the excitonic coupling between neighboring Pheos on the MNP surface (each Pheo may be represented by another part of the MD data). On the other hand, the coupling between neighboring molecules may be neglected; it has to be assumed that the MNP couples to each molecule, regardless of the presence of the other molecules. However, in what follows, this approximation is made. The number of Pheos on the MNP surface is chosen to be 10000. On the one hand, this is the number that was utilized in recent experiments [33] (with another porphyrin - tetraphenylporphyrin). On the other hand, 10000 is exactly the number of Pheos that cover the surface of the MNP (using a diameter of 1 nm for Pheo). The number of P_{16} molecules that cover an MNP with a radius of 30 nm was calculated to be 930 (using a diameter of 4 nm for P_{16}).

The linear absorption curves for the MNP covered with Pheo, on the one hand, and P_{16} , on the other hand, is shown in Fig. 6.3. The results look very similar for both molecules. Concerning the calculated amplification of the Pheo and P_{16} linear absorption due to the presence of

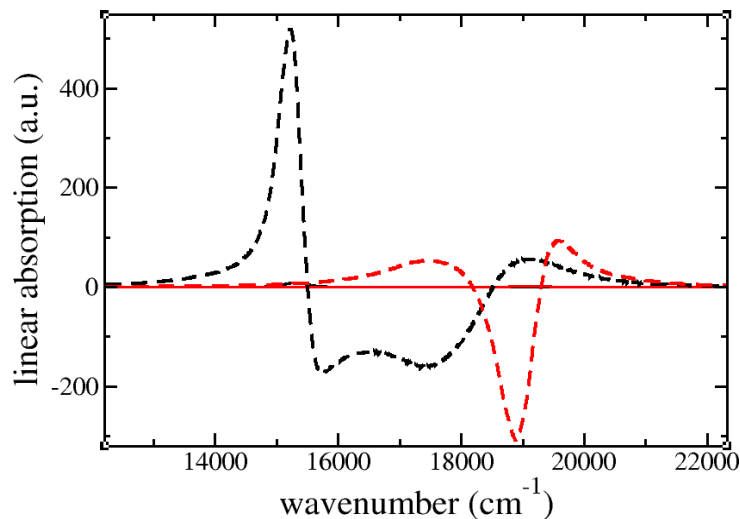


Figure 6.4: Q_y and Q_x band linear absorption for the Pheo-MNP system in ethanol. Full black line: Q_y linear absorption band calculated for a single Pheo. Full red line: Q_x linear absorption band. The respective dashed lines show the differences between the Pheo-MNP Q_y and Q_x band linear absorption lineshapes and the linear absorption lineshape of the MNP.

the MNP and the fact that the number of Pheos within 930 P_{16} molecules is 14880, the result is reasonable.

6.3.3 Linear absorption of the Q_x band

Utilizing the theory that was discussed in Sec. 3.6.1, additionally to the Q_y band, the Q_x band for Pheo next to an MNP is calculated. Since the Q_x band is in resonance with the MNP absorption, the amplification of the absorption signal is expected to be larger than for the Q_y band. In Fig. 6.4 the differences between the respective Pheo-MNP Q_y and Q_x band linear absorption lineshapes and the linear absorption lineshape of the MNP are shown. For the Q_x band, the peak is overlaid by a deep dip. In Fig. 6.5 the Q_y and Q_x band linear absorption for an MNP that is covered with 10000 Pheos is shown. As in the foregoing section, the interaction between the Pheos was neglected. It can be seen that the dip at the Q_x band position is overlaid by the MNP absorption. In respective experiments, the MNP absorption is additionally affected by scattering effects [33]. Thus, Fig. 6.5 shows that the treatment of the Q_x band can be neglected for this system, even though the Q_x band is resonant with the MNP absorption.

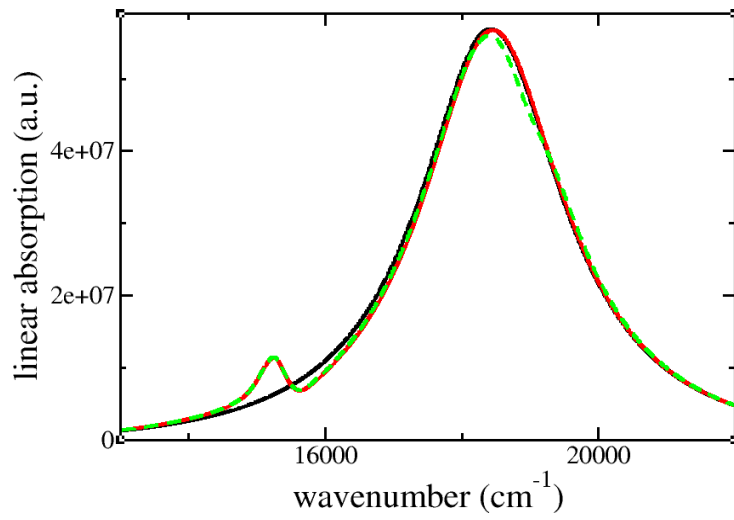


Figure 6.5: Q_y and Q_x band linear absorption for a MNP covered with Pheo molecules in ethanol. Black line: linear absorption of the MNP. Red line: Q_y linear absorption of 10000 Pheos on the surface of a MNP. Green line: combined Q_x and Q_y band linear absorption of 10000 Pheos on the surface of an MNP.

7 Screening in supramolecular complexes

7.1 Introduction

It was explained in the chapters 3 and 4 how to derive optical properties of a CC in solution from classical MD simulations. The key to those computations was the calculation of the energy gap function $U_m^{eg}(t)$ of chromophore m (cf. Sec. 4.3).

However, even if the energy gap functions $U_m^{eg}(t)$ can be calculated in good approximation, the quality of the CC description depends strongly on the quality of the transition couplings J_{mn} between two chromophores m and n (Sec. 4.3.2). As discussed earlier in Sec. 4.3.2, the transition density of a chromophore can be translated to respective transition partial charges $\{q_i^{\text{tr}}\} = \{q_i(\text{ge})\}$. As explained in Sec. 3.3.3, the transition partial charges have to be normalized to an experimental value of the transition dipole moment [32]. Then Eq. 3.49 can be utilized to compute the coupling energy J_{mn} between two chromophores m and n .

However, this formula neglects the screening of partial charges via the surrounding medium. The two chromophores m and n interact not only with themselves, but with all the other molecules around. This electrostatic coupling to the other molecules effectively changes the coupling between the chromophores m and n . The coupling J_{mn} is screened.

There exist mainly two approaches to compute the screening within large chromophore complexes in solution. The method that will be utilized within this thesis was proposed by the group of Renger and computes the transition density of a chromophore without taking the specific conformation of the surrounding medium into account [34, 35]. The effective potential of the respective transition partial charges is computed by solving the Poisson equation. Other approaches of the group that compute the transition densities, taking the surrounding medium into account, can be found in [174, 175, 176]. A more sophisticated but also much more computationally expensive ansatz has been pursued in the group of Menucci. In their ansatz, the conformation of each solvent and protein molecule near the chromophore contributes to the screening, which is obtained by DFT computations of the electronic coupling between two chromophores, involving solvent and protein molecules [23, 177, 178].

The following chapter refers to the work of the Renger group. The computation is much more practicable. It can be utilized to compute the screening for a lot of chromophore pairs with different distance and mutual orientation. This data will be utilized to find a fitting procedure that includes not only the distance dependence (as utilized for example in [28, 29]), but also the conformational dependence of the screening between two chromophores (cf. [179]).

7.2 Calculation of the screening factor utilizing the Poisson-TrEsp method

The screening factor F_{mn}^{scr} for the excitonic coupling between two chromophores m and n is then defined as

$$F_{mn}^{\text{scr}} = \frac{J_{mn}^{\text{scr}}}{J_{mn}}. \quad (7.1)$$

The unscreened excitonic coupling J_{mn} (according Chap.3, the notation J_{mn} without brackets refers to the excitonic coupling $J_{mn}(\text{eg}, \text{eg})$) is computed via the sum over the Coulomb interactions between transition partial charges (Eq. 3.49, cf. Sec. 3.3.3).

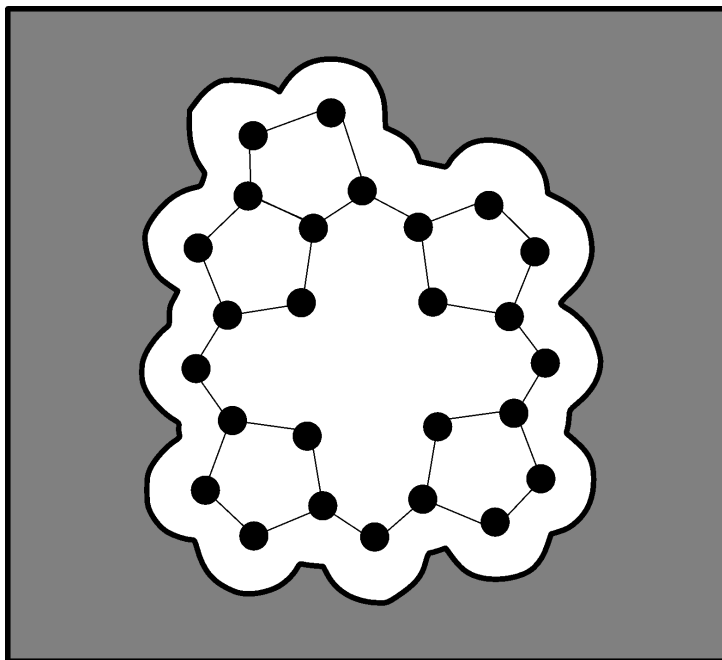


Figure 7.1: The sketch illustrates the principal idea for computing the potential of a chromophore from transition partial charges. The partial charges were put into chromophore shaped cavities sketched by the white area. The dielectric constant within and outside the cavity were set to $\epsilon = 1$ (white) and $\epsilon = 2$ (gray), respectively.

7.2.1 Poisson-TrEsp calculations

The computation of the screened excitonic coupling between two chromophores by the Poisson-TrEsp (transition charges from electrostatic potentials) method [34, 35] was invented in the group of Thomas Renger. The method utilizes the possibility to relate the excitonic coupling between two chromophores to the Coulomb coupling of the respective transition partial charges. This isomorphism was derived in [180].

The chromophores' transition partial charges (cf. Sec. 3.3.3) were obtained from electronic structure calculations. The partial charges were put into chromophore shaped cavities. This is illustrated in Fig. 7.1. The dielectric constant ϵ inside the cavity was set to $\epsilon = 1$, and outside the cavity the dielectric constant was set to $\epsilon = 2$ [34, 176]. For comparison, the dielectric constant for water and for visible light is $\epsilon_{\text{H}_2\text{O}} = 1.77$, for the protein structure it is about $\epsilon_{\text{protein}} \approx 2.3$ [178]. Treating the environment as a dielectric medium neglects the conformation of the surrounding molecules in atomic detail ([174, 175] include such a description at the cost of longer computational time).

For the transition partial charges inside the cavity, the Poisson equation was solved to compute the potential $\Psi_m(\mathbf{r})$ of the charges outside of the cavity:

$$\nabla (\epsilon(\mathbf{r}) \nabla \Psi_m(\mathbf{r})) = -4\pi \sum_i q_{mi}(\text{ge}) \delta(\mathbf{r} - \mathbf{R}_{mi}). \quad (7.2)$$

According to the notation of Chap. 3, q_{mi}^{tr} is the transition partial charge of atom i at chromophore m . \mathbf{R}_{mi} is the position of this atom. The potential $\Psi_m(\mathbf{r})$ may then be utilized to compute the screened excitonic coupling J_{mn}^{scr} as [34]

$$J_{mn}^{\text{scr}} = \sum_i \Psi_m(\mathbf{R}_{ni}) q_{ni}(\text{ge}). \quad (7.3)$$

The screened Coulomb coupling J_{mn}^{scr} is calculated by multiplying the potential of chromophore

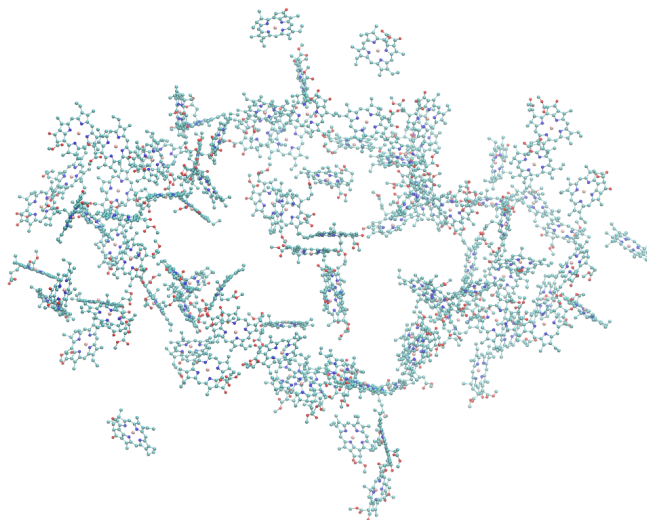


Figure 7.2: Photosystem I consists of 96 chlorophyll *a* molecules. The screening factors were calculated by Thomas Renger for each chromophore pair within photosystem I.

m at each atom position \mathbf{R}_{ni} of chromophore n with the transition partial charge of the respective i th atom of chromophore n , $q_{ni}(ge)$.

7.2.2 Poisson-TrEsp results for Photosystem I

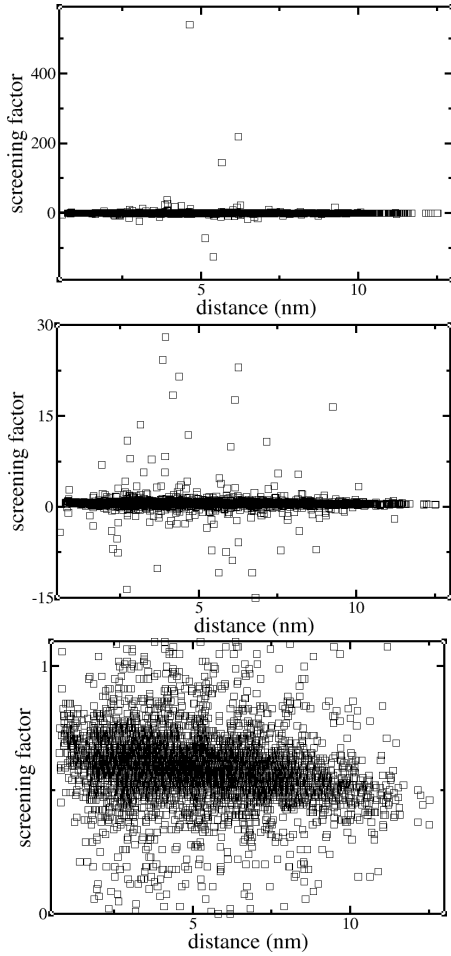


Figure 7.3: Screening factors of chromophore pairs within Photosystem I depending on the distance between the chromophore centers. The scaling in the panels is different, but all three panels show the same result. The fluctuation of the screening factors is due to the fact that the screening is not only distance dependent, but distance and conformation dependent. The computation was performed by Thomas Renger and the results are taken with permission from [35]

The TrEsp and the Poisson-TrEsp methods were utilized to compute the excitonic coupling within a Photosystem I trimer [35]. For the parameterization of the later defined screening functions f_{mn}^{ij} , the excitonic couplings between the chromophores within a photosystem I monomer were utilized. The respective couplings J_{mn} without screening effect and the J_{mn}^{scr} that include screening were calculated by Thomas Renger with the TrEsp [32] and the Poisson-TrEsp method [34]. The respective results for the screening factors are shown in Fig. 7.3. The screening factors are drawn against the distance between the chromophore pairs. The high fluctuation of the distance dependent screening factors is due to the fact that the screening is not only distance, but distance and conformation dependent. The screening factors are shown for three different orders of magnitude. Screening factors whose absolute value exceeds a value of 1 will be referred to as off-size screening factors. The reason for the appearance of those off-size screening factors has to be clarified.

7.3 Fitting of the Poisson-TrEsp calculated screening factor

7.3.1 Fitting procedure

Next, the fitting of the Poisson-TrEsp data as calculated in the group of Thomas Renger to chlorophyll *a* molecules will be introduced. The screened transition partial charge interaction J_{ij}^{scr} be-

tween atom i on chromophore m and atom j on chromophore n with the distance R_{mn}^{ij} is written as

$$J_{ij}^{\text{scr}} = \frac{1}{4\pi\epsilon_0} \frac{f_{mn}^{ij} q^i q^j}{R_{mn}^{ij}}, \quad (7.4)$$

with the definition of the screening functions

$$f_{mn}^{ij} = f_{mn}^{ij}(\epsilon(\mathbf{r})) = \sum_k F_0^k e^{-R_{mn}^{ij}/R_0^k}. \quad (7.5)$$

Note that the screening functions are not directly related to the screening factor F_{mn}^{scr} defined in Eq. 7.1.

The screening functions f_{mn}^{ij} for each atom pair i, j (with atom i from molecule m and atom j from molecule n) include the effect of the environment on the coupling between transition partial charges indirectly via infinite sets of parameters F_0^k and R_0^k . The screened excitonic coupling between the chromophores m and n can be written as sum over the interactions J_{ij}^{scr} :

$$J_{mn}^{\text{scr}} = \sum_{i,j} J_{ij}^{\text{scr}}. \quad (7.6)$$

No approximation was made so far. However, the screening functions have to be approximated in order to obtain computable functions. It was found within this thesis that the following approximation of the screening functions gave good results:

$$f_{mn}^{ij} = \sum_k F_0^k e^{-R_{mn}^{ij}/R_0^k} \approx \tilde{f}_{mn}^{ij} = F_0^1 e^{-R_{mn}^{ij}/R_0^1} + F_0^2 e^{-R_{mn}^{ij}/R_0^2} + R_{mn} C_0^1 + C_0^2. \quad (7.7)$$

R_{mn} is the distance of the centers of the porphyrin rings. \tilde{f}_{mn}^{ij} includes only two instead of an infinite number of exponential functions. It was found that the last term $R_{mn} C_0^1 + C_0^2$ is necessary to minimize the deviations between the Poisson-TrEsp calculated screening factors F_{mn}^{scr} and the approximated screening factors $\tilde{F}_{mn}^{\text{scr}}$. The approximated screening factors $\tilde{F}_{mn}^{\text{scr}}$ are computed as

$$\tilde{F}_{mn}^{\text{scr}} = \frac{\tilde{J}_{mn}^{\text{scr}}}{J_{mn}}, \quad (7.8)$$

with

$$\tilde{J}_{mn}^{\text{scr}} = \sum_{i,j} \tilde{J}_{ij}^{\text{scr}}, \quad (7.9)$$

and

$$\tilde{J}_{ij}^{\text{scr}} = \frac{1}{4\pi\epsilon_0} \frac{\tilde{f}_{mn}^{ij} q^i q^j}{R_{mn}^{ij}}. \quad (7.10)$$

The screening functions \tilde{f}_{mn}^{ij} include five free parameters. For an initial choice of the five parameters, the J_{ij}^{scr} and from those the $\tilde{F}_{mn}^{\text{scr}}$ were computed for all chromophore pairs within Photosystem I. The values of the $\tilde{F}_{mn}^{\text{scr}}$ were compared with the F_{mn}^{scr} that were computed with the Poisson-TrEsp method in the Renger group. Only those chromophore pairs were considered which fulfilled $0 < \tilde{F}_{mn}^{\text{scr}} < 1$ and $0 < F_{mn}^{\text{scr}} < 1$. The inclusion of the off-size screening factors would cause a domination of the fitting procedure by a small amount of chromophore pairs. For each chromophore pair that is included in the fitting procedure, the test function χ was defined as

$$\chi(F^1, F^2, R^1, R^2, C^1, C^2) = \sum_{m,n} (\tilde{F}_{mn}^{\text{scr}} - F_{mn}^{\text{scr}})^2. \quad (7.11)$$

This test function χ was minimized to get the set of parameters $\{F_0^1, F_0^2, R_0^1, R_0^2, C_0^1, C_0^2\}$ whose generated screening factors $\tilde{F}_{mn}^{\text{scr}}$ match the Poisson-TrEsp generated screening factors F_{mn}^{scr} best. The parameter set $\{F^1, F^2, R^1, R^2, C\}$ represents a respective non-optimized parameter set.

The minimization of the parameter set was done numerically. The initial choice of R^1 and R^2 is approximately given by the occurring distances of the chromophores. For P₁₆ the screening factors should give qualitatively good results for distances between one and five nanometers (4 nm is the diameter of P₁₆). For the parameters F^1 and F^2 the relation $F^1 + F^2 < 1$ holds, which means that there is always some screening between two transition partial charges. The initial value of C was set to zero.

The numerical parameter search in the 6-dimensional parameter space was done afterwards,

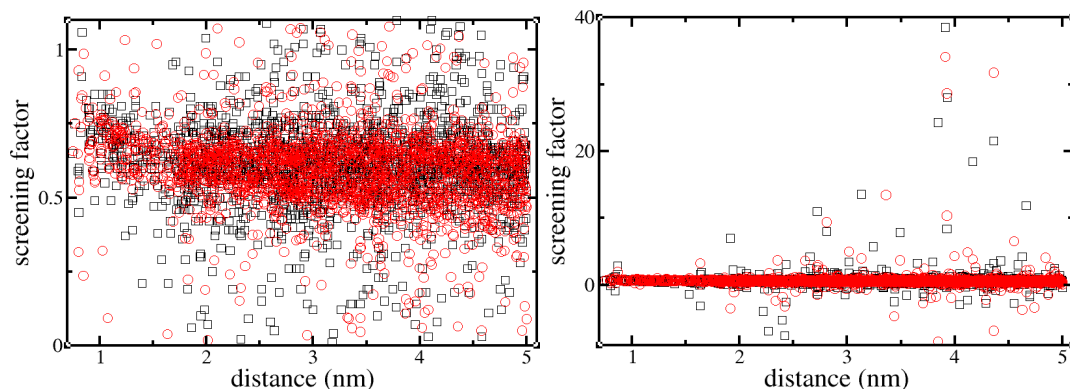


Figure 7.4: Shown are the approximated photosystem I screening factors against the Poisson-TrEsp results for two different regimes (screening factors between 0 and 1 as well as off-size screening factors). Both figures give the same result. Black squares: screening factors computed utilizing Poisson-TrEsp, red spheres: fitted screening factors.

and the parameters were optimized one after another. This was done repeatedly till a minimum was found. The complete 6-dimensional parameter space exhibits a very large number of local minima. A lot of parameter searches with different initial parameter sets $\{F^1, F^2, R^1, R^2, C^1, C^2\}$ and varying order of parameter optimizing were executed. The set $\{F_0^1, F_0^2, R_0^1, R_0^2, C_0^1, C_0^2\}$ that minimized $\chi(F^1, F^2, R^1, R^2, C^1, C^2)^2$ was utilized to compute the screening between Pheo molecules in the P₁₆ CC. The respective values are $F_0^1 = 3$, $F_0^2 = 5.7$, $R_0^1 = 2.5$, $R_0^2 = 23$, $C_0^1 = 0.0055$ and $C_0^2 = 0.006$.

7.3.2 Quality of the fitted screening

In order to prove the quality of the approach, Fig. 7.4 shows the approximated screening factors compared to the Poisson-TrEsp calculated screening factors. It is obvious that the distribution of the approximated screening factors against the chromophore pair distance (the distribution is due to the conformational dependence of the screening) is the same as the distribution of the Poisson-TrEsp calculated screening factors. This, of course, is not a surprise, since the distribution of the screening factors was the leading aim of the fit. More surprising is the fact that also the values for the off-size screening factors (the screening factors $F \gg 1$ or $F \ll 0$) are matched very well.

To prove that not only the distribution of screening factors in dependence of the mutual chromophore distance is obtained well by the method, the mean difference between Poisson-TrEsp and fitted data was computed. For excitonic couplings above 1 meV the mean difference between Poisson TrEsp and the fitted screening factors was $\Delta F \approx 0.067$. For excitonic couplings above 10 meV the difference was $\Delta F \approx 0.037$. This is a very satisfying result concerning the distribution of the screening factors. The larger the excitonic coupling between the chromophores, the better the matching between the fitted screening factors and the Poisson-TrEsp data.

7.4 Results

7.4.1 Off-size screening factors and distance dependent screening factors

When the full Poisson-TrEsp data are observed, some pairs of chromophores exhibit screening factors that are much larger than 1 or even smaller than 0. This holds also for the fitted screening factors. These off-size screening factors can be explained by the formation of specific mutual conformations of the chromophores m and n , which can be seen in Fig. 7.5. If J_{mn} is equal to zero, the screened value J_{mn}^{scr} is not necessarily zero, since the screening changes the effective

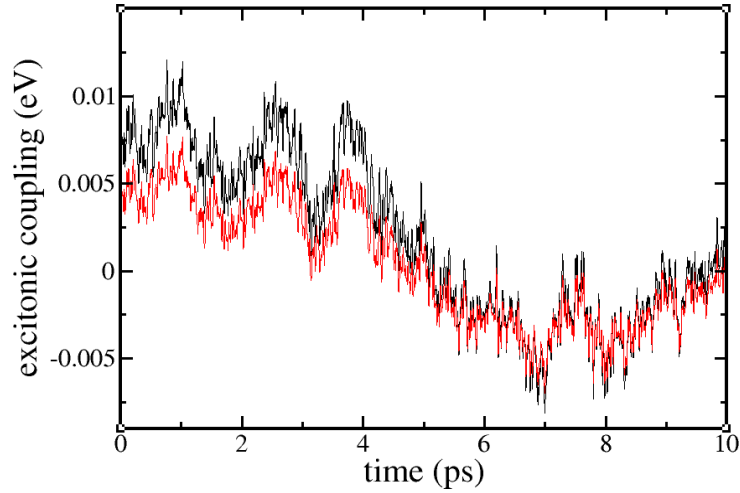


Figure 7.5: Excitonic coupling J_{mn} between two chromophores 1 and 2 (P_{16} in ethanol) for 10 ps of MD simulation. This MD sample was chosen, since the sign of the excitonic coupling changes within the example. Black curve: excitonic coupling without any screening effects. Red curve: excitonic coupling including the screening effect calculated with the new method. It can be seen that the screening factor changes in this MD sample (screening factor was defined as the quotient between the red and the black curve). When the excitonic coupling becomes small or switches its sign, the screening factor may become extremely large. This is due to the fact that the two curves cross the $J=0$ point at different times. This explains the appearance of off-size screening factors.

interaction of the sets of transition partial charges $\{q_i^{\text{tr}}\}_m$ and $\{q_i^{\text{tr}}\}_n$. This is due to the fact that the different atom pairs are screened differently, which may lead to an 'effective polarization'. This effective polarization differs for unequal mutual conformations of the Pheos m and n . This explains the distribution of the screening factors, when distance dependent screening is examined. Furthermore this effective polarization may result in off-size screening factors, if the unscreened excitonic coupling J_{mn} is near zero.

7.4.2 Linear absorption for different screening methods

The optimized parameter set $\{F_0^1, F_0^2, R_0^1, R_0^2, C_0^1, C_0^2\}$ that gives the screening functions \tilde{f}_{mn}^{ij} was computed for Photosystem I. This system consists of chlorophyll a molecules. Chlorophyll a is very similar to Pheo. The porphyrin structure is the same, only side chains vary. Besides, the chlorophyll a molecules within Photosystem I contain a magnesium base, while the Pheo molecules in P_{16} are free base molecules. For the screening of the molecules these differences should give no crucial effect. The dielectric constant of ethanol is $\epsilon_{\text{ethanol}} = 1.86$, and the dielectric constant of the Pheo molecules can be approximated by the chromophore value $\epsilon_{\text{chromophore}} \approx 2.3$ given in [178]. The environmental dielectric constant of $\epsilon = 2.0$ thus seems a good choice for P_{16} in ethanol. The parameter set $\{F_0^1, F_0^2, R_0^1, R_0^2, C_0^1, C_0^2\}$ for the approximated screening functions \tilde{f}_{mn}^{ij} was utilized to compute the screening between the Pheos in P_{16} . With this data the linear absorption from Eq. 3.73 was calculated.

Additionally, the linear absorption was computed for two other approaches taking the screening of excitonic coupling into account. The first of those approaches simply assumes a constant screening of each coupling. In order to do that, the average value (for chromophore distances between one and five nanometers) of $F^{\text{scr}} = 0.61$ was chosen. The second approach assumes an exponential dependence of the screening factor in dependence on the chromophores' center distance. The chromophore center distances between one and five nanometers give a screening factor function of $F^{\text{scr}}(R_{mn}) = 0.39\exp(-R_{mn}/7\text{\AA}) + 0.61\exp(-R_{mn}/2000\text{\AA})$ that approximates the available data best.

The result is shown in Fig. 7.6. The linear absorption linewidths for the four (including the

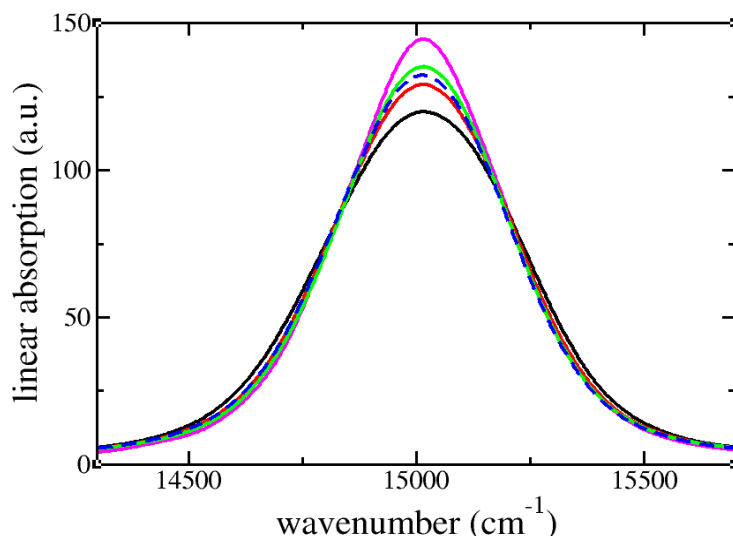


Figure 7.6: The P_{16} in ethanol linear absorption for five different calculation modalities: no screening factor (black), no excitonic coupling (magenta), screening factor with the constant value of 0.61 (green), screening factor defined by a double-exponential distance dependent function (blue), and the new method which treats the screening distance and conformation dependent (red).

neglecting of screening) different screening factor methods vary only slightly. The approach that assumes an exponential dependence of the screening factor on the chromophores' center distance approximates the result of the new method best. However, when linear absorption is to be computed, utilizing the new method that accounts for distance and conformation dependent screening is only meaningful if the error for the energy gap fluctuation and thus the error for the single molecules' absorption linewidth can be assumed to be small. As discussed in Sec. 5.1.1, this is the case for Pheo.

7.4.3 Solution of the TDSE for different screening methods

The optimized parameter set $\{F_0^1, F_0^2, R_0^1, R_0^2, C_0^1, C_0^2\}$ together with the MD data II was utilized to solve the TDSE for P_{16} . Again, the four different screening methods introduced in the last subsection are compared. Fig. 7.7 shows the mean time-dependent populations for the four screening methods, each calculated as average from the 16 different population curves of the respective initially excited Pheos: $P(t) = \sum_m^{16} P_m(t; m) / 16$. Here, $P_m(t; n)$ is the time-dependent population of chromophore m , when chromophore n was initially excited. The figure shows that the screening of excitonic coupling decelerates the EET within P_{16} . Furthermore, it shows that the explicit treating of distance and conformation dependent screening results in a much faster EET than the two other screening methods. This underlines the importance of the conformation dependent screening.

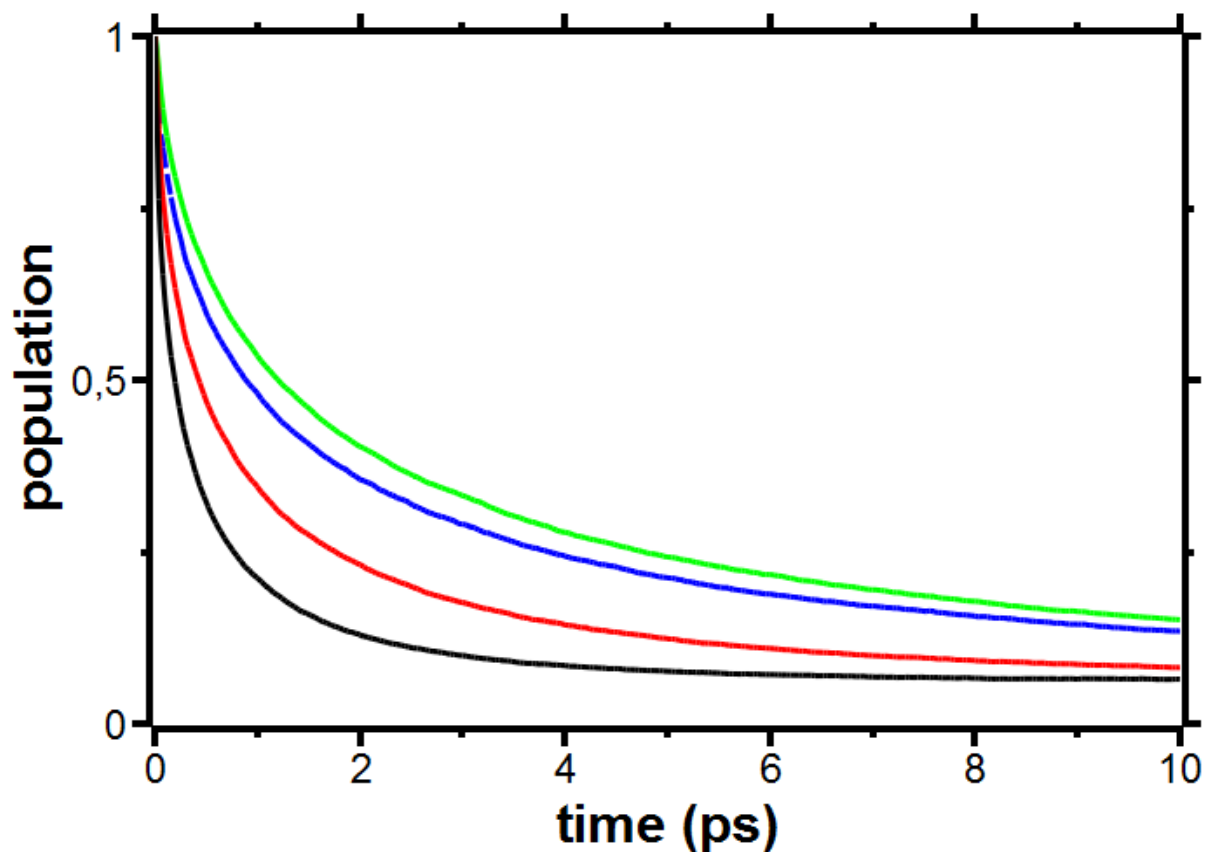


Figure 7.7: EET within P_{16} . Mean time-dependent populations of the initially excited Pheo, calculated from the solution of the TDSE for different screening methods: no screening factor (black), screening factor with the constant value of 0.61 (green), screening factor defined by a double-exponential distance dependent function (blue), and the new method which treats the screening distance and conformation dependent (red).

8 Summary

In this thesis the theoretical investigation of excitation energy transfer in the chromophore complexes P_4 and P_{16} in ethanol solution was presented. P_N is a dendrimer with N covalently bound pheophorbide a molecules. A mixed quantum-classical methodology was utilized to calculate optical properties of the system. Classical molecular dynamics simulations were carried out to compute the nuclei trajectories.

The key to the results shown in this thesis was to compute the intramolecular part of the energy gap fluctuation for a single pheophorbide a in harmonic approximation. In order to realize this, reference trajectories of each relevant electronic state had to be calculated from the respective molecular dynamics trajectories. The second derivatives of the potential energy surface were computed by co-workers from theoretical chemistry. The method is much less computationally expensive than other common methods and nonetheless yields an unmatched quality of the computed energy gap function, at least for the system considered in this thesis. The intermolecular part of the energy gap fluctuation was obtained in a standard way by computing the Coulomb interactions between respective atomic partial charges.

Utilizing the energy gap fluctuation, the time-dependent Schrödinger equation for the chromophore complex wave function was solved, parametrically dependent on the nuclei coordinates. The expansion coefficients from the solution of the time-dependent Schrödinger equation were utilized to compute optical properties of the systems in the dynamic classical limit. Linear absorption was computed for Pheo, P_4 and P_{16} in ethanol. The linear absorption line shape of Pheo matches the measured linewidth perfectly, without introducing any free parameters. The same holds for the Q_y band absorption. Unfortunately, no measurements of pure P_4 and P_{16} in ethanol have been carried out until now.

The time development of excitation energy transfer was investigated by three approaches. Firstly, the expansion coefficients from the solution of the time-dependent Schrödinger equation were averaged for many initial conformations of the chromophore complex. From those averaged expansion coefficients populations were computed. Secondly, Förster-like excitation energy transfer rates were computed in second order of the excitonic coupling. It could be shown how the presence of multiple conformations of the supramolecular complex affects the excitation energy transfer within the complex. The respective population dynamics can not be described by a set of averaged rates. The third approach was the calculation of transient absorption for P_4 , utilizing different delay times between the pump and probe beam. The calculation of nonlinear response functions was circumvented by solving the time-dependent Schrödinger equation including the electromagnetic field. From the transient absorption, transient anisotropy was computed and related to respective populations. The time development of excitation energy transfer is the same for the three approaches. On the one hand, the computed transient anisotropy is a quantity that may be directly compared with experimental results. On the other hand, the solution of the time-dependent Schrödinger equation, constricted to the first excited electronic state, gives the same information about the excitation energy transfer dynamics. The latter is much easier to compute within a mixed quantum-classical methodology.

In addition, the existing molecular dynamics data were utilized to compute optical properties of the molecular systems coupling to metal nano-particles. The respective properties of the nano-particles were introduced parametrically. The computation of linear absorption of the combined Pheo-nano-particle (P_{16} -nano-particle) system shows the expected amplification of the molecules' linear absorption. Calculations including the Q_y and Q_x band showed that the

Pheo Q_x band absorption plays only a minor role in the Pheo-nano-particle absorption. On the one hand, the Q_x band absorption is more amplified than the Q_y band absorption (since the Q_x energy is in resonance with the nano-particle excitation energy). On the other hand, this effect is small compared to the large nano-particle absorption curve.

Furthermore, within this thesis a method was introduced to incorporate distance and conformation dependent screening to the mixed quantum-classical methodology. This was achieved by finding screening functions for the interaction between single atoms that finally yield the distance and conformation dependent screening between chromophore pairs as calculated from the Poisson-TrEsp (transition charges from electrostatic potentials) method [34, 35]. In previous mixed quantum-classical approaches only distance dependent screening could be treated. It was shown that the distance and conformation dependent screening yields much faster EET dynamics than the distance dependent screening, or the screening with a constant number.

The newly introduced methods, especially the method to compute the intramolecular energy gap fluctuation in harmonic approximation, give powerful tools within a mixed quantum-classical method. The calculation of excitation energy transfer within supramolecular complexes depends on both the accurate computation of the energy gap fluctuation as well as the appropriate description of the excitonic coupling. Within this thesis, two corresponding methods were proposed and successfully applied to the supramolecular complex P_{16} . The methods may also enhance the quality of excitation energy transfer computations for other supramolecular systems.

Appendix A

1 Computing the correlation function

The computation starts with the definition of the correlation function in Eq. 3.169:

$$\begin{aligned} \text{tr}\{\hat{\mu}U[\hat{\mu}, \hat{W}]U^+\} = & \text{tr}\{-\Pi_2\mu_{21}U_1\hat{W}_{11}\mu_{12}U_2^+\Pi_2 + \Pi_1\mu_{12}U_2\mu_{21}\hat{W}_{11}U_1^+\Pi_1 \\ & - \Pi_0\mu_{01}U_1\hat{W}_{11}\mu_{10}U_0^+\Pi_0 + \Pi_1\mu_{10}U_0\mu_{01}\hat{W}_{11}U^+\Pi_1 \\ & - \Pi_1\mu_{10}U_0\hat{W}_{00}\mu_{01}U_1^+\Pi_1 + \Pi_0\mu_{01}U_1\mu_{10}\hat{W}_{00}U_0^+\Pi_0 + \text{non-diagonal terms}\}. \end{aligned} \quad (1)$$

The first of the six terms in Eq. 1 reads as follows:

$$\begin{aligned} & \text{tr}\{\Pi_2\mu_{21}U_1\hat{W}_{11}\mu_{12}U_2^+\Pi_2\} \\ & = \text{tr}\left\{\sum_i \sum_{j>i} d_j \langle \phi_i | U_1 \sum_q \sum_k W_{qk} | \phi_q \rangle \langle \phi_k | \sum_{l>k} d_l | \phi_k \rangle \langle \phi_{kl} | U_2^+ | \phi_{ij} \rangle \right. \\ & + \sum_i \sum_{j>i} d_i \langle \phi_j | U_1 \sum_q \sum_k W_{qk} | \phi_q \rangle \langle \phi_k | \sum_{l>k} d_l | \phi_k \rangle \langle \phi_{kl} | U_2^+ | \phi_{ij} \rangle \\ & + \sum_i \sum_{j>i} d_j \langle \phi_i | U_1 \sum_q \sum_k W_{qk} | \phi_q \rangle \langle \phi_k | \sum_{l<k} d_l | \phi_k \rangle \langle \phi_{l,k} | U_2^+ | \phi_{ij} \rangle \\ & \left. + \sum_i \sum_{j>i} d_i \langle \phi_j | U_1 \sum_q \sum_k W_{qk} | \phi_q \rangle \langle \phi_k | \sum_{l<k} d_l | \phi_k \rangle \langle \phi_{l,k} | U_2^+ | \phi_{ij} \rangle\right\}. \end{aligned} \quad (2)$$

The term covers the stimulated emission. It treats a CC which was in the first excited electronic state after the pump pulse and contributes to the second excited state absorption via the dipole operator matrix element μ_{21} (cf. Eq. 3.50). The projection operators were translated into the single chromophore basis (cf. Eqs. 3.13, 3.14, 3.15).

The second part of Eq. 1 (in the following, the statistical operator matrix elements W_{ij} always denote the respective statistical operator matrix elements $W_{ij}(t_{\text{delay}} \rightarrow 0)$ after very short delay times)

$$\begin{aligned} & \text{tr}\{\Pi_1\mu_{12}U_2\mu_{21}\hat{W}_{11}U_1^+\Pi_1\} \\ & = \text{tr}\left\{\sum_i \sum_{j>i} d_j \langle \phi_{ij} | U_2 \sum_k \sum_{l>k} d_k | \phi_{kl} \rangle \langle \phi_l | \sum_q W_{lq} | \phi_l \rangle \langle \phi_q | U_1^+ | \phi_i \rangle \right. \\ & + \sum_i \sum_{j>i} d_j \langle \phi_{ij} | U_2 \sum_k \sum_{l>k} d_l | \phi_{kl} \rangle \langle \phi_k | \sum_q W_{kq} | \phi_k \rangle \langle \phi_q | U_1^+ | \phi_i \rangle \\ & + \sum_j \sum_{i<j} d_i \langle \phi_{ij} | U_2 \sum_k \sum_{l>k} d_k | \phi_{kl} \rangle \langle \phi_l | \sum_q W_{lq} | \phi_l \rangle \langle \phi_q | U_1^+ | \phi_j \rangle \\ & \left. + \sum_j \sum_{i<j} d_i \langle \phi_{ij} | U_2 \sum_k \sum_{l>k} d_l | \phi_{kl} \rangle \langle \phi_k | \sum_q W_{kq} | \phi_k \rangle \langle \phi_q | U_1^+ | \phi_j \rangle\right\} \end{aligned} \quad (3)$$

covers the part next of Eq. 5 which treats the population being in the first excited electronic state after pump and probe pulse excitation. Eq. 3 is related to the dipole operator matrix element μ_{21} . The equation treats the part of the population which is not part of the second excited state

absorption. It is the counterpart to Eq. 2. The third term in Eq. 1

$$\begin{aligned}
 & \text{tr}\{\Pi_0\mu_{01}U_1\hat{W}_{11}\mu_{10}U_0^+\Pi_0\} \\
 &= \text{tr}\left\{\sum_i d_i \langle \phi_i | U_1 \sum_{m,n} W_{mn} | \phi_m \rangle \langle \phi_n | \sum_j d_j | \phi_j \rangle \langle \phi_i | U_1 | \phi_m \rangle \langle \phi_0 | U_0^+ | \phi_0 \rangle\right\} \\
 &= \text{tr}\left\{\sum_i \sum_j \sum_m d_i d_j W_{mj} \langle \phi_i | U_1 | \phi_m \rangle \langle \phi_0 | U_0^+ | \phi_0 \rangle\right\}
 \end{aligned} \tag{4}$$

treats the stimulated emission due to the dipole operator matrix element μ_{01} . The fourth part of Eq. 1 is written

$$\begin{aligned}
 & \text{tr}\{\Pi_1\mu_{10}U_0\mu_{01}\hat{W}_{11}U_1^+\Pi_1\} \\
 &= \text{tr}\left\{\sum_i \langle \phi_i | \sum_j d_j | \phi_j \rangle \langle \phi_0 | U_0 \sum_k d_k | \phi_0 \rangle \langle \phi_k | \sum_{m,n} W_{mn} | \phi_m \rangle \langle \phi_n | U_1^+ | \phi_i \rangle\right\} \\
 &= \text{tr}\left\{\sum_i d_i \langle \phi_0 | U_0 | \phi_0 \rangle \sum_{k,m,n} d_k \langle \phi_k | W_{mn} | \phi_m \rangle \langle \phi_n | U_1^+ | \phi_i \rangle\right\} \\
 &= \text{tr}\left\{\sum_i d_i \langle \phi_0 | U_0 | \phi_0 \rangle \sum_{m,n} d_m \langle \phi_m | W_{mn} | \phi_m \rangle \langle \phi_n | U_1^+ | \phi_i \rangle\right\} \\
 &= \text{tr}\left\{\sum_i d_i \langle \phi_0 | U_0 | \phi_0 \rangle \sum_{m,n} d_m W_{mn} \langle \phi_n | U_1^+ | \phi_i \rangle\right\}.
 \end{aligned} \tag{5}$$

Eq. 5 covers the part of the population of the CC which is in the first excited electronic state after pump and probe pulse excitation. The equation is related to the dipole operator matrix element μ_{01} and treats the part of the first excited electronic state population which was not part of stimulated emission. It is the counterpart to Eq. 4. The term

$$\begin{aligned}
 & \text{tr}\{\Pi_1\mu_{10}U_0\hat{W}_{00}\mu_{01}U_1^+\Pi_1\} \\
 &= \text{tr}\left\{\sum_i \langle \phi_i | \sum_j d_j | \phi_j \rangle \langle \phi_0 | U_0 \hat{W}_{00} \sum_k d_k | \phi_0 \rangle \langle \phi_k | U_1^+ | \phi_i \rangle\right\} \\
 &= \text{tr}\left\{\hat{W}_{00} \sum_i d_i \langle \phi_0 | U_0 | \phi_0 \rangle \sum_k d_k \langle \phi_k | U_1^+ | \phi_i \rangle\right\}
 \end{aligned} \tag{6}$$

covers the population of the CC which is in the first excited state after the probe pulse, but was in the electronic ground state after the pump pulse. It is related to the dipole operator matrix element μ_{10} and represents the part of the population which was excited from the electronic ground to the first excited state.

Finally the sixth and last part of Eq. 1

$$\begin{aligned}
 & \text{tr}\{\Pi_0\mu_{01}U_1\mu_{10}\hat{W}_{00}U_0^+\Pi_0\} = \text{tr}\left\{\sum_i d_i \langle \phi_i | U_1 \sum_j d_j | \phi_j \rangle \langle \phi_0 | \hat{W}_{00} U_0^+ | \phi_0 \rangle\right\} \\
 &= \text{tr}\left\{\sum_i \sum_j \hat{W}_{00} d_i d_j \langle \phi_i | U_1 | \phi_j \rangle \langle \phi_0 | U_0^+ | \phi_0 \rangle\right\}
 \end{aligned} \tag{7}$$

covers the CC population which has been in the electronic ground state after the pump pulse and remains there after the probe pulse. It is the counterpart to Eq. 6.

Inserting Eqs. 2, 3, 4, 5, 6, 7 into Eq. 1 gives

$$\begin{aligned}
& \text{tr}\{\hat{\mu}U[\hat{\mu}, \hat{W}]U^+\} \\
&= \text{tr}\left\{\sum_i \sum_{j>i} \sum_k \sum_{l>k} \sum_q ((W_{lq}d_jd_k + W_{kq}d_jd_l) \langle \phi_q | U_1^+ | \phi_i \rangle + \right. \\
&\quad (W_{kq}d_id_l + W_{lq}d_id_k) \langle \phi_q | U_1^+ | \phi_j \rangle) \langle \phi_{ij} | U_2 | \phi_{kl} \rangle \\
&\quad - \sum_i \sum_{j>i} \sum_k \sum_{l>k} \sum_q ((W_{ql}d_jd_k + W_{qk}d_jd_l) \langle \phi_j | U_1 | \phi_q \rangle + \\
&\quad (W_{qk}d_id_l + W_{ql}d_id_k) \langle \phi_i | U_1 | \phi_q \rangle) \langle \phi_{kl} | U_2^+ | \phi_{ij} \rangle \\
&\quad + \sum_i \sum_k \sum_q d_id_k W_{kq} \langle \phi_q | U_1^+ | \phi_i \rangle \langle \phi_0 | U_0 | \phi_0 \rangle \\
&\quad - \sum_i \sum_k \sum_q d_id_k W_{qk} \langle \phi_i | U_1 | \phi_q \rangle \langle \phi_0 | U_0^+ | \phi_0 \rangle \\
&\quad + \sum_i \sum_k \hat{W}_{00} d_id_k \langle \phi_i | U_1 | \phi_k \rangle \langle \phi_0 | U_0^+ | \phi_0 \rangle \\
&\quad \left. - \sum_i \sum_k \hat{W}_{00} d_id_k \langle \phi_k | U_1^+ | \phi_i \rangle \langle \phi_0 | U_0 | \phi_0 \rangle\right\} \\
&= \text{tr}\left\{2\text{Im} \sum_{i,k,q} \sum_{j>i} \sum_{l>k} ((W_{lq}d_jd_k + W_{kq}d_jd_l) \langle \phi_q | U_1^+ | \phi_i \rangle \right. \\
&\quad + (W_{kq}d_id_l + W_{lq}d_id_k) \langle \phi_q | U_1^+ | \phi_j \rangle) \langle \phi_{ij} | U_2 | \phi_{kl} \rangle \\
&\quad + 2\text{Im} \sum_i \sum_k \sum_q d_id_k W_{kq} \langle \phi_q | U_1^+ | \phi_i \rangle \langle \phi_0 | U_0 | \phi_0 \rangle \\
&\quad \left. + 2\text{Im} \sum_i \sum_k \hat{W}_{00} d_id_k \langle \phi_i | U_1 | \phi_k \rangle \langle \phi_0 | U_0^+ | \phi_0 \rangle\right\}.
\end{aligned} \tag{8}$$

The first two terms on the right hand side of Eq. 8 arise from the Eqs. 3, 2 and treat second excited state absorption. The third and the fourth term in Eq. 8 stem from Eqs. 5, 4 and cover stimulated emission. The last two terms in Eq. 8 arise from Eqs. 6, 7 which are related to the excitation of first excited electronic states of the CC.

Appendix B

2 Computing the transient absorption for very short delay times

In the following the approximation is made that the mutual orientation of the Pheos is equally distributed. The starting point is Eq. 3.172:

$$\begin{aligned}
 & \text{tr}\{\hat{\mu}U[\hat{\mu}, \hat{W}]U^+\} \\
 &= \text{tr}\{2\text{Im} \sum_{i,k,q} \sum_{j>i} \sum_{l>k} ((W_{lq}d_jd_k + W_{kq}d_jd_l) \langle \phi_q | U_1^+ | \phi_i \rangle \\
 &+ (W_{kq}d_id_l + W_{lq}d_id_k) \langle \phi_q | U_1^+ | \phi_j \rangle) \langle \phi_{ij} | U_2 | \phi_{kl} \rangle \\
 &+ 2\text{Im} \sum_i \sum_k \sum_q d_id_k W_{kq} \langle \phi_q | U_1^+ | \phi_i \rangle \langle \phi_0 | U_0 | \phi_0 \rangle \\
 &+ 2\text{Im} \sum_i \sum_k \hat{W}_{00} d_id_k \langle \phi_i | U_1 | \phi_k \rangle \langle \phi_0 | U_0^+ | \phi_0 \rangle\}.
 \end{aligned} \tag{9}$$

The first term in Eq. 9 will be discussed in the end, since additional approximations will be necessary to simplify this term. The middle term on the right hand side of Eq. 9 corresponds to the stimulated emission. It can then be written as

$$\begin{aligned}
 & 2\text{tr}\{\text{Im} \sum_i \sum_k \sum_q d_id_k W_{kq} \langle \phi_q | U_1^+ | \phi_i \rangle \langle \phi_0 | U_0 | \phi_0 \rangle\}_{\text{ther}} \\
 &= 2\text{tr}\{\text{Im} \sum_i d_id_i W_{ii} \langle \phi_i | U_1^+ | \phi_i \rangle \langle \phi_0 | U_0 | \phi_0 \rangle \\
 &+ \text{Im} \sum_i \sum_{k \neq i} \sum_q d_id_k W_{kq} \langle \phi_q | U_1^+ | \phi_i \rangle \langle \phi_0 | U_0 | \phi_0 \rangle \\
 &+ \text{Im} \sum_i \sum_k \sum_{q \neq i} d_id_k W_{kq} \langle \phi_q | U_1^+ | \phi_i \rangle \langle \phi_0 | U_0 | \phi_0 \rangle\} \\
 &= 2\text{tr}\{\text{Im} \sum_i d_id_i W_{ii} \langle \phi_i | U_1^+ | \phi_i \rangle \langle \phi_0 | U_0 | \phi_0 \rangle \\
 &+ \text{Im} \sum_i \sum_{k \neq i} d_id_k W_{ki} \langle \phi_i | U_1^+ | \phi_i \rangle \langle \phi_0 | U_0 | \phi_0 \rangle\}.
 \end{aligned} \tag{10}$$

The sum over the $k \neq i$ is small since the averaging over the ensemble will give only a finite value for $q = i$. The sum over the $q \neq i$ has to be separated into two parts. The part $q \neq i, k$ is negligible, since it disappears in the ensemble-average. The part $q \neq i, q = k$ becomes zero. The matrix element $\langle \phi_i | U_1^+ | \phi_k \rangle$ itself becomes finite during the propagation in time, since the first excited state ϕ_i is propagated via the time evolution operator U_1^+ . However, the term vanishes during the ensemble averaging due to the single appearance of index i .

In the following, the last term in Eq. 9 is considered. It is responsible for the excited state

absorption. After the ensemble-average this term can be rewritten as

$$\begin{aligned}
& 2\text{tr}\{\text{Im} \sum_i \sum_k \hat{W}_{00} d_i d_k \langle \phi_i | U_1 | \phi_k \rangle \langle \phi_0 | U_0^+ | \phi_0 \rangle_{\text{ther}} \\
& = 2\text{tr}\{\text{Im} \sum_i \sum_k \sum_q (1 - \sum_{q \neq i} W_{qq}) d_i d_k \langle \phi_i | U_1 | \phi_k \rangle \langle \phi_0 | U_0^+ | \phi_0 \rangle \\
& = 2\text{tr}\{\text{Im} \sum_i (1 - W_{ii}) d_i d_i \langle \phi_i | U_1 | \phi_i \rangle \langle \phi_0 | U_0^+ | \phi_0 \rangle \\
& + \text{Im} \sum_i (1 - \sum_{q \neq i} W_{qq}) d_i d_i \langle \phi_i | U_1 | \phi_i \rangle \langle \phi_0 | U_0^+ | \phi_0 \rangle\}.
\end{aligned} \tag{11}$$

The first of the two terms on the right hand side of Eq. 11 covers the part where all indices are the same. In the second part, the matrix element of the statistical operator has another index than the dipole operator matrix element. All sums in Eq. 11 with $k \neq i$ become zero since the ensemble-average of a single d_k gives zero.

Before discussing the first term on the right hand side of Eq. 9, some additional considerations have to be made. Therefore, the eigenstates $|\alpha\rangle$ of the Hamiltonian H_1 as well as the eigenstates $|\beta\rangle$ of the Hamiltonian H_2 are defined. The respective eigenenergies are ϵ_α and ϵ_β . The product with the localized states $|\phi_m\rangle$ and $|\phi_{mn}\rangle$, respectively, are written as

$$\langle \alpha | \phi_m \rangle = A_m^\alpha, \tag{12}$$

and

$$\langle \beta | \phi_{mn} \rangle = A_{mn}^\beta. \tag{13}$$

With the completeness relation terms of the form $\langle \phi_m | U_1^+ | \phi_n \rangle \langle \phi_{ij} | U_2 | \phi_{kl} \rangle$ can be written as

$$\langle \phi_m | U_1^+ | \phi_n \rangle \langle \phi_{ml} | U_2 | \phi_{nl} \rangle = \sum_{\alpha, \beta} e^{-\frac{it}{\hbar}(\epsilon_\alpha - \epsilon_\beta)} A_m^\alpha(t) (A_n^\alpha(t))^* A_{ij}^\beta(t) (A_{kl}^\beta(t))^*. \tag{14}$$

When the ensemble-average is executed, those terms $\langle \phi_m | U_1^+ | \phi_n \rangle \langle \phi_{ij} | U_2 | \phi_{kl} \rangle$ that include non-diagonal matrix elements with $m \neq n$, $i \neq k$ or $j \neq l$ will dephase very fast compared to the diagonal parts. In the following the approximation will be made that those terms are neglected.

The first term on the right hand side of Eq. 9 which treats the second excited state absorption can then be rewritten. The first \approx neglects non-diagonal matrix elements of the statistical operator. Those non-diagonal matrix elements would result in fast dephasing terms of the form

$$\begin{aligned}
 & \langle \phi_m | U_1^+ | \phi_n \rangle \langle \phi_{ij} | U_2 | \phi_{kl} \rangle \\
 & 2\text{tr}\{ \text{Im} \sum_{i,k,q} \sum_{j>i} \sum_{l>k} (W_{lq} d_j d_k + W_{kq} d_j d_l) \langle \phi_q | U_1^+ | \phi_i \rangle \langle \phi_{ij} | U_2 | \phi_{kl} \rangle \\
 & + (W_{kq} d_i d_l + W_{lq} d_i d_k) \langle \phi_q | U_1^+ | \phi_j \rangle \langle \phi_{ij} | U_2 | \phi_{kl} \rangle) \} \\
 & \approx 2\text{tr}\{ \text{Im} (\sum_{i,k} \sum_{j>i} \sum_{l>k} (W_{ll} d_j d_k \langle \phi_l | U_1^+ | \phi_i \rangle + W_{kk} d_j d_l \langle \phi_k | U_1^+ | \phi_i \rangle) \langle \phi_{ij} | U_2 | \phi_{kl} \rangle \\
 & + \sum_{i,k} \sum_{j>i} \sum_{l>k} (W_{kk} d_i d_l \langle \phi_k | U_1^+ | \phi_j \rangle + W_{ll} d_i d_k \langle \phi_l | U_1^+ | \phi_j \rangle) \langle \phi_{ij} | U_2 | \phi_{kl} \rangle) \} \\
 & = 2\text{tr}\{ \text{Im} (\sum_i \sum_{j>i} W_{ii} d_j d_j \langle \phi_i | U_1^+ | \phi_i \rangle \langle \phi_{ij} | U_2 | \phi_{ij} \rangle \\
 & + \sum_i \sum_{j<i} W_{ii} d_j d_j \langle \phi_i | U_1^+ | \phi_i \rangle \langle \phi_{ji} | U_2 | \phi_{ji} \rangle \\
 & + \sum_i \sum_{j>i} \sum_{k \neq i, k < j} W_{ii} d_j d_j \langle \phi_i | U_1^+ | \phi_k \rangle \langle \phi_{ij} | U_2 | \phi_{kj} \rangle \\
 & + \sum_i \sum_{j>i} \sum_{k \neq i, k > j} W_{ii} d_j d_j \langle \phi_i | U_1^+ | \phi_k \rangle \langle \phi_{ij} | U_2 | \phi_{jk} \rangle \\
 & + \sum_i \sum_{j<i} \sum_{k \neq i, k < j} W_{ii} d_j d_j \langle \phi_i | U_1^+ | \phi_k \rangle \langle \phi_{ji} | U_2 | \phi_{kj} \rangle \\
 & + \sum_i \sum_{j<i} \sum_{k \neq i, k > j} W_{ii} d_j d_j \langle \phi_i | U_1^+ | \phi_k \rangle \langle \phi_{ji} | U_2 | \phi_{jk} \rangle \\
 & + \sum_i \sum_{j>i} \sum_{l \neq j, l > i} W_{ii} d_j d_l \langle \phi_i | U_1^+ | \phi_i \rangle \langle \phi_{ij} | U_2 | \phi_{il} \rangle \\
 & + \sum_i \sum_{j>i} \sum_{l \neq j, l < i} W_{ii} d_j d_l \langle \phi_i | U_1^+ | \phi_i \rangle \langle \phi_{ij} | U_2 | \phi_{li} \rangle \\
 & + \sum_i \sum_{j<i} \sum_{l \neq j, l > i} W_{ii} d_j d_l \langle \phi_i | U_1^+ | \phi_i \rangle \langle \phi_{ji} | U_2 | \phi_{il} \rangle \\
 & + \sum_i \sum_{j<i} \sum_{l \neq j, l < i} W_{ii} d_j d_l \langle \phi_i | U_1^+ | \phi_i \rangle \langle \phi_{ji} | U_2 | \phi_{li} \rangle \\
 & + \sum_i \sum_{j>i} W_{ij} d_j d_i \langle \phi_i | U_1^+ | \phi_i \rangle \langle \phi_{ij} | U_2 | \phi_{ij} \rangle \\
 & + \sum_i \sum_{j<i} W_{ij} d_j d_i \langle \phi_i | U_1^+ | \phi_i \rangle \langle \phi_{ji} | U_2 | \phi_{ji} \rangle) \}.
 \end{aligned} \tag{15}$$

The first ten terms on the right hand side of Eq. 15 include a statistical operator matrix element that is diagonal. The last two terms in Eq. 15 include the only non-disappearing non-diagonal matrix elements. The other terms that include non-diagonal matrix elements either contain an odd number of one particular index or they include matrix elements of the form $\langle \phi_i | U_1^+ | \phi_k \rangle \langle \phi_{ij} | U_2 | \phi_{kj} \rangle$. As stated above, those terms dephase fast and are neglected.

Appendix B

Eq. 15 can then be simplified to

$$\begin{aligned}
& 2\text{tr}\{\text{Im} \sum_{i,k,q} \sum_{j>i} \sum_{l>k} ((W_{lq}d_jd_k + W_{kq}d_jd_l) \langle \phi_q | U_1^+ | \phi_i \rangle \langle \phi_{ij} | U_2 | \phi_{kl} \rangle \\
& + (W_{kq}d_id_l + W_{lq}d_id_k) \langle \phi_q | U_1^+ | \phi_j \rangle \langle \phi_{ij} | U_2 | \phi_{kl} \rangle)\} \\
& \approx 2\text{tr}\{\text{Im}(\sum_i \sum_{j>i} W_{ii}d_jd_i \langle \phi_i | U_1^+ | \phi_i \rangle \langle \phi_{ij} | U_2 | \phi_{ij} \rangle \\
& + \sum_i \sum_{j<i} W_{ii}d_jd_i \langle \phi_i | U_1^+ | \phi_i \rangle \langle \phi_{ji} | U_2 | \phi_{ji} \rangle \\
& + \sum_i \sum_{j>i} W_{ij}d_jd_i \langle \phi_i | U_1^+ | \phi_i \rangle \langle \phi_{ij} | U_2 | \phi_{ij} \rangle \\
& + \sum_i \sum_{j<i} W_{ij}d_jd_i \langle \phi_i | U_1^+ | \phi_i \rangle \langle \phi_{ji} | U_2 | \phi_{ji} \rangle)\}.
\end{aligned} \tag{16}$$

Inserting the right hand sides of Eqs. 10, 11, 16 into Eq. 9 gives

$$\begin{aligned}
\text{tr}\{\hat{\rho}U[\hat{\rho}, \hat{W}]U^+\} & \approx 2\text{tr}\{\text{Im}(\sum_i \sum_{j>i} W_{ii}d_jd_i \langle \phi_i | U_1^+ | \phi_i \rangle \langle \phi_{ij} | U_2 | \phi_{ij} \rangle \\
& + \sum_i \sum_{j<i} W_{ii}d_jd_i \langle \phi_i | U_1^+ | \phi_i \rangle \langle \phi_{ji} | U_2 | \phi_{ji} \rangle \\
& + \sum_i \sum_{j>i} W_{ij}d_jd_i \langle \phi_i | U_1^+ | \phi_i \rangle \langle \phi_{ij} | U_2 | \phi_{ij} \rangle \\
& + \sum_i \sum_{j<i} W_{ij}d_jd_i \langle \phi_i | U_1^+ | \phi_i \rangle \langle \phi_{ji} | U_2 | \phi_{ji} \rangle \\
& + \sum_i d_id_i W_{ii} \langle \phi_i | U_1^+ | \phi_i \rangle \langle \phi_0 | U_0 | \phi_0 \rangle \\
& + \sum_i \sum_{j \neq i} d_id_j W_{ji} \langle \phi_i | U_1^+ | \phi_i \rangle \langle \phi_0 | U_0 | \phi_0 \rangle \\
& + \sum_i (1 - W_{ii})d_id_i \langle \phi_i | U_1 | \phi_i \rangle \langle \phi_0 | U_0^+ | \phi_0 \rangle \\
& + \sum_i (1 - \sum_{j \neq i} W_{jj})d_id_i \langle \phi_i | U_1 | \phi_i \rangle \langle \phi_0 | U_0^+ | \phi_0 \rangle)\}.
\end{aligned} \tag{17}$$

In the following the eigenstates $|\alpha\rangle$ and $|\beta\rangle$ of the Hamiltonians H_1 and H_2 are utilized again. The eigenstate for the electronic ground state is $|0\rangle$. The eigenenergy of the electronic ground state is denoted ϵ_0 . The diagonal matrix elements can be written (according to Eq. 14)

$$\langle \phi_m | U_1 | \phi_m \rangle = \sum_{\alpha} e^{-\frac{it}{\hbar}\epsilon_{\alpha}} A_m^{\alpha}(t) (A_m^{\alpha}(t))^* \tag{18}$$

for the first excited electronic CC states and

$$\langle \phi_{mn} | U_2 | \phi_{mn} \rangle = \sum_{\alpha, \beta} e^{-\frac{it}{\hbar}\epsilon_{\beta}} A_{mn}^{\beta}(t) (A_{mn}^{\beta}(t))^* \tag{19}$$

for the second excited electronic CC states.

2 Computing the transient absorption for very short delay times

With this definitions Eq. 17 can be rewritten in terms of the excitonic CC eigenenergies as

$$\begin{aligned}
\text{tr}\{\hat{\mu}U[\hat{\mu}, \hat{W}]U^+\} \approx & 2\text{tr}\{\text{Im} \sum_i \sum_{\alpha} [W_{ii}d_id_ie^{-\frac{it}{\hbar}(\epsilon_{\alpha}-\epsilon_0)}A_m^{\alpha}(t)(A_m^{\alpha}(t))^* \\
& + (1-W_{ii})d_id_ie^{\frac{it}{\hbar}(\epsilon_{\alpha}-\epsilon_0)}A_m^{\alpha}(t)(A_m^{\alpha}(t))^* \\
& + (1-\sum_{j \neq i} W_{jj})d_id_ie^{\frac{it}{\hbar}(\epsilon_{\alpha}-\epsilon_0)}A_m^{\alpha}(t)(A_m^{\alpha}(t))^* \\
& + \sum_{\beta} \sum_{j \neq i} W_{jj}d_id_ie^{\frac{it}{\hbar}(\epsilon_{\beta}-\epsilon_{\alpha})}A_m^{\alpha}(t)(A_m^{\alpha}(t))^*A_{mn}^{\beta}(t)(A_{mn}^{\beta}(t))^* \\
& + \sum_{\beta} \sum_{j \neq i} W_{ij}d_id_ie^{\frac{it}{\hbar}(\epsilon_{\beta}-\epsilon_{\alpha})}A_m^{\alpha}(t)(A_m^{\alpha}(t))^*A_{mn}^{\beta}(t)(A_{mn}^{\beta}(t))^* \\
& + \sum_{j \neq i} W_{ji}d_id_ie^{-\frac{it}{\hbar}(\epsilon_{\alpha}-\epsilon_0)}A_m^{\alpha}(t)(A_m^{\alpha}(t))^*]\}.
\end{aligned} \tag{20}$$

The probability $\mathcal{P}_m(t)$ that a CC in the initial state $|\phi_m\rangle$ (at $t = t_0$) will be in the same state after time t is defined as

$$\mathcal{P}_m(t) = \sum_{\alpha} A_m^{\alpha}(t)(A_m^{\alpha}(t))^*. \tag{21}$$

Accordingly the probability $\mathcal{P}_{mn}(t)$ that a CC in the initial state $|\phi_{mn}\rangle$ (at $t = t_0$) will be in the same state after time t is written

$$\mathcal{P}_{mn}(t) = \sum_{\beta} A_{mn}^{\beta}(t)(A_{mn}^{\beta}(t))^*. \tag{22}$$

With this definitions of the $\mathcal{P}_m(t)$ and $\mathcal{P}_{mn}(t)$, Eq. 17 can be simplified by making the following approximation: if the excitonic coupling between the chromophores is small (below 10 meV) it can be assumed that

$$\epsilon_{\beta} - \epsilon_{\alpha} \approx \epsilon_{\alpha} - \epsilon_0 \approx \Delta E_{g \rightarrow e}. \tag{23}$$

The transition energy $\Delta E_{g \rightarrow e}$ was defined in Sec. 3.2. Furthermore, the above defined probabilities $\mathcal{P}_m(t)$ and $\mathcal{P}_{mn}(t)$ vary slowly for small excitonic coupling. The ensemble-averaged correlation function vanishes fast due to dephasing after about 50 fs (compare with Sec. 4.5.1). Thus it can be assumed that during the dephasing time $t_{\text{dephasing}}$ the following relation holds:

$$\mathcal{P}_m(t_{\text{dephasing}}) \approx \mathcal{P}_{mn}(t_{\text{dephasing}}) \approx 1. \tag{24}$$

Therefore, for very small excitonic couplings, Eq. 20 can be further simplified to

$$\text{tr}\{\hat{\mu}U[\hat{\mu}, \hat{W}]U^+\} \approx 4\text{tr}\{\text{Im} \sum_i [(1-W_{ii})d_id_ie^{\frac{it}{\hbar}(\Delta E_{g \rightarrow e})}]\}. \tag{25}$$

The time scale of EET within P_4 is about 1-10 ps, dependent on the respective conformation. Thus, if the correlation function vanishes after 50 fs, the respective excitonic couplings within P_4 (1-10meV) can be assumed to be small.

Appendix C

3 Computing the electronic ground state reference trajectories

The following explanation on how to compute the ground state reference trajectories is mainly based on [84], the respective notation is slightly changed to match the notation utilized in this thesis. The coordinate index μ is dropped for simplification.

The ground state reference trajectory $R^g(t_j)$ at the discrete time $t_j = j\Delta t$ of the MD trajectory (time step $\Delta t = 1$ fs) is to be computed. The time and coordinate dependent period of oscillation, denoted as $T(t_j) = l_j\Delta t$ (l_j discretizes T_j), is utilized to calculate the value of the ground state reference trajectory at time t_j :

$$R^g(t_j) = \frac{1}{l_j} \sum_{n=-\{(l_j-1)/2\}}^{\{(l_j-1)/2\}} R(t_j + n\Delta t) + \frac{\{(l_j-1)/2\}}{2l_j} (R(t_j - l_j\Delta t/2) + R(t_j + l_j\Delta t/2)) . \quad (26)$$

$\{(l_j-1)/2\}$ defines the floor function, mapping the real number $(l_j-1)/2$ to the largest integer which is not greater than $(l_j-1)/2$. In the following, j will be determined by the tuple $n(j)$ and $k_{n(j)}$ as $j(n(j), k_{n(j)})$. $n(j)$ counts the maxima of the trajectory until the time t_j and $k_n(j)$ is the number of time steps between the actual time t_j and the last maximum at $t_{n,1}$ (note $k_{n(j)} = 1, \dots, k_n^{(\max)}$, below the index j will be dropped for n and k_n). All maxima of the trajectory have the index $k_n = 1$ by definition. Hence, j may be calculated from n and k_n by

$$j = \sum_{n'=0}^{n-1} \sum_{k_{n'}=1}^{k_{n'}^{(\max)}} 1 + k_n . \quad (27)$$

In the following, the time arguments $t_n^c = j^c\Delta t$ are introduced, which are positioned in the centers between the n' th and $(n+1)$ 'th maximum of the trajectory, i.e. $j^c = \{(j(n,1) + j(n+1,1))/2\}$. Since the time interval between the n' th and $(n+1)$ 'th maximum is $k_n^{(\max)}\Delta t$, the averaging time $l_j\Delta t$ for the time point t_n^c can be identified with $k_n^{(\max)}\Delta t$. The l_j in between may be calculated by a linear interpolation between two neighboring j^c :

$$l_j = k_n^{(\max)} + \left\{ \frac{(j - j^c) (k_{n+1}^{(\max)} - k_n^{(\max)})}{k_{n+1}^{(\max)} + k_n^{(\max)}} + \frac{1}{2} \right\} , \quad (28)$$

with $t_n^c/\Delta t < j < t_{n+1}^c/\Delta t$.

Bibliography

- [1] R. P. Feynman. *The Feynman Lectures on Physics*. Addison/Wesley, Reading, MA, 1963. ISBN 0-201-02115-3.
- [2] Th. Förster. Zwischenmolekulare Energiewanderung und Fluoreszenz. *Annalen der Physik*, 437(1-2):55–75, 1948.
- [3] D. L. Dexter. A theory of sensitized luminescence in solids. *The Journal of Chemical Physics*, 21(5):836–850, 1953.
- [4] Anne M. Brun and Anthony Harriman. Energy- and electron-transfer processes involving palladium porphyrins bound to dna. *Journal of the American Chemical Society*, 116(23): 10383–10393, 1994.
- [5] Jonathan L. Sessler, Bing Wang, and Anthony Harriman. Photoinduced energy transfer in associated, but noncovalently-linked photosynthetic model systems. *Journal of the American Chemical Society*, 117(2):704–714, 1995.
- [6] Vicki Cleave, Goghan Yahiloglu, Pierre Le Barny, Richard H. Friend, and Nir Tessler. Harvesting singlet and triplet energy in polymer leds. *Advanced Materials*, 11(4):285–288, 1999.
- [7] Vygintas Jankus, Edward W. Snedden, Daniel W. Bright, Victoria L. Whittle, J. A. G. Williams, and Andy Monkman. Energy upconversion via triplet fusion in super yellow PPV films doped with palladium tetraphenyltetrabenzoporphyrin: a comprehensive investigation of exciton dynamics. *Advanced Functional Materials*, 2012.
- [8] H. Van Amerongen, L. Valkunas, and R. Van Grondelle. *Photosynthetic Excitons*. World Scientific, 2000. ISBN 9789810232801.
- [9] J.R. Lakowicz. *Principles of Fluorescence Spectroscopy*. Number Bd. 1 in Principles of Fluorescence Spectroscopy. Springer, 2006. ISBN 9780387312781.
- [10] Kevin Truong and Mitsuhiro Ikura. The use of fret imaging microscopy to detect protein-protein interactions and protein conformational changes in vivo. *Current Opinion in Structural Biology*, 11(5):573 – 578, 2001.
- [11] Prashant V. Kamat. Meeting the clean energy demand: Nanostructure architectures for solar energy conversion. *The Journal of Physical Chemistry C*, 111(7):2834–2860, 2007.
- [12] Gopal K. Mor, James Basham, Maggie Paulose, Sanghoon Kim, Oomman K. Varghese, Amit Vaish, Sorachon Yoriya, and Craig A. Grimes. High-efficiency förster resonance energy transfer in solid-state dye sensitized solar cells. *Nano Letters*, 10(7):2387–2394, 2010.
- [13] Gregory S. Engel, Tessa R. Calhoun, Elizabeth L. Read, Tae-Kyu Ahn, Tomas Mancal, Yuan-Chung Cheng, Robert E. Blankenship, and Graham R. Fleming. Evidence for wave-like energy transfer through quantum coherence in photosynthetic systems. *Nature*, 446: 782–786, 2007.

Bibliography

- [14] Yuan-Chung Cheng and Graham R. Fleming. Dynamics of light harvesting in photosynthesis. *Annual Review of Physical Chemistry*, 60(1):241–262, 2009.
- [15] Mamoru Fujitsuka, Ayumi Okada, Sachiko Tojo, Fumie Takei, Kiyotaka Onitsuka, Shigetoshi Takahashi, and Tetsuro Majima. Rapid exciton migration and fluorescent energy transfer in helical polyisocyanides with regularly arranged porphyrin pendants. *The Journal of Physical Chemistry B*, 108(32):11935–11941, 2004.
- [16] Eve Hindin, Robert A. Forties, Robert S. Loewe, Arounaguiry Ambroise, Christine Kirmaier, David F. Bocian, Jonathan S. Lindsey, Dewey Holten, and Robert S. Knox. Excited-state energy flow in covalently linked multiporphyrin arrays: The essential contribution of energy transfer between nonadjacent chromophores. *The Journal of Physical Chemistry B*, 108(34):12821–12832, 2004.
- [17] Ying-Zhong Ma, Rebekah A. Miller, Graham R. Fleming, and Matthew B. Francis. Energy transfer dynamics in light-harvesting assemblies templated by the tobacco mosaic virus coat protein. *The Journal of Physical Chemistry B*, 112(22):6887–6892, 2008.
- [18] Hongzhen Lin, Rafael Camacho, Yuxi Tian, Theo E. Kaiser, Frank Wuürthner, and Ivan G. Scheblykin. Collective fluorescence blinking in linear J-aggregates assisted by long-distance exciton migration. *Nano Letters*, 10(2):620–626, 2010.
- [19] Debangshu Chaudhuri, Dongbo Li, Yanke Che, Eyal Shafran, Jordan M. Gerton, Ling Zang, and John M. Lupton. Enhancing long-range exciton guiding in molecular nanowires by H-aggregation lifetime engineering. *Nano Letters*, 11(2):488–492, 2011.
- [20] S. Masuo, T. Vosch, M. Cotlet, P. Tinnefeld, S. Habuchi, T.D.M. Bell, I. Oesterling, D. Beljonne, B. Champagne, K. Mullen, M. Sauer, J. Hofkens, and F.C. de Schryver. Multichromophoric dendrimers as single-photon sources: A single-molecule study. *Journal of Physical Chemistry B*, 108(43):16686–16696, 2004.
- [21] Jane Larsen, Ben Brüggemann, Tony Khoury, Joseph Sly, Maxwell J. Crossley, Villy Sundström, and Eva Åkesson. Structural induced control of energy transfer within zn(ii)-porphyrin dendrimers. *The Journal of Physical Chemistry A*, 111(42):10589–10597, 2007.
- [22] S. Hackbarth, E.A. Ermilov, and B. Röder. Interaction of pheophorbide-*a* molecules covalently linked to DAB dendrimers. *Optics Communications*, 248(1-3):295 – 306, 2005.
- [23] Gregory D. Scholes, Carles Curutchet, Benedetta Mennucci, and Roberto Cammi. How solvent controls electronic energy transfer and light harvesting: Toward a quantum-mechanical description of reaction field and screening effects. *The Journal of Physical Chemistry B*, 111(46):13253–13265, 2007.
- [24] Douglas L. Strout and Gustavo E. Scuseria. A quantitative study of the scaling properties of the Hartree-Fock method. *The Journal of Chemical Physics*, 102(21):8448–8452, 1995.
- [25] Xiao He and Kenneth M. Merz. Divide and conquer Hartree-Fock calculations on proteins. *Journal of Chemical Theory and Computation*, 6(2):405–411, 2010.
- [26] Volkhard May and Oliver Kühn. *Charge and energy transfer dynamics in molecular systems*. Wiley-VCH, 3rd edition, 2011. ISBN 978-3-527-40732-3.
- [27] Jang Sook Kwon, Chang Min Choi, Hwan Jin Kim, Nam Joon Kim, Joonkyung Jang, and Mino Yang. Combined theoretical modeling of photoexcitation spectrum of an isolated protonated tyrosine. *The Journal of Physical Chemistry A*, 113(12):2715–2723, 2009.

- [28] Carsten Olbrich and Ulrich Kleinekathöfer. Time-dependent atomistic view on the electronic relaxation in light-harvesting system ii. *The Journal of Physical Chemistry B*, 114(38):12427–12437, 2010.
- [29] Carsten Olbrich, Thomas L. C. Jansen, Jörg Liebers, Mortaza Aghtar, Johan Strümpfer, Klaus Schulten, Jasper Knoester, and Ulrich Kleinekathöfer. From atomistic modeling to excitation transfer and two-dimensional spectra of the FMO light-harvesting complex. *The Journal of Physical Chemistry B*, 115(26):8609–8621, 2011.
- [30] Yuanyuan Jing, Renhui Zheng, Hui-Xue Li, and Qiang Shi. Theoretical study of the electronic-vibrational coupling in the Q_y states of the photosynthetic reaction center in purple bacteria. *The Journal of Physical Chemistry B*, 116(3):1164–1171, 2012.
- [31] Sangwoo Shim, Patrick Rebentrost, Stéphanie Valleeau, and Alán Aspuru-Guzik. Atomistic study of the long-lived quantum coherences in the Fenna-Matthews-Olson complex. *Biophysical Journal*, 102(3):649 – 660, 2012.
- [32] M. E. Madjet, A. Abdurahman, and T. Renger. Intermolecular coulomb couplings from ab initio electrostatic potentials: Application to optical transitions of strongly coupled pigments in photosynthetic antennae and reaction centers. *The Journal of Physical Chemistry B*, 110(34):17268–17281, 2006.
- [33] Tobias Bornhütter. Private communication, August 2012.
- [34] Julia Adolphs, Frank Müh, Mohamed El-Amine Madjet, and Thomas Renger. Calculation of pigment transition energies in the FMO protein. *Photosynth Res*, 95, 2008.
- [35] Thomas Renger and Frank Müh. Theory of excitonic couplings in dielectric media. *Photosynthesis Research*, 111:47–52, 2012.
- [36] I. Eichwurzel, H. Stiel, and B. Röder. Photophysical studies of the pheophorbide-*a* dimer. *Journal of Photochemistry and Photobiology B: Biology*, 54(2-3):194–200, 2000.
- [37] Ellen M. M. de Brabander-van den Berg and E. W. Meijer. Poly(propylene imine) dendrimers: Large-scale synthesis by heterogeneously catalyzed hydrogenations. *Angewandte Chemie International Edition in English*, 32(9), 1993.
- [38] Minghui Chai, Yanhui Niu, Wiley J. Youngs, and Peter L. Rinaldi. Structure and conformation of DAB dendrimers in solution via multidimensional NMR techniques. *Journal of the American Chemical Society*, 123(20):4670–4678, 2001.
- [39] Jörg Megow, Beate Röder, Alexander Kulesza, Vlasta Bonačić-Koutecký, and Volkhard May. A mixed quantum-classical description of excitation energy transfer in supramolecular complexes: Förster theory and beyond. *ChemPhysChem*, 12(3):645 – 656, 2011.
- [40] B. Röder. *Einführung in die molekulare Photobiophysik*. Teubner Studienbücher. Teubner, 1999. ISBN 9783519032410.
- [41] Yasuhiro Matsumura and Hiroshi Maeda. A new concept for macromolecular therapeutics in cancer chemotherapy: Mechanism of tumoritropic accumulation of proteins and the antitumor agent smancs. *Cancer Research*, 46(12 Part 1):6387–6392, 1986.
- [42] Martin Gouterman, Georges H. Wagnière, and Lawrence C. Snyder. Spectra of porphyrins: Part II. four orbital model. *Journal of Molecular Spectroscopy*, 11(1-6):108 – 127, 1963.

Bibliography

- [43] P. J. Spellane, M. Gouterman, A. Antipas, S. Kim, and Y. C. Liu. Porphyrins. 40. electronic spectra and four-orbital energies of free-base, zinc, copper, and palladium tetrakis(perfluorophenyl)porphyrins. *Inorganic Chemistry*, 19(2):386–391, 1980.
- [44] J. H. Van Vleck. The correspondence principle in the statistical interpretation of quantum mechanics. *PNAS*, 14(2):178 – 188, 1928.
- [45] Michael Thoss and Haobin Wang. Semiclassical description of molecular dynamics based on initial-value representation methods. *Annual Review of Physical Chemistry*, 55(1):299–332, 2004.
- [46] Hagen Kleinert. *Pfadintegrale in Quantenmechanik, Statistik und Polymerphysik*. Spektrum Akademischer Verlag, Heidelberg, 1st edition, 1993. ISBN 3-86025-613-0.
- [47] William H. Miller. Classical s matrix: Numerical application to inelastic collisions. *The Journal of Chemical Physics*, 53(9):3578–3587, 1970.
- [48] William H. Miller. The semiclassical initial value representation: A potentially practical way for adding quantum effects to classical molecular dynamics simulations. *The Journal of Physical Chemistry A*, 105(13):2942–2955, 2001.
- [49] Michael F. Herman and Edward Kluk. A semiclassical justification for the use of non-spreading wavepackets in dynamics calculations. *Chemical Physics*, 91(1):27 – 34, 1984.
- [50] Edward Kluk, Michael F. Herman, and Heidi L. Davis. Comparison of the propagation of semiclassical frozen gaussian wave functions with quantum propagation for a highly excited anharmonic oscillator. *The Journal of Chemical Physics*, 84(1):326–334, 1986.
- [51] Kenneth G. Kay. Semiclassical initial value approximation for green’s function. *The Journal of Chemical Physics*, 132(24), 2010.
- [52] Norah E. Shemetulskis and Roger F. Loring. Semiclassical theory of the photon echo: Application to polar fluids. *The Journal of Chemical Physics*, 97(2):1217–1226, 1992.
- [53] E. Wigner. On the quantum correction for thermodynamic equilibrium. *Phys. Rev.*, 40: 749–759, 1932.
- [54] Qiang Shi and Eitan Geva. Semiclassical theory of vibrational energy relaxation in the condensed phase. *The Journal of Physical Chemistry A*, 107(43):9059–9069, 2003.
- [55] Qiang Shi and Eitan Geva. A comparison between different semiclassical approximations for optical response functions in nonpolar liquid solutions. *The Journal of Chemical Physics*, 122(6), 2005.
- [56] Qiang Shi and Eitan Geva. A comparison between different semiclassical approximations for optical response functions in nonpolar liquid solution. ii. the signature of excited state dynamics on two-dimensional spectra. *The Journal of Chemical Physics*, 129(12), 2008.
- [57] Jian Liu and William H. Miller. Linearized semiclassical initial value time correlation functions with maximum entropy analytic continuation. *The Journal of Chemical Physics*, 129(12), 2008.
- [58] Nancy Makri and Keiran Thompson. Semiclassical influence functionals for quantum systems in anharmonic environments. *Chemical Physics Letters*, 291(1-2):101 – 109, 1998.
- [59] Kenneth G. Kay. Semiclassical initial value treatments of atoms and molecules. *Annual Review of Physical Chemistry*, 56(1):255–280, 2005.

- [60] Eric J. Heller. Time-dependent approach to semiclassical dynamics. *The Journal of Chemical Physics*, 62(4):1544–1555, 1975.
- [61] Eric J. Heller. Frozen gaussians: A very simple semiclassical approximation. *The Journal of Chemical Physics*, 75(6):2923–2931, 1981.
- [62] Dominik Marx and Jürg Hutter. Ab initio molecular dynamics: Theory and implementation. In J. Grotendorst, editor, *Modern Methods and Algorithms of Quantum Chemistry*, pages 301–449. John von Neumann Institute for Computing, Julich, 1. edition, 2000. ISBN 3-00-005618-1.
- [63] John C. Tully. Mixed quantum-classical dynamics. *Faraday Discuss.*, 110:407–419, 1998.
- [64] Nikos L. Doltsinis and Dominik Marx. Nonadiabatic car-parrinello molecular dynamics. *Phys. Rev. Lett.*, 88:166402, 2002.
- [65] John C. Tully. Molecular dynamics with electronic transitions. *The Journal of Chemical Physics*, 93(2):1061–1071, 1990.
- [66] Karen Drukker. Basics of surface hopping in mixed quantum/classical simulations. *Journal of Computational Physics*, 153(2):225 – 272, 1999.
- [67] Eric R. Bittner and Peter J. Rossky. Quantum decoherence in mixed quantum-classical systems: Nonadiabatic processes. *The Journal of Chemical Physics*, 103(18):8130–8143, 1995.
- [68] Adolfo Bastida, Miguel A. Soler, José Zúñiga, Alberto Requena, Adrián Kalstein, and Sebastián Fernández-Alberti. Hybrid quantum/classical simulations of the vibrational relaxation of the amide i mode of n-methylacetamide in d2o solution. *The Journal of Physical Chemistry B*, 116(9):2969–2980, 2012.
- [69] Sebastian Fernandez-Alberti, Valeria D. Kleiman, Sergei Tretiak, and Adrian E. Roitberg. Nonadiabatic molecular dynamics simulations of the energy transfer between building blocks in a phenylene ethynylene dendrimer. *The Journal of Physical Chemistry A*, 113(26):7535–7542, 2009.
- [70] M. Born and R. Oppenheimer. Zur Quantentheorie der Molekeln. *Annalen der Physik*, 389(20), 1927.
- [71] R. Car and M. Parrinello. Unified approach for molecular dynamics and density-functional theory. *Phys. Rev. Lett.*, 55:2471–2474, Nov 1985.
- [72] Jürg Hutter and Alessandro Curioni. Car-parrinello molecular dynamics on massively parallel computers. *ChemPhysChem*, 6(9):1788–1793, 2005.
- [73] E. Gindensperger, C. Meier, and J. A. Beswick. Mixing quantum and classical dynamics using bohmian trajectories. *The Journal of Chemical Physics*, 113(21):9369–9372, 2000.
- [74] C. Meier and J. A. Beswick. Femtosecond pump-probe spectroscopy of I₂ in a dense rare gas environment: A mixed quantum/classical study of vibrational decoherence. *The Journal of Chemical Physics*, 121(10):4550–4558, 2004.
- [75] Hui Zhu, Volkhard May, Beate Röder, Mohamed El-Amine Madjet, and Thomas Renger. The pheophorbide-a DAB dendrimer P₄ in solution: MD simulations based studies of exciton states. *Chemical Physics Letters*, 444(1-3):118 – 124, 2007.
- [76] V. A. Ermoshin, A. K. Kazansky, and V. Engel. Quantum-classical molecular dynamics simulation of femtosecond spectroscopy on I₂ in inert gases: Mechanisms for the decay of pump-probe signals. *The Journal of Chemical Physics*, 111(17):7807–7817, 1999.

- [77] Oliver Kühn and Nancy Makri. Forward-backward semiclassical calculation of spectral line shapes: I2 in a rare gas cluster. *The Journal of Physical Chemistry A*, 103(47):9487–9493, 1999.
- [78] Michele Ceotto, Sule Atahan, Sangwoo Shim, Gian Franco Tantardini, and Alan Aspuru-Guzik. First-principles semiclassical initial value representation molecular dynamics. *Phys. Chem. Chem. Phys.*, 11, 2009.
- [79] P. Ehrenfest. Bemerkung über die angenäherte Gültigkeit der klassischen Mechanik innerhalb der Quantenmechanik. *Zeitschrift für Physik A Hadrons and Nuclei*, 45:455–457, 1927.
- [80] David E. Shaw, Martin M. Deneroff, Ron O. Dror, Jeffrey S. Kuskin, Richard H. Larson, John K. Salmon, Cliff Young, Brannon Batson, Kevin J. Bowers, Jack C. Chao, Michael P. Eastwood, Joseph Gagliardo, J. P. Grossman, C. Richard Ho, Douglas J. Jerardi, István Kolossváry, John L. Klepeis, Timothy Layman, Christine McLeavey, Mark A. Moraes, Rolf Mueller, Edward C. Priest, Yibing Shan, Jochen Spengler, Michael Theobald, Brian Towles, and Stanley C. Wang. Anton, a special-purpose machine for molecular dynamics simulation. *Commun. ACM*, 51(7):91–97, July 2008.
- [81] Charles Kittel. *Einführung in die Festkörperphysik*. Oldenburg, 13th edition, 2002. ISBN 3-486-27219-5.
- [82] Hui Zhu, Volkhard May, Beate Röder, and Thomas Renger. Linear absorbance of the pheophorbide-*a* butanedi-amine dendrimer P₄ in solution: Computational studies using a mixed quantum classical methodology. *The Journal of Chemical Physics*, 128(15), 2008.
- [83] Hui Zhu, Volkhard May, and Beate Röder. Mixed quantum classical simulations of electronic excitation energy transfer: The pheophorbide-*a* DAB dendrimer P₄ in solution. *Chemical Physics*, 351(1-3):117 – 128, 2008.
- [84] Jörg Megow, Alexander Kulesza, Zheng wang Qu, Thomas Ronneberg, Vlasta Bonačić-Koutecký, and Volkhard May. A harmonic approximation of intramolecular vibrations in a mixed quantum-classical methodology: Linear absorbance of a dissolved pheophorbide-*a* molecule as an example. *Chemical Physics*, 377(1-3):10 – 14, 2010.
- [85] Jörg Megow, Yaroslav Zelinsky, Beate Röder, Alexander Kulesza, Roland Mitrić, and Volkhard May. Transient absorption spectra of excitation energy transfer in supramolecular complexes: A mixed quantum-classical description of pheophorbide-*a* systems. *Chemical Physics Letters*, 522(0):103 – 107, 2012.
- [86] Glauciete S. Maciel and Edgardo Garcia. Charges derived from electrostatic potentials: Exploring dependence on theory and geometry optimization levels for dipole moments. *Chemical Physics Letters*, 409(1-3):29 – 33, 2005.
- [87] Hui Zhu, Beate Röder, and Volkhard May. Time and frequency resolved spontaneous emission from supramolecular pheophorbide-*a* complexes: A mixed quantum classical computation. *Chemical Physics*, 362(1-2):19 – 26, 2009.
- [88] Frank Neese. Prediction of molecular properties and molecular spectroscopy with density functional theory: From fundamental theory to exchange-coupling. *Coordination Chemistry Reviews*, 253(5-6):526 – 563, 2009.
- [89] B. M. Auer and J. L. Skinner. Dynamical effects in line shapes for coupled chromophores: Time-averaging approximation. *The Journal of Chemical Physics*, 127(10), 2007.

- [90] J. G. Saven and J. L. Skinner. A molecular theory of the line shape: Inhomogeneous and homogeneous electronic spectra of dilute chromophores in nonpolar fluids. *The Journal of Chemical Physics*, 99(6):4391–4402, 1993.
- [91] Shaul Mukamel. *Principles of nonlinear optical spectroscopy*. N.Y. and Oxford: Oxford University Press, 1st edition, 1997.
- [92] S. A. Egorov, Eran Rabani, and B. J. Berne. Vibronic spectra in condensed matter: A comparison of exact quantum mechanical and various semiclassical treatments for harmonic baths. *Journal of Chemical Physics*, 108(4):1407–1422, 1998.
- [93] Giuseppe Zucchelli, Robert C. Jennings, Flavio M. Garlaschi, Gianfelice Cinque, Roberto Bassi, and Oliviero Cremonesi. The calculated in vitro and in vivo chlorophyll-*a* absorption bandshape. *Biophysical Journal*, 82(1):378 – 390, 2002.
- [94] Jason D. Weibel, Charles F. Jackels, and Robert L. Swofford. Experimental and ab initio investigation of the o-h overtone vibration in ethanol. *The Journal of Chemical Physics*, 117(9):4245–4254, 2002.
- [95] K. Huang and A. Rhys. Untitled. *Proc. Roy. Soc. London*, A204, 1950.
- [96] Seogjoo Jang, Marshall D. Newton, and Robert J. Silbey. Multichromophoric Förster resonance energy transfer. *Phys. Rev. Lett.*, 92:218301, May 2004.
- [97] Brent P. Krueger, Gregory D. Scholes, and Graham R. Fleming. Calculation of couplings and energy-transfer pathways between the pigments of lh2 by the ab initio transition density cube method. *The Journal of Physical Chemistry B*, 102(27):5378–5386, 1998.
- [98] Ana Damjanovic, Thorsten Ritz, and Klaus Schulten. Excitation transfer in the peridinin-chlorophyll-protein of amphidinium carterae. *Biophysical journal*, 79(4):1695–1705, 2000.
- [99] I. A. Howard, F. Zutterman, G. Deroover, D. Lamoen, and C. Van Alsenoy. Approaches to calculation of exciton interaction energies for a molecular dimer. *The Journal of Physical Chemistry B*, 108(50):19155–19162, 2004.
- [100] Burkhard Fückel, Andreas Kohn, Michael E. Harding, Gregor Diezemann, Gerald Hinze, Thomas Basche, and Jürgen Gauss. Theoretical investigation of electronic excitation energy transfer in bichromophoric assemblies. *The Journal of Chemical Physics*, 128(7), 2008.
- [101] Robert S. Knox and Bryan Q. Spring. Dipole strengths in the chlorophylls. *Photochemistry and Photobiology*, 77(5):497–501, 2003.
- [102] David Beljonne, Carles Curutchet, Gregory D. Scholes, and Robert J. Silbey. Beyond Förster resonance energy transfer in biological and nanoscale systems. *The Journal of Physical Chemistry B*, 113(19):6583–6599, 2009.
- [103] Seogjoo Jang. Generalization of the Förster resonance energy transfer theory for quantum mechanical modulation of the donor-acceptor coupling. *The Journal of Chemical Physics*, 127(17), 2007.
- [104] Z. G. Yu. Fluorescent resonant energy transfer: Correlated fluctuations of donor and acceptor. *The Journal of Chemical Physics*, 127(22), 2007.
- [105] S. A. Egorov, Eran Rabani, and B. J. Berne. Nonradiative relaxation processes in condensed phases: Quantum versus classical baths. *Journal of Chemical Physics*, 110(11): 5238–5248, 1999.

Bibliography

- [106] Volkhard May. Higher-order processes of excitation energy transfer in supramolecular complexes: Liouville space analysis of bridge molecule mediated transfer and direct photon exchange. *The Journal of Chemical Physics*, 129(11), 2008.
- [107] Shaul Mukamel and Darius Abramavicius. Many-body approaches for simulating coherent nonlinear spectroscopies of electronic and vibrational excitons. *Chemical Reviews*, 104(4):2073–2098, 2004.
- [108] Minhaeng Cho, Harsha M. Vaswani, Tobias Brixner, Jens Stenger, and Graham R. Fleming. Exciton analysis in 2D electronic spectroscopy. *The Journal of Physical Chemistry B*, 109(21):10542–10556, 2005.
- [109] Minhaeng Cho. Coherent two-dimensional optical spectroscopy. *Chemical Reviews*, 108(4):1331–1418, 2008.
- [110] Thomas la Cour Jansen and Jasper Knoester. Nonadiabatic effects in the two-dimensional infrared spectra of peptides: Application to alanine dipeptide. *The Journal of Physical Chemistry B*, 110(45):22910–22916, 2006.
- [111] Thomas I. C. Jansen and Jasper Knoester. Waiting time dynamics in two-dimensional infrared spectroscopy. *Accounts of Chemical Research*, 42(9):1405–1411, 2009.
- [112] Being J. Ka and Eitan Geva. A nonperturbative calculation of nonlinear spectroscopic signals in liquid solution. *The Journal of Chemical Physics*, 125(21), 2006.
- [113] Luis Seidner, Gerhard Stock, and Wolfgang Domcke. Nonperturbative approach to femtosecond spectroscopy: General theory and application to multidimensional nonadiabatic photoisomerization processes. *The Journal of Chemical Physics*, 103(10):3998–4011, 1995.
- [114] F. Bloch and A. Siegert. Magnetic resonance for nonrotating fields. *Phys. Rev.*, 57, Mar 1940.
- [115] Ben Brüggemann, Petter Persson, Hans-Dieter Meyer, and Volkhard May. Frequency dispersed transient absorption spectra of dissolved perylene: A case study using the density matrix version of the MCTDH method. *Chemical Physics*, 347(1-3):152 – 165, 2008.
- [116] Haobin Wang and Michael Thoss. Nonperturbative simulation of pump-probe spectra for electron transfer reactions in the condensed phase. *Chemical Physics Letters*, 389(1-3): 43 – 50, 2004.
- [117] Pär Kjellberg, Ben Brüggemann, and Tönu Pullerits. Two-dimensional electronic spectroscopy of an excitonically coupled dimer. *Phys. Rev. B*, 74:024303, Jul 2006.
- [118] Ben Brüggemann, Pär Kjellberg, and Tönu Pullerits. Non-perturbative calculation of 2D spectra in heterogeneous systems: Exciton relaxation in the FMO complex. *Chemical Physics Letters*, 444(1-3):192 – 196, 2007.
- [119] S. Hess, E. Åkesson, R.J. Cogdell, T. Pullerits, and V. Sundström. Energy transfer in spectrally inhomogeneous light-harvesting pigment-protein complexes of purple bacteria. *Biophysical Journal*, 69(6):2211 – 2225, 1995.
- [120] Bernard R. Brooks, Robert E. Bruccoleri, Barry D. Olafson, David J. States, S. Swaminathan, and Martin Karplus. Charmm: A program for macromolecular energy, minimization, and dynamics calculations. *Journal of Computational Chemistry*, 4(2), 1983.

- [121] D. A. Case, T. A. Darden, T. E. Cheatham, III, C. L. Simmerling, J. Wang, R. E. Duke, R. Luo, K. M. Merz, B. Wang, D. A. Pearlman, M. Crowley, S. Brozell, V. Tsui, H. Gohlke, J. Mongan, V. Hornak, G. Cui, P. Beroza, C. Schafmeister, J. W. Caldwell, W. S. Ross, and P. A. Kollman. *AMBER 8*. University of California, San Francisco, CA, 2004.
- [122] David Van Der Spoel, Erik Lindahl, Berk Hess, Gerrit Groenhof, Alan E. Mark, and Herman J. C. Berendsen. Gromacs: Fast, flexible, and free. *Journal of Computational Chemistry*, 26(16):1701–1718, 2005.
- [123] James C. Phillips, Rosemary Braun, Wei Wang, James Gumbart, Emad Tajkhorshid, Elizabeth Villa, Christophe Chipot, Robert D. Skeel, Laxmikant Kale, , and Klaus Schulten. Scalable molecular dynamics with NAMD. *Journal of Computational Chemistry*, 26:1781–1802, 2005.
- [124] Junmei Wang, Romain M. Wolf, James W. Caldwell, Peter A. Kollman, and David A. Case. Development and testing of a general amber force field. *Journal of Computational Chemistry*, 25(9):1157–1174, 2004.
- [125] Thomas Fox and Peter A. Kollman. Application of the resp methodology in the parametrization of organic solvents. *The Journal of Physical Chemistry B*, 102(41):8070–8079, 1998.
- [126] Tom Darden, Darrin York, and Lee Pedersen. Particle mesh ewald: An $N \times \log(N)$ method for ewald sums in large systems. *The Journal of Chemical Physics*, 98(12):10089–10092, 1993.
- [127] P. P. Ewald. Die berechnung optischer und elektrostatischer gitterpotentiale. *Annalen der Physik*, 369(3):253–287, 1921.
- [128] Wendy D. Cornell, Piotr Cieplak, Christopher I. Bayly, Ian R. Gould, Kenneth M. Merz, David M. Ferguson, David C. Spellmeyer, Thomas Fox, James W. Caldwell, and Peter A. Kollman. A second generation force field for the simulation of proteins, nucleic acids, and organic molecules. *Journal of the American Chemical Society*, 117(19):5179–5197, 1995.
- [129] M. Germana Paterlini and David M Ferguson. Constant temperature simulations using the langevin equation with velocity Verlet integration. *Chemical Physics*, 236(1-3):243 – 252, 1998.
- [130] Glenn J. Martyna, Douglas J. Tobias, and Michael L. Klein. Constant pressure molecular dynamics algorithms. *The Journal of Chemical Physics*, 101(5):4177–4189, 1994.
- [131] Scott E. Feller, Yuhong Zhang, Richard W. Pastor, and Bernard R. Brooks. Constant pressure molecular dynamics simulation: The langevin piston method. *The Journal of Chemical Physics*, 103(11):4613–4621, 1995.
- [132] M. Bhandarkar, R. Brunner, C. Chipot, A. Dalke, S. Dixit, P. Grayson, J. Gullingsrud, A. Gursoy, D. Hardy, W. Humphrey, D. Hurwitz, N. Krawetz, M. Nelson, J. Phillips, A. Shinozaki, and F. Zhu G. Zheng. NAMD user’s guide, 2012.
- [133] Sadaf R. Alam, Jeffrey S. Vetter, Pratul K. Agarwal, and Al Geist. Performance characterization of molecular dynamics techniques for biomolecular simulations. In *Proceedings of the eleventh ACM SIGPLAN symposium on Principles and practice of parallel programming*, PPOPP ’06, pages 59–68. ACM, 2006. ISBN 1-59593-189-9.
- [134] Tim Isgro. NAMD tutorial. *October*, 67(October), 2010.

Bibliography

- [135] Peter J. Steinbach and Bernard R. Brooks. Protein simulation below the glass-transition temperature. dependence on cooling protocol. *Chemical Physics Letters*, 226(5-6):447 – 452, 1994.
- [136] M. J. Frisch, G. W. Trucks, H. B. Schlegel, G. E. Scuseria, M. A. Robb, J. R. Cheeseman, G. Scalmani, V. Barone, B. Mennucci, G. A. Petersson, H. Nakatsuji, M. Caricato, X. Li, H. P. Hratchian, A. F. Izmaylov, J. Bloino, G. Zheng, J. L. Sonnenberg, M. Hada, M. Ehara, K. Toyota, R. Fukuda, J. Hasegawa, M. Ishida, T. Nakajima, Y. Honda, O. Kitao, H. Nakai, T. Vreven, J. A. Montgomery, Jr., J. E. Peralta, F. Ogliaro, M. Bearpark, J. J. Heyd, E. Brothers, K. N. Kudin, V. N. Staroverov, R. Kobayashi, J. Normand, K. Raghavachari, A. Rendell, J. C. Burant, S. S. Iyengar, J. Tomasi, M. Cossi, N. Rega, J. M. Millam, M. Klene, J. E. Knox, J. B. Cross, V. Bakken, C. Adamo, J. Jaramillo, R. Gomperts, R. E. Stratmann, O. Yazyev, A. J. Austin, R. Cammi, C. Pomelli, J. W. Ochterski, R. L. Martin, K. Morokuma, V. G. Zakrzewski, G. A. Voth, P. Salvador, J. J. Dannenberg, S. Dapprich, A. D. Daniels, Ö. Farkas, J. B. Foresman, J. V. Ortiz, J. Cioslowski, and D. J. Fox. Gaussian 09 Revision A.1, 2009.
- [137] A. D. Becke. Density-functional exchange-energy approximation with correct asymptotic behavior. *Phys. Rev. A*, 38:3098–3100, Sep 1988.
- [138] Axel D. Becke. Density-functional thermochemistry. iii. the role of exact exchange. *The Journal of Chemical Physics*, 98(7):5648–5652, 1993.
- [139] Chengteh Lee, Weitao Yang, and Robert G. Parr. Development of the colle-salvetti correlation-energy formula into a functional of the electron density. *Phys. Rev. B*, 37:785–789, Jan 1988.
- [140] R. Krishnan, J. S. Binkley, R. Seeger, and J. A. Pople. Self-consistent molecular orbital methods. xx. a basis set for correlated wave functions. *The Journal of Chemical Physics*, 72(1):650–654, 1980.
- [141] Julian Tirado-Rives and William L. Jorgensen. Performance of b3lyp density functional methods for a large set of organic molecules. *Journal of Chemical Theory and Computation*, 4(2):297–306, 2008.
- [142] Jacopo Tomasi, Benedetta Mennucci, and Roberto Cammi. Quantum mechanical continuum solvation models. *ChemInform*, 36(42), 2005.
- [143] Giovanni Scalmani, Michael J. Frisch, Benedetta Mennucci, Jacopo Tomasi, Roberto Cammi, and Vincenzo Barone. Geometries and properties of excited states in the gas phase and in solution: Theory and application of a time-dependent density functional theory polarizable continuum model. *The Journal of Chemical Physics*, 124(9), 2006.
- [144] Maurizio Cossi and Vincenzo Barone. Time-dependent density functional theory for molecules in liquid solutions. *The Journal of Chemical Physics*, 115(10):4708–4717, 2001.
- [145] Curt M. Breneman and Kenneth B. Wiberg. Determining atom-centered monopoles from molecular electrostatic potentials. the need for high sampling density in formamide conformational analysis. *Journal of Computational Chemistry*, 11(3), 1990.
- [146] Evelyn Mayaan, Adam Moser, Alexander D. MacKerell, and Darrin M. York. Charmm force field parameters for simulation of reactive intermediates in native and thio-substituted ribozymes. *Journal of Computational Chemistry*, 28(2):495–507, 2007.
- [147] Christopher I. Bayly, Piotr Cieplak, Wendy Cornell, and Peter A. Kollman. A well-behaved electrostatic potential based method using charge restraints for deriving atomic charges: the resp model. *The Journal of Physical Chemistry*, 97(40):10269–10280, 1993.

- [148] Dirk Porezag and Mark R. Pederson. Infrared intensities and raman-scattering activities within density-functional theory. *Phys. Rev. B*, 54:7830–7836, 1996.
- [149] Zheng-wang Qu, Hui Zhu, and Volkhard May. Unambiguous assignment of vibrational spectra of cyclosporins a and h. *The Journal of Physical Chemistry A*, 114(36):9768–9773, 2010.
- [150] Abraham. Savitzky and M. J. E. Golay. Smoothing and differentiation of data by simplified least squares procedures. *Analytical Chemistry*, 36(8):1627–1639, 1964.
- [151] M. Rätsep, T. W. Johnson, P. R. Chitnis, and G. J. Small. The red-absorbing chlorophyll a antenna states of photosystem I: A hole-burning study of *synechocystis* sp. pcc 6803 and its mutants. *The Journal of Physical Chemistry B*, 104(4):836–847, 2000.
- [152] Naranbaatar Dashdorj, Wu Xu, Peter Martinsson, Parag R Chitnis, and Sergei Savikhin. Electrochromic shift of chlorophyll absorption in photosystem I from *synechocystis* sp. pcc 6803: a probe of optical and dielectric properties around the secondary electron acceptor. *Biophys J*, 86(5):3121–30, 2004.
- [153] Ksenia Dolgaleva. *Local-Field Effects and Nanostructuring for Controlling Optical Properties and Enabling Novel Optical Phenomena*. PhD thesis, University of Rochester, Rochester, New York, 2008.
- [154] Jörg Megow and Volkhard May. Pheophorbide-*a* Q_x - and Q_y -band vibrational progression in a mixed quantum-classical description. 2012. in preparation.
- [155] Martin Regehly, Eugeny A. Ermilov, Matthias Helmreich, Andreas Hirsch, Norbert Jux, and Beate Röder. Photoinduced energy and electron transfer processes in hexapyropheophorbide-*a*- fullerene [C60] molecular systems. *The Journal of Physical Chemistry B*, 111(5):998–1006, 2007.
- [156] Naomi J. Halas. Plasmonics: An emerging field fostered by nano letters. *Nano Letters*, 10(10):3816–3822, 2010.
- [157] Takayuki Uwada, Ryo Toyota, Hiroshi Masuhara, and Tsuyoshi Asahi. Single particle spectroscopic investigation on the interaction between exciton transition of cyanine dye J-aggregates and localized surface plasmon polarization of gold nanoparticles. *The Journal of Physical Chemistry C*, 111(4):1549–1552, 2007.
- [158] Itai Carmeli, Itai Lieberman, Leon Kravetsky, Zhiyuan Fan, Alexander O. Govorov, Gil Markovich, and Shachar Richter. Broad band enhancement of light absorption in photosystem I by metal nanoparticle antennas. *Nano Letters*, 10(6):2069–2074, 2010.
- [159] J. Bellessa, C. Bonnand, J. C. Plenat, and J. Mugnier. Strong coupling between surface plasmons and excitons in an organic semiconductor. *Phys. Rev. Lett.*, 93:036404, Jul 2004.
- [160] E.E. Jelley. Spectral absorption and fluorescence of dyes in the molecular state. *Nature*, 136:1009, 1936.
- [161] Y. Sugawara, T. A. Kelf, J. J. Baumberg, M. E Abdelsalam, and P. N. Bartlett. Strong coupling between localized plasmons and organic excitons in metal nanovoids. *Phys. Rev. Lett.*, 97, 2006.
- [162] N. I. Cade, T. Ritman-Meer, and D. Richards. Strong coupling of localized plasmons and molecular excitons in nanostructured silver films. *Phys. Rev. B*, 79:241404, Jun 2009.

Bibliography

- [163] Martin Aeschlimann, Michael Bauer, Daniela Bayer, Tobias Brixner, Stefan Cunovic, Frank Dimler, Alexander Fischer, Walter Pfeiffer, Martin Rohmer, Christian Schneider, Felix Steeb, Christian Strüber, and Dmitri V. Voronine. Spatiotemporal control of nanooptical excitations. *Proceedings of the National Academy of Sciences*, 2010.
- [164] Gerold Kyas, Yaroslav Zelinskyy, Yuan Zhang, and Volkhard May. Spatio-temporal excitation energy localization in a supramolecular complex coupled to a metal-nanoparticle. *Annalen der Physik*, 2012.
- [165] Anne Myers Kelley. A molecular spectroscopic description of optical spectra of J-aggregated dyes on gold nanoparticles. *Nano Letters*, 7(10):3235–3240, 2007.
- [166] Nche T. Fofang, Tae-Ho Park, Oara Neumann, Nikolay A. Mirin, Peter Nordlander, and Naomi J. Halas. Plexcitonic nanoparticles: Plasmon-exciton coupling in nanoshell-J-aggregate complexes. *Nano Letters*, 8(10):3481–3487, 2008.
- [167] Vitaliy N. Pustovit and Tigran V. Shahbazyan. Cooperative emission of light by an ensemble of dipoles near a metal nanoparticle: The plasmonic Dicke-effect. *Phys. Rev. Lett.*, 102, Feb 2009.
- [168] Vitaliy N. Pustovit and Tigran V. Shahbazyan. Plasmon-mediated superradiance near metal nanostructures. *Phys. Rev. B*, 82, 2010.
- [169] Gerold Kyas and Volkhard May. Density matrix based microscopic theory of molecule metal-nanoparticle interactions: Linear absorbance and plasmon enhancement of intermolecular excitation energy transfer. *The Journal of Chemical Physics*, 134(3), 2011.
- [170] Yaroslav Zelinskyy and Volkhard May. Optical properties of supramolecular complexes coupled to a metal-nanoparticle: A computational study. *Chemical Physics Letters*, 511(4 - 6):372 – 377, 2011.
- [171] Yaroslav Zelinskyy Volkhard May, Jörg Megow. Excitation energy transfer in molecular complexes: Transport processes, optical properties and effects of nearby placed metal nano-particles. *Proc. SPIE*, 8424(842403-1), 2012.
- [172] Jörg Megow and Volkhard May. Pheophorbide-*a* and the P₁₆ chromophore complex coupling to a gold nano particle. a mixed quantum-classical description. 2012. in preparation.
- [173] Ugo Fano. Effects of configuration interaction on intensities and phase shifts. *Phys. Rev.*, 124:1866–1878, 1961.
- [174] Julia Adolphs and Thomas Renger. How proteins trigger excitation energy transfer in the FMO complex of green sulfur bacteria. *Biophysical journal*, 91(8), 2006.
- [175] Frank Müh, Mohamed El-Amine Madjet, Julia Adolphs, Ayjamal Abdurahman, Björn Rabenstein, Hiroshi Ishikita, Ernst-Walter Knapp, and Thomas Renger. α -helices direct excitation energy flow in the Fenna-Matthews-Olson protein. *Proceedings of the National Academy of Sciences*, 104(43):16862–16867, 2007.
- [176] Thomas Renger. Theory of excitation energy transfer: from structure to function. *Photosynthesis Research*, 102:471–485, 2009.
- [177] Carles Curutchet, Aurora Muñoz-Losa, Susanna Monti, Jacob Kongsted, Gregory D. Scholes, and Benedetta Mennucci. Electronic energy transfer in condensed phase studied by a polarizable qm/mm model. *Journal of Chemical Theory and Computation*, 5(7):1838–1848, 2009.

- [178] Carles Curutchet, Jacob Kongsted, Aurora Muñoz-Losa, Hoda Hossein-Nejad, Gregory D. Scholes, and Benedetta Mennucci. Photosynthetic light-harvesting is tuned by the heterogeneous polarizable environment of the protein. *Journal of the American Chemical Society*, 133(9):3078–3084, 2011.
- [179] Jörg Megow, Thomas Renger, and Volkhard May. Screening of excitonic coupling in supramolecular complexes. incorporation of Poisson-TrEsp to a mixed quantum-classical methodology. 2012. in preparation.
- [180] Chao-Ping Hsu, Graham R. Fleming, Martin Head-Gordon, and Teresa Head-Gordon. Excitation energy transfer in condensed media. *The Journal of Chemical Physics*, 114(7): 3065–3072, 2001.

Danksagung

Mein Dank gebührt zuallererst PD Dr. habil. Volkhard May, der mich zu jeder Zeit bei der Bearbeitung dieses hochinteressanten Themas unterstützt hat. Die unzähligen Diskussionen mit Herrn Dr. May haben einen großen Anteil an den Ergebnissen dieser Arbeit.

Ich bedanke mich auch bei Dr. Alex Kulesza, der sämtliche Elektronenstrukturrechnungen durchgeführt hat und für mich permanent ansprechbar war und ist. Ein großer Dank gebührt Prof. Bonačić-Koutecký, welche die Zusammenarbeit mit der Gruppe der theoretischen Chemie möglich gemacht hat. Ebenso dankbar bin ich Dr. Ronald Mitric, der diese Zusammenarbeit weitergeführt hat und seine Hilfe für zukünftige Fragestellungen, die theoretische Chemie betreffend, angeboten hat.

Ich möchte auch Prof. Dr. Beate Röder und der AG Photobiophysik meinen Dank für die Begleitung während der letzten Jahre aussprechen. Die vielen Gespräche mit Prof. Röder, Dr. Steffen Hackbarth, Dr. Ronald Steffen, Tobias Bornhütter, Jan Schlothauer, Roel Menting und Sebastian Jungwirth haben mir die experimentellen Problem- und Fragestellungen nahegebracht.

Ich bekunde weiterhin meinen Dank an Prof. Dr. Thomas Renger, der mir die Daten zur Verfügung gestellt hat, die für die Berechnungen im letzten Kapitel meiner Arbeit unerlässlich waren. Bei Prof. Dr. Ulrich Kleinekathöfer und Dr. Carsten Olbrich bedanke ich mich für einige zusätzliche Rechnungen am von mir untersuchten Molekül. Die jährlichen Workshops mit der Gruppe von Prof. Dr. Jörn Manz im Umland von Berlin haben mich sehr motiviert.

Für die Pflege des Institutsnetzwerks und die permanente Ansprechbarkeit gilt ein großer Dank auch Dr. Burkhard Bunk. Bei Inna Megow, Roel Menting, Arne Schönwald, Sophie Schuster, Dr. Yaroslav Zelinsky und Yuan Zhang bedanke ich mich für das Korrekturlesen dieser Arbeit. Dr. Zelinsky hat mich zudem noch bei vielen weiteren Fragestellungen unterstützt. Inna gebührt ein großer Dank für die Entlastung während der letzten Wochen. Inna und meinen Eltern danke ich für die emotionale Unterstützung vor der Abgabe dieser Arbeit. Bei meinen Bürokollegen Luxia Wang, Gerold Kyas und Julie Krainau bedanke ich mich für die sehr angenehme Zeit, sowie bei Gerold und Julie für die simultane Übersetzung ins Englische von spontan in den Raum geworfenen Phrasen.

Nicht zuletzt bedanke ich mich bei der DFG für die Finanzierung des Projektes, auf dessen Grundlage diese Arbeit entstand.

Selbständigkeitserklärung

Ich erkläre, dass ich die vorliegende Arbeit selbständig und nur unter Verwendung der angegebenen Literatur und Hilfsmittel angefertigt habe.

Ich habe mich anderweitig nicht um einen Doktorgrad beworben und besitze einen entsprechenden Doktorgrad nicht.

Die dem Verfahren zugrunde liegende Promotionsordnung der Mathematisch-Naturwissenschaftlichen Fakultät I der Humboldt Universität zu Berlin habe ich zur Kenntnis genommen.

Berlin, den 25.09.2012

Jörg Megow